

NORTHWESTERN UNIVERSITY

Development and Optimization of Functionalized Self-Assembling Polymeric Nanobiomaterials

A DISSERTATION

SUBMITTED TO THE GRADUATE SCHOOL IN PARTIAL FULFILLMENT OF THE REQUIREMENTS

for the degree

DOCTOR OF PHILOSOPHY

Field of Interdisciplinary Biological Sciences

By

Molly Alexandra Frey

EVANSTON, ILLINOIS

December 2021

© Copyright by Molly Alexandra Frey 2021  
All Rights Reserved

## ABSTRACT

# Development and Optimization of Functionalized Self-Assembling Polymeric Nanobiomaterials

**Molly Alexandra Frey**

Nanocarriers as structures with at least one dimension in the nanometer scale are capable of loading small molecule therapeutics that would otherwise have poor bioavailability, non-specific uptake, and off target effects. Polymeric nanocarriers can be modified to tune their chemical and biological behavior to better suit the intended application. This work investigates the development of two such examples of polymeric nanocarriers, poly(ethylene glycol)-block-poly(propylene sulfide) (PEG-*b*-PPS) and the class of poly(amino acid)-block-poly(propylene sulfide) (PAA-*b*-PPS), that can be modified to incorporate a range of unique functionalities. The purpose of these efforts is to demonstrate the versatility of these two diblock copolymer classes of material to be used in a range of biomedical applications.

The optimized synthesis of PEG-*b*-PPS is described to reduce complexities and enhance product quality, followed by two applications that showcase the tuning of PEG-*b*-PPS properties to enhance uptake into non-phagocytic cells, and to deliver a small molecule therapeutic for modulating the inflammasome. Extensive work details the development and optimization of the completely novel PAA-*b*-PPS class of biomimetic self-assembling diblock copolymers that have a vast potential for forming multiple stable morphologies and incorporating modular functionality based on general sequence control of the monomer units.

I found that the synthesis of PEG-*b*-PPS can be significantly improved to produce material of high quality in very high yields while requiring less time and resources compared to previous protocols. I demonstrated that uptake of PEG-*b*-PPS nanocarriers into non-phagocytic DAOY and ASZ cells can be enhanced by selecting the correct morphology, size, and introducing a cationic surface charge. I show that micelles make an effective delivery vehicle for the encapsulation and delivery of the small hydrophobic FiVe1 drug, which may have a number of relative biomedical applications.

I designed an effective strategy to rapidly synthesize PAA-*b*-PPS diblock copolymers in a range of weight ratios using a rationally selected linker for unrestricted combinatorial pairing of polymer blocks. I assembled and characterized representative formulations via three orthogonal techniques to show that this material is capable of forming unique morphologies at defined weight ratios. I then expanded these PAA backbones to more complex functional amino acid units to demonstrate the versatility of this delivery system. Finally, I present an approach to use experimental results and computational analysis to exert general sequence control and synthesize a copolymer with a statistically random order of monomers.

I conclude that these two PEG-*b*-PPS and PAA-*b*-PPS materials are effective platforms for designing nanocarrier therapeutics for biomedical applications with specifically tuned physiochemical characteristics. Additionally, I present the novel PAA-*b*-PPS material as a platform with significant potential as a biomimetic nanocarrier platform worth further investigation.

## Acknowledgments

My journey through this chapter of my life has been marked by periods of highs and lows that I have only been able to overcome with the support of many people to celebrate and suffer together by my side. To each of you, thank you for making this journey possible.

I would first like to thank my thesis committee: Dr. Gregory Beitel, Dr. Neha Kamat, and Dr. Guillermo Ameer. In addition to the mountain of other responsibilities to their own labs and institutional positions, they have followed the development of my thesis work and professional development since my qualifying exam with exceptional patience and expertise. Thank you.

My sincere appreciation goes to the MSTP staff, who have been an anchor through these long years navigating the MD/PhD program. Especially Lindsey and Joyce – your patience and expertise have been immensely helpful. Thank you.

I would like to thank my PI, Evan Scott. I first rotated in the lab back when it was freshly established in a tiny room at the top of Tech, still working to setup many key instruments of a functioning space. Evan agreed to take me on as the first MSTP student when I resurfaced after a couple years of medical school, easily matching my sky-high enthusiasm. I would like to thank Evan for his support as I set out to work on the development of an entirely new nanocarrier material, turning away from the wealth of expertise on the single material that ties together every project in the Scott Lab. Anyone else would have tried to convince me to reconsider in favor of a much less risky project. Without Evan's support, this work which I consider to be an integral part of my contributions to the scientific community would not have been realized. Thank you.

To my mentor, Tom Meade, you have played a unique role in my development as a scientist in unexpected ways on top of your scientific guidance. I will always be grateful for your confidence that helped me find strength for each stressful situation. Thank you.

I would like to acknowledge the members of the Scott Lab throughout the years as my lab home. Our group has always been on the smaller side, making our relationships especially meaningful as we form the lab's culture. Thank you to Fanfan, Sijia, Debora, Sun-Young, Nick, Trevor, Mike, Clayton, JB, and Chamille. Each of you are what makes the Scott Lab successful.

In addition to this list are members of the lab that I've had the opportunity to work with more closely. Sharan – you have been a professor to us all since day one with your teaching and contributions. Just as our chapters begin and end at the same time, let's find success as we move on to bigger things. Raj – you may never realize how much your optimism encouraged me to push through one of the more difficult times of my PhD. I look forward your future as an MD/PhD student (which I will take full credit for inspiring you!). To Mallika and Sophia, my MSTP friends - you two have been my anchor to the real world, always coming up with ideas to spend free time. Let's finish this journey together. Megan – my CLP friend and beyond, thank you keeping track of me and my schedule, and for letting me ride your horse off a cliff. Please take care of yourself!

To my friends, Sean, Jen, Meghan: I'll keep this short because I would much rather spend an afternoon talking with you in person about my feelings. But I'll emphasize here that each of you have played a crucial role in my life both personally and professionally. This dissertation and everything it took to push through it was possible in part because of you. Thank you.

Finally, to my family. To my parents, thank you for always supporting me, even though this career path means that it is hard to explain to our extended family why I am *still* in school at each holiday. Mom – you have always inspired me to pursue medicine since as early as I can remember, especially instilling in me the fact that nurses are the backbones of the healthcare industry which will serve me well through my career. Dad – our different backgrounds make it so that you are always able to give me a fresh perspective on any difficult situation to help me find balance when my perspective narrows. To my sister, Sadie. You are the definition of family to me. We are always there for each other, even if we disagree. There isn't a problem in any aspect of our lives that we can't navigate through together and won't sprinkle in a bit of our fully incomprehensible style of humor. Thank you.

## List of Abbreviations

<b><sup>1</sup>H NMR</b>	Proton nuclear magnetic resonance
<b><sup>13</sup>C NMR</b>	Carbon nuclear magnetic resonance
<b>1-MT</b>	1-methyl tryptophan
<b>ABC</b>	Accelerated blood clearance
<b>AcOH</b>	Acetic acid
<b>ADH</b>	Alcohol dehydrogenase
<b>ANOVA</b>	Analysis of variance
<b>Ar</b>	Argon gas
<b>ASC</b>	Adaptor molecule apoptosis-associated speck-like protein containing a CARD
<b>APC</b>	Antigen presenting cell
<b>ATP</b>	Adenosine triphosphate
<b>BBB</b>	Blood brain barrier
<b>BCC</b>	Basal cell carcinoma
<b>BCN</b>	Bicontinuous nanosphere
<b>BMDM</b>	Bone marrow-derived macrophage
<b>Bz</b>	Benzyl, benzyl ester
<b>BzBr</b>	Benzyl bromide
<b>BzGlu</b>	Glutamic acid $\gamma$ -benzyl ester
<b>BzGlu NCA</b>	Glutamic acid $\gamma$ -benzyl ester N-carboxyanhydride

<b>Ca<sup>2+</sup></b>	Calcium ions
<b>CARPA</b>	Complement activation-related pseudoallergy
<b>CDCl<sub>3</sub></b>	Deuterated chloroform
<b>CIJ</b>	Confined impingement jet
<b>CO<sub>2</sub></b>	Carbon dioxide
<b>CryoTEM</b>	Transmission electron cryomicroscopy
<b>CYP</b>	Cytochrome P450
<b>d</b>	Diameter
<b>DAMPs</b>	Damage-associated molecular patterns
<b>DBPS</b>	Dulbecco's Phosphate Buffered Saline
<b>DCM</b>	Dichloromethane
<b>DFA</b>	Difluoroacetic acid
<b>DFT</b>	Density functional theory
<b>Dil</b>	1.1'-Dioctadecyl-3,3,3',3'-tetramethylindocarbocyanine perchlorate
<b>DLS</b>	Dynamic light scattering
<b>DMEM</b>	Dulbecco's Modified Eagle Medium
<b>DMF</b>	Dimethylformamide
<b>DMSO</b>	Dimethylsulfoxide
<b>DMSO-d<sub>6</sub></b>	Deuterated dimethylsulfoxide
<b>DNA</b>	Deoxyribonucleic Acid
<b>DND-CAT</b>	DuPont-Northwestern-Dow Collaborative Access Team

<b>DP<sub>n</sub></b>	Degree of polymerization
<b>EE</b>	Ethyl eosin
<b>ELISA</b>	Enzyme-linked immunosorbent assay
<b>ELS</b>	Electrophoretic light scattering
<b>EMT</b>	Epithelial-mesenchymal transition
<b>EPR</b>	Enhanced permeation and retention
<b>Eq</b>	Equivalent(s)
<b>Et<sub>2</sub>O</b>	Diethyl ether
<b>Ext</b>	Extraction
<b>FBS</b>	Fetal bovine serum
<b>FiVe1</b>	FOXC2-inhibiting Vimentin effector 1
<b>FM</b>	Filomicelle
<b>FNP</b>	Flash nanoprecipitation
<b>f<sub>PEG</sub></b>	PEG (hydrophilic) weight fraction
<b>f<sub>pSarc</sub></b>	pSarc (hydrophilic) weight fraction
<b>FTS</b>	Phenylthiosulfonyl
<b>FTS-Cys</b>	Phenylthiosulfonyl-cysteine
<b>FTS-PAA</b>	Phenylthiosulfonyl-poly(amino acid)
<b>FTS-pGlu</b>	Phenylthiosulfonyl-poly(glutamic acid)
<b>FTS-pLys</b>	Phenylthiosulfonyl-poly(lysine)
<b>FTS-pSarc</b>	Phenylthiosulfonyl-poly(sarcosine)

<b>FTS-pTrp</b>	Phenylthiosulfonyl-poly(tryptophan)
<b>FTS-pTyr</b>	Phenylthiosulfonyl-poly(tyrosine)
<b>GA</b>	Glatiramer acetate
<b>Glu</b>	Glutamic acid
<b>Gly</b>	Glycine
<b>Gly NCA</b>	Glycine N-carboxyanhydride
<b>HBr</b>	Hydrogen bromide
<b>HCl</b>	Hydrochloride
<b>HPLC</b>	High performance liquid chromatography
<b>HSAc</b>	Thioacetic acid
<b>HSR</b>	Hypersensitivity reaction
<b>IC<sub>50</sub></b>	Half-maximal inhibitory concentration
<b>IDO</b>	Indoleamine 2,3 dioxygenase
<b>IL</b>	Interleukin
<b>IRF3</b>	IFN regulatory factor 3
<b>K<sup>+</sup></b>	Potassium ion
<b>K<sub>2</sub>CO<sub>3</sub></b>	Potassium Carbonate
<b>Kyn</b>	Kynurenine
<b>LADMET</b>	Liberation, absorption, distribution, metabolism, excretion, and toxicity
<b>LDH</b>	Lactate dehydrogenase
<b>LogP</b>	Logarithm of the partition coefficient, P

<b>LogD</b>	Logarithm of the distribution coefficient, D
<b>LPS</b>	Lipopolysaccharide
<b>Lys</b>	Lysine
<b>LysZ</b>	<i>N</i> <sub>6</sub> -carbobenzyloxy-L-lysine
<b>LysZ NCA</b>	<i>N</i> <sub>6</sub> -carbobenzyloxy-L-lysine N-carboxyanhydride
<b>MC</b>	Micelle
<b>MeOH</b>	Methanol
<b>MFI</b>	Median fluorescence intensity
<b>mPEG<sub>m</sub></b>	Monomethoxy poly(ethylene glycol), MW subscript (750 g/mol, 2000 g/mol)
<b>mPEG-OMs</b>	Monomethoxy poly(ethylene glycol)-mesylate
<b>mPEG-OTs</b>	Monomethoxy poly(ethylene glycol)-tosylate
<b>mPEG-SAc</b>	Monomethoxy poly(ethylene glycol)-thioacetate
<b>MPS</b>	Mononuclear phagocyte system
<b>MQ</b>	Milli-Q water
<b>mRNA</b>	Messenger RNA
<b>MS</b>	Multiple sclerosis
<b>MsCl</b>	Methanesulfonyl chloride
<b>MTS</b>	3-(4,5-dimethylthiazol-2-yl)-5-(3-carboxymethoxyphenyl)-2-(4-sulfophenyl)-2H-tetrazolium, inner salt
<b>MTT</b>	3-(4,5-dimethylthiazol-2-yl)-2,5-diphenyltetrazolium bromide)
<b>MW</b>	Molecular weight

<b>N<sub>2</sub></b>	Nitrogen gas
<b>Na<sup>+</sup></b>	Sodium ion
<b>NaCl</b>	Sodium chloride
<b>NaOH</b>	Sodium hydroxide
<b>Na<sub>2</sub>SO<sub>4</sub></b>	Sodium sulfate
<b>NaOCH<sub>3</sub></b>	Sodium methoxide (NaOMe)
<b>NCA</b>	N-carboxyanhydride
<b>N.d.</b>	Not detected
<b>NF-κB</b>	Nuclear factor kappa-light-chain-enhancer of activated B cells
<b>NH<sub>4</sub>Cl</b>	Ammonium chloride
<b>NMP</b>	N-Methyl-2-pyrrolidone
<b>NIOSH</b>	National Institute for Occupational Safety and Health
<b>NLRP3</b>	NLR family pyrin domain containing 3
<b>NOD2</b>	Nucleotide-binding oligomerization domain-containing protein 2
<b>NP</b>	Nanoparticle
<b>nsTEM</b>	negative stain transmission electron microscopy
<b>OMs</b>	Mesylate group
<b>OTs</b>	Tosylate group
<b>PAA</b>	poly(amino acid)
<b>PAA-<i>b</i>-PPS</b>	poly(amino acid)-block-poly(propylene sulfide)
<b>PAMPs</b>	Pathogen-associated molecular patterns

<b>PBS</b>	Phosphate Buffered Saline
<b>pBzGlu</b>	Poly(glutamic acid $\gamma$ -benzyl ester)
<b>P<sub>c</sub></b>	Packing parameter
<b>PDI</b>	Polydispersity index
<b>PEG</b>	Poly(ethylene glycol)
<b>PEG-<i>b</i>-PPS</b>	Poly(ethylene glycol)-block-poly(propylene sulfide)
<b>PEI</b>	Polyethylenimine
<b>pGlu</b>	Poly(glutamic acid)
<b>pGlu-<i>b</i>-PPS</b>	Poly(glutamic acid)-block-poly(propylene sulfide)
<b>pGly</b>	Poly(glycine)
<b>pK<sub>a</sub></b>	Acid dissociation constant
<b>pLys</b>	Poly(lysine)
<b>pLysZ</b>	Poly( <i>N</i> <sub>6</sub> -carbobenzyloxy-L-lysine)
<b>PPO</b>	Poly(propylene oxide)
<b>PPS</b>	Poly(propylene sulfide)
<b>ppt</b>	Precipitation
<b>PS</b>	Polymersomes
<b>pSarc</b>	Poly(sarcosine)
<b>pSarc-<i>b</i>-PPS</b>	Poly(sarcosine)-block-poly(propylene sulfide)
<b>PTP</b>	Permeability transition pore
<b>pTrp</b>	Poly(tryptophan)

<b>pTrp-<i>b</i>-PPS</b>	Poly(tryptophan)-block-poly(propylene sulfide)
<b>pTyr</b>	Poly(tyrosine)
<b>pTyr-<i>b</i>-PPS</b>	Poly(tyrosine)-block-poly(propylene sulfide)
<b>QRV</b>	Quenched rotary evaporation
<b>RES</b>	Reticuloendothelial system
<b>ROP</b>	Ring-opening polymerization
<b>ROS</b>	Reactive oxygen species
<b>RV</b>	Rotary evaporation
<b>SAc</b>	Thioacetate
<b>Sarc</b>	Sarcosine, n-methyl glycine
<b>Sarc NCA</b>	Sarcosine N-carboxyanhydride
<b>SAXS</b>	Small-angle s-ray scattering
<b>SPPS</b>	Solid-phase peptide synthesis
<b>TEA</b>	Triethylamine
<b>TEM</b>	Transmission electron microscopy
<b>TF</b>	Thin-film (re)hydration
<b>TFA</b>	Trifluoroacetic acid
<b>T<sub>g</sub></b>	Glass transition temperature
<b>THF</b>	Tetrahydrofuran
<b>Trp</b>	Tryptophan
<b>Trp NCA</b>	Tryptophan N-carboxyanhydride

<b>Tyr</b>	Tyrosine
<b>Tyr NCA</b>	Tyrosine N-carboxyanhydride
<b>UF</b>	Uranyl formate
<b>UTC</b>	Untreated control
<b>UV-Vis</b>	Ultraviolet–visible spectroscopy
<b>WT</b>	Wild type
<b>ZP</b>	Zeta potential

## Table of Contents

Abstract .....	3
Acknowledgments.....	5
List of Abbreviations.....	8
Table of Contents .....	17
List of Figures .....	23
List of Schemes.....	26
List of Tables.....	27
<b>CHAPTER 1: Overview and Review of Literature .....</b>	<b>28</b>
<b>1.1 Dissertation Overview .....</b>	<b>28</b>
1.1.1 Motivations and Objectives.....	28
1.1.2 Dissertation Outline .....	28
<b>1.2 Review of Literature .....</b>	<b>30</b>
1.2.1 Nanoparticle delivery systems for biomedical applications .....	30
1.2.2 Tuning nanoparticle physiochemical characteristics to enhance biological function...	34
1.2.3 Non-specific immune uptake of nanoparticles .....	45
1.2.4 Enhanced pharmacokinetics with poly(ethylene glycol) .....	49
1.2.5 Poly(ethylene glycol)- <i>block</i> -poly(propylene sulfide) nanomaterial .....	54
<b>1.3 Scope of this work .....</b>	<b>61</b>
<b>1.4 Publication information.....</b>	<b>61</b>
<b>CHAPTER 2: Optimized synthesis and purification of poly(ethylene glycol)-block-poly(propylene sulfide).....</b>	<b>62</b>
<b>2.1 Abstract .....</b>	<b>62</b>
<b>2.2 Introduction.....</b>	<b>62</b>
2.2.1 Initial PEG functionalization to thioacetate.....	64
2.2.2 PEG thioacetate initiator for PPS polymerization and PEG- <i>b</i> -PPS self-assembly .....	66
2.2.3 Development of PEG- <i>b</i> -PPS as a drug delivery vehicle .....	68
2.2.4 Benchmarking the modern PEG- <i>b</i> -PPS syntheses protocol.....	68

2.2.5 Assembly via flash nanoprecipitation and characterization .....	70
2.2.6 Chapter objectives .....	71
<b>2.3 Materials and Methods .....</b>	<b>74</b>
2.3.1 Materials and Instrumentation.....	74
2.3.2 Previous protocols for the synthesis of mPEG-OMs, mPEG-SAc, and PEG- <i>b</i> -PPS .....	75
2.3.3 Synthesis of mPEG-OMs .....	75
2.3.4 Synthesis of mPEG-SAc .....	76
2.3.5 Synthesis of mPEG- <i>b</i> -PPS.....	77
2.3.6 Nanoparticle assembly and purification.....	78
2.3.7 Nanoparticle characterization .....	79
<b>2.4 Results and Discussion.....</b>	<b>80</b>
2.4.1 mPEG starting material preparation .....	80
2.4.2 mPEG-OMs reaction condition optimizations.....	81
2.4.3 mPEG-SAc reaction condition optimizations.....	85
2.4.4 Optimized workup based on PEG chain length .....	90
2.4.5 PEG- <i>b</i> -PPS polymerization .....	94
2.4.6 Time, cost, and yield of optimized protocols .....	98
<b>2.5 Conclusion .....</b>	<b>99</b>
<b>2.6 Acknowledgments .....</b>	<b>102</b>
<b>2.7 Publication information.....</b>	<b>102</b>
<b>CHAPTER 3: Tailoring nanocarrier morphology and surface charge for uptake in non-APC cell lines .....</b>	<b>103</b>
<b>3.1 Abstract .....</b>	<b>103</b>
<b>3.2 Introduction.....</b>	<b>104</b>
3.2.1 Routes of nanoparticle uptake into cells.....	104
3.2.2 Enhancing uptake: size, charge, morphology.....	105
3.2.3 Toxicities of size, charge, morphology .....	109
3.2.4 ASZ, DAOY cells .....	113
3.2.5 Chapter objectives .....	115
<b>3.3 Materials and Methods .....</b>	<b>116</b>
3.3.1 Materials and Instrumentation.....	116
3.3.2 ASZ and DAOY cell culture .....	116
3.3.3 Synthesis of NH <sub>3</sub> -PEG- <i>b</i> -PPS diblock copolymer .....	117
3.3.4 Assembly of cationic formulations .....	118
3.3.5 Nanoparticle characterization: Size, polydispersity, and zeta potential .....	118
3.3.6 Uptake and confocal microscopy .....	119
3.3.7 Cytotoxicity .....	119

3.3.8 Flow cytometry .....	120
<b>3.4 Results and Discussion.....</b>	<b>121</b>
3.4.1 Initial uptake into DAOY and ASZ cell lines by morphology .....	121
3.4.2 Enhancing uptake into DAOY and ASZ cell lines with charged formulations .....	123
3.4.3 Cytotoxicity profile of charged formulations .....	127
<b>3.5 Conclusion .....</b>	<b>128</b>
<b>3.6 Acknowledgements .....</b>	<b>130</b>
<b>3.7 Publication information.....</b>	<b>130</b>
<b>CHAPTER 4: Development of FiVe-1-loaded nanocarriers for inhibiting vimentin .....</b>	<b>131</b>
<b>4.1 Abstract .....</b>	<b>131</b>
<b>4.2 Introduction.....</b>	<b>132</b>
4.2.1 Inflammasome activation and regulation .....	132
4.2.2 Targeting vimentin to inhibit inflammasome-mediated damage.....	134
4.2.3 Small molecule FiVe1 as a vimentin inhibitor for potential prevention of inflammasome-mediated damage.....	135
4.2.4 Chapter objectives .....	137
<b>4.3 Materials and Methods .....</b>	<b>139</b>
4.3.1 Materials and Instrumentation.....	139
4.3.2 Assembly and loading of PEG- <i>b</i> -PPS micelles.....	139
4.3.3 Nanoparticle characterization .....	140
4.3.4 Quantification of FiVe1 .....	141
4.3.5 BMDM cell culture and differentiation .....	141
4.3.6 Cytotoxicity (LDH assay).....	141
4.3.7 IL-1 $\beta$ quantification and flow cytometry .....	142
<b>4.4 Results and Discussion.....</b>	<b>142</b>
4.4.1 FiVe1 loading into micelles .....	142
4.4.2 Establishing baseline <i>innnnnn</i> conditions for FiVe1-loaded micelles .....	145
4.4.3 Therapeutic effect of free FiVe1 on inflammasome inhibition.....	148
4.4.4 Therapeutic effect of FiVe1-loaded micelles on inflammasome inhibition .....	150
4.4.5 Considerations of FiVe1 as a vimentin inhibitor .....	152
<b>4.5 Conclusion .....</b>	<b>155</b>
<b>4.6 Acknowledgements .....</b>	<b>156</b>
<b>4.7 Publication information.....</b>	<b>157</b>

<b>CHAPTER 5: Development of a self-assembling poly(amino acid)-<i>b</i>-PPS nanocarrier platform</b> .....	158
5.1 Abstract .....	158
5.2 Introduction.....	159
5.2.1 PEG disadvantages.....	159
5.2.2 Poly(amino acids) as materials for biomedical applications.....	163
5.2.3 Poly(amino acid) synthesis via N-carboxyanhydride chemistry.....	164
5.2.4 Considerations for nanoparticle self-assembly.....	167
5.2.5 Strategies to rapidly screen the self-assembly of novel materials.....	168
5.2.6 Chapter objectives.....	171
5.3 Materials and Methods.....	174
5.3.1 Materials and instrumentation.....	174
5.3.2 Preparation of Gly NCA, Sarc NCA, BzGlu NCA, LysZ NCA, Trp NCA, and Tyr NCA.....	175
5.3.3 Preparation of phenylthiosulfonyl cysteine (FTS-Cys).....	177
5.3.4 Preparation of FTS-poly(sarcosine) (FTS-pSarc), FTS-poly(tryptophan) (FTS-pTrp), FTS-poly(tyrosine) (FTS-pTyr), FTS-poly(glutamic acid) (FTS-pGlu), and FTS-poly(lysine) (FTS-pLys).....	179
5.3.5 Preparation of PPS homopolymer.....	182
5.3.6 Synthesis of PAA- <i>b</i> -PPS copolymers.....	183
5.3.7 Assembly of PAA- <i>b</i> -PPS copolymers.....	185
5.3.8 Characterization of PAA- <i>b</i> -PPS copolymers.....	186
5.3.9 RAW 264.7 cell culture.....	189
5.3.10 Cytotoxicity.....	190
5.4 Results and Discussion.....	190
5.4.1 A note on phosgene safety.....	190
5.4.2 Finding a suitable pilot backbone.....	191
5.4.3 Finding a suitable NCA/PPS linker.....	195
5.4.4 Synthesis of pSarc- <i>b</i> -PPS copolymers.....	201
5.4.5 Assembly of pSarc- <i>b</i> -PPS copolymers.....	206
5.4.6 Characterization of pSarc- <i>b</i> -PPS copolymers.....	211
5.4.7 Synthesis of NCA monomers for expanded PAA- <i>b</i> -PPS backbones.....	219
5.4.8 Synthesis, assembly, and characterization of expanded PAA- <i>b</i> -PPS backbones.....	227
5.5 Conclusion.....	231
5.6 Acknowledgements.....	236
5.7 Publication information.....	236
<b>CHAPTER 6: Implementing general sequence control over the NCA copolymerization of protected lysine and glutamic acid</b> .....	238

6.1 Abstract .....	238
6.2 Introduction.....	239
6.2.1 Bioactive peptide synthesis and specific sequence control.....	239
6.2.2 Structural poly(amino acids) and general sequence control .....	241
6.2.3 General polymer sequence types.....	242
6.2.4 Monomer reactivity ratios as critical determinants of copolymer sequence .....	246
6.2.5 Determining reactivity ratios.....	251
6.2.6 General sequence control using applied reactivity ratios .....	252
6.2.7 Accounting for monomer feed consumption.....	255
6.2.8 Chapter objectives .....	256
6.3 Materials and Methods .....	259
6.3.1 Materials and instrumentation.....	259
6.3.2 BzGlu and LysZ homopolymer kinetic studies.....	260
6.3.3 Preparation of poly(LysZ-co-BzGlu) copolymer with defined feed ratios.....	261
6.3.4 Drift correction protocol for extended poly(LysZ-co-BzGlu) copolymer .....	262
6.3.5 Experimental analysis of copolymers .....	263
6.3.7 Computation and modeling.....	263
6.4 Results and Discussion.....	263
6.4.1 Quenching for fractional conversion analysis .....	263
6.4.2 Homopolymer kinetics to find reactivity ratios.....	264
6.4.3 Identifying the ideal monomer feed composition .....	268
6.4.4 Copolymerization with adjusted and unadjusted feed composition.....	269
6.4.5 Drift correction with monomer supplementation .....	272
6.5 Conclusion .....	275
6.6 Acknowledgements .....	278
6.7 Publication information.....	279
<b>CHAPTER 7: Concluding Remarks and Future Directions .....</b>	<b>280</b>
7.1 Concluding remarks.....	280
7.1.1 PEG- <i>b</i> -PPS optimizations .....	280
7.1.2 Tuning PEG- <i>b</i> -PPS nanocarriers for uptake and therapeutic potential .....	281
7.1.3 Development of NCA-based nanocarriers.....	282
7.1.4 General sequence control of NCA-based functional materials .....	284
7.2 Future directions .....	284
7.2.1 Further development of PEG- <i>b</i> -PPS synthesis for scaling up and improving the assembly of unique morphologies .....	285
7.2.2 Applications for the uptake of PEG- <i>b</i> -PPS nanocarriers into ASZ and DAOY cell lines .....	287

7.2.3 Optimization of FiVe1-loaded micelles for vimentin inhibition and other therapeutics for inflammasome modulation.....	288
7.2.4 Expanding the library of functional NCA monomers for structural and therapeutic applications.....	289
7.2.5 Development of the PAA- <i>b</i> -PPS platform for drug delivery and biological applications .....	292
7.2.6 Incorporating general sequence control for biologically relevant motifs .....	294
References.....	296
Curriculum Vitae .....	332

## List of Figures

- Figure 1-1.** The disadvantages of free small molecule therapeutics in biological systems.
- Figure 1-2.** The advantages and disadvantages of polymer coatings on small molecule therapeutics in biological systems.
- Figure 1-3.** The advantages of nanocarrier delivery systems on small molecule therapeutics in biological systems.
- Figure 1-4.** Commonly modified properties of nanocarrier delivery vehicles to enhance performance in biological applications.
- Figure 1-5.** The organ-level biodistribution of nanoparticles with different sizes and morphologies.
- Figure 1-6.** The general effects of nanoparticle size and charge on circulation time and relevant clearance events.
- Figure 1-7.** Loading of hydrophilic and hydrophobic cargo based on internal architecture and nanoparticle size.
- Figure 1-8.** Opsonization and non-specific immune uptake of nanoparticles.
- Figure 1-9.** Water coordination of PEG units to form a protective hydration shell.
- Figure 1-10.** Diverse morphologies of self-assembling PEG-*b*-PPS materials based on the hydrophilic weight fraction.
- Figure 1-11.** Oxidation-triggered PPS transition to hydrophilic sulfone units and subsequent disassembly.
- Figure 2-1.** Significant events in the development of PEG-*b*-PPS diblock copolymers for drug delivery.
- Figure 2-2.** NMR monitoring of reaction times for the mesylate synthesis of mPEG<sub>750</sub> and mPEG<sub>2000</sub>.
- Figure 2-3.** Heatmap of reaction conversion comparing reagent equivalents for mPEG-SAc.
- Figure 2-4.** NMR monitoring of reaction times and corresponding color development for the thioacetate synthesis of mPEG<sub>750</sub> and mPEG<sub>2000</sub>.
- Figure 2-5.** Schematic of summarized conditions for efficient workup and purification of both mPEG<sub>750</sub>-OMs and mPEG<sub>2000</sub>-OMs in the previous and proposed protocols.

- Figure 2-6.** Schematic of summarized conditions for efficient workup and purification of both mPEG<sub>750</sub>-SAC and mPEG<sub>2000</sub>-SAC in the previous and proposed protocols.
- Figure 2-7.** Characterization of MC, PS, and BCN nanostructures.
- Figure 3-1.** The effects of particle size and charge on cellular uptake.
- Figure 3-2.** Major mechanisms for cationic-induced cytotoxicity.
- Figure 3-3.** Characterization of micelle and polymersome formulations.
- Figure 3-4.** Uptake of micelles and polymersomes into DAOY and ASZ cells.
- Figure 3-5.** Uptake of charged micelle formulations into ASZ and DAOY cells via flow cytometry.
- Figure 3-6.** Uptake of charged polymersome formulations into DAOY cells via flow cytometry.
- Figure 3-7.** Cytotoxicity of the two highest cationic formulations.
- Figure 4-1.** Overview of the signaling cascade after pathogenic infiltration to form the NLRP3 inflammasome.
- Figure 4-2.** Structure of the small molecule FiVe1 inhibitor of vimentin.
- Figure 4-3.** HPLC quantification of free and loaded FiVe1 samples.
- Figure 4-4.** Loading and characterization of micelle nanoparticles with FiVe1.
- Figure 4-5.** *In vitro* baseline establishment of micelle inflammasome activation and cytotoxicity of all formulations.
- Figure 4-6.** Uptake of blank micelles in BMDMs after LPS challenge.
- Figure 4-7.** Normalized ELISA quantification of IL-1 $\beta$  production in BMDM cells treated with matched FiVe1 concentrations after LPS challenge in two replicate plates
- Figure 5-1.** Summary of PEG limitations and disadvantages.
- Figure 5-2.** General scheme of N-carboxyanhydride (NCA) polymer chemistry.
- Figure 5-3.** Efficient strategy to assemble diverse diblock copolymers using a combinatorial library and rational linker.
- Figure 5-4.** Intermolecular associations between poly(glycine) and poly(sarcosine) chains.
- Figure 5-5.** <sup>1</sup>H NMR of FTS-pSarc homopolymer and pSarc-*b*-PPS diblock copolymer.

- Figure 5-6.** Overview of pSarc-*b*-PPS diblock copolymer assembly via thin film rehydration.
- Figure 5-7.** Overview of pSarc-*b*-PPS diblock copolymer assembly via flash nanoprecipitation.
- Figure 5-8.** DLS results for optimized pSarc-*b*-PPS formulations.
- Figure 5-9.** Negative stain TEM of pSarc-*b*-PPS formulations.
- Figure 5-10.** SAXS scattering and model fits for pSarc-*b*-PPS formulations.
- Figure 5-11.** Schematic of pSarc-*b*-PPS micelle and vesicle morphology ranges on the scale of hydrophilic weight fraction.
- Figure 5-12.** Cytotoxicity of representative pSarc-*b*-PPS formulations.
- Figure 5-13.** Structures of amino acid monomers and polymers synthesized for this chapter.
- Figure 5-14.**  $^1\text{H}$  NMR of FTS-PAA expanded chains of pLysZ, pBzGlu, pTrp, and pTyr.
- Figure 5-15.** Fluorescence of pBzGlu and pSarc polymers with and without Trp.
- Figure 5-16.** Synthesis and assembly of expanded PAA-*b*-PPS copolymer backbones.
- Figure 6-1**
- .
- Integration of charged monomers in a copolymer chain to produce a zwitterionic material.
- Figure 6-2.** Three types of general copolymer sequences for two-monomer systems.
- Figure 6-3.** The four deterministic (Markov) outcomes and corresponding reactivity ratios of a two-monomer system based on the active terminal end.
- Figure 6-4.** Three general copolymer sequences with the associated relationship to reactivity ratios.
- Figure 6-5.** The four deterministic outcomes based on the terminal Markov model.
- Figure 6-6.** Homopolymer kinetics to solve for the homopolymerization rates of  $k_{11}$  for BzGlu and  $k_{22}$  for LysZ.
- Figure 6-7.** The Fineman-Ross approach to solving for reactivity ratios for BzGlu and LysZ NCA monomers.
- Figure 6-8.** Copolymerization of poly(Lys-*co*-Glu) chains with monomer feed adjustment.
- Figure 6-9.** Copolymerization of poly(Lys-*co*-Glu) chains with semi-batch drift correction.

## List of Schemes

- Scheme 2-1.** Preparation of mPEG-OMs using previously established and optimized protocols.
- Scheme 2-2.** Preparation of mPEG-SAc.
- Scheme 2-3.** Preparation of PEG-*b*-PPS diblock copolymer.
- Scheme 5-1.** Preparation of amino acid NCA monomers from glycine, sarcosine, protected lysine, protected glutamic acid, tryptophan, and tyrosine.
- Scheme 5-2.** Preparation of phenylthiosulfonyl-cysteine (FTS-Cys).
- Scheme 5-3.** Preparation of poly(amino acids) from glycine, sarcosine, protected lysine, protected glutamic acid, tryptophan, and tyrosine.
- Scheme 5-4.** Preparation of deprotected poly(amino acids) from lysine and glutamic acid.
- Scheme 5-5.** Preparation of poly(propylene sulfide) homopolymer.
- Scheme 5-6.** Preparation of PAA-*b*-PPS copolymers from sarcosine, lysine, glutamic acid, tryptophan, and tyrosine.
- Scheme 5-7.** Preparation of pSarc-*b*-PPS using the FTS-Cys linker for combinatorial block pairing.
- Scheme 6-1.** Copolymerization of LysZ NCA and BzGlu NCA with a hexylamine initiator.

## List of Tables

- Table 2-1.** Optimization of reagent equivalents and solvent concentrations for the mesylate synthesis of mPEG<sub>750</sub> and mPEG<sub>2000</sub>.
- Table 2-2.** Optimization of workup conditions for the mesylate synthesis of mPEG<sub>750</sub> and mPEG<sub>2000</sub>.
- Table 2-3.** Optimization of workup conditions for the thioacetate synthesis of mPEG<sub>750</sub> and mPEG<sub>2000</sub>.
- Table 2-4.** Summary characterization metrics of MC, PS, and BCN PEG-*b*-PPS polymer formulations.
- Table 2-5.** Summary of optimized time, cost, and yield calculations for the mesylate and thioacetate synthesis of mPEG<sub>750</sub> and mPEG<sub>2000</sub>.
- Table 5-1.** Potential linker strategies for unrestricted pairing of PAA and PPS polymer blocks and chemical considerations.
- Table 5-2.** Library of pSarc-*b*-PPS copolymers after FTS-Cys linker-mediated combinatorial pairing.
- Table 5-3.** Optimization and characterization of pSarc-*b*-PPS formulations assembled via FNP.
- Table 5-4.** Characterization of pSarc-*b*-PPS formulations via DLS, nsTEM, and SAXS.

## CHAPTER 1

### Overview and Review of Literature

#### 1.1 Dissertation Overview

##### 1.1.1 Motivations and Objectives

The field of nanoparticle therapeutics has been developing at a significant pace with the advancement of rationally designed and highly tuned material constructs to best suit the biomedical application. Despite this enthusiasm, close attention must be paid to the continued exploration of novel materials with unique functional capabilities and chemical signatures that can be synthesized reliably. This work details two such diblock copolymer materials for self-assembled drug delivery vehicles: the optimized synthesis and selected applications of poly(ethylene glycol)-*block*-poly(propylene sulfide) (PEG-*b*-PPS), and the development of a novel biomimetic copolymer class of poly(amino acid)-*block*-poly(propylene sulfide) (PAA-*b*-PPS) as a highly modular material with vast functionalization capabilities.

##### 1.1.2 Dissertation Outline

The remainder of Chapter 1 provides a comprehensive review of the challenges associated with small molecule drug administration and the advantages provided by nanocarrier delivery systems. This section discusses the vast range of tunable characteristics of nanocarriers and how they can be specifically tuned to enhance biological outcomes including circulation, biodistribution, and cargo loading and release. The mechanism and impact of non-specific

immune uptake is introduced followed by a detailed discussion of the features of PEG polymers that impart stealth character. Finally, a brief overview of PEG-*b*-PPS and the PPS polymer block describes the key features that contribute to their potency and potential as nanoparticle therapeutic delivery vehicles. Chapter 2 features the in-depth optimization of PEG-*b*-PPS material to increase yield and purity while decreasing the required time, cost, and material consumption. Chapter 3 demonstrates the approach to modifying PEG-*b*-PPS nanoparticles to enhance uptake in the non-phagocytic cell lines ASZ and DAOY without inducing cytotoxicity. Chapter 4 discusses the development of PEG-*b*-PPS nanocarriers for the loading and delivery of a small molecule vimentin inhibitor, FiVe1, for the inhibition of inflammasome-mediated tissue injury. In Chapter 5, I introduce N-carboxyanhydride (NCA) polymer chemistry to develop a novel class of PAA-*b*-PPS materials as drug delivery vehicles using poly(sarcosine) as a pilot. I first develop the synthesis of a combinatorial library, assembly of stable formulations, and subsequent probing of the assembly space to identify several morphologies for this material before expanding the backbone to more complex PAA polymers. Chapter 6 builds on this NCA polymer work by developing a reciprocal computational approach to synthesizing mixed PAA copolymers with general sequence control. Finally, Chapter 7 summarizes this work and presents a number of exciting future directions for each project detailed throughout these chapters for both PEG-*b*-PPS and PAA-*b*-PPS materials.

## 1.2 Review of Literature

### 1.2.1 Nanoparticle delivery systems for biomedical applications

Small molecules comprise the vast majority of biologically active therapeutics used in modern medicine.<sup>1</sup> Their small size enables them to cross membrane barriers or be completely enveloped into the pocket of target enzymes such as inhibitors, ligands, or modulators. However, the effectiveness of these therapeutics is significantly limited by a number of factors related to their size, chemical properties, and non-specific targeting (**Figure 1-1**).<sup>2,3</sup> The resulting decrease in pharmacokinetic performance can easily remove the compound from the therapeutic developmental pipeline.<sup>4</sup> Specifically, nearly 90% of all identified small molecules with therapeutic potential are poorly water soluble which significantly impacts their stability in the aqueous biological environment and reduces bioavailability (**Figure 1-1a**).<sup>2,5</sup> In circulation, free

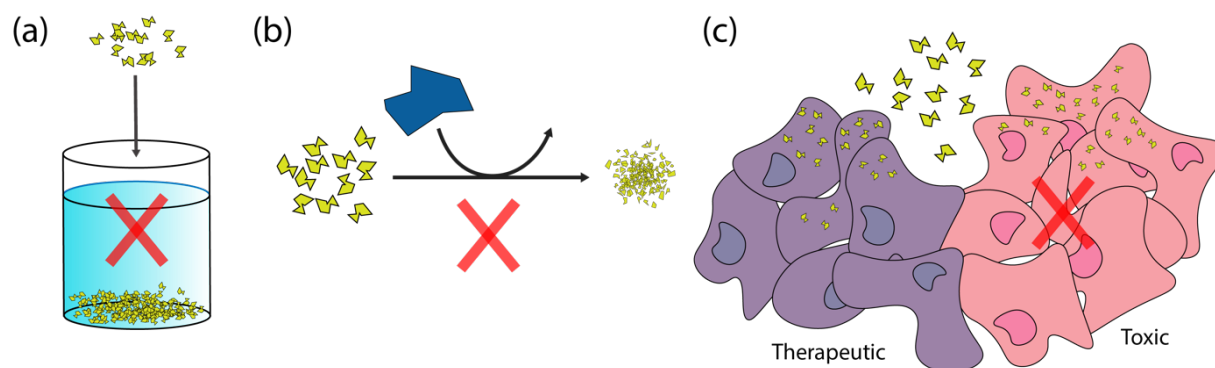


**Figure 1-1. The disadvantages of free small molecule therapeutics in biological systems.** (a) Small molecule therapeutics are poorly soluble and prone to aggregation in aqueous media including blood circulation. (b) Free drug is susceptible to enzymatic degradation and non-specific immune uptake, reducing the half-life. (c) Free drugs are often taken up non-specifically by multiple cell types, inducing significant cytotoxicity and organ level side effects.

drug is susceptible to proteolytic degradation which destroys the therapeutic and non-specific immune uptake, thus reducing its half-life (**Figure 1-1b**).<sup>6</sup> Small molecules with poor targeting may also cause significant side effects in off-target tissues that can result in severe toxicity (**Figure 1-1c**) as seen in the well-known case of doxorubicin as a chemotherapeutic drug with severe off-target cardiotoxicity in its free form.<sup>3,7</sup>

Some of these drawbacks can be addressed by the conjugation of a biologically inert polymer coating as a protective shell with materials such as polysaccharides, poloxamines, and poloxamers.<sup>8,9</sup> These are most often added through a covalent attachment at lysine residues or the N-terminal amine.<sup>10-12</sup> While this solves several issues by increasing solubility (**Figure 1-2a**) and reducing degradation (**Figure 1-2b**), it risks inhibiting the biological activity of the therapeutic, as the direct conjugation may prevent effective interactions with the cellular target (**Figure 1-2c**).<sup>13-15</sup> These therapeutics may be less able to fit into the binding pocket, bind as a

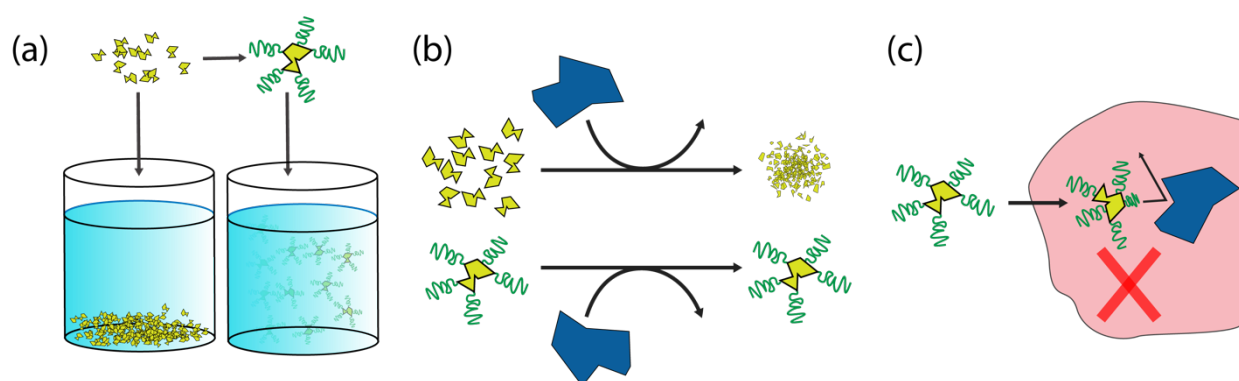


**Figure 1-2. The advantages and disadvantages of polymer coatings on small molecule therapeutics in biological systems.** (a) Hydrophilic polymer coatings can enhance the solubility of poorly soluble hydrophobic drugs and reduce aggregation in aqueous media. (b) Polymer coatings can serve as a barrier to enzymatic degradation of the therapeutic. (c) The covalent attachment of polymer coatings can interfere with the biological activity of the therapeutic if the point of conjugation interferes with target binding.

receptor ligand, and have high variance in activity if there are several conjugation sites and positional isomers.<sup>16</sup> In this way, the trade-off between longer blood circulation half-life and therapeutic potential is imbalanced by simply adding a protective polymer coat.<sup>13</sup>

An alternative to this direct conjugation approach is the encapsulation of the small molecule into a nanoparticle (NP) delivery vehicle (**Figure 1-3**). These NPs offer the same benefits

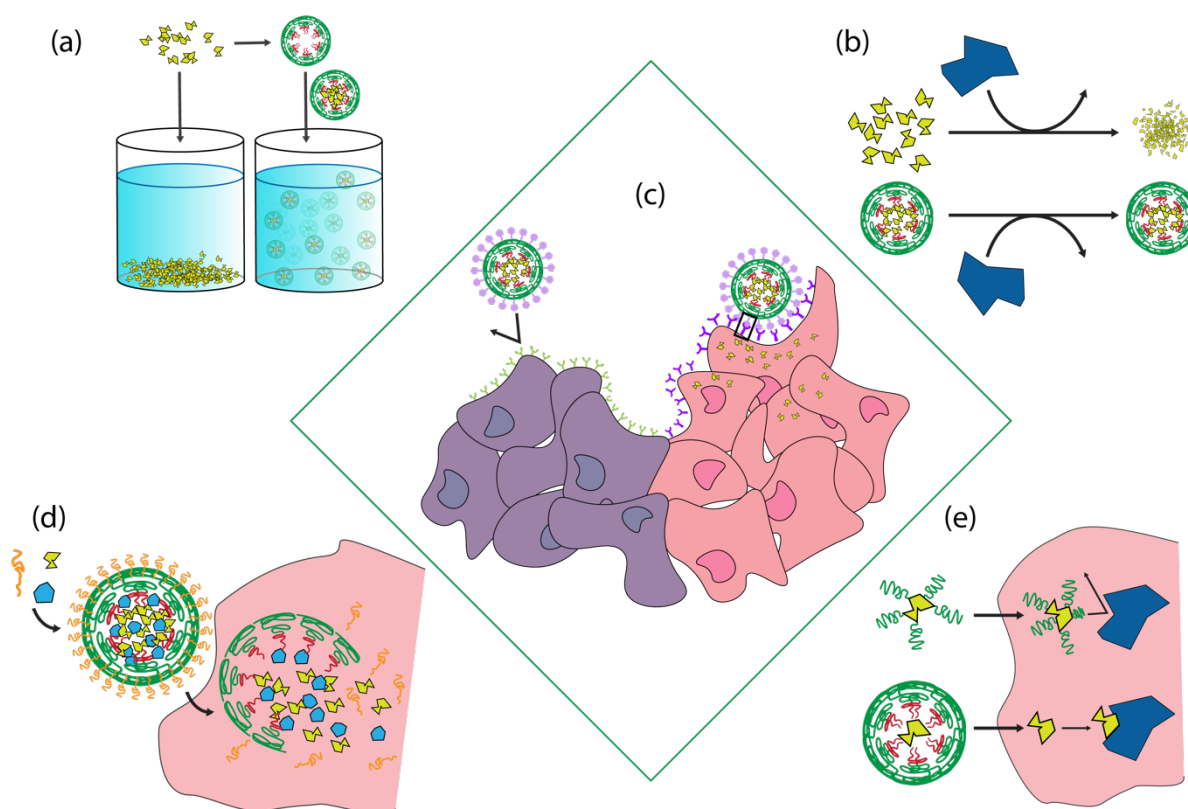


**Figure 1-3. The advantages of nanocarrier delivery systems on small molecule therapeutics in biological systems.** (a) Nanoparticles encapsulate hydrophobic cargo to form stable aqueous suspensions that are fully soluble in biological environments. (b) Encapsulated cargo is completely protected from enzymatic degradation and non-specific immune uptake to maximize the circulation half-life of the drug. (c) Nanocarriers can be designed to target specific cell populations to minimize off-target effects and reduce the required doses of drug to have a therapeutic effect. (d) Multiple types of cargo can be encapsulated into nanoparticles to control release kinetics as a burst or sustained depot. (e) Encapsulated cargo is not covalently modified and maintains or improves biological activity when it is released from the nanocarrier.

as polymer coatings, given that NPs stable in aqueous media can encapsulate hydrophobic small molecule drugs to maintain their solubility (**Figure 1-3a**) and offer physical protection from enzymatic digestion (**Figure 1-3b**), aggregation, and off-target effects (**Figure 1-3c**).<sup>17,18</sup> However, a critical difference is that the association of cargo to the NP during encapsulation is temporary and non-covalent (**Figure 1-3e**). When the drug is delivered to the target location, it is released from the NP in its original free form without modifications, thereby maintaining or improving its therapeutic potential.<sup>19,20</sup>

Encapsulation into NPs enables the concept of release kinetics, as the amount of drug loaded into the NP and the rate that the drug exits the construct can be tightly controlled. NPs have been used to release cargo quickly as a burst (**Figure 1-3d**),<sup>21</sup> slowly as a sustained depot,<sup>22</sup> and as a combination of both mechanisms by releasing at different rates from different compartments.<sup>23</sup> Given that multiple cargos can be loaded into NP carriers, they can each take advantage of these release kinetics based on the compartment the drug is encapsulated within.<sup>24</sup> This approach allows for the development of systems that require multiple components to be present at controlled ratios, such as antigen-adjuvant systems for immune modulation.<sup>25,26</sup>

With these considerations, nanoparticle delivery platforms offer a wide range of biologically relevant features to enhance nearly all pharmacokinetic principles. In pharmacology, the behavior of a therapeutic within an organism is defined within the categories of liberation, absorption, distribution, metabolism, excretion, and toxicity (LADMET). The most significant impacts of NP carriers within the LADMET framework are the enhanced circulation time, reduced side effects, maximized bioavailability, and improved localization to the target tissue offered by

NP encapsulation and controlled release of cargo.<sup>5,17,27</sup> Individually, each of these aspects vastly enhances the potency of the loaded therapeutic. All together, they synergistically improve clinical outcomes for the disease process with a smaller therapeutic dose. In this way, insoluble small molecule therapeutics that are at risk of falling out of the development pipeline are revitalized with a nanocarrier delivery vehicle.

### 1.2.2 Tuning nanoparticle physiochemical characteristics to enhance biological function

Within the broad category of nanoparticle biomaterials, there is a vast and growing range of materials and assemblies tailored specifically to the biomedical application of interest. The synthetic nature of these materials allows for this rational selection of physiochemical characteristics that optimize the therapeutic outcome including size, charge, surface chemistry, and morphology (**Figure 1-4**).<sup>28</sup> For example, the hydrophobic interior of micelle-type structures is ideal for loading hydrophobic drugs, thus allowing the utilization of the rest of the vehicle to enhance solubility in the aqueous biological environment. Hydrophilic drugs require an aqueous core to load effectively, as seen in vesicle-type NPs with bilayer membranes or hollow interiors. Further still, other NPs can accommodate both hydrophilic and hydrophobic drugs within their structures, offering an even wider range of possibilities to tune the system toward the intended therapeutic cargo and application.<sup>29</sup>

The external architecture also plays a critical role in how the NP acts within the biological environment. The overall size determines factors including which proteins or cell types preferentially interact with the surface, how the NP is internalized, and the route of excretion. The epithelial characteristics of the vasculature and specific organs greatly influence their ability to take up and interact with NPs of a specific size as a form of passive targeting. This holds true within specific disease states as well, as demonstrated in the well-studied enhanced permeation

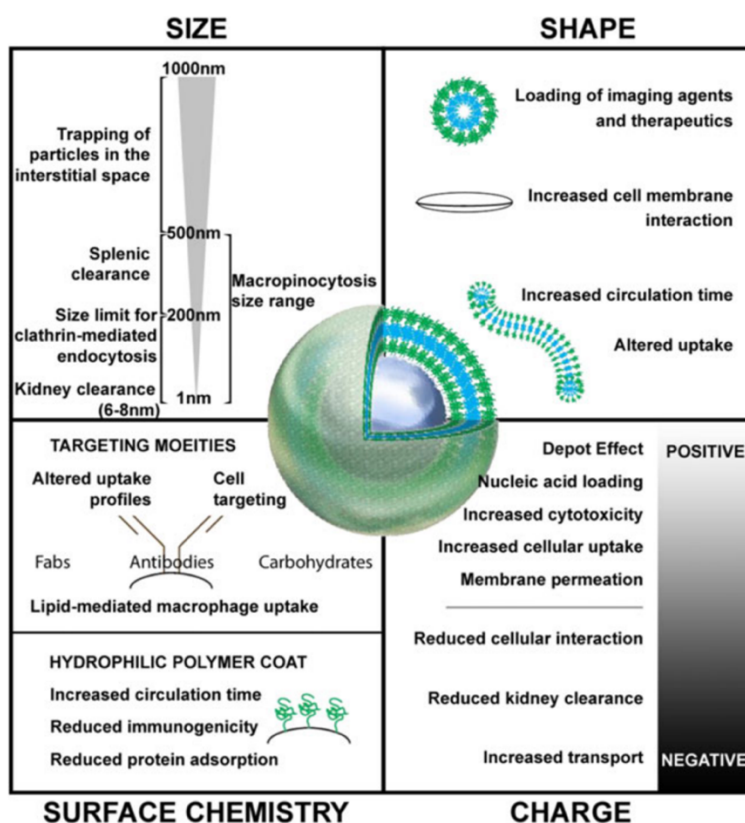


**Figure 1-4. Commonly modified properties of nanocarrier delivery vehicles to enhance performance in biological applications.** Size, shape, surface chemistry, and charge can all impact the uptake, biodistribution, clearance, and toxicity of therapeutic nanocarriers in cell-specific mechanisms. Rational design of these platforms involves the considerations of these properties and modifying the nanocarrier system to enhance the intended therapeutic effect. Reprinted with permission from reference <sup>28</sup> © 2016 American Chemical Society.

and retention (EPR) effect for leaky vasculature in tumor tissues along with any pathophysiology that results in neovascularization.<sup>30,31</sup>

The charge of the particle as determined by the chemical functionalization of the NP surface has significant impacts on biological behavior within the body. Certain slightly charged particles have been shown to passively aggregate in biological environments via Van der Waals forces or hydrophobic forces if any portion of the surface is hydrophobic.<sup>32,33</sup> Charged particles of any type are more able to resist aggregation through self-repulsion and are often considered necessary for maintaining stable formulations.<sup>34</sup> Within charged particles, cationic formulations attract negatively charged serum proteins such as albumin which greatly affect trafficking, secondary aggregation, and immune scavenging.<sup>35,36</sup> However, not all effects are beneficial. This positive charge has also been shown to disrupt erythrocytes and cause widespread cytotoxicity via membrane disruption.<sup>36</sup> Anionic particles are less conspicuous in biological systems but, as with all NP, are still able to attract counterions given the high ionic strength of circulation fluids and may be prone to aggregation.<sup>37,38</sup>

In addition to size, the shape of NP carriers determines a number of outcomes for biomedical applications. A spherical morphology is often the most thermodynamically favorable arrangement of component parts, but a vast range of diverse and creative architectures have been developed over the past decades for specific applications.<sup>39</sup> Common alternatives include rod-like shapes, elongated worm structures, biconcave discs, cages, and many more.<sup>40</sup> Each of these has an associated set of physical parameters such as aspect ratio and degree of curvature that impact their impression on biological surfaces and fate within the body.<sup>41</sup>

Among many other NP attributes, these three aspects of size, surface charge, and morphology have been specifically explored in a vast number of studies to understand their impact on the outcome of nanoparticles in biological systems. Each can be modified to impact the pharmacokinetic parameters such as biodistribution, circulation, and clearance, as well as engineering principles including cargo loading, surface functionalization, and release profile. It is difficult to make specific conclusions about physiochemical characteristics that are heavily interdependent and therefore cannot be fully isolated. However, broad trends can be found that are used to direct the rational design for the NP material based on its application.

### *Biodistribution*

Nanoparticle biodistribution is significantly influenced by its size as each organ contains a number of physical barriers and filters to accessing the tissue.<sup>42 43</sup> Two especially strict barrier examples include the GI mucosal barrier and blood brain barrier (BBB) which must be specifically addressed by the NP design to overcome these physical challenges and reach the target tissue.<sup>44,45</sup> A number of studies demonstrate this size dependence using spheres of various diameters and evaluating the resulting accumulation in relevant organs.<sup>46-48</sup> Overall, larger nanoparticles partition into the liver and spleen, as those tissues have larger gaps for the purpose of filtering waste.<sup>46,47</sup> In contrast, smaller particles may be able to penetrate more delicate tissues such as the lung or more protected tissues such as the brain which is heavily guarded by the BBB.<sup>43,46,47</sup> These concepts were demonstrated in a recent study that compared the organ biodistribution of larger spheres (polymersome vesicles) and smaller spheres (micelles) and

found differences according to these broad patterns along with a dependence on size for organ retention (**Figure 1-5**).<sup>48</sup>

Charged nanoparticles have biodistributions dependent on their interactions with serum components that can result in aggregates or non-specific uptake by the cells of the mononuclear phagocytic system (MPS). Overall, positively charged particles show the highest tissue accumulation.<sup>49</sup> In several studies, cationic nanoparticles tended to distribute into the lungs likely due to electrostatic interactions with the anionic serum proteins that are large enough to become trapped in the lung capillaries.<sup>50,51</sup> For organ-specific effects, positively charged particles are also less able to penetrate the variety of barriers in the skin compared to negatively charged particles,

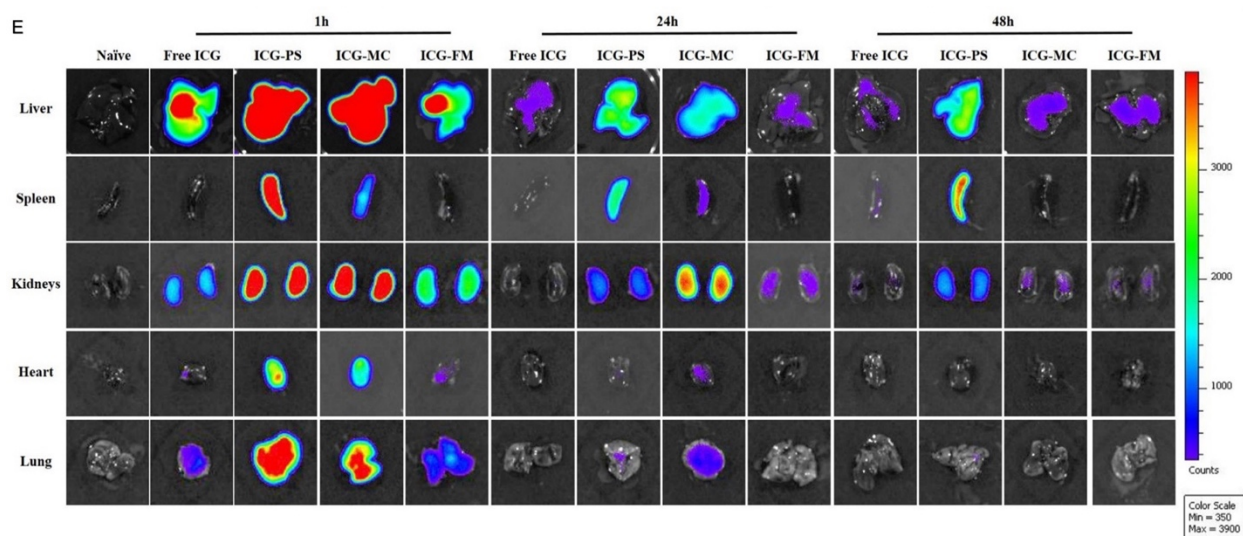


**Figure 1-5. The organ-level biodistribution of nanoparticles with different sizes and morphologies.** IVIS optical imaging was used to track the accumulation of ICG-loaded 100 nm spherical polymersomes (PS), 20 nm spherical micelles (MC), and 50 nm x 1  $\mu$ m filomicelles (FM) at 1 hour, 24 hours, and 48 hours post-IV injection into C57BL/6 mice. Representative organs for nanoparticle biodistribution and retention based on size (PS vs. MC) and shape (PS/MC vs. FM) are demonstrated in the liver, spleen, kidney, heart, and lung. Reprinted (adapted) with permission from reference <sup>48</sup> © 2016 American Chemical Society.

and the glomeruli are able to retain cationic particles more readily than anionic or neutral particles which impacts renal distribution.<sup>49,52</sup>

Nanoparticle morphology is subjected to the same organ barriers as mentioned for the influence of size on biodistribution along with related physical properties of the structures. A recent study found that nanospheres could enter tissues more readily than nanorods, while nanostars were able to penetrate lung parenchyma and accumulate in high amounts.<sup>53</sup> For rods and worms, shorter lengths were found in greater amounts in the liver while longer lengths were located in the spleen.<sup>54</sup> A similar trend was found with spheres as the larger vesicle shapes were found in the spleen compared to the smaller micelles and remained there for much longer.<sup>48</sup> Long, flexible worm-like structures are known to have a lower tissue accumulation overall, given the dynamics of motion within the bloodstream, with an organ level biodistribution and nanoparticle retention demonstrated in comparison to spherical particles (**Figure 1-5**).<sup>48,55,56</sup> Beyond these organ-level biodistributions, NP morphology has been shown to influence uptake into specific cell populations within organs.<sup>48,57</sup>

### *Clearance/Circulation*

Strict limits for the clearance of nanoparticles by size are determined by the internal filters of the kidney and the non-specific uptake of the MPS, both of which can rapidly clear particles from circulation (**Figure 1-6**). In general, nanoparticles of diameter less than 10 nm pass directly through the renal filtration barrier for immediate clearance, drastically reducing the circulation half-life of the formulation.<sup>58,59</sup> On the other end, particles greater than 200 nm tend to activate the complement system for rapid uptake by the MPS into the spleen and liver for clearance.<sup>42,60,61</sup>

Between these values, smaller particles tend to remain in circulation longer and avoid clearance, with a size below 150 nm recommended to avoid spleen accumulation.<sup>62,63</sup>

Given the effect of charge on non-specific uptake, the circulation time and clearance of nanoparticles is highly dependent on the zeta potential (ZP).<sup>31,43,64</sup> Positively charged particles with a ZP of +10 mV or more are subject to serum protein aggregation via opsonization and subsequent MPS uptake while negatively charged particles with a ZP of the same -10 mV or less can also trigger interaction with cells of the reticuloendothelial system (RES).<sup>65</sup> Neutral particles with a ZP in the  $\pm 10$  mV range have the longest circulation time without non-specific clearance by either the circulating cell of the MPS or by the liver Kupffer cells that rapidly clear particles with charges of greater magnitude.<sup>66,67</sup>

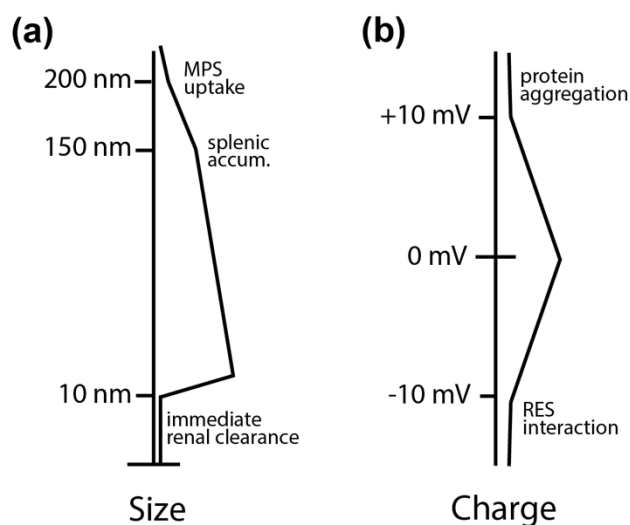


**Figure 1-6. The general effects of nanoparticle size and charge on circulation time and relevant clearance events.** (a) Nanoparticles of diameter smaller than 10 nm are immediately cleared through the kidneys, while above that cutoff, smaller particles are retained longer than larger particles as they are accumulated in the spleen around 150 nm and trigger MPS uptake at 200 nm and higher. (b) Neutral nanoparticles have the highest circulation time while cationic particles above +10 mV aggregate with anionic serum proteins and anion particles below -10 mV trigger interaction with the reticuloendothelial system (RES) for more rapid clearance.

The most significant impact of morphology on the circulation and clearance of NPs is based on the aspect ratio, as it influences the uptake into circulating immune cells and the physical passage of filtration barriers. In general, high aspect ratio morphologies such as worm-like or filomicelle structures have significantly longer circulation time and reduced clearance when compared to spherical structures such as micelles and vesicles.<sup>48,68</sup> Seminal work by Geng in 2007 identified this phenomenon and found an additional dependence on the length of the filamentous particles where shorter filomicelles were cleared more quickly from circulation compared to their longer counterparts, with fractionization being a key component of eventual uptake.<sup>54,55</sup> A vital element to this mechanism of persistence is the flow of circulation that channels the worm-like structures around potential endocytosing cells and opposes uptake.

### *Cargo loading*

Size determines the cargo-loading capacity of a nanocarrier both for the size of the individual cargo and the quantity loaded. The diameter of a nanoparticle is comprised of both the internal cores as well as the membrane thickness which both contribute to the loading of a given drug that may reside in either space.<sup>69,70</sup> The delivery dynamics of particle size can be tuned through these considerations based on the drug per particle and the number of particles per formulation to influence the local and intracellular dosing of the drug.<sup>71</sup>

Charge has played an extremely important role in the development of nanoparticles by loading ionizable cargo through electrostatic interactions or host-guest chemistry.<sup>37,72</sup> A prevalent example is the loading of nucleic acid therapeutics which is enhanced by increasing associations of the negatively-charged phosphate sugar backbone to the cationic nanoparticle

interior.<sup>73,74</sup> For a more nuanced approach, ionizable nanoparticle materials that hold specific charge states across a range of pH levels can be used to temporarily enhance loading behavior. By buffering the pH to specific setpoints, these stimuli-responsive materials can modify assembly and associate with charged cargo during preparation conditions while resisting protein adsorption and cationic toxicity at physiological pH.<sup>75,76</sup>

Variations in nanoparticle morphology offer distinct capabilities for the number and type of cargo that can be encapsulated. Beyond the hydrophobic loading into the lipophilic core of micelles, hydrophilic cargo requires the aqueous reservoir of vesicles or hollow core structures (**Figure 1-7**). More complex morphologies and polymeric nanocarriers with bilayer membranes are able to load both types of cargo.<sup>70,77</sup> These nanoparticles have independent capacities for encapsulating both types of cargo based on the internal architecture of the spaces within the structure.<sup>29,78</sup> Recent strategies utilize morphologies with multiple loading spaces to demonstrate independent loading and integrity of the spaces, as cargo can be released separately in response to environmental conditions or signaling.<sup>72</sup>

### *Ligands/functionalization*

The surface of the NP can also be fully tuned to enhance activity and targeting capabilities. Many of the materials used to fabricate the NP carrier can be chemically modified to incorporate specific surface charges or chemical moieties that are known to impact aggregation, targeting, or direct conjugation to other bioactive molecules.<sup>79</sup> For example, covalent attachment of ligands or antibodies will target specific cells or prevent non-specific uptake into off-target cell populations such as the 'self-ligand' CD47 which prevents macrophage uptake of red blood

cells.<sup>80</sup> This strategy also allows for supramolecular linking between NPs such as in the development of hydrogels that swell within the net between particles.<sup>22</sup> For NPs made of polymers, chemical linkers or biologically active molecules can also be non-covalently embedded within the loose associations between chains.<sup>81,82</sup>

Nanocarrier morphology can be engineered to optimize the conformation and display of simple small molecule targeting moieties or antigen fragments to enhance interactions with larger, more complex target ligands. The characteristics of particle decoration are greatly

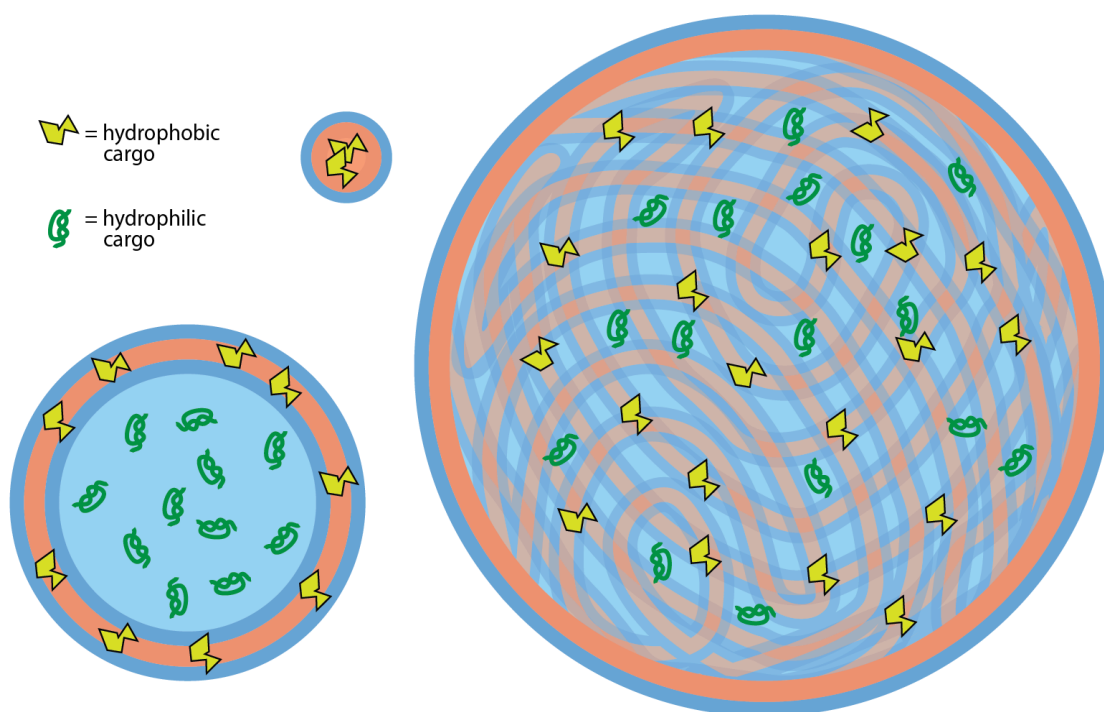


**Figure 1-7. Loading of hydrophilic and hydrophobic cargo based on internal architecture and nanoparticle size.** Smaller micelles (middle top) with a hydrophobic core are able to load a modest amount of hydrophobic drug. Larger vesicles (bottom left) with a hydrophilic core can load hydrophobic cargo in the bilayer membrane and hydrophilic cargo in the aqueous center. The largest BCNs with multiple interlocking channels are capable of loading high amounts of both hydrophilic and hydrophobic cargo in the extensive aqueous channel volume and hydrophobic bilayer membrane.

affected by features of surface geometry. The aspect ratio, surface area, and organization impact ligand density, arrangement, and conformation, which can all influence the efficacy and mechanism of cellular uptake.<sup>83-85</sup> A variety of studies have explored the effect of ligand density on the immune response to stimulants and antigens with a range of conclusions.<sup>86,87</sup> Particles with a higher degree of curvature were found to have an increased ligand response to deeper epitopes, indicating that the increased spacing between ligands on a curved surface allows for better penetration into those areas.<sup>88</sup> Conversely, more planar constructs were found to produce high ligand responses with highest surface density when there is no curvature to take advantage of the internal spacing.<sup>88</sup>

### *Sustained release*

Nanostructures have frequently been utilized successfully as central components within sustained delivery systems. Though not every morphology has been adapted for this purpose, two structures, namely cylindrical nanofibers and bicontinuous nanostructures, have exhibited characteristics that make them adept for this purpose. Relying on physical interactions, peptide-based nanofibers can be coalesced into hydrogel scaffolds or matrices for use in single-dose therapeutic systems.<sup>89</sup> Charged nanofibers capable of forming supramolecular hydrogels when mixed in the presence of antigen outperformed the alum-based control due to their ability to more effectively control the release of antigen.<sup>89</sup>

Cylindrical nanostructures permit the formation of drug depots through the development of a network via cross-linking the cylinders into a net that can absorb and trap therapeutic cargo. Many recent studies demonstrate the use of this type of morphology for creating a hydrogel

scaffold as a sustained release system that depends on the integrity of the hydrogel matrix.<sup>90-92</sup> An additional level of release control is offered by nanoparticles with a morphological fluidity that can exist through a sequential pattern of distinct structures triggered by specific stimuli.<sup>22,93</sup> In one example, a hydrogel of oxidation-sensitive material induced a slow transition of the original cylindrical or filamentous nanostructures to spherical micelles.<sup>22</sup> These micelles served as the mobile intracellular delivery vehicle *in vitro* and *in vivo* while the slowly transforming hydrogel acted as a depot for the controlled release of therapeutic at the injection site.

In addition to filamentous and cylindrical morphologies, bicontinuous nanospheres (BCNs), a type of polymeric cubosomes, have also demonstrated a capacity for sustained delivery systems.<sup>94</sup> These morphologies can encapsulate a very high amount of both hydrophobic and hydrophilic drugs given the complex internal architecture that features multiple, separate, non-intersecting aqueous channels.<sup>29,94-96</sup> Cargo loaded into these BCN morphologies can slowly diffuse out of the structures as they navigate the winding internal organization, resulting in a constant supply of the therapeutic to the local environment.<sup>97</sup> Additionally, if they are made from stimuli-responsive materials, the rate of cargo release can be modulated by the application of an external influence such as photooxidation which can alter the morphology of the formulation and release cargo.<sup>96</sup>

### 1.2.3 Non-specific immune uptake of nanoparticles

Regardless of the myriad benefits offered by NPs designed to effectively load, protect, and deliver therapeutic cargo, a critical factor in the success of any delivery system is the ability

to avoid non-specific immune uptake and clearance from blood circulation. The human immune system is extremely well equipped to identify, neutralize, and dispose of foreign materials or organisms to prevent pathogenic morbidity and mortality. Several overlapping layers of immune components and interlinked systems combine to ensure very few gaps or exploits, including a very conservative approach to any substance with the possibility of being foreign. NP formulations as foreign material are especially affected by these defense systems and must be designed to address the major contributing immune components to maximize survival in the blood stream and allow delivery to the target tissue.

The first interaction of any foreign particle entering into the bloodstream is coating by plasma components in a process known as opsonization (**Figure 1-8a**).<sup>64,99</sup> The type of opsonins

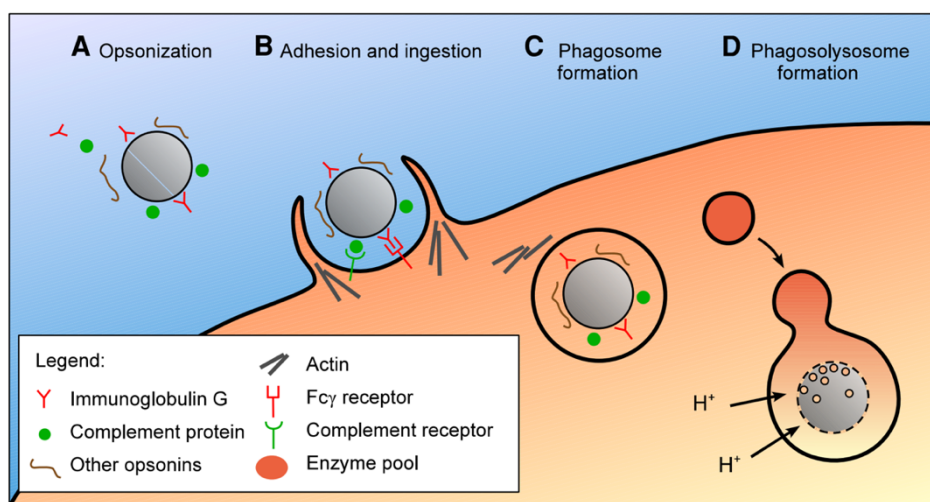


**Figure 1-8. Opsonization and non-specific immune uptake of nanoparticles.** (a) Particles identified as foreign through specific molecular patterns or unnatural surface chemistries are coated with opsonins in circulation. (b) Opsonized particles are recognized by phagocytic cells and internalized by phagocytosis. (c) The internalized portion of the membrane known as the phagosome fuses with other intracellular components to develop into the lysosome (d) where the particle is rapidly digested by the acid pH and active enzymes. Reprinted with permission from reference <sup>112</sup> © 2009 Springer

and the extent of their coating is largely determined by the physiochemical surface characteristics of the foreign particles. In addition to entropy-driven binding, major contributors to opsonin association with the particle surface include hydrophobic interactions,<sup>98</sup> hydrogen bonding,<sup>99</sup> and electrostatic interactions on surfaces with a high charge density,<sup>100</sup> all of which physically enhance attachment of opsonins to the foreign particle.<sup>8</sup>

Serum proteins adsorbed onto the surface of any given particle are called a protein corona and represent a molecular signature that gives the particle a new identity. The protein coat also masks any functional markers for targeting or therapeutic effect and determines the ultimate outcome of the particle in that biological system.<sup>101</sup> Additionally, coated particles are much more likely to aggregate together due to the slight deformation of the adsorbed proteins and increased exposure of hydrophobic domains.<sup>102,103</sup> These aggregates can become large enough to become lodged in narrow capillary beds as an additional route of clearance.<sup>35</sup>

Opsonins include complement proteins, blood clotting proteins, apolipoproteins, fibronectin, and immunoglobins that adsorb to the particle surface and mark it for uptake into cells of the MPS to be digested and presented to T cells.<sup>11,104</sup> In addition to these more typical serum proteins, it is also the binding of other innate immune components including lectins and other pattern recognition molecules along with any existing anti-particle antibodies that may have been developed from previous exposure.<sup>105</sup> In this way, it is the involvement of both the innate and adaptive immune systems that contributes to the local inflammation and phagocytosis of the coated particles.<sup>106</sup>

Circulating monocytes, granulocytes, dendritic cells, and tissue-resident macrophages in the liver, spleen, and lymph nodes with the necessary opsonin receptors will recognize the protein-coated particles and undergo phagocytosis for further processing (**Figure 1-8b**).<sup>63,107</sup> The vasculature in these organs is especially fenestrated to allow for the filtering and capture of suspicious particles marked for uptake up to about 100 nm.<sup>31,108</sup> Macrophages may also take up foreign particles through scavenger receptors designed to recognize and clear dead cells and debris.<sup>104,109</sup> Tissue-resident phagocytes also play an important role in the uptake of foreign particles, specifically in the alveolar spaces for inhaled particles, the spleen, and the liver (Kupffer cells) which are the main cell population responsible for the overall circulation half-life of a given particle.<sup>110</sup> This rapidly cascading process is capable of clearing foreign particles without appropriate defenses from the blood stream in 10 minutes and results in less than 5% of intravenous particles reaching the intended target organ or cell population.<sup>8,107,111</sup>

The opsonized particles are taken up into the cells of the MPS using the membrane to form the phagosome that carries the internalized particle through the cytoplasm (**Figure 1-8c**). Through a series of fusion events, the phagosome develops into a highly acidic and enzyme-rich vesicle called the lysosome where the particle and anything else internalized is rapidly digested (**Figure 1-8d**).<sup>112</sup> In this way, the process of opsonization of foreign particles leads directly to the non-specific immune uptake and destruction of the particle, eliminating the possibility of a therapeutic effect. All rationally designed nanoparticles for biomedical applications must therefore address this highly efficient process of opsonization and immune scavenging to prevent the rapid removal and destruction of the therapeutic particle.

#### 1.2.4 Enhanced pharmacokinetics with poly(ethylene glycol)

One such approach to reducing non-specific uptake of administered NPs into cells of the RES is adding poly(ethylene glycol) (PEG) to the external surface of the carrier. PEG is used ubiquitously in this manner as a coating considered to have stealth characteristics and a vastly increased blood circulation in biological systems.<sup>41,113,114</sup> This polymer is comprised of repeating ethylene glycol units that impart significantly beneficial physiochemical properties to the material as a protective barrier against aggregation, protein adsorption, immune recognition, and rapid clearance.<sup>12</sup> The process of conjugating PEG directly to small molecules or proteins, called PEGylation, is one of the most common strategies to enhance the pharmacokinetic parameters of the therapeutic.<sup>41,114</sup> For NP carriers, PEG can be attached through covalent or non-covalent associations to also benefit from the essential biocompatible properties of PEG.<sup>10</sup> For more fluid NP formulations such as liposomes or polymeric nanocarriers, PEG is often attached to a lipid tail or lipophilic polymer, anchored to the internal hydrophobic portion of the membrane, and aligned with the amphiphilic chains that make up the NP.<sup>34,81,115,116</sup>

PEG chains are highly polar, hydrophilic, and electrically neutral across the full pH range.<sup>117</sup> Each ethylene glycol unit is able to coordinate several water molecules at varying degrees of tightness to create a hydration shell on the surface of the particle (**Figure 1-9**).<sup>118</sup> This shell sterically blocks potential interactions with serum proteins as is it thermodynamically and entropically unfavorable to embed within the rapid free motion of the PEG chains.<sup>104,119</sup> The association with water molecules also creates a separation of charge as a dipole moment that repulses potential interactions of charged proteins.<sup>120</sup> NPs with a PEG outer component have a reduced charge density and a broadly masked shape and surface which provides additional stealth character against potential recognition by proteolytic enzymes or antibodies.<sup>121</sup>

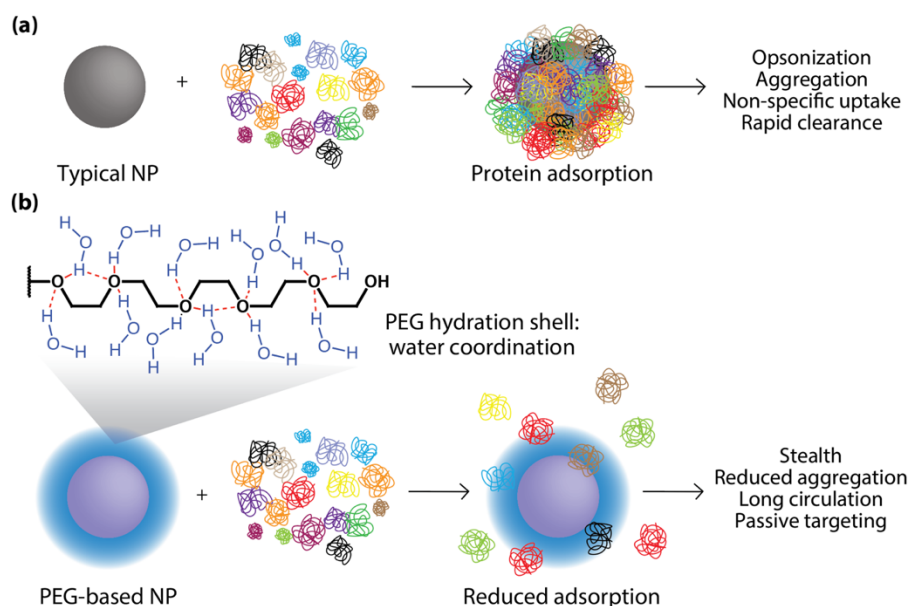


**Figure 1-9. Water coordination of PEG units to form a protective hydration shell.** (a) Serum proteins readily adsorb to the surface of naked nanoparticles (NPs) upon biological administration that increase aggregation, non-specific uptake, and rapid clearance. (b) The repeating ethylene glycol units in PEG are able to coordinate and retain several water molecules to form a water shell that reduces protein adsorption. This hydration shell imparts a stealth character as these NPs have reduced aggregation, longer circulation, and passive targeting.

The practical result of PEG outer components has been shown innumerable times in the literature in the vastly increased circulation time and anti-biofouling of small molecule drugs,<sup>122</sup> proteins, viral gene vectors,<sup>123</sup> nucleic acids, liposomes,<sup>124</sup> polymeric carriers,<sup>125</sup> and bio-resident surfaces.<sup>126</sup> As a result, PEG is the only synthetic polymer with FDA approval for 21 PEGylated drugs for clinical use along with 20 others undergoing clinical trials, as well as an innumerable number of non-biomedical commercial products.<sup>34,127,128</sup>

As a fully synthesized polymer, PEG is also amenable to chemical and physical modifications of its length and terminal ends. The length or molecular weight of the associated PEG chains determines the thickness of the protective hydration shell. Increasing PEG length on particles results in a much-increased hydrodynamic diameter,<sup>129</sup> decreased protein adsorption,<sup>130</sup> and longer circulation time *in vivo*.<sup>131</sup> The changes in diameter from this PEG shell can increase 3 to 5 times more than a globular protein of similar weight and can alter the metabolism and excretion of the particle.<sup>12,132</sup> It is broadly accepted that PEG chains of molecular weight at 2000 Da or above are necessary for sufficient reduction of protein absorption, with a heavy dependence on the particle size and morphology.<sup>46,133</sup>

The density of the PEG layer is also a tunable property and can be modified based on the intended application. Most commercially available PEG is linear given the straightforward synthesis but adding branches can modify its effects on the surface.<sup>12</sup> The size and morphology of the surface being functionalized also plays a significant role in the density of the PEG shell, as the radius of curvature defines the physical movement of the chains. A thicker layer of PEG can

more effectively shield the NP surface and distribute charge densities that can attract serum proteins, thereby increasing circulation time.<sup>134</sup>

Closely related to PEG grafting density is the aspect of PEG chain conformation. These conformations largely fall into several distinct categories that depend directly on the surface grafting as defined by the Flory radius, extension length, and distance between chains. When the graft density is high (low distance between chains), the polymer chains have reduced conformational freedom and must align more strictly in a brush conformation.<sup>125,135</sup> For surfaces with greater freedom for chain motion due to decreased density or increased surface curvature, the PEG adopts a mushroom conformation.<sup>136</sup> These assemblies play a critical role in the stealth character of the PEG-functionalized material, with a general agreement that PEG densities beyond the brush-to-mushroom transition are ideal.<sup>109,114,125,137</sup>

Compared to other hydrophilic polymer coatings that impart a stealth character onto biomedical surfaces, PEG remains the most effective based on the properties of the water shell. PEG is especially polar which enhances its ability to associate with both hydrophilic and hydrophobic components of the surface and maximize solubility.<sup>118</sup> Compared to gelatin, PEG is significantly less prone to phagocytosis,<sup>138</sup> while dextran coatings lack the conformational freedom of long PEG chains and are too stiff to impart a reliable stealth character given the glycosidic linkage.<sup>139</sup> Finally, PEG is susceptible to metabolism by cytochrome P450<sup>140</sup> and alcohol dehydrogenase<sup>141</sup> which may enhance excretion compared to other polymers.<sup>142</sup>

These significant advantages offered by PEG as a stealth functionalization have a critical impact on the pharmacokinetic properties of biological therapeutics as passive targeting.

Decreased opsonization of intravenous NPs results in a decreased recognition of the material as foreign by phagocytes and minimal non-specific immune uptake.<sup>46,114</sup> A slower clearance of particles by the MPS results in a significantly extended circulation half-life and a greater probability that the therapeutic will reach the target tissue.<sup>34</sup> Long-circulating therapeutics can take advantage of the leaky vasculature seen in tumor microenvironments, as demonstrated by the EPR effect, and for conditions with a component of neovascularization.<sup>31,114</sup> These therapeutics are also much more likely to encounter and productively interact with the target receptor.<sup>17</sup>

Along with the benefits of nanocarrier delivery systems, the addition of a PEG component results in products that have an enhanced therapeutic effect with a lower dose and minimal off-target interactions.<sup>12</sup> The loaded therapeutics are fully soluble within the envelope regardless of hydrophobic character. They are protected from degradation and uptake while preserving the sites of action that may be disrupted from direct PEG conjugation to the drug. PEG protection from non-specific uptake by phagocytic cells enhances circulation time to maximize delivery to the target tissue. The outer surface can be further modified to incorporate ligands for active targeting of specific cell populations, which take up the carrier for burst or sustained release. Each of these aspects provide critical contributions to the development of a biomedical therapeutic that improves patient quality of life with reduced clinical costs.<sup>143</sup>

As a synthetic polymer with incredible utility for biomedical applications, extensive efforts have been made to develop covalent and non-covalent attachment strategies to connect PEG to the therapeutic of interest.<sup>12,144</sup> Modifying the terminal end of the PEG chain allows for grafting

onto a surface through covalent linkages, often through amines, carboxylic acids, and acrylates.<sup>145</sup> Special attention has been given to develop functionalized PEG derivatives that can be conjugated directly to specific amino acid residues on bioactive molecules such as antibodies, small molecules, ligands, oligonucleotides,<sup>146</sup> receptors,<sup>11</sup> chelators,<sup>147</sup> and more.<sup>34</sup> Initially, amino groups were targeted for alkylation as they are found ubiquitously in lysine residues or at the N-terminus of every peptide sequence.<sup>10,12</sup> Since then, the reaction space has been vastly expanded to include conjugation strategies for hydroxyl, amide, and thiol groups for enhanced specificity and maintaining bioactivity.<sup>12,15,148</sup>

#### 1.2.5 Poly(ethylene glycol)-*block*-poly(propylene sulfide) nanomaterial

Along with PEG, poly(propylene sulfide) (PPS) is a unique polymer utilized as the hydrophobic block of self-assembling amphiphilic diblock copolymers used in the Scott Lab. These PEG-*b*-PPS materials are able to form a diverse range of highly tunable nanostructures for a wide diversity of biomedical applications. These nanostructures are formed by altering the weight ratio of hydrophilic PEG to hydrophobic PPS, known as the hydrophilic weight fraction ( $f$ ), which determines the supramolecular assembly of these polymer chains to form micelles, filamentous worm-like micelles, polymersome vesicles, and bicontinuous nanospheres (**Figure 1-10**). Indeed, this platform can be customized to optimize the size, charge, morphology, surface functionalization, and loading capacity of nanocarriers to impart specific effects on release kinetics,<sup>22,149</sup> organ-<sup>48</sup> and cellular-level<sup>57</sup> biodistribution, stimuli-responsiveness,<sup>96</sup> modulated cellular uptake,<sup>82</sup> specific interactions with serum proteins and APC uptake,<sup>103</sup> and many more

developing applications. In addition to these ongoing investigations, the PEG-*b*-PPS material is non-toxic in non-human primates at relevant concentrations, showing no adverse outcomes in the liver, spleen, kidney, or blood.<sup>150</sup> The features provided by the hydrophilic PEG portion of this diblock copolymer have been discussed previously; however, the selection of the PPS hydrophobic block enables several features critical to an effective nanocarrier delivery system.

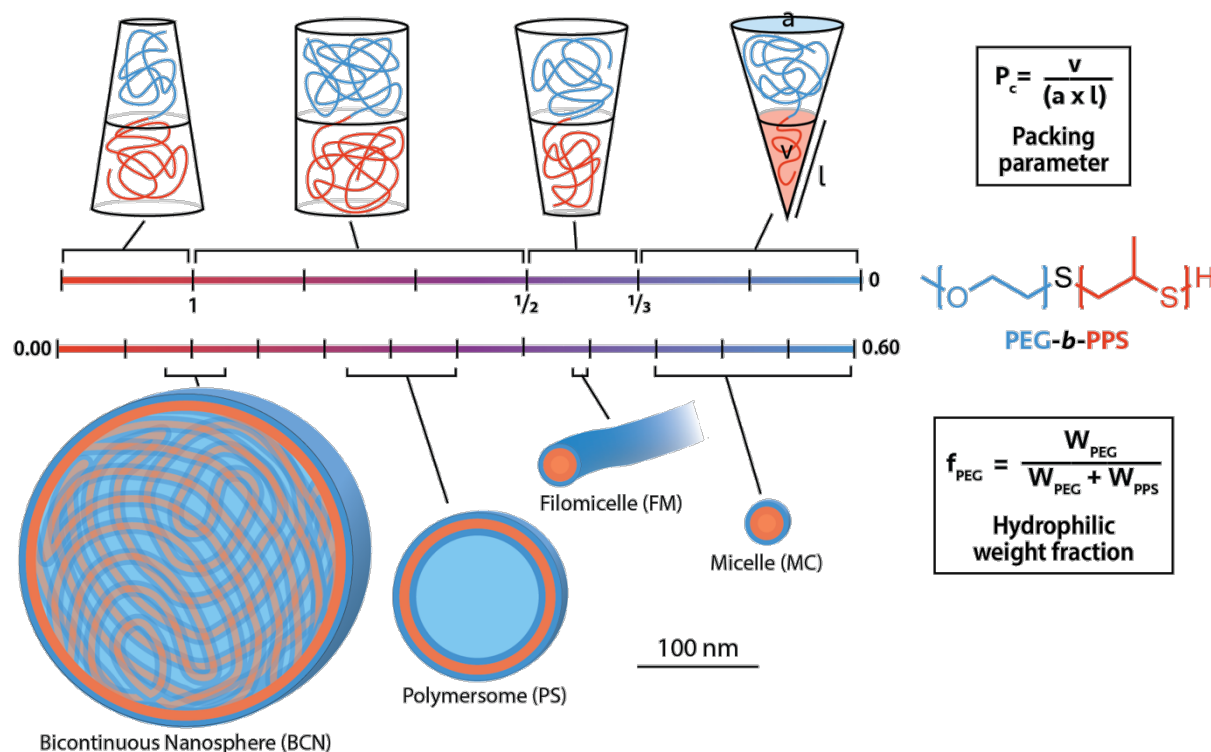


**Figure 1-10. Diverse morphologies of self-assembling PEG-*b*-PPS materials based on the hydrophilic weight fraction.** The structure of PEG-*b*-PPS diblock copolymer with the hydrophilic PEG represented in blue and the hydrophobic PPS represented in orange. The mass ratio of these blocks is meaningfully quantified by the packing parameter ( $P_c$ ) and the PEG hydrophilic weight fraction ( $f_{PEG}$ ) shown on the right. The  $P_c$  of the self-assembled diblock copolymer in 3D space is measured according to the volume of the hydrophobic block ( $v$ ), the area of the hydrophilic block ( $a$ ), and the length of the hydrophobic block ( $l$ ). These wedges determine the supramolecular assembly of polymer chains as they form specific morphologies according to the ranges marked on the scale below. The  $f_{PEG}$  of a given polymer can be used to estimate the  $P_c$  parameter where bicontinuous nanospheres (BCN), polysome (PS), filomicelle (FM), and micelle (MC) morphologies form reliably in the scale above.

First synthesized in 1961, PPS has undergone a number of rigorous examinations of its physiochemical properties that have identified it as an ideal material for drug delivery applications.<sup>151</sup> However, despite these efforts, PPS remains underutilized given its unique functionalities and straightforward synthesis.<sup>152</sup> The repeating units of the PPS chain are reminiscent of the well-studied poly(propylene oxide) (PPO) in poloxamers except with a sulfur atom replacing the oxygen, thus maintaining many similar properties but making PPS more hydrophobic.<sup>153</sup> One such example of these similarities is that both are synthesized through an anionic ring-opening polymerization (ROP).<sup>153,154</sup> For PPS, the monomer is propylene sulfide that is initiated with a nucleophile, often a thiolate ion, in living fashion.<sup>155,156</sup> The active thiolate terminal end is amenable to a wide range of functionalization options including nucleophilic substitution, Michael-type additions, and disulfide bridging, including between chains as dimers.<sup>152,156-158</sup> The mild thiolate propagating species does not require extensive anhydrous conditions and is amenable to the attachment of biologically active components.<sup>159</sup>

As mentioned previously, the PPS block has a number of useful functionalities that make it an ideal component of a drug delivery platform based on its specific physiochemical properties. First, the glass transition temperature ( $T_g$ ) of 230 K is very low for hydrophobic polymer components and allows this material to remain flexible at low temperatures.<sup>151,153</sup> Replacing the oxygen atom with a sulfur atom in the chain makes PPS have less hydrogen bonding compared to PPO, which also has a low  $T_g$ .<sup>151</sup> The low  $T_g$  enables lyotropic behavior as materials with PPS, as PEG-*b*-PPS materials form lamellar gels that transition to vesicular aggregates upon dilution without additional cosolvents.<sup>158</sup> This feature makes these PPS-based materials especially

versatile and capable of diverse supramolecular morphologies. It is also hypothesized to contribute to the ability of PPS-based materials to be assembled into nanostructures via the high-turbulent mixing regime of flash nanoprecipitation.<sup>160,161</sup> Having access to these assembly strategies enables the formation of unique morphologies and enhanced cargo loading that can be tuned based on the nanocarrier application, as described previously.

A critical feature offered by PPS is based on its polysulfide oxidation sensitivity that induces the triggered release of cargo upon exposure to oxidative or acidic stimuli (**Figure 1-11**). These oxidative spaces exist in a number of physiologically relevant locations both extracellularly and intracellularly and as markers of disease processes.<sup>162,163</sup> In these areas, the polysulfide chains of PPS are oxidized to polysulfoxides and finally polysulfones with increasing hydrophilic character.<sup>153</sup> For nanoparticles utilizing the hydrophobic interactions of the PPS chains to maintain their supramolecular structure, this transition to the polysulfone significantly weakens

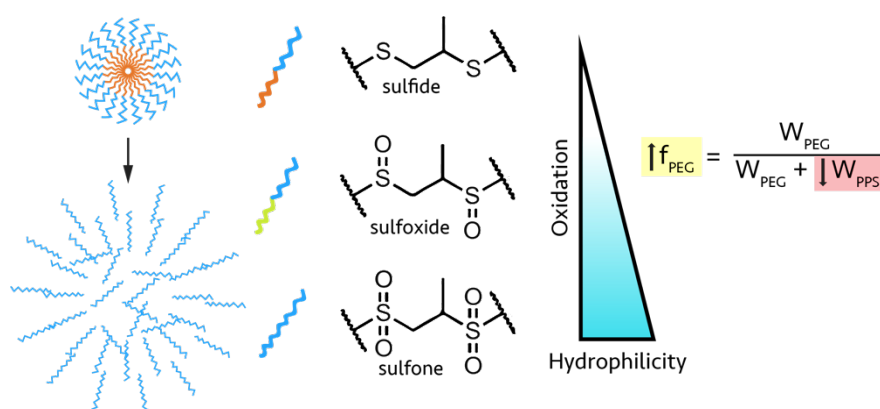


**Figure 1-11.** Oxidation-triggered PPS transition to hydrophilic sulfone units and subsequent disassembly. As the sulfide units of PPS are exposed to acidic or oxidative conditions, they transition to the increasingly hydrophilic sulfoxide and sulfone units. The resulting diblock copolymer has an altered hydrophilic weight fraction (right) as the hydrophobic block becomes hydrophilic. This induces a morphological transition and eventually disassembly of the nanostructure as the hydrophobic interactions diminish with the oxidation of PPS units.

these forces and the nanoparticle disassembles and releases any loaded cargo. One such significant cellular location of strong oxidizing power is the endo-lysosome system after particle internalization.<sup>164</sup> Nanocarriers with a PPS component have been found to release cargo only once they are taken into the cell as a stimuli-responsive triggered release mechanism.<sup>165,166</sup> For delivery vehicles, this feature is vital to the prevention of early drug release and off-target effects while maximizing the efficacy of the therapeutic delivered only once it is internalized into the cellular target. Specifically, PEG-*b*-PPS nanocarriers were found to release cargo in the more mild environment of the endosome,<sup>165</sup> potentially preserving the integrity of the delivered cargo by releasing it before the destructive chemical and enzymatic digestion in the lysosome.

An additional result of this oxidation sensitivity is the transformation of the former amphiphilic copolymer to an entirely new copolymer with two mainly hydrophilic blocks. Extensive investigation of this process found that the oxidation of PEG-*b*-PPS nanostructures initiates a morphological transition along the pathway of vesicles to worm-like micelles to spherical micelles.<sup>22,96,153</sup> The resulting PEG-*b*-polysulfone material at this end-point appeared to form non-associating unimolecular units of a hydrodynamic diameter small enough to be excreted renally.<sup>10,167,168</sup> This work also found that the oxidative process did not cleave within or between the copolymer blocks, ensuring that the expended material would be cleared from the system cleanly and efficiently.<sup>153</sup> This clearance mechanism is a critical component for any exogenous material meant for biomedical applications to prevent accumulation and potential toxicity that is seen with other materials.<sup>169</sup>

While cargo loaded into PEG-*b*-PPS materials is successfully released in the endosome before the development into the digestive lysosome environment, the released cargo must still find a way into the cytosol to reach its therapeutic target. A number of endosomolytic strategies have been developed for nanocarrier systems as this critical step is not only rate-determining but also determines the therapeutic effect.<sup>170</sup> The major mechanisms for endosomal escape of nanoparticles include membrane fusion, osmotic pressure, induced swelling, and membrane destabilization, all of which are induced by polymers with a specific surface charge, buffering capacity, morphology, or route of cellular entry.<sup>171</sup> For PEG-*b*-PPS materials, cargo delivered intracellularly was found in the cytosol of target cells shortly after localization in the endosome, indicating successful endosomal escape.<sup>165,166</sup> Given the lack of known endosomolytic features on this PEG-*b*-PPS material that would link it to a specific disruptive route, the mechanism of escape is thought to be due to the permeabilization of the endosomal membrane by the polymer.<sup>165</sup> Further, based on the tracking of these compartments developing into lysosomes after endosomal escape of cargo, the porosity is both temporary and non-destructive to these compartments which maintains the integrity of the cell.<sup>166</sup> Considering the extensive efforts to understand and develop these mechanisms for endosomal escape and intracellular delivery, this inherent feature of PEG-*b*-PPS is a vital component to successful drug delivery.

A final consideration of PPS-based materials is the ability of the repeating sulfide units to irreversibly bind ROS as anti-inflammatory scavengers within the cellular environment.<sup>172</sup> Many studies have investigated these properties of PPS recently in the applications of neuroprotection after ischemic stroke,<sup>173</sup> wound healing and tissue regeneration,<sup>174</sup> diabetic peripheral arterial

disease,<sup>175</sup> osteoporosis,<sup>176</sup> bone and soft tissue infections,<sup>177</sup> and the reduction of immunosuppression in tumor microenvironments,<sup>178</sup> among many more. The interactions with ROS can also be utilized for engineering controls to modulate cargo release from injected nanoparticle depots via disease-state specific stimulation or externally applied photooxidation.<sup>96</sup> This unique feature of PPS as both a structural material component as well as having independent therapeutic activity allows for the synergistic effect of any immunomodulatory drugs loaded for delivery.<sup>179</sup>

Together, this PEG-*b*-PPS diblock copolymer material provides several critical advantages to the development of therapeutic drug delivery vehicles. Nanocarrier delivery enables superior solubility, cargo protection, reduced off-target effects, multi-cargo delivery, and maintained biological activity of encapsulated therapeutics. The enhanced pharmacokinetics of PEG offer a stealth character that greatly enhances circulation time and decreases non-specific immune uptake for maximized delivery of therapeutic to the target tissue. PPS offers a low glass transition temperature for the formation of diverse morphologies, an oxidation-sensitive triggered release of cargo, a transformation to a unimolecular structure for renal clearance, and a synergistic ROS scavenging ability for anti-inflammatory applications. This material has shown incredible benefits towards a number of biomedical applications that will continue to grow as it is explored more deeply.

### 1.3 Scope of this work

Nanocarriers have a vast potential to be tuned to impart specific behaviors in biological systems that improve the therapeutic outcome. In this work, I explore two nanocarrier materials with expanding potential for drug delivery to a wide range of applications. The first portion of this work pertains to PEG-*b*-PPS as an established platform for immunoengineering applications as described. I begin by optimizing its synthesis, followed by two applications that demonstrate the tunability of the material to improve nanoparticle uptake and effectively deliver a small molecule drug. The second portion of this work details the development of a novel copolymer platform that incorporates the vast modular functionality of amino acids into the hydrophilic block as PAA-*b*-PPS. This biomimetic class of polymer materials has the potential to form stable nanostructures of multiple morphologies with a number of amino acid backbones. Additionally, the NCA chemistry utilized to synthesize the PAA blocks can impart general sequence control over a mixed monomer system for a more nuanced application of these modular amino acid blocks. Overall, this work seeks to expand the capabilities of nanocarrier delivery platforms by optimizing both of these self-assembling diblock copolymer platforms for biomedical applications.

### 1.4 Publication information

Portions of this chapter have been published with the following citation information:

**Frey M**, Bobbala S, Karabin N & Scott EA. Influences of nanocarrier morphology on immunotherapy. *Nanomedicine*. **13**, 1795-1811 (2018). doi: 10.2217/nnm-2018-0052.

## CHAPTER 2

# Optimized synthesis and purification of poly(ethylene glycol)-block-poly(propylene sulfide)

### 2.1 Abstract

The synthesis of poly(ethylene glycol)-block-poly(propylene sulfide) (PEG-*b*-PPS) as an amphiphilic diblock copolymer for nanocarriers has developed over the last 20 years with a diverse set of conditions and outcomes. As this material continues to be studied across a wide range of applications *in vitro* and *in vivo*, it is worth revisiting this synthesis to standardize and optimize the conditions to reliably produce high-quality material. Each of the three main synthetic steps are analyzed across the metrics of reagent equivalents, concentration, reaction time, conditions, and workup protocol. To show the preservation of the final product quality, PEG-*b*-PPS nanocarriers of micelle, vesicle, and bicontinuous nanosphere morphologies were formed and characterized by dynamic light scattering (DLS) and small-angle x-ray scattering (SAXS). The overall modified procedure has significant improvements on purity and yield of the material as well as significantly reduced time, material, and cost requirements.

### 2.2 Introduction

Poly(ethylene glycol) (PEG) is an immensely useful polymer used in applications spanning from commercial household products to therapeutic modulation to reducing the biofouling of long-term medical implants. Surfaces modified with this polymer are shown to have enhanced

circulation time, neutral immune presence, and longer resistance to protein accumulation on surfaces.<sup>11,114</sup> Each of these features is due in part to the capacity of the repeating ethylene glycol unit to coordinate water molecules and form a protective shell around the material or therapeutic (**Figure 1-9**).<sup>118,119</sup> With the vast range of applications for PEGylated products in the industrial and biomedical fields, ongoing investigations into developing synthetic protocols to modify the terminal ends remain worthwhile.

For the last 30 years, the self-assembling diblock copolymer poly(ethylene glycol)-block-poly(propylene sulfide) (PEG-*b*-PPS) has been developed as an extremely versatile drug delivery vehicle for biomedical applications (**Figure 2-1**). In this material, the oxidation-sensitive PPS imparts a number of important functionalities that contribute to the success of this nanocarrier platform including triggered intracellular cargo release, endosomal escape, and a hydrophilic transition for effective clearance.<sup>153</sup> Additionally, the low glass transition temperature allows for

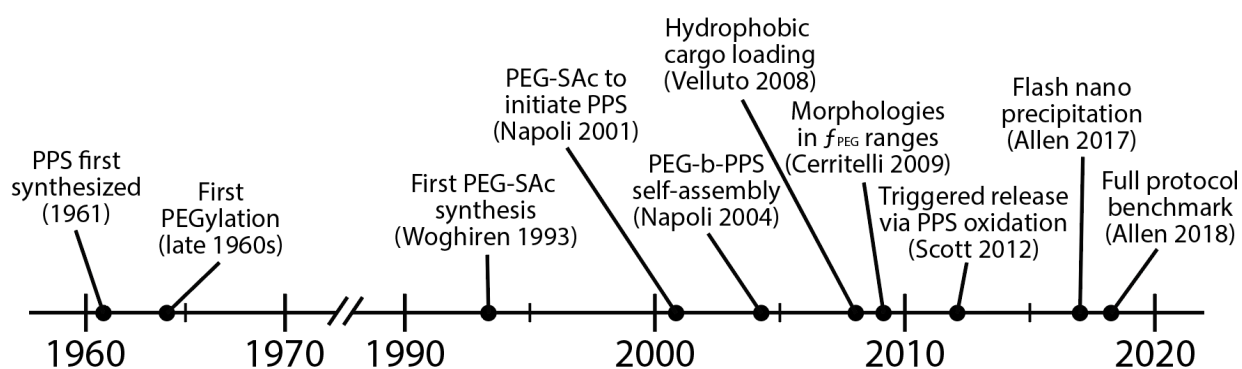


**Figure 2-1. Significant events in the development of PEG-*b*-PPS diblock copolymers for drug delivery.** Major early events for the first synthesis of PPS and the first PEGylation for stealth character occurred in the 1960s while the first pairing of these two blocks was not accomplished about 30 years later in 1993. Since then, there has been a rapid development of the synthesis, assembly, loading, and tuning of PEG-*b*-PPS materials for a wide variety of biomedical applications.

the formation of diverse stable nanoparticle morphologies based on the hydrophilic weight fraction ( $f_{\text{PEG}}$ ) of the two polymer blocks and the method of assembly, including micelles, polymersome vesicles, filamentous micelles, and bicontinuous nanospheres (**Figure 1-10**).<sup>160</sup> This enables the loading of many types of hydrophilic and hydrophobic cargo along with the ability to affect targeting, uptake, and biodistribution within the biological environment.<sup>48</sup> Importantly, this material was non-toxic in non-human primates, further increasing its potential as a drug delivery vehicle for clinical applications.<sup>150</sup> This present work systematically examines and optimizes the synthesis of the PEG-*b*-PPS material through monomethoxy PEG-mesylate (mPEG-OMs) and monomethoxy PEG-thioacetate (mPEG-SAc). The mPEG-SAc acts as a protected thiol material that can be deprotected and conjugated directly in a one-pot synthesis to form PEG-*b*-PPS diblock copolymers for drug delivery to a diverse range of applications.<sup>22,81,82,180</sup>

### 2.2.1 Initial PEG functionalization to thioacetate

One of the first publications to describe the preparation of PEG-OMs and PEG-SAc, by Woghiren in 1993, was motivated by the development of a PEG derivative capable of directly conjugating to bioactive molecules.<sup>181</sup> PEG is often functionalized with groups able to conjugate to amino sites on the protein that can often disrupt the bioactivity of the substance as seen with certain antibodies and enzymes.<sup>13-15,182</sup> Instead, Woghiren targeted the less-abundant cysteine group as an attachment site much less likely to inactivate the biomolecule. As with many thiol applications, one of the main considerations is the stability of the thiol moiety that readily oxidizes to form disulfide bridges between compounds as dimers. In this work, mPEG (MW 5000)

chains were functionalized with a tosylate and thioacetate before alcoholysis to reveal the free thiol and subsequent protection with 4,4'-dipyridyl disulfide. This construct was tested by further conjugation to the protein papain known to contain an active free thiol in its active site. The successful attachment was shown in the purification and recovery of papain that was 5000 Da larger than free protein. The first steps of this PEG synthetic path were utilized in the initial PEG-*b*-PPS protocols.

The preparation began with dissolving mPEG<sub>5k</sub>-OH in pyridine as a solvent and a base along with 50 equivalents of tosyl chloride. The reaction was heated to 65°C for 3 hours and left to spin at room temperature overnight. The partial workup included evaporation of the pyridine to dryness followed by separation of unreacted tosyl chloride from the product over Sephadex G-25 resin with 0.1 N acetic acid. Full removal of the eluate solvent via freeze drying resulted in the mPEG-tosylate product in good yields (80%).

For thioacetate preparation, the mPEG-OTs was again dissolved in pyridine and agitated via vortex mixing before adding to potassium thioacetate solubilized in a 2:1 pyridine/methanol mixture along with triethylamine base. This reaction ran overnight under a N<sub>2</sub> atmosphere and was purified as in the previous step with Sephadex G-25. The mPEG-SAc was collected in yields of 70% as a brown-to-dark-purple product. Interestingly, the dark color of this product mentioned here is also referenced often in subsequent variations of its preparation and is a point of optimization for this work.

### 2.2.2 PEG thioacetate initiator for PPS polymerization and PEG-*b*-PPS self-assembly

The protocols described in Woghiren's work are incorporated into the preparation of mPEG-thioacetate as a macroinitiator of propylene sulfide in a paper by Napoli in 2001.<sup>159</sup> Here, the primary objective is the development of an amphiphilic diblock copolymer for self-assembly in aqueous media as a drug delivery vehicle. They note specifically the synthetic complexities in generating asymmetric multiblock polymers with diverse functional groups that can incorporate biological species. In addition to the preparation of PEG- and PPS-based di- and tri-blocks via two separate routes, this work highlights the *in situ* generation of thiolates that are prone to deactivate via disulfide bridging and the mild nature of the reactive thiol end that can conjugate to many bioactive substances. This work by Napoli represents the first documented synthesis of the PEG-*b*-PPS nanomaterial before assembly into nanocarriers.

The first route to prepare mPEG-OTs is based on the previous work by Woghiren using the shorter mPEG<sub>750</sub> with a modified purification via double precipitation in diethyl ether for a 74% yield. Similarly, the mPEG-SAc preparation is repeated as before with more extensive workup protocol including a DCM/water extraction, charcoal incubation, and double precipitation in cold hexane. Despite these efforts, this route produces in a dark, brownish oil in 50% yields. This color is presumed to be due to dark oxidation impurities.

In addition to the direct substitution route of Woghiren, Napoli describes an approach via radical addition to a PEG allyl ether to yield a near-colorless material in high purity. For this synthesis, mPEG<sub>750</sub> is dried in refluxing toluene using a Soxhlet apparatus with molecular sieves

for 3 to 4 hours. The solution is then cooled to 0°C and reacted with sodium hydride followed by allyl bromide before overnight stirring at room temperature. A DCM/water extraction followed by charcoal incubation and double precipitation in hexanes yielded a mPEG-allyl ether (82%). The mPEG-allyl ether was added to a prepared Schlenk flask of THF, AIBN, and thioacetic acid before freeze-thawing and backfilling with an argon atmosphere. The reaction was heated to 65°C for 18 to 20 hours before cooling to room temperature and adding Dowex ion-exchange resin to stir for an additional hour. The reaction is filtered, evaporated, and extracted with DCM/5% sodium bicarbonate. Double precipitation in cold ether yielded mPEG-SAc as a white solid in 65% yield.

mPEG-thioacetate from either of these routes was used to initiate PPS via dissolution into THF in a prepared Schlenk flask and deprotection via 1.05 equivalents of sodium methoxide over 30 minutes. Propylene sulfide monomer was added via syringe in the equivalents equal to the intended chain length and reacted for 45 minutes before capping. The pure polymer was extracted twice with methanol in yields above 90%. This one-pot approach is vital to the complete activation of the initiator and resulting polymer monodispersity and utilized in PPS polymerization through the present work.

This publication was followed shortly after by a publication by Napoli in 2004 that describes the PEG-*b*-PPS nanomaterial forming lyotropic lamellar mesophases in aqueous media using a number of analytical techniques.<sup>158</sup> After hydrating a dried film of polymer on a microscope slide, the elution of vesicular aggregates marks the initial foray into the use of this material as a self-assembling nanostructure for drug delivery.

### 2.2.3 Development of PEG-*b*-PPS as a drug delivery vehicle

Following the seminal investigation of PEG-*b*-PPS self-assembly by Napoli, a number of works developed both the synthesis and assembly of these nanocarriers to further understand the physicochemical properties, unique end cap functionalities, loading capabilities, and release profile of the material. In 2008, Velluto describes the assembly of micelles via cosolvent dispersion and hot water suspension that can stably load the highly hydrophobic drug cyclosporin A.<sup>183</sup> The 70% encapsulation efficiency and 19% w/w loading of this drug was accompanied by a spontaneous release of drug over 9 to 12 days based on the PPS block length. Shortly after, Cerritelli probed a wide range of hydrophilic weight fractions to fully elucidate the supramolecular assembly space of PEG-*b*-PPS materials.<sup>184</sup> Through both thin-film rehydration and cosolvent dispersion, this material was identified via transmission electron cryomicroscopy (cryoTEM) to form spherical micelles, vesicles, cylinders, and unimolecular sheets to exploit as carriers for many types of cargo. Work by Vasdekis and Scott explores the oxidation sensitivity of the PPS block to induce intracellular triggered release of cargo and endosomal escape into the cytosol.<sup>166,185</sup> Many more recent publications highlight the vast potential of PEG-*b*-PPS nanoparticles in immunomodulatory biomedical applications using similar syntheses as detailed previously.

### 2.2.4 Benchmarking the modern PEG-*b*-PPS syntheses protocol

The next major source of PEG-*b*-PPS synthetic information is published in a 2018 paper in JoVE by Allen that details not only the reaction conditional and purification stepwise but also the

assembly and characterization of formed nanostructures as a complete compendium of accessible information about this material.<sup>186</sup> This synthesis was largely used as the most current protocol for the comparisons in this optimization paper. The significant changes that have developed over the 10 years previous to this paper are summarized concisely as follows.

The mPEG-OH starting material is dried of excess water through an azeotropic distillation in toluene using a Dean-Stark trap at 165°C for 2 to 3 hours. The solution is cooled to room temperature and then to 0°C in an ice bath for the addition of 3 equivalents of triethylamine base and 3 equivalents of MsCl added dropwise and allowed to react overnight under an argon (Ar) or nitrogen (N<sub>2</sub>) atmosphere. The reaction is filtered through celite and the solvent is removed to re-dissolve in dichloromethane and filter through celite once more. The solvent is reduced, and the remaining volume is precipitated in cold ether to yield a white mPEG-OMs product.

The mPEG-SAc synthesis begins with the addition of mPEG-mesylate to dimethylformamide along with 3 equivalents of the insoluble potassium carbonate base and 3 equivalents of thioacetic acid under an Ar or N<sub>2</sub> atmosphere. This protocol notes the difficulty maintaining stable stirring due to the insoluble potassium carbonate and general thickening of the solution as it proceeds overnight at room temperature. After filtering through celite, the mixture is heated to 60°C for DMF removal via rotary evaporation. The slurry is then dissolved in THF and passed through a large-scale neutral alumina column. The single fraction is reduced via rotary evaporation and brought up in DCM with an optional paper filtration before precipitation into cold ether and additional cooling in a -20°C freezer. Collection of the solid and vacuum desiccation yields a dark red mPEG-SAc product in yields between 25% to 30%.

The final PPS polymerization step utilizes a prepared Schlenk flask in a water bath with anhydrous DMF to dissolve the mPEG-SAc initiator along with 1.1 equivalents of sodium methoxide as a 0.5 M solution in methanol. This first deprotection step requires 5 to 10 minutes for full preparation of the thiolate initiator before the swift addition of propylene sulfide monomer. After allowing sufficient time for polymerization, the reaction is capped and the DMF is removed via rotary evaporation before it is re-dissolved in DCM and precipitated into methanol. A polymer pellet is formed by centrifugation and decanted for a final vacuum desiccation to yield the PEG-*b*-PPS product.

### 2.2.5 Assembly via flash nanoprecipitation and characterization

While previous works have described the successful self-assembly of PEG-*b*-PPS nanostructures through cosolvent dispersion, hot water suspension, and thin film rehydration, the development of flash nanoprecipitation (FNP) was a critical turning point in the advancement of this drug delivery system.<sup>160,183,184</sup> FNP is a rapid and scalable regime that impinges the aqueous and organic phases together for nanoparticle assembly on the millisecond timescale (**Figure 5-7a**).<sup>187,188</sup> The turbulent mixing of the phases induces supersaturation conditions that nucleate the coprecipitation of nanostructures with any included hydrophilic or hydrophobic cargo. Given these high energy associations, the resulting structures are highly monodisperse after multiple impingements that negate the need for any additional extrusion. Since some therapeutics and nanoparticle morphologies are more amenable to one assembly approach over another, the incorporation of this FNP strategy into the more traditional techniques allows for

the selection of the most ideal conditions for the target formulation. The work outlined in this 2017 publication by Allen describes the efficient formation of PEG-*b*-PPS micelles, vesicles, bicontinuous nanospheres, and worm-like filomicelles among other morphologies that can be produced reliably in gram scales.<sup>160</sup> Since then, FNP has been an indispensable tool for the development of PEG-*b*-PPS nanoparticles.

### 2.2.6 Chapter objectives

The initial step of mPEG mesylation or tosylation plays a vital role in transforming the hydroxyl terminal end of mPEG into a moiety more capable of substitution by a suitable nucleophile. Up to now, these protocols have presented a synthesis with good yields (74% to 83%) but have not yet converged on a cohesive approach to the conditions and workup. Based on the well-established reliability and efficiency of alcohol mesylation throughout synthetic strategies, there are several areas for potential optimization that I hypothesize will have a significant impact on the reaction outcome. First, it is essential to confirm the required reagent equivalents for each step in the synthesis which I hypothesize are lower than the reported amounts. Additionally, the nearly immediate production of the TEA HCl byproduct as an insoluble white salt in DCM leads me to hypothesize that the reaction time can be significantly reduced. Finally, I hypothesize that the workup should remain simple given the possible byproducts and general approach to the functionalization of polymer terminal ends.

The second step of nucleophilic substitution to a thioacetate terminal end offers a thiolate protecting group that can be removed with mild conditions *in situ* before using the thiolate ion

directly in one pot. Previous work describes a wide number of reaction conditions, glassware setups, and extensive purification steps to yield a darker colored product in modest yields. A protocol for functionalizing non-PEG compounds even describes a successful conversion in aqueous conditions heated to 80°C for two hours.<sup>189</sup> Similar to the mesylation step, it is essential to confirm the reagent equivalents necessary for complete conversion. Given the lower yields, I hypothesize that more base or thioacetic acid would improve the conversions. Additionally, the darkening of the reaction mixture as it stirs overnight requires careful consideration especially given the extensive workup to remove this color which I hypothesize is likely due to the development of colored oxidation impurities. The decoupling of the dark red to brown to black reaction color from the overall reaction progress would be a significant paradigm shift in the approach to this synthetic step. Identifying the specific time requirement for complete conversion and halting the reaction before colored impurities develop would drastically improve the required purification protocol, which I hypothesize is much a much shorter time than the published overnight protocols.

Given that these first two synthetic steps are the simple modification of the long PEG chain terminal ends, I hypothesize that the workup of each step can be optimized based on the physiochemical properties of the PEG length instead of the terminal modifications. For the shorter mPEG<sub>750</sub> length, an extraction may be a possible approach as its less hydrophilic character partitions into an organic layer. Additionally, the longer mPEG<sub>2000</sub> can be effectively recovered through an ether precipitation.

For the last PPS polymerization step, I hypothesize that a reduction of the sodium methoxide base to only one equivalent could improve the copolymer purity. Sodium methoxide is a strong base capable of initiating PPS chains that are not purified out with the final methanol precipitation. Reducing the equivalents to a non-excess amount of sodium methoxide and an additional ether precipitation to remove PPS homopolymer would prevent its presence in the final product. Additionally, the final polymerization step can be used as an indicator of mPEG-SAc initiator quality as any small deviation is compounded by the number of polymer units. All potential optimizations of these mPEG-OMs and mPEG-SAc materials will be confirmed by the standard chemical analysis techniques, but this purity measurement can often differ from the functional capability of the products, especially given the highly reactive thiol moieties. Utilizing the mPEG-SAc initiator from the new synthesis to create high quality nanostructures would fully validate the synthetic optimizations and advocate for their implementation. I hypothesize that these optimization conditions will still form nanostructures of equal quality to the previous protocols. I will evaluate the formation of PEG-*b*-PPS formation of micelles (MC), polymersomes (PS), and bicontinuous nanospheres (BCNs) as representative morphologies that use various PEG and PPS block lengths.

Finally, the purpose of this work is to systematically optimize each aspect of this synthetic pathway to maximize the yield of pure product and minimize the required time and material investments. Having a standardized protocol for future work using these PEG-based materials will ensure a more reliable, reproducible product of highest quality for all *in vitro* and *in vivo* biomedical applications. Reducing the required time, materials, and costs associated with the

reaction conditions and especially the workup process will enable a more efficient scaling up for more extensive *in vivo* applications or industrial production. Additionally, a simplified protocol will make this synthesis more accessible to those without a more rigorous chemistry background and allow for more focus on translational projects. In this chapter, I describe the approach and outcome of this systematic optimization for each step along with evidence of functionality in the assembly and characterization of nanoparticles made from the PEG-*b*-PPS material.

## 2.3 Materials and Methods

### 2.3.1 Materials and Instrumentation

Monomethoxy PEG of molecular weights 2000 g/mol (mPEG<sub>2000</sub>) and 750 g/mol (mPEG<sub>750</sub>), triethylamine (TEA), methanesulfonyl chloride (MsCl), potassium carbonate (K<sub>2</sub>CO<sub>3</sub>), thioacetic acid (HSAc), 0.5 M sodium methoxide in methanol (NaOMe, NaOCH<sub>3</sub>), benzyl bromide (BzBr), toluene, dichloromethane (DCM), dimethylformamide (DMF), diethyl ether (Et<sub>2</sub>O), hydrogen chloride (HCl), sodium sulfate (Na<sub>2</sub>SO<sub>4</sub>), celite, alumina, activated carbon (charcoal), and hexanes were obtained from Sigma-Aldrich (St. Louis, MO, USA) and used without further purification unless noted. Methanol (MeOH), sodium chloride (NaCl, brine), ammonium chloride (NH<sub>4</sub>Cl), and Dil were obtained from Fisher Science (Pittsburgh, PA, USA) and used as received. Propylene sulfide was obtained from TCI America (Boston, MA, USA) and used as received. <sup>1</sup>H NMR spectra were recorded on Bruker Avance III 500 MHz system and analyzed with MestReNova (Mestrelab Research, Spain).

### 2.3.2 Previous protocols for the synthesis of mPEG-OMs, mPEG-SAc, and PEG-*b*-PPS

All previous protocols for these PEG intermediates and final PEG-*b*-PPS polymer are described extensively in Allen 2018 JoVE.<sup>186</sup> These protocols were repeated several times to ascertain the average yields and purities for comparison to the optimized synthetic modifications.

### 2.3.3 Synthesis of mPEG-OMs

mPEG<sub>750</sub> (10 g, 13.33 mmol, 1 eq.) or mPEG<sub>2000</sub> (10 g, 5 mmol, 1 eq.) previously dried via rotary evaporation three times over anhydrous toluene was dissolved in 20 mL anhydrous DCM and cooled to 0°C in an ice bath. TEA (PEG<sub>750</sub>: 2.32 mL, 16.7 mmol, 1.25 eq.; mPEG<sub>2000</sub>: 870 µL, 6.15 mmol, 1.25 eq.) was added slowly via syringe and the system was allowed to fully cool back to 0°C. MsCl (PEG<sub>750</sub>: 1.28 mL, 16.7 mmol, 1.25 eq.; mPEG<sub>2000</sub>: 490 µL, 6.25 mmol, 1.25 eq.) was diluted in an additional 5 mL of anhydrous DCM and added dropwise with complete mixing between drops. The reaction was allowed to stir for 15 minutes during which the development of the insoluble TEA-HCl byproduct turned the reaction mixture slightly cloudy.

PEG<sub>750</sub>: The reaction mixture was transferred directly to a separatory funnel and rinsed with additional DCM and the 2M HCl:brine (1:1) aqueous phase. The mixture was washed with the aqueous phase three times and once with brine only. The organic layers were pooled and dried over sodium sulfate. Filtration of the sodium sulfate, solvent removal via rotary evaporation, and subsequent drying in vacuo overnight of the mPEG<sub>750</sub>-OMs yielded a waxy white solid in yields of 96%. <sup>1</sup>H NMR (500 MHz, CDCl<sub>3</sub>) δ: 3.6 (s, 68H, PEG), 3.3 (s, 3H, PEG-OCH<sub>3</sub>), 3.0 (2, 3H, SO<sub>2</sub>CH<sub>3</sub>).

PEG<sub>2000</sub>: Solid TEA-HCl was removed via paper or cotton ball filtration before solvent removal via rotary evaporation and precipitation into excess cold ether. The solid mPEG<sub>2000</sub>-OMs product was collected and dried overnight in vacuo to yield a white chalky solid at yields of 98%. <sup>1</sup>H NMR (500 MHz, CDCl<sub>3</sub>) δ: 3.6 (s, 180H, PEG), 3.3 (s, 3H, PEG-OCH<sub>3</sub>), 3.0 (2, 3H, SO<sub>2</sub>CH<sub>3</sub>).

### 2.3.4 Synthesis of mPEG-SAc

mPEG<sub>750</sub>-OMs (5 g, 6.04 mmol, 1 eq.) or mPEG<sub>2000</sub>-OMs (5 g, 2.41 mmol, 1 eq.) fully dried of residual DCM was dissolved in 50 mL anhydrous DMF. Potassium carbonate (PEG<sub>750</sub>: 2.5 g, 18.1 mmol, 3 eq.; mPEG<sub>2000</sub>: 995 mg, 7.22 mmol, 3 eq.) was added carefully, ensuring strong and stable stirring with the insoluble powder. Thioacetic acid (PEG<sub>750</sub>: 1.3 mL, 18.1 mmol, 3 eq.; mPEG<sub>2000</sub>: 508 μL, 7.22 mmol, 3 eq.) was added dropwise with complete mixing between drops. The reaction was allowed to stir for 60 minutes with frequent confirmation of stable stirring during which the mixture developed a deep orange color.

PEG<sub>750</sub>: The reaction was vacuum filtered to remove excess solid K<sub>2</sub>CO<sub>3</sub>, precipitated into cold ether, and cooled in a -80°C freezer for 30 minutes to enhance solid formation. The precipitate was collected via paper filtration and solubilized in DCM and saturated NH<sub>4</sub>Cl aqueous solution. The mixture was extracted three times with the aqueous layer and once with brine. The organic layers were pooled and dried over sodium sulfate. Filtration of the sodium sulfate, solvent removal via rotary evaporation, and subsequent drying in vacuo overnight of the mPEG<sub>750</sub>-SAc product yielded a waxy orange-yellow solid in yields of 92%. <sup>1</sup>H NMR (500 MHz, CDCl<sub>3</sub>) δ: 3.6 (s, 68H, PEG), 3.3 (s, 3H, PEG-OCH<sub>3</sub>), 3.1 (t, 2H, PEG-CH<sub>2</sub>CH<sub>2</sub>-SAc), 2.3 (s, 3H, SCOCH<sub>3</sub>).

PEG<sub>2000</sub>: The reaction was vacuum filtered to remove excess solid K<sub>2</sub>CO<sub>3</sub> and precipitated into excess cold ether. The solid mPEG<sub>2000</sub>-SAC product was collected, rinsed with additional cold ether, and dried overnight in vacuo to yield a light-tan, chalky solid at yields of 96%. <sup>1</sup>H NMR (500 MHz, CDCl<sub>3</sub>) δ: 3.6 (s, 180H, PEG), 3.3 (s, 3H, PEG-OCH<sub>3</sub>), 3.1 (t, 2H, PEG-CH<sub>2</sub>CH<sub>2</sub>-SAC), 2.3 (s, 3H, SCOCH<sub>3</sub>).

### 2.3.5 Synthesis of mPEG-*b*-PPS

An oven-dried Schlenk flask was prepared with a nitrogen atmosphere and placed in a water bath. Each reagent addition was followed by a degas/gas cycle to maintain the inert atmosphere. mPEG<sub>750</sub>-SAC (PS: 200 mg, 0.247 mmol, 1 eq.; BCN: 100 mg, 0.124 mmol, 1 eq.) or mPEG<sub>2000</sub>-SAC (MC: 400 mg, 0.194 mmol, 1 eq.) initiator and 0.5 M NaOCH<sub>3</sub> in MeOH (PS: 495 μL, 0.247 mmol, 1 eq.; BCN: 274 μL, 0.124 mmol, 1 eq.; MC: 389 μL, 0.194 mmol, 1 eq.) were added to anhydrous DMF in 5x excess with respect to the base (PS: 2.5 mL; BCN: 1.5 mL.; MC: 2 mL). The initiator and base were allowed to react for 10 minutes for complete deprotection of the thioacetate. Propylene sulfide was added via syringe without a rubber septum (PS: 586 μL, 7.426 mmol, 30 eq.; BCN: 677 μL, 8.665 mmol, 75 eq.; MC: 304 μL, 3.887 mmol, 20 eq.) and left to react for 20 to 40 minutes based on the PPS chain length. Benzyl bromide (PS: 589 μL, 4.950 mmol, 20 eq.; BCN: 295 μL, 2.48 mmol, 20 eq.; MC: 462 μL, 3.887 mmol, 20 eq.) was added as a cap and reacted for an additional 60 minutes. PS and BCN polymers were precipitated into excess cold MeOH and cooled to -20°C overnight. MC polymers were precipitated in excess cold ether and cooled overnight at -80°C. The cooled samples were centrifuged to form a polymer pellet before

decanting and drying in vacuo overnight. The PEG-*b*-PPS polymer products were a light-yellow, waxy solid (MC) to viscous oil (PS, BCN).

PS (PEG<sub>750</sub>-*b*-PPS<sub>30</sub>): <sup>1</sup>H-NMR (400 MHz, CDCl<sub>3</sub>) δ: 3.6 (s, 68H, PEG), 3.3 (s, 3H, PEG-OCH<sub>3</sub>), 2.9 (m, 60H, -S-CH<sub>2</sub>CH(CH<sub>3</sub>)-S-), 2.6 (m, 30H, -S-CH<sub>2</sub>CH(CH<sub>3</sub>)-S-), 1.3 (m, 90H, -S-CH<sub>2</sub>CH(CH<sub>3</sub>)-S-).

BCN (PEG<sub>750</sub>-*b*-PPS<sub>75</sub>): <sup>1</sup>H-NMR (400 MHz, CDCl<sub>3</sub>) δ: 3.6 (s, 68H, PEG), 3.3 (s, 3H, PEG-OCH<sub>3</sub>), 2.9 (m, 150H, -S-CH<sub>2</sub>CH(CH<sub>3</sub>)-S-), 2.6 (m, 75H, -S-CH<sub>2</sub>CH(CH<sub>3</sub>)-S-), 1.3 (m, 225H, -S-CH<sub>2</sub>CH(CH<sub>3</sub>)-S-).

MC (PEG<sub>2000</sub>-*b*-PPS<sub>20</sub>): <sup>1</sup>H-NMR (400 MHz, CDCl<sub>3</sub>) δ: 3.6 (s, 180H, PEG), 3.3 (s, 3H, PEG-OCH<sub>3</sub>), 2.9 (m, 40H, -S-CH<sub>2</sub>CH(CH<sub>3</sub>)-S-), 2.6 (m, 20H, -S-CH<sub>2</sub>CH(CH<sub>3</sub>)-S-), 1.3 (m, 60H, -S-CH<sub>2</sub>CH(CH<sub>3</sub>)-S-).

### 2.3.6 Nanoparticle assembly and purification

Polymer formulations were assembled as described previously using flash nanoprecipitation.<sup>29,150,160</sup> For each formulation, 20 mg of each polymer along with 0.0625% by weight of the hydrophilic Dil were solubilized in THF to 500 μL total. This organic phase and 500 μL of either 1X PBS (MC, PS) or Milli-Q water (BCN) as the aqueous phase were loaded into separate 1 mL syringes and anchored to a confined impingement jet (CIJ) block.<sup>187,188</sup> The phases were impinged together into the mixing chamber of the block once for BCN and MC formulations and directly into a 1.5 mL aqueous reservoir. The PS formulation was impinged a total of three times before the final deposit into the 1.5 mL aqueous reservoir. All formulations were desiccated overnight to remove residual THF and filtered through a gravity column packed with Sephadex LH-20 hydrophobic resin and a 1X PBS mobile phase to yield stable nanoparticle formulations.

### 2.3.7 Nanoparticle characterization

#### *Size, polydispersity, and zeta potential*

Nanostructure size distribution and polydispersity index (PDI) were measured by dynamic light scattering (DLS) using a Zetasizer Nano (Malvern Instruments) with a 4 mW He-Ne 633 nm laser. Each nanoparticle formulation was diluted 1:100 or 1:1000 into Milli-Q water and analyzed as two rounds of three runs ( $n = 6$ ).

#### *Small-angle x-ray scattering data acquisition and analysis*

Small-angle x-ray scattering (SAXS) experiments were performed using synchrotron radiation at the DuPont-Northwestern-Dow Collaborative Access Team (DND-CAT) beamline at Argonne National Laboratory's Advanced Photon Source (Argonne, IL, USA) with 10 keV (wavelength  $\lambda = 1.24 \text{ \AA}$ ) collimated X-rays. Polymersome formulations were analyzed in the  $q$ -range ( $0.001\text{--}0.5 \text{ \AA}^{-1}$ ) with a sample-to-detector distance of approximately 7.5 m and an exposure time of 1 s. The diffraction patterns of silver behenate were utilized to calibrate the  $q$ -range from 0.001 to  $0.5 \text{ \AA}^{-1}$ . The momentum transfer vector  $q$  is defined as  $q = 4\pi \sin\theta/\lambda$ , where  $\theta$  is the scattering angle. Data reduction, consisting of the removal of solvent/buffer scattering from the acquired sample scattering, was completed using the PRIMUS 2.8.2 software while model fitting was completed using the SASView 4.0.1 software package (<http://www.sasview.org/>).

## 2.4 Results and Discussion

### 2.4.1 mPEG starting material preparation

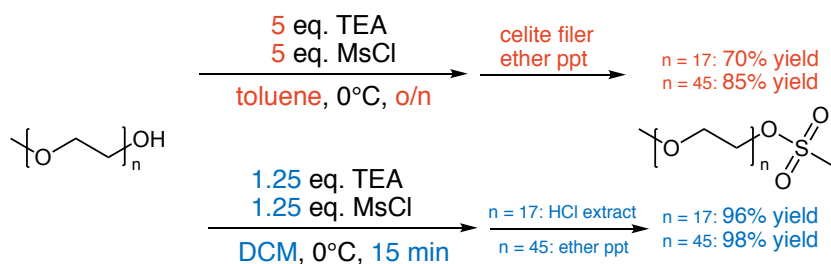
The first step of this synthesis must be carried out in anhydrous conditions to prevent the hydrolysis of the tosyl or mesyl chloride. In addition to using anhydrous solvents, this has previously been accomplished by maintaining an inert atmosphere of nitrogen or argon and an initial drying of the hygroscopic PEG starting material through azeotropic distillation in toluene with a Dean-Stark apparatus.<sup>184,190</sup> This initial preparation step is often time- and attention-intensive, requiring 3 to 4 hours of carefully-monitored refluxing of excess toluene in an oil bath at 165°C to distill the azeotrope, followed by slow cooling to room temperature, and further cooling in an ice bath to carry out the first mesylation step. For these reasons, the first step in the optimization of this synthetic route was to investigate another method of sufficiently drying the PEG starting material. For this task, lyophilization was considered as a significantly less attention-intensive and solvent-free process. This option worked well for drying adsorbed moisture and is recommended as an improvement, but it remains time intensive as a full freezing and lyophilization can take several hours to overnight.

A second option for drying the PEG starting material was distillation in toluene via rotary evaporation. In this process, PEG is dissolved in toluene and evaporated to dryness three times via reduced pressure in a hot water bath. This produced a well-dried product using significantly less solvent at much safer and self-contained conditions and in much less time compared to the azeotropic distillation with a Dean Stark apparatus. The warmed, dry PEG product was also easily

and accurately aliquoted into amounts for use directly in the first mesylation step. It was also found that prior preparation of these dried PEG aliquots via either lyophilization or rotary evaporation allows them to remain sufficiently anhydrous if stored in airtight falcon tubes at room temperature for over a year. This represents a significant improvement in synthesis planning and accessibility to the less-experienced researcher who may not be familiar with the techniques and safety considerations of a high temperature refluxing setup.

#### 2.4.2 mPEG-OMs reaction condition optimizations

Organosulfonates such as methanesulfonate, *p*-toluenesulfonate, and triflate are commonly used to modify alcohol moieties into better substrates for SN1 and SN2 reactions without the drawback of an acidic proton that can react with nucleophiles. The initial step in this synthesis is the addition of a mesylate leaving group to the hydroxy terminal end of mPEG as shown in **Scheme 2-1**. The red text denotes the previously described conditions for reagent equivalents, DCM solvent, overnight reaction time, and multiple workup steps to an overall yield of about 70%. The blue text shows the optimized conditions including a reduced 1.25 equivalents



**Scheme 2-1. Preparation of mPEG-OMs. Previous protocol (top) with examined values in red. Optimized protocol (bottom) with optimized values in blue.**

for each TEA and mesyl chloride, a decrease reaction time to 15 minutes, and a division of the workup to best suit the mPEG length being used: HCl extraction for the shorter mPEG<sub>750</sub> and precipitation for the longer mPEG<sub>2000</sub>. These simplified and scaled changes resulted in an overall yield of 96%. Each of these aspects were optimized systematically to maximize the yield and purity of the new product without wasting materials or time.

The trials to reach these optimal values are shown in **Table 2-1** with the relevant changes highlighted in yellow. Published PEG syntheses have added from 1.5 eq of the mesyl chloride up to 50 equivalents and base from 2 equivalents up to using it as the system solvent (>300 eq).<sup>181</sup> With this in mind, the number of equivalents was reduced from 5 to 2.5 and then to 1.25 without a significant change in yield according to NMR analysis. Similar results were obtained when the mPEG concentration was increased to 0.2 g/mL solvent for reduced chemical waste, simplified workup, and improved safety due to less potential solvent exposure. These optimized conditions

**Table 2-1. Optimization of reagent equivalents and solvent concentrations for the mesylate synthesis of mPEG750 and mPEG2000.**

#	PEG	Scale	[PEG]	Solvent	TEA eq	MsCl eq	Time	Workup	Funct%	Yield
1	750	2 g	0.1 g/mL	DCM	5	5	18h	full	100%	70%
2	750	2 g	0.1 g/mL	DCM	2.5	2.5	18h	full	100%	72%
3	750	2 g	0.1 g/mL	DCM	1.25	1.25	18h	full	100%	69%
4	750	2 g	0.2 g/mL	DCM	1.25	1.25	18h	full	100%	70%
5	2000	2 g	0.1 g/mL	DCM	5	5	18h	full	100%	85%
6	2000	2 g	0.2 g/mL	DCM	1.25	1.25	18h	full	100%	86%

Yellow highlight indicates changing parameters between trials. PEG: 750 g/mol or 2000 g/mol; scale: grams of PEG starting material used; [PEG]: concentration of PEG in g PEG / mL solvent; TEA eq, MsCl eq: number of equivalents; Time: reaction length in hours; full: each step of the previous protocol (celite filtration, rotary evaporation of solvent, precipitation in cold ether and 33% hexanes); Funct%: functionalization of PEG terminal end via NMR; yield: experimental mass compared to theoretical mass.

for mPEG<sub>750</sub> were applied to several mPEG<sub>2000</sub> trials for an equivalent yield compared to the previous protocols. After successful verification of functionalization using the characteristic SAC NMR peaks, these amounts of 1.25 eq for TEA and MsCl were tentatively preserved for the subsequent optimization studies as each aspect may affect the final product quality.

For solvent selection, this reaction step was previously performed most often in toluene or DCM with similar results. Deciding between these solvents or a third option was deferred until the optimization of the product workup given the functional role of the solvent in filtering, chromatography, extraction, and precipitation considerations. The amount of solvent added to a reaction must be sufficient to fully solubilize the reactants and developing products, but not so excessive that it slows down the reaction rate or wastes materials. A similar approach to the previous protocol of 10 mL per gram of PEG was used in halving the amount each time. From 10 mL / g PEG to 5 mL / g PEG, and finally 2.5 mL / g of PEG all showed similar outcomes in solubility and product functionalization despite the increased concentration of the TEA-HCl precipitate. The tentative solvent:PEG ratio was set to 2.5 mL / g of PEG, as the standard scaling of 10 g mPEG-OH in 25 mL DCM.

Next, the reaction conditions and time were systematically examined for improvements in time and product quality. As this exothermic reaction can easily reach temperatures that exceed the low boiling point of DCM, the 0°C ice bath conditions were not modified. Aside from boiling the solvent, a high temperature can result in a yellowing of the mPEG-OMs product that is maintained throughout the synthetic route. While no functional differences are noted for this

yellow product in future steps, it is an undesirable product and may interfere with any spectroscopic techniques that may be used on the material.

Previous protocols for this mesylation step uniformly allow for overnight stirring at room temperature. Using the insoluble TEA-HCl byproduct formation several minutes after its addition as a qualitative marker of progress, it is likely that this reaction proceeds much faster than an overnight protocol. This byproduct is formed after the mesyl group successfully attaches to the PEG terminal end and leaves the chloride ion to interact with the TEA base. To evaluate the time necessary for complete reaction progress, a single flask was prepared and aliquots of sufficient size for analysis were removed at the specified time points. The aliquots were quickly filtered through a cotton ball and precipitated in cold ether to quench the reaction and isolate the mixture of reactants and products. The NMR spectra shown in **Figure 2-2** represent the peaks

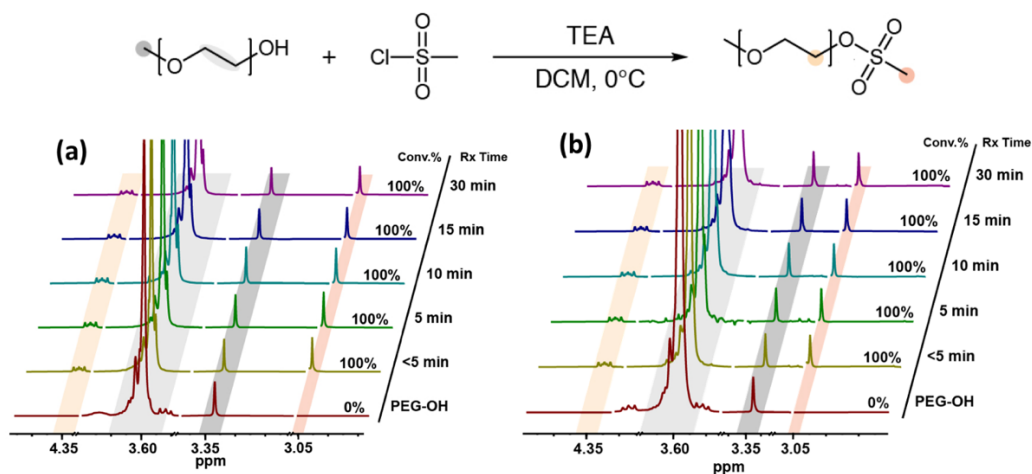
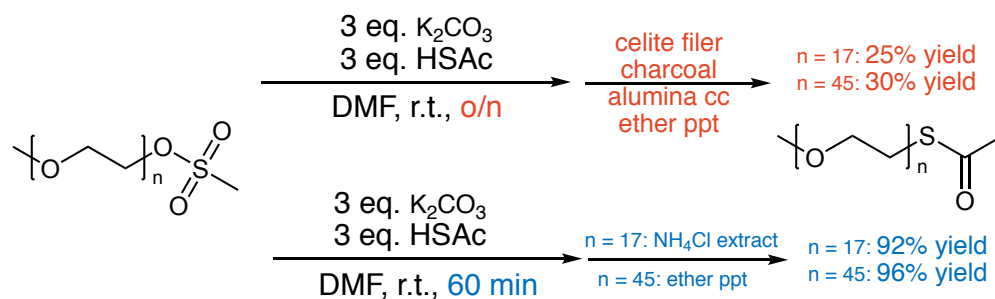


**Figure 2-2. NMR monitoring of reaction times for the mesylate synthesis of mPEG<sub>750</sub> and mPEG<sub>2000</sub>.** For (a) mPEG<sub>750</sub>-OMs and (b) mPEG<sub>2000</sub>-OMs reactions, the gray peaks at 3.3 ppm and 3.6 ppm represent static protons between both starting material and product. The orange and red peaks at 4.35 ppm and 3.05 ppm represent the successful attachment of the mesylate to the PEG terminal end. Conversion was calculated with NMR peak integrations using the 3.3 ppm peak (dark gray) as a reference of 3 protons.

used to determine conversion, as noted by the appearance of two characteristic mPEG-mesylate peaks: 3.05 ppm (s, 3H) representing the methyl group on the mesylate itself and 4.35 ppm (m, 2H) representing the attachment of the mesylate influencing the shift of the nearest PEG units. Both of these peaks are necessary to show both the presence and attachment of the mesyl group to the PEG chain. The initial design of this study was from time points starting at 5 minutes to 18 hours (not shown) before narrowing the range from immediately after reagent addition (<5 minutes) to 30 minutes in order better specify the minimal reaction time necessary. For both mPEG<sub>750</sub> and mPEG<sub>2000</sub>, the reaction proceeded to completion almost immediately after reagent addition to the flask. To ensure full functionalization, the reaction time suggested for the optimized protocol is 15 minutes, which is a significant improvement from the previous protocols having the reaction run overnight.

### 2.4.3 mPEG-SAc reaction condition optimizations

The second step of the synthetic route is the conversion of mPEG-OMs to the protected initiator PEG thioacetate (PEG-SAc) as shown in **Scheme 2-2**. This protecting group is more stable



**Scheme 2-2. Preparation of mPEG-SAc.** Previous protocol (top) with examined values in red. Optimized protocol (bottom) with optimized values in blue.

than mPEG-thiol compounds which are known to quickly oxidize to disulfide dimers. The thioacetate is easily deprotected in mild basic conditions for *in situ* thiolate ion generation to use immediately in one-pot procedures. In addition to the unpleasant sulfur smell, this product is often the lowest yield, lowest purity, and has a high production of brown or dark purple byproducts despite the highest effort in purification. Any optimizations of this synthetic step would provide significant improvements on the overall quality of the final material made from the mPEG-thiolate. As before, the previous protocol is shown on the top in red text as 3 equivalents of both potassium carbonate and thioacetic acid, DMF solvent, an overnight reaction length, and an extensive workup with celite filtration, charcoal incubation, alumina gravity column, and cold ether precipitation for a 20% to 35% yield of a dark orange product. The improved conditions shown in blue text at the bottom confirm that 3 equivalents are sufficient for a reaction in DMF but indicate that full conversion is reached after only 60 minutes of reaction time. Additionally, the workup is split based on the PEG length with the shorter mPEG<sub>750</sub> undergoing an extraction with saturated ammonium chloride and DCM while the longer mPEG<sub>2000</sub> is simply precipitated into cold ether. These modifications result in a yield of 80% to 95% of a light tan product.

Initial optimization of the reaction conditions for the thioacetate substitution reaction is shown visually in **Figure 2-3** as a heat map of yields as determined by NMR integration. Since the functionalization and overall yield of this reaction is low, the optimization for reagent equivalents included values higher than previously reported to investigate any potential improvements. Evaluation of all combinations of potassium carbonate and thioacetic acid in equivalents of 1.5,

3, or 6 showed that 3 equivalents is sufficient for complete conversion and suggest that the low yield is a result of the workup. The solvent volume as represented by PEG concentration in grams of PEG per mL solvent was found to have a similar conversion when reduced to half the solvent volume at 0.2 g PEG / mL DMF. Broad time points of 30 or 180 minutes were used to direct more specific time studies in future optimizations but indicate high conversion even at 30 minutes.

These results indicate that the equivalents of thioacetic acid have a stronger effect on reaction progress than potassium carbonate, dropping conversion significantly between 3 and 1.5 equivalents. The conversion was not significantly affected by doubling the reagent equivalents from 3 to 6 equivalents under these conditions. The optimized reaction conditions were thusly maintained at 3 equivalents for both reagents.

A major consideration for this reaction is the insolubility of the potassium carbonate base which contributes largely to the thickening and inefficient stirring as this reaction proceeds.

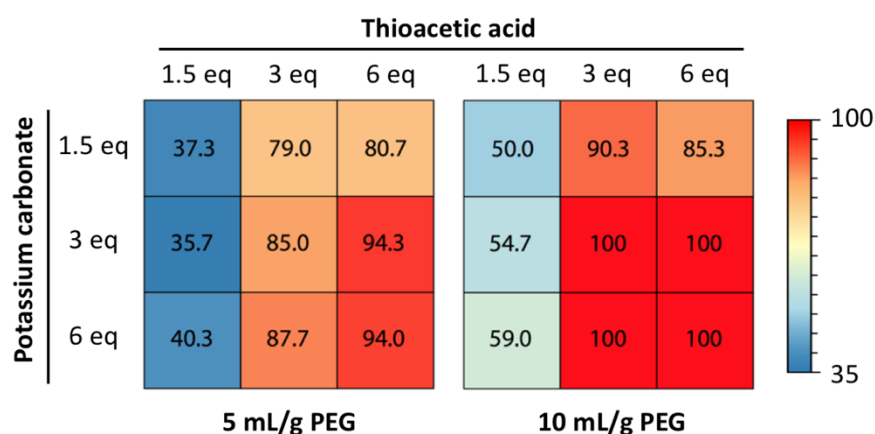


**Figure 2-3. Heatmap of reaction conversion comparing reagent equivalents for mPEG-SAc.** All combinations of potassium carbonate and thioacetate at 1.5, 3, and 6 equivalents were evaluated at two PEG concentrations. Conversion is calculated based on NMR integration of peaks associated with the corresponding mesylate and thioacetate products.

This results in a viscous reaction mixture that stirs unreliably overnight, often stopping completely, and is difficult to manage during the workup. Unfortunately, switching solvents from DMF to avoid this insolubility and overall thickening did not yield many worthwhile options out of dichloromethane, acetonitrile, methanol, ethyl acetate, and water. Additional potential approaches to this include vortexing,<sup>181</sup> mechanical stirring, or adding a large excess of solvent to reduce thickening. Given the unpleasant nature of the sulfur-based reaction, many of these options introduce undesirable effects related to maintaining the reaction barrier. Despite these difficulties, optimization of the solvent included attempts to reduce the ratio of solvent to mass of PEG starting material. A limited range of 10 mL / g PEG found in previous protocols and 5 mL / g PEG were attempted with similar outcomes. It is therefore recommended that the solvent volume is selected based on the intended scale and available glassware, sizing up to allow for extra space in the event of unstable stirring or the addition of more solvent.

Similar to the mesylation reaction, previous protocols have the thioacetate substitution proceeding overnight. This extended time is when the darker color develops in the mixture, often reaching a dark brown to black pigmentation. A large portion of the following 8 to 10 hours of workup described in previous publications is dedicated to removing this color and impurities. Finding an optimized set of conditions to reduce the formation of byproducts during the reaction could greatly aid in purification of the mixture. Along with these optimization efforts was the decoupling of color development and reaction progress with the consideration that additional darkening may represent the development of colored byproducts.

A worthwhile consideration for reducing the production of byproducts is to ensure that the reaction is halted at a timepoint balanced between product conversion and impurity accumulation. The improved reaction time is shown in **Figure 2-4** with the NMR spectra and corresponding peak shifts as the reaction converts to the mPEG-SAc product. Aliquots from a single reaction were filtered through a cotton ball, precipitated into cold ether, and collected for NMR analysis. For this step, reaction progress is indicated by the disappearance of the 4.35 ppm and 3.05 ppm peaks associated with mPEG-OMs as described previously, and the appearance of the peaks associated with SAc attachment to the PEG chain: 2.33 ppm (s, 3H) representing the methyl group on the thioacetate and 3.1 ppm (t, 2H) representing the shifting PEG backbone after attachment to the thioacetate group. As before, both of these peaks are necessary for indicating successful attachment of the SAc to the PEG terminal end, and the corresponding integration was used to calculate conversion. Initially, the range of time points extended through 18 hours (not shown) but was later narrowed to the more relevant scale from immediately after the reagents were added (<5 minutes) to 60 minutes.

NMR analysis shows the substitution to thioacetate reaching completion within 60 minutes which is significantly faster than the overnight protocol in previous publications. The corresponding color of the reaction mixture at these fully converted time points was a deep orange, found much earlier in the progression to a dark brown or black achieved overnight (**Figure 2-4c**). This suggests that the additional darkening is due to the development of oxidation products as impurities.<sup>159</sup> Reactions stopped at this much earlier time point should provide a significant improvement in purification required to achieve a clean final product and overall

quality. Future syntheses of mPEG-SAc are recommended to halt the reaction at 30 minutes for mPEG<sub>750</sub> and 60 minutes for mPEG<sub>2000</sub>.

#### 2.4.4 Optimized workup based on PEG chain length

For mPEG-OMs, published procedures describe purification steps that include G25 resin gravity columns, celite and paper filtration, multiple solvent switching via rotary evaporation, charcoal incubation, extraction, and precipitation. The purification protocols for mPEG-SAc are even more extensive, including G25 resin gravity columns, celite filtrations, charcoal incubation, large-scale alumina gravity columns, and multiple precipitations. Instead of sorting through the combination and order of these steps, I took an approach that prioritized the length of the PEG chain. Given that the vast majority of physiochemical properties of these materials are imparted by the long polymer chain and not the terminal functionalization, it would vastly simplify the purification protocol to effectively recover the PEG chain collectively.

Here, I describe the optimizations for mPEG-OMs in **Table 2-2** with changes in workup highlighted in yellow. This table summarizes the workup as ‘full’ for the most recent published protocol, ‘extract’ for a 2M HCl:brine extraction with DCM, and ‘ppt’ for the precipitation in cold ether. Additionally, **Table 2-3** shows the optimizations for mPEG-SAc in a similar way, with a ‘full’ workup as the previously reported protocol, ‘ext’ for a DCM/ammonium chloride extraction, ‘QRT’ as a quenched reaction and solvent removal via rotary evaporation, and ‘ppt’ as an ether

**Table 2-2. Optimization of workup conditions for the mesylate synthesis of mPEG<sub>750</sub> and mPEG<sub>2000</sub>.**

#	PEG	Scale	[PEG]	Solvent	MsCl eq	TEA eq	Time	Workup	Conv. %	Yield
1	750	2 g	0.1 g/mL	DCM	1.25	1.25	15 min	full	100%	68%
2	750	2 g	0.1 g/mL	DCM	1.25	1.25	15 min	extract	100%	93%
3	750	2 g	0.2 g/mL	DCM	1.25	1.25	15 min	extract	100%	96%
4	2000	2 g	0.2 g/mL	DCM	1.25	1.25	15 min	full	100%	88%
5	2000	2 g	0.2 g/mL	DCM	1.25	1.25	15 min	extract	100%	60%
6	2000	2 g	0.2 g/mL	DCM	1.25	1.25	15 min	ppt	100%	98%

Yellow highlight indicates changing parameters between trials. PEG: 750 g/mol or 2000 g/mol; Scale: grams of PEG starting material used; [PEG]: concentration of PEG in g PEG / mL solvent; TEA eq, MsCl eq: number of equivalents; Time: reaction length in minutes; full: each step of the previous protocol (celite filtration, rotary evaporation of solvent, precipitation in cold ether and 33% hexanes); extract: extraction with 2 M HCl:brine and DCM; ppt: precipitation into cold ether; Conv. %: conversion of PEG terminal end via NMR; Yield: experimental mass compared to theoretical mass.

**Table 2-3. Optimization of workup conditions for the thioacetate synthesis of mPEG<sub>750</sub> and mPEG<sub>2000</sub>.**

#	PEG	Scale	Workup	Purity	Yield
1	750	2 g	full	73%	31%
2	750	2 g	ext	100%	92%
3	750	2 g	ppt	71%	43%
4	750	2 g	ext, ppt	100%	38%
5	2000	2 g	full	76%	24%
6	2000	2 g	ppt	95%	96%
7	2000	2 g	ppt, ext	81%	46%
8	2000	2 g	QRV, ppt, ext	84%	38%
9	2000	2 g	QRV, ext	83%	41%

Red text indicates poor results and associated steps. Blue text represents successful results and associated steps. Full: celite filtration, alumina column, ether precipitation; ext: NH<sub>4</sub>Cl/brine extraction; ppt: paper filtration and ether precipitation; QRV: NH<sub>4</sub>Cl quench and DMF removal via rotary evaporation.

precipitation. Between these two tables, several broader patterns can be identified between the polymer lengths. The schematics shown in **Figure 2-5** and **Figure 2-6** are meant to serve as roadmaps for these workup changes and outcomes.

For mPEG<sub>750</sub>, the previous workup resulted in a modest 68% yield for mPEG-OMs and 31% for mPEG-SAc. Both of these reaction workups benefit from the introduction of an acid extraction with DCM. In this approach, mPEG<sub>750</sub>-OMs extraction in 1:1 2M HCl/brine<sup>191</sup> and mPEG<sub>750</sub>-SAc extraction in saturated ammonium chloride<sup>191</sup> as the aqueous layers with DCM resulted in significant yield improvements to 96% and 92% respectively. In comparison, precipitation of mPEG<sub>750</sub>-OMs and mPEG<sub>750</sub>-SAc into cold ether resulted in yields dropping to 68% from the

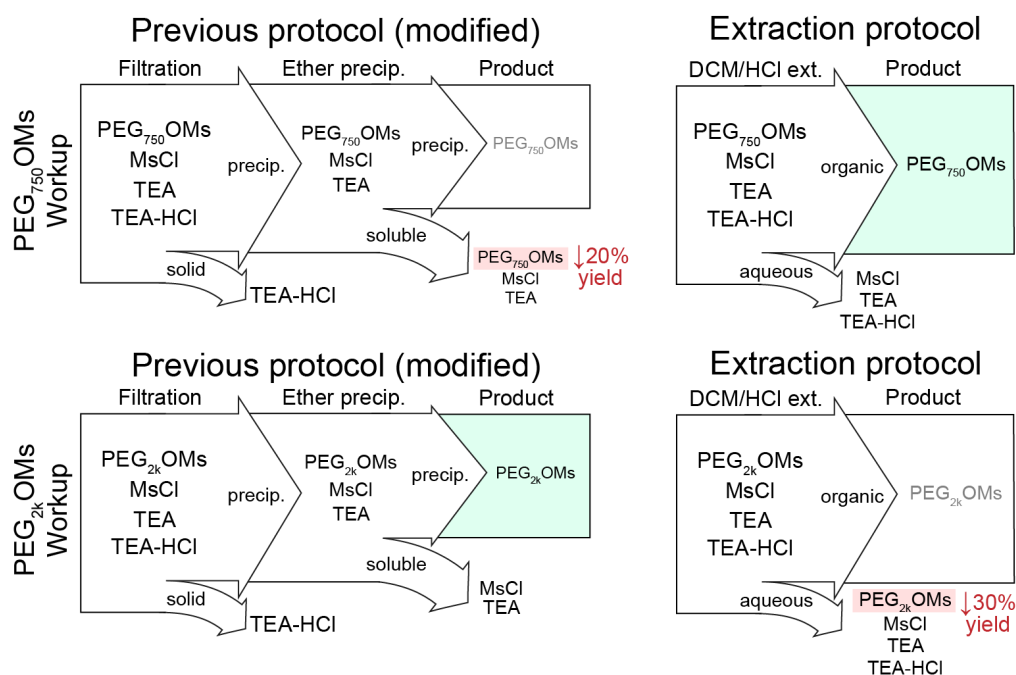


**Figure 2-5. Schematic of summarized conditions for efficient workup and purification of both mPEG750-OMs and mPEG2000-OMs in the previous and proposed protocols.** The products and impurities are traced through each workup step as indicated by the arrows, with incomplete separation denoted as gray text. Losses in yield or purity are indicated in red while the final proposed pathway is marked in green.

original workup and 43% respectively. The cold ether precipitation describes an additional several hours in the freezer and/or the addition of 33% hexanes to enhance solid formation. However, the moderate solubility of mPEG<sub>750</sub> in the ether antisolvent makes some product loss to the supernatant unavoidable, resulting in an incomplete recovery and a drop in yield.

For the mPEG<sub>2000</sub> compounds, the opposite was found. Workup protocols with an extraction decreased the yield of mPEG<sub>2000</sub>-OMs to 60% from the original 88% and to 41% for mPEG<sub>2000</sub>-SAC. This decrease is likely due to the mPEG<sub>2000</sub> chain being too long to effectively partition into the DCM layer of the extraction and product loss to the aqueous washes. Instead, a return to ether precipitation restores the yields of both compounds and improves them to

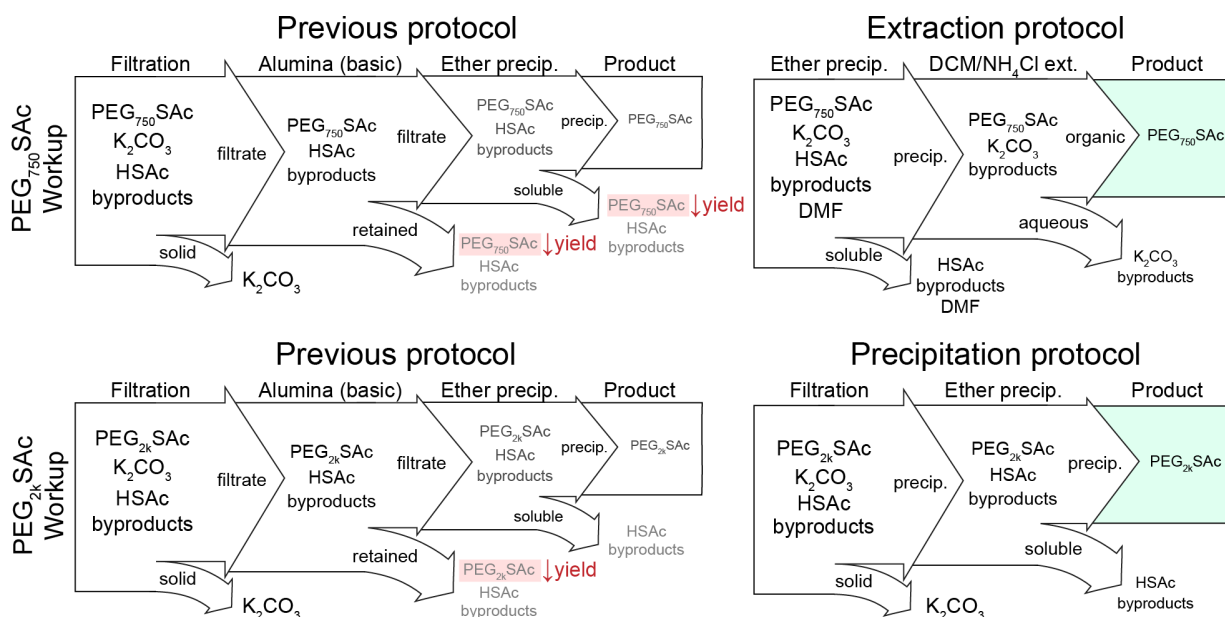


**Figure 2-6. Schematic of summarized conditions for efficient workup and purification of both mPEG<sub>750</sub>-SAC and mPEG<sub>2000</sub>-SAC in the previous and proposed protocols.** The products and impurities are traced through each workup step as indicated by the arrows, with incomplete separation denoted as gray text. Losses in yield or purity are indicated in red while the final proposed pathway is marked in green.

96-98%, indicating that the extra steps of filtration and column separation reduce the yield without improvement in purity. The ether precipitation works well for the longer mPEG<sub>2000</sub> because the long hydrophilic chain is fully insoluble in the ether antisolvent and a full product recovery is achieved.

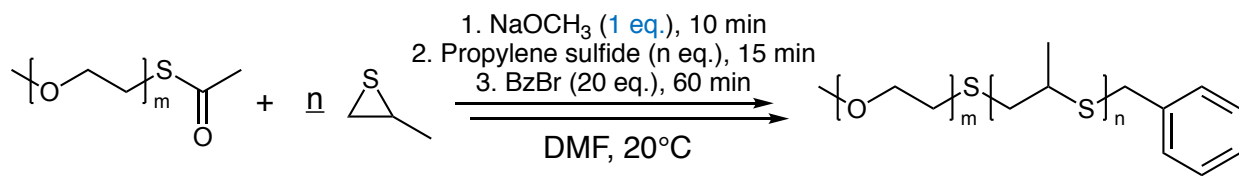
It should also be noted for the more complex mPEG-SAc step that the significant changes to the reaction conditions, especially the drastically reduced reaction time and corresponding lighter color of the reaction mixture, allowed for a much simpler workup protocol. Included in this process is the avoidance of the previous rotary evaporation step to remove the DMF solvent after reacting overnight. In trials with the shorter reaction time and lighter color, the mixture darkened significantly in the hot water bath of the rotavap as the reagents were never quenched after the flask was removed from the stir plate. The table entry of QRV represents an option to have this same rotary evaporation step but includes a quench with saturated ammonium chloride. Alternatively, the reaction can be directly precipitated into ether to dilute the DMF and collect via filtration. As with the shorter reaction time, these efforts to prevent the generation of these impurities allows for significantly less effort to isolate a higher quality final product at excellent yields.

#### 2.4.5 PEG-*b*-PPS polymerization

The protocol for synthesizing the diblock copolymer PEG-*b*-PPS has been largely consistent over the decades it has been studied. A minor adjustment to the amount of base used to deprotect the mPEG-SAc initiator down to 1 eq from 1.1 eq is shown along with the rest of the

conditions in **Scheme 2-3**. This adjustment was carried through to all three polymers for micelles, polymersomes, and bicontinuous nanospheres to yield the NMR spectra shown in **Figure 2-7a-c**. The PPS chain length is calculated from the NMR integration of the three corresponding peaks with respect to the methoxy of mPEG initiator (3.3 ppm, s, 3H): for each PPS unit, peaks at 1.3 ppm (3H), 2.6 ppm (1H), and 2.9 ppm (2H). The sum of these divided by the 6 total protons give an accurate estimate of the PPS chain length attached to mPEG. The integration of the PEG backbone at 3.6 ppm (4H / unit) offers insight into the presence of PPS homopolymer initiated by excess sodium methoxide as both the terminal end of mPEG and the sodium methoxide PPS initiator will add into the area of the 3.3 ppm signal. In this situation, the larger reference integration will suggest the PEG backbone is shorter than the expected 4H / unit. If this is seen, an additional precipitation in cold ether will remove the PPS homopolymer that remains soluble while the PPS attached to PEG will crash out after incubation at low temperatures.

These resulting polymers were assembled into nanostructures via flash nanoprecipitation and characterized via DLS (**Figure 2-7d-f**) and SAXS (**Figure 2-7g-i**). To evaluate the polydispersity of the formed nanostructure, DLS was performed as a measurement of hydrodynamic diameter. In this technique, a laser is passed through a dilute suspension that tracks the Brownian motion



**Scheme 2-3. Preparation of PEG-*b*-PPS diblock copolymer.** The reduced sodium methoxide equivalents are marked in blue.

of the particles diffusing through water in order to calculate diameter. The values for each formulation are shown in **Table 2-4**. Based on DLS, the MC formulation was comprised of a single monodisperse peak at 18.5 nm with a PDI of 0.053, the PS formulation was also comprised of a single monodisperse peak at 100.8 nm with a PDI of 0.0900, and finally the BCN formulation showed a peak at 247.8 nm with a PDI of 0.299. High quality PEG-*b*-PPS particles should have a PDI of 0.400 or lower and fall into the established ranges for each morphology: for MC from 15

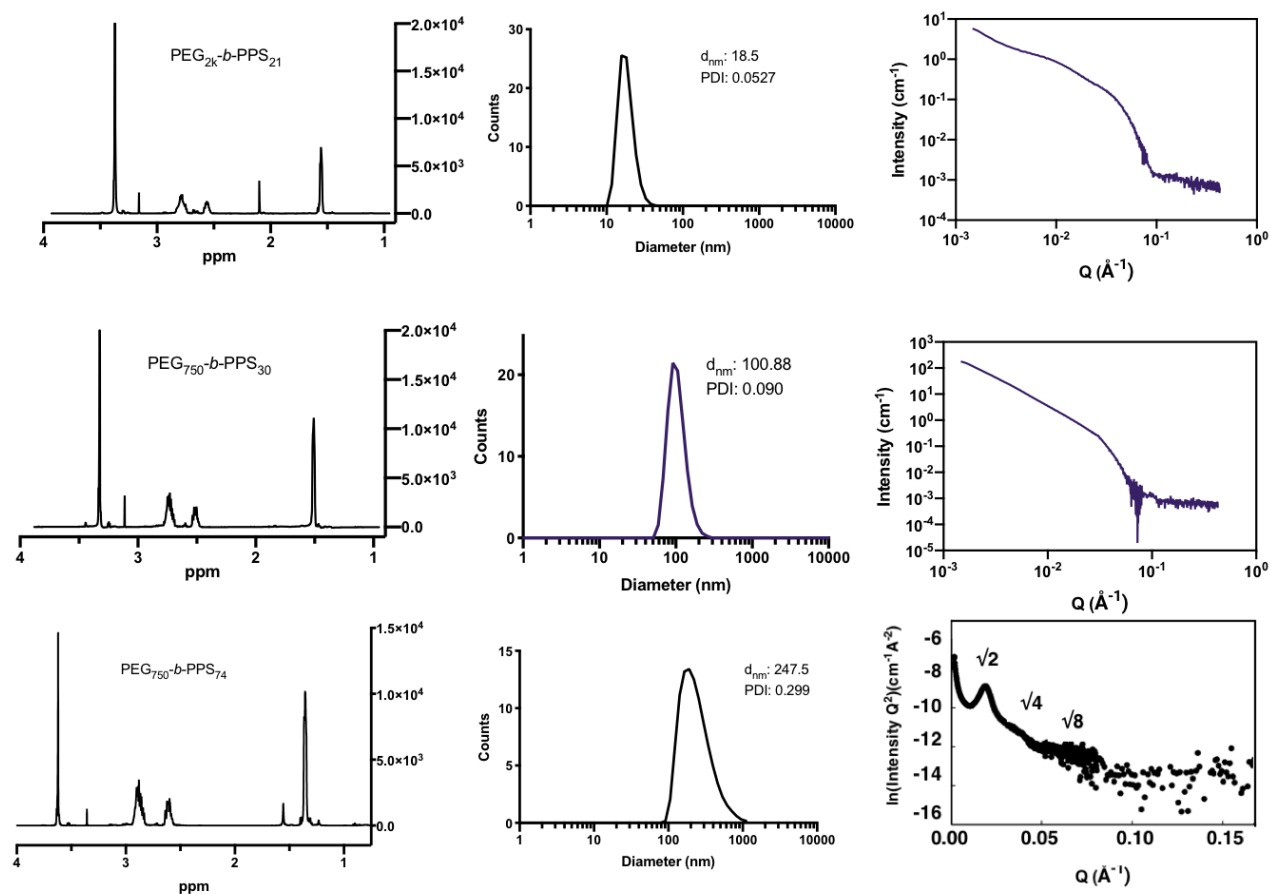


**Figure 2-7. Characterization of MC, PS, and BCN nanostructures.** Analysis by NMR (a-c) for polymer chain length, DLS (d-f) for population level hydrodynamic diameter, and SAXS (g-i) for internal architecture are shown for three nanoparticle morphologies.

to 30 nm, for PS from 70 to 120 nm, and for BCNs from 200 to 300 nm. These DLS results are promising for the formation of high-quality MC, PS, and BCN morphologies from PEG-*b*-PPS polymer made with the optimized synthesis conditions.

SAXS (small-angle x-ray scattering) is an orthogonal technique to DLS that is used to examine the internal architecture of complex nanostructure based on the scattering pattern as a beam passes through the sample. Fitting this scattering pattern to a model of core-shell, vesicular, or Bragg peak distribution reveals the nature of the internal structure of the nanoparticle morphology on a population level. As shown in the SAXS traces, the scattering pattern for the MC, PS, and BCN formulations align with the expected shapes for each morphology according to previous work.<sup>29,78,81,150,192</sup> These two reliable and robust techniques provide strong evidence that the new PEG-*b*-PPS polymer synthesis can produce stable nanomaterials of three different morphologies and validates its adoption into future nanocarrier formulations.

**Table 2-4. Summary characterization metrics of MC, PS, and BCN PEG-*b*-PPS polymer formulations.**

	PEG	PPS	$f_{\text{PEG}}$	d.nm	PDI
MC	2000	21	0.563	18.5	0.053
PS	750	30	0.253	100.8	0.090
BCN	750	74	0.120	247.8	0.299

PEG: PEG MW as 750 g/mol or 2000 g/mol; PPS: number of PPS units from NMR;  $f_{\text{PEG}}$ : calculated hydrophilic PEG weight fraction; d.nm: diameter in nm from DLS; PDI: polydispersity index from DLS; MC: micelle formulation; PS: polymersome formulation; BCN: bicontinuous nanosphere formulation.

#### 2.4.6 Time, cost, and yield of optimized protocols

In addition to improving the yield and purity of the final mPEG products, it is also important to consider the effects of the synthesis and workup protocols on the overall cost of materials and time required. The cost of the required materials for both the previous and optimized protocols for each synthetic step are shown in **Table 2-5**. The estimations for reagent costs are based on the current prices from chemical manufacturers including Sigma-Aldrich, Fisher Chemical, and TCI America. The values are normalized to the final amount of product incorporating the overall yield of each step into the final calculation. For the initial mPEG-OMs synthesis, the required time drops 94% and the cost of materials is reduced to 71%. These decreases are paired with a 137% increased yield for mPEG<sub>750</sub>-OMs and 115% for mPEG<sub>2000</sub>-OMs. For mPEG-SAc, the effects are even more significant with the required time decreasing 90% compared to the previous protocol and 99% fewer material costs. Again, these decreases are compounded by the significantly increased yields of 386% for mPEG<sub>750</sub>-SAc and 320% for

**Table 2-5. Summary of optimized time, cost, and yield calculations for the mesylate and thioacetate synthesis of mPEG<sub>750</sub> and mPEG<sub>2000</sub>.**

	PEG	Time			Cost			Yield		
		Old	New	Δ	Old	New	Δ	Old	New	Δ
OMs	750	24h	1h 15m	-94%	\$10.34	\$3.07	-71%	70%	96%	137%
	2000							85%	98%	115%
SAc	750	24h	2h 20m	-90%	\$104.24	\$1.23	-99%	25%	92%	368%
	2000							30%	96%	320%

PEG: PEG MW as 750 g/mol or 2000 g/mol; Time: reaction time required; Old: previous protocol; New: optimized protocol; Δ: difference between protocols; Cost: total cost of materials for the synthesis; Yield: amount of functionalized final product formed.

mPEG<sub>2000</sub>-SAC. The effects on the final polymerization step are about equal between the protocols as only the amount of sodium methoxide base has been changed and are therefore not included.

## 2.5 Conclusion

Overall, the goals of this synthesis optimization were to definitively understand each contributing aspect to the yield and purity of these PEG derivatives and to find the ideal balance between maximized product quality and minimized material and time costs. The lack of cohesion and clarity among previous protocols presents conceptual and practical barriers to the successful implementation of this PEG-*b*-PPS material. Meeting these goals is essential for its establishment as an accessible, scalable, and reliable drug delivery vehicle that can be synthesized efficiently for a broad range of biomedical applications. The systematic approach I took to this work was extensive but rewarding as the final optimizations offered significant benefits not only to the synthesized products, but also to the quality of life of the person implementing them. Each component of starting material preparation, reagent equivalents, solvent selection, volume management, conditions, reaction time, and purification for the three steps to make the final diblock copolymer were confirmed or improved according to established organic synthetic principles.

For the first step of the synthesis, I found that the mPEG starting material can be effectively dried from the commercial state with a simple rotavap protocol that can be completed

much quicker, more safely, and ahead of time compared to the azeotropic approach previously utilized. I found that mPEG-OMs requires much less TEA base and mesyl chloride to effectively functionalize the terminal end, only requiring a slight excess at 1.25 equivalents. Additionally, I found that the reaction happens at a rate much faster than previously assumed, requiring only a few minutes for complete conversion to the mesylated product. These changes to the protocol for this step are modest but confirm that this mesylation is quick, robust, and can tolerate a more efficient approach to its preparation.

The second step of synthesizing mPEG-SAc was a more complex task but also offered a higher potential for improvement as this step was responsible for low yields and variable product quality. The approach to this optimization involved both practical considerations of the reagents and solvents, and also a conceptual reframing as the reaction color was decoupled from the qualitative measurement of reaction progress. I was able to confirm that 3 equivalents of potassium carbonate and thioacetic acid were sufficient for reaction conversion, and that DMF remains an acceptable, though not ideal, solvent. The most critical improvement for this step was the indication that the reaction is essentially complete in 30 to 60 minutes while the reaction remains a bright orange color. The significance of this is two-fold: unnecessary time was eliminated, as the previous protocol required waiting overnight, and evidence shows that the dark pigmentation is due in large part to impurities rather than the mPEG-SAc itself. This meant that I was able to improve the purification of the final thioacetate product before adjusting that portion of the protocol simply by preventing the development of impurities from the start. These

changes resulted in a higher quality product in less time with less effort compared to the previous complex protocols.

For the workup of these two steps, I took an approach that depended on the PEG length for efficient product recovery. One of the main goals in previous workup protocols is the strict avoidance of water coming into contact with the mPEG products. Instead, I was able to confirm that the mesylate and thioacetate derivatives are able to not only tolerate water, but can utilize it as a quenching strategy and purification approach. In this way, I could introduce an extraction to the workup of the shorter mPEG<sub>750</sub> as it would be able to partition into a DCM later across multiple aqueous washes. For the larger mPEG<sub>2000</sub>, I showed that a simple ether precipitation was sufficient purification given the optimized reaction conditions found previously. Through these optimized protocols, the time and materials required for sufficient purification were significantly improved compared to the previous protocols and yielded products of higher purity at better yields.

Finally, I was able to show that the dramatic changes to the PEG-*b*-PPS synthesis were still able to produce nanoparticles of expected quality compared to the previous protocols. I found that the optimized mPEG-SAc initiator was able to reliably polymerize PPS and create micelle, polymersome, and bicontinuous nanosphere morphologies via FNP that were confirmed by DLS and SAXS analysis. This final quality control study gives strong evidence that the mPEG derivatives confirmed by chemical analysis are also able to act as functional initiators for creating the PEG-*b*-PPS diblock copolymer material for drug delivery applications.

## 2.6 Acknowledgments

I would like to acknowledge the help of Sharan Bobbala for help with data acquisition, analysis, and interpretation of SAXS results for nanoparticle characterization.

## 2.7 Publication information

Portions of this chapter are being prepared for publication with the following working citation information:

Frey MA & Scott EA. Improved synthesis and purification of functionalized poly(ethylene glycol) for the preparation of thiolate-initiated copolymer blocks for nanomaterials. (2021).

## CHAPTER 3

# Tailoring nanocarrier morphology and surface charge for uptake in non-APC cell lines

### 3.1 Abstract

Rationally designed nanoparticle drug delivery vehicles can be chemically modified in several ways to enhance uptake into the target cell type based on characteristics such as size, morphology, and surface charge. This optimization is especially important for uptake into non-phagocytic cells which often have limited uptake mechanisms and preferences for these nanoparticle characteristics for internalization. Generally, particles of a smaller diameter and cationic surface charge are taken up by cells more readily than their larger, neutral-to-negatively charged counterparts. However, the extreme ends of the scale for each of these characteristics can induce widespread cytotoxicity and negate the therapeutic effects of the nanoparticle construct. In this chapter, PEG-*b*-PPS nanoparticles of micelle or polymersome morphologies/sizes and a range of surface charges are prepared to evaluate the ideal uptake conditions for the non-phagocytic DAOY and ASZ cell lines without inducing cytotoxicity.

## 3.2 Introduction

### 3.2.1 Routes of nanoparticle uptake into cells

Immunoengineering-based strategies often target professional phagocytic cells of the immune system for the uptake of nanoparticles to modulate immune function. In comparison to these cell types that routinely and readily internalize foreign materials, the approach to targeting non-phagocytic cells for nanoparticle uptake requires an additional set of considerations that take advantage of the phagocytosis and endocytosis mechanisms of the target cell population.

Nanoparticles can be internalized by cells through many well-established routes based on the physiochemical characteristics of the nanomaterial and overall aggregate structure. Given that a majority of nanoparticles are larger than a couple of nanometers and are charged or have polar moieties on the surface for enhanced aqueous stability, they cannot passively cross the cell membrane and must utilize a route of active transport.<sup>193</sup> These routes of endocytosis can be broadly classified into two groups as pinocytosis or phagocytosis.

Pinocytosis is a type of internalization used by cells of all types to take up foreign particles that can fit within small membrane invaginations as triggered by a number of well-studied mechanisms. Each of these routes has a range of particle diameters and processing pathways that can be considered when rationally designing nanoparticles for uptake by specific cell types. Clathrin- and caveolae-mediated endocytosis are processes both limited to the uptake of particles of diameters less than 200 nm.<sup>194</sup> Material internalized by clathrin-coated pits is directed through the endo-lysosomal pathway for digestion while caveolae-mediated uptake

retains the material in neutral caveosomes which is an important consideration for nanoparticle cargo release.<sup>195,196</sup> Macropinocytosis is a large-scale internalization of material through an invagination up to 10 microns wide that can take up entire apoptotic cells, pathogens, or micron-sized nanoparticles.<sup>197</sup> Finally, phagocytosis is responsible for 'eating' a wider range of particles including large debris and cell materials especially after opsonization by serum proteins.<sup>198</sup>

These different internalization mechanisms are found across separate cell populations with the necessary cellular machinery to carry out the process. Caveolae-mediated endocytosis is seen to occur in epithelial cells, endothelial cells, muscle cells, fibroblasts, and adipocytes.<sup>199</sup> In contrast to pinocytosis, phagocytosis is largely limited to the specialized phagocytes of the immune system which are able to take up foreign particles with less discretion for the sake of maintaining defenses to pathogens.<sup>198</sup> In this way, it is important to consider the types of internalization available to the target cell population when designing nanoparticle therapeutics. In general, a major distinction is for the targeting of phagocytic or non-phagocytic cells, of which the latter is subject to much more restricted routes of uptake and smaller nanoparticle diameter without the ability to undergo phagocytosis.

### 3.2.2 Enhancing uptake: size, charge, morphology

Modifying particle size is the most easily and commonly tailored property of tunable nanomaterials as it plays a critical role in target cell internalization and processing. There is no shortage of reviews on this topic that are applied to a wide range of more specific conditions and applications.<sup>51,200-202</sup> While there are many physiochemical components of a nanoparticle that

determine the cellular uptake, this section will focus on three main considerations: diameter, surface charge, and morphology. The diameter of nanoparticles influences the amount and type of cellular uptake based on biological and thermodynamic properties (**Figure 3-1a**). The surface charge determines the electrostatic interactions of the particle with the cell surface to increase the likelihood of internalization (**Figure 3-1b**). The morphology as defined by the aspect ratio, degree of curvature, and surface area dictates the point of contact on a cell surface and dictates if the cell is capable of internalizing the particle.

Broadly, there appears to be an ideal size range for nanoparticle uptake between particles that are too small to have efficient cell membrane interactions and particles that are too large to attempt internalization. A larger particle requires more energy, membrane, and time to become engulfed into the cell, while at the same time it must be large enough to effectively drive this enthalpic engulfing process.<sup>61,203</sup> This phenomenon of endocytosis is known as the “wrapping

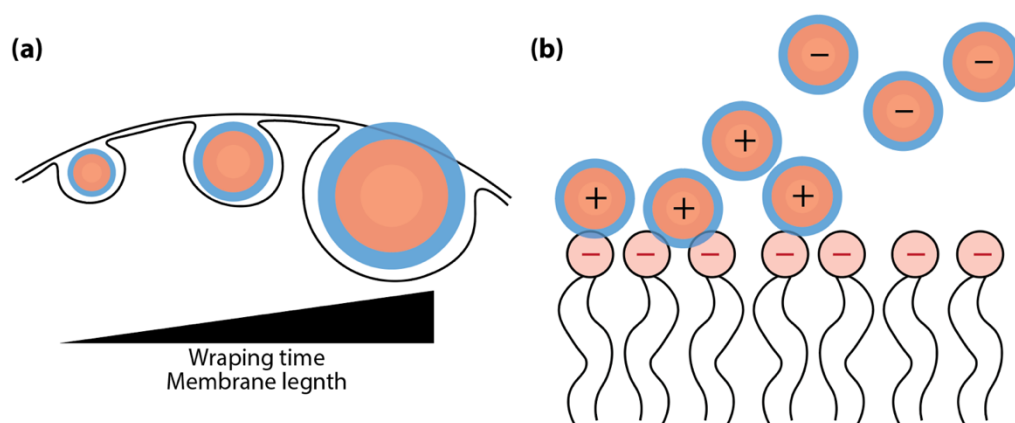


**Figure 3-1. The effects of particle size and charge on cellular uptake.** (a) Nanoparticles with a smaller diameter are taken up more readily given the lower requirement for wrapping time and membrane length to thermodynamically favor internalization compared to larger particles. (b) Cationic particles associate with the anionic cell membrane via electrostatic forces that enhance uptake compared to anionic particles.

time” and has been explored in a number of studies that note the efficient uptake of particles between 10 and 60 nm.<sup>61,204,205</sup> Aside from more rigid cutoff values based on cell size and available membrane to bud off, this range shifts based on the cell population which may have associated preferences and capabilities based on its cellular machinery.<sup>200</sup> With this caveat in mind, a number of studies have shown that particles of a size below 20 nm or above 100 nm are taken up more slowly.<sup>193,206</sup> For spherical particles, a higher efficiency adhesion to cell surface receptors occurs with smaller diameters as a larger size particle would experience a receptor shortage which is less entropically favored.<sup>203,204</sup> However, despite these considerations of maximal efficiency and speed, there are numerous examples showing nanoparticles of sizes well outside of these ranges being taken up in sufficient amounts to have the intended therapeutic effect.<sup>29,48,207</sup> Is it worth the efforts to explore the uptake of nanocarriers of multiple diameters into the target cell population with the understanding that there is likely an ideal window for the most successful uptake.

In comparison to particle size, which often determines the physical capabilities of cell internalization, the surface charge of a particle plays a significant role in the preferential rate of uptake into the target cell population. The outcome of surface charge is dictated by several main concepts. The most prevalent is that the outer membrane of the cell is negatively charged due to the presence of several anionic phospholipids embedded in the leaflets.<sup>10,15,20,21</sup> This causes cationic nanoparticles to have a much higher rate of association with the anionic cell membrane due to the electrostatic interactions between the surfaces, thus enhancing uptake of these particles.<sup>208-210</sup> This effect is also charge-dependent as seen in a wide number of studies that

demonstrate uptake to be impacted differentially based on surface charge, with anionic formulations having reduced uptake.<sup>51,211</sup> However, the effect of nanoparticles with a negative surface charge is subject to a more complex system of interactions that result in studies showing a reduced uptake, a similar uptake, and even an enhanced uptake.<sup>51,208,209</sup> Additionally, charge appears to influence the mechanism of endocytosis which is cell-type specific.<sup>51,212</sup> Overall, the most reliable way of enhancing uptake through surface charge is by incorporating cationic functionalities. Any other modifications to maintain neutral or anionic charges are material- and cell-specific and must be explored thoroughly for each case.

The last major consideration for enhancing nanoparticle uptake is the modification of morphology. A majority of self-assembling nanoparticles will be of a spherical morphology based on the most thermodynamically stable arrangement of components and is a highly efficient way of inducing nanoparticle uptake. However, a wide range of morphologies have been developed for drug delivery applications including rods, discs, cubes, worms/filaments, and more.<sup>39</sup> The effect of these shapes on internalization are dictated largely by the specific point of contact made on the target cell which uses a number of mechanisms to attempt to distinguish the overall particle morphology before deciding whether or not to internalizing the nanoparticle.<sup>193,213</sup> The characteristics of aspect ratio, flexibility, and the presence of harsher corners or edges can be utilized to impart features including enhanced cellular uptake or increased circulation time as detailed previously.<sup>214</sup> In one study, nanospheres were taken up more readily than nanorods or nanodiscs except when the particles were coated with an antibody where nanorods had the highest uptake.<sup>215</sup> This was credited to the higher surface area per unit volume of nanorods which

led to higher adsorption of antibody. As with size and charge, the effects of morphology can be specific to the target cell population and should be explored thoroughly for both rate and mechanism.<sup>48,216,217</sup>

### 3.2.3 Toxicities of size, charge, morphology

Despite the advantages offered by rationally designing these nanoparticle properties to suit the application, the extreme ends of the scale can result in significant toxicity. Disrupting the balance within the complex biological system can result in non-specific and widespread cell death and tissue injury. These negative effects can easily negate the advantages offered by the tuned quality and must be taken into account for any nanoparticle application. It is vital to ensure that the characteristics of nanoparticles designed to maximize uptake or other biological outcomes do not approach the toxic range.

For size-dependent toxicity, particles that are small enough to pass through mechanical barriers can interfere with delicate cellular machinery. Nanoparticles of sizes smaller than 6 nm are able to enter the cell nucleus and even smaller sizes around 1.4 nm are able to interact with the DNA phosphate backbone to induce apoptosis.<sup>218,219</sup> While most toxicity trends indicate that smaller nanoparticles are more damaging, large nanoparticles around 600 nm can deform cell membranes and damage the internal architecture to cause a physical destruction of the cell.<sup>220</sup>

A primary toxicity consideration is the surface charge of nanoparticles. As mentioned previously, the most reliable and effective way to increase the uptake of a nanomaterial is to add a cationic charge that electrostatically associates with the anionic cell membrane. However,

cationic charges in biological environments are known to disrupt the integrity of the cell membrane and cause non-specific cytotoxicity associated with a number of mechanisms

(Figure 3-2).<sup>221-224</sup>

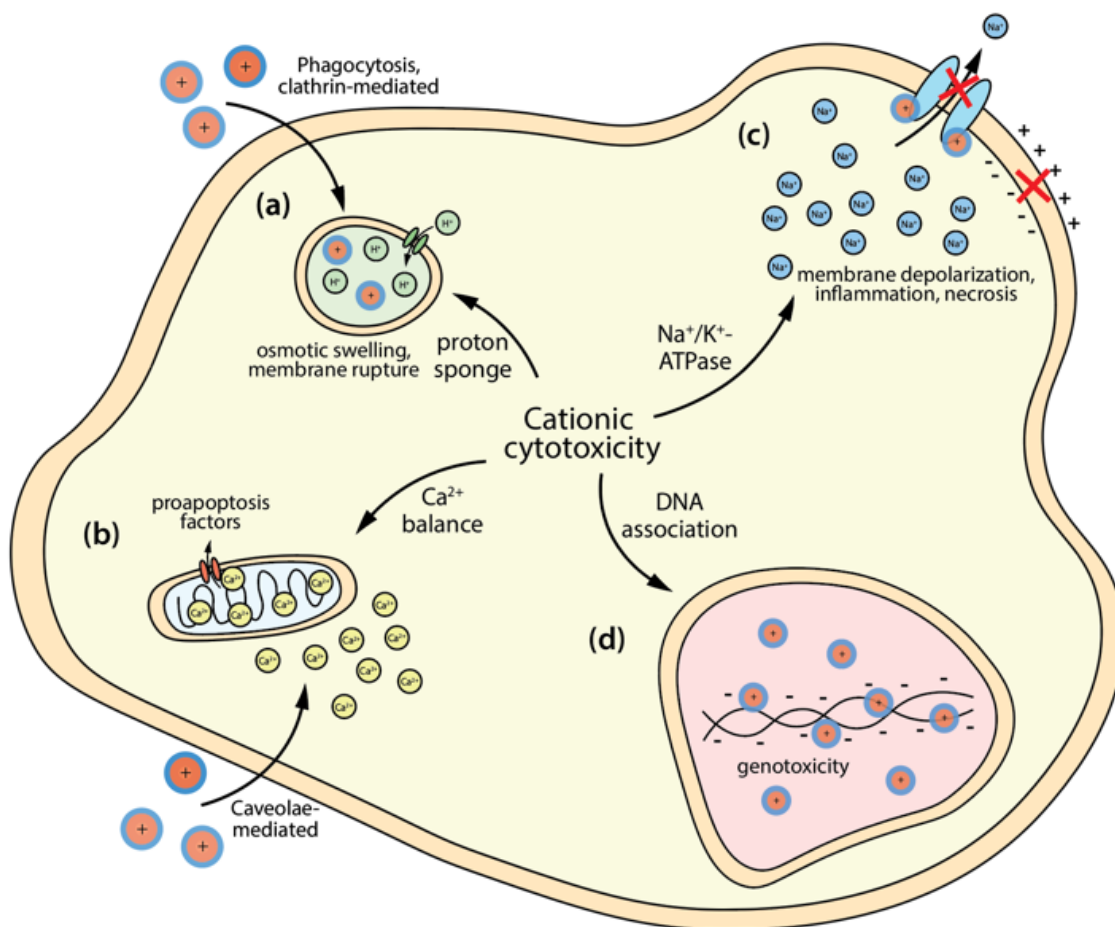


**Figure 3-2. Major mechanisms for cationic-induced cytotoxicity.** (a) Cationic particles with proton buffering capacity taken into cells for lysosome processing act as a 'proton sponge' to reduce compartment acidity, induce proton pump activity and osmotic swelling to lyse the compartment and induce apoptosis. (b) Cationic particles can increase calcium concentration and cause mitochondrial sequestering. A high enough level of calcium induces the PTP complex to release proapoptotic factors into the cytosol and damage the mitochondria. (c) Cationic particles bind to the cationic binding site of the  $\text{Na}^+/\text{K}^+$ -ATPase and inhibit sodium ion efflux. The imbalanced sodium ion concentration causes membrane depolarizes and inflammation resulting in rapid cellular necrosis. (d) Cationic particles that can enter the nucleus induce genotoxicity by associating with the anionic sugar phosphate backbone of nucleic acid material.

One of the most well-understood mechanisms of cationic-induced cytotoxicity is the proton sponge effect. This mainly occurs when particles are taken up through endocytic routes that involve a lysosomal processing pathway such as phagocytosis and clathrin-mediated uptake.<sup>225</sup> Cationic particles and especially those with a high number of titratable amines are able to buffer the proton content of the lysosome, reducing the acidity of the compartment and inducing proton pump activity to attempt to restore balance (**Figure 3-2a**).<sup>221</sup> The resulting proton pump overactivity causes osmotic swelling that can ultimately rupture the lysosomal membrane, releasing proapoptotic factors and active enzymes that induce cell death.<sup>226</sup> Cell types that do not typically take up particles through routes with this lysosomal involvement are much less susceptible to this specific mechanism of cationic cytotoxicity.<sup>221</sup>

Another well-studied mechanism of cationic-induced cytotoxicity affects endocytic routes independent of lysosome processing by affecting intracellular balance of calcium ions ( $\text{Ca}^{2+}$ ) (**Figure 3-2b**). The uptake of cationic particles has shown to induce  $\text{Ca}^{2+}$  sequestering in the cytosol and subsequent mitochondrial buffering of  $\text{Ca}^{2+}$ .<sup>221</sup> This increased level of  $\text{Ca}^{2+}$  uptake into the mitochondria triggers the permeability transition pore (PTP) complex which damages the mitochondria on a wide scale, releases proapoptotic factors, and induces cell death.<sup>227,228</sup> This mechanism also appears to be closely related to the caveolae-mediated route of endocytosis based on the role of calveolin-1 in regulating intracellular  $\text{Ca}^{2+}$  flux, mitochondrial function, and cellular apoptosis.<sup>222,229</sup>

In the past several years, a novel mechanism of inflammation and necrosis induced by cationic particles was identified as involving the  $\text{Na}^+/\text{K}^+$ -ATPase (**Figure 3-2c**). Cationic particles

were found to interact with the cationic binding site of this enzyme and prevent Na<sup>+</sup> efflux, causing intracellular Na<sup>+</sup> overload and membrane depolarization almost immediately after uptake.<sup>223</sup> Cells treated with cationic particles experienced granular cytoplasmic swelling, membrane rupture, and subsequent necrosis through this Na<sup>+</sup>/K<sup>+</sup>-ATPase mechanism.<sup>230</sup> Further, cationic particles induced the release of mitochondrial DNA and severe inflammation in the local microenvironment much earlier than the apoptotic mechanisms discussed previously, suggesting this mechanism contributes to cationic cytotoxicity two-fold.<sup>223,231</sup>

Other studies have indicated a genotoxicity associated with cationic liposome or polymer nanoparticle formulations which is thought to be related to the electrostatic interactions between the cationic particles and the anionic nucleic acid backbones (**Figure 3-2d**).<sup>224,232</sup> A final consideration is the affect that widespread uptake of charged particles can have on the flexibility of the cell membrane, with cationic particles increasing fluidity and anionic particles inducing a gelation effect.<sup>233</sup> Each of these outcomes would negate any potential benefits of increased nanoparticle uptake, making the evaluation of cationic particle cytotoxicity a vital component to these strategies.

Morphology-induced toxicity is often a result of irregular shapes getting physically stuck while cellular-level toxicity is often a result of a stiff, high-aspect-ratio particles attempting to enter a cell that cannot offer the membrane area or the internal volume to contain it.<sup>234,235</sup> Since the mechanisms of determining particle size at the cell membrane surface are robust, this situation often happens unintentionally when presented with uncommon morphologies.<sup>236</sup> That is, if a nanoparticle with a high aspect ratio contacts the cell membrane at an angle that makes it

appear to be much smaller, the cell will attempt to internalize a particle that might be too large for the cell to handle.<sup>237</sup> Investigations of carbon nanotubes have uncovered the concept of frustrated phagocytosis in a mechanism similar to asbestos pathogenicity, where macrophages are unable to engulf high aspect ratio particles with lengths greater than 15-20  $\mu\text{m}$ .<sup>238,239</sup> The resulting phagocytic burst produces pro-inflammatory cytokines and reactive oxygen species (ROS) that cause significant toxicity. In a study by Boyles et al., systematic investigation of multi-walled carbon nanotubes revealed that these harmful effects were dependent on the fiber length while crystallinity and metal content had little influence.<sup>240</sup> For spherical particles, however, the regular and expected morphology is significantly less likely to result in this type of outcome.

#### 3.2.4 ASZ, DAOY cells

The work in this chapter is centered around selecting the PEG-*b*-PPS nanocarrier morphology and charge best suited for uptake into the non-phagocytic ASZ and DAOY cell lines. While each cell line corresponds to highly useful *in vitro* disease models, there is not yet much work on DAOY or ASZ cells for the uptake of engineered nanoparticles. Given that these cell lines are not professional phagocytic cells, it is likely that they will require additional nanoparticle modifications for optimized uptake based on size, morphology, and charge. A baseline understanding of each cell line will provide insight into how to approach this goal.

ASZ cells are a murine basal cell carcinoma (BCC) line harvested from the nodular tumors of *ptch*<sup>+/-</sup> mice exposed to UV irradiation.<sup>241</sup> This cell line is often a model for the investigation of BCC tumor therapies that are resistant to the typical hedgehog pathway modulators in the p53-

positive context.<sup>242,243</sup> As a type of basal cell, ASZ cells are relatively undifferentiated in order to enable the continuous proliferation of new keratinocytes.<sup>244</sup> Given that BCC lesions are located mainly at the skin surface, most potential therapeutics are applied topically, directly on the surface of the lesion, which simplifies many aspects of delivery including avoidance of non-specific reticuloendothelial system uptake and cell population targeting.<sup>245,246</sup> The handful of studies on uptake into this cell type suggest that there is an upper limit diameter cutoff for internalization and that a cationic charge may improve uptake.<sup>247-249</sup>

DAOY cells are a primary human medulloblastoma line harvested from the cerebellum of a four-year old boy.<sup>250</sup> As a type of neuroepithelial brain tumor, DAOY cells show epithelial morphology.<sup>250</sup> This cell line is widely used for the study of this common brain tumor in children that has similar connections to the hedgehog signaling pathway as the ASZ BCC pathophysiology.<sup>251</sup> Given its widespread use, nanoparticle uptake in this line is better understood than in the ASZ cell line and can offer additional insight into increasing uptake. Several studies suggest that smaller nanoparticles are taken up with higher success, but that particles of diameters near 200 nm can be internalized.<sup>207,252</sup> Additionally, surface charge did not have as strong of an association with increased uptake in DAOY cells which were able to take up nanoparticles conjugated to highly anionic fluorophores.<sup>252-254</sup> Overall, DAOY cells appear to be more tolerant of a wider range of nanoparticle characteristics for internalization.

### 3.2.5 Chapter objectives

The goal of this chapter is to conduct the preliminary studies necessary to select a suitable PEG-*b*-PPS nanocarrier for delivery of therapeutics to two non-phagocytic cell lines, ASZ and DAOY. The applications for these two cell lines are centered around BCC and medulloblastoma as two disease pathologies affected by the hedgehog signaling pathway. Given that these are not professional phagocytic cells, I hypothesize that the initial cellular uptake will be low compared to that of antigen presenting cells (APCs) and will require additional modifications to the nanoparticle vehicle to improve internalization. Based on the respective cell types and previous work, I expect that ASZ cells will be less amenable to uptake overall and especially to larger morphologies such as polymersomes. I expect DAOY cells to be able to internalize both the micelle and polymersome morphologies but perhaps at different efficiencies. The neutral-to-slight negative charge of methoxy-functionalized PEG-*b*-PPS materials should be a non-offensive starting point for nanoparticle uptake.

As described previously, there are several aspects of rationally designed nanoparticles that can be modified to suit the needs and preferences of the target cell population. Beginning with size, I hypothesize that uptake in both cell lines will be higher for the smaller micelle morphology over the larger polymersome morphology. Since both of these structures are spherical, the different internal morphologies are representative of two size conditions. Additionally, I hypothesize that adding a cationic charge to the surface of these nanocarriers will increase the uptake into both cell lines, but especially that of ASZ cells.

Given the addition of a cationic charge in the following studies, it is of vital importance to ensure that the positive charge is not high enough to disrupt the integrity of the target cell population. An ideal formulation would have a zeta potential within a range that enhances uptake without cytotoxic consequences, although this overlap is not always possible. I hypothesize that the range of cationic surface charges explored for this uptake enhancement study will be balanced by their cytotoxicity. Overall, optimization of these uptake conditions for DAOY and especially ASZ cell lines will provide a strong foundation for future work with PEG-*b*-PPS nanocarriers as delivery vehicles.

### 3.3 Materials and Methods

#### 3.3.1 Materials and Instrumentation

Unless indicated below, chemical reagents were purchased from Sigma-Aldrich (St Louis, MO, USA) and used as received. Methanol (MeOH), sodium chloride (NaCl, brine), ammonium chloride (NH<sub>4</sub>Cl), and Dil were obtained from Fisher Science (Pittsburgh, PA, USA) and used as received. Propylene sulfide was obtained from TCI America (Boston, MA, USA) and used as received. <sup>1</sup>H NMR spectra were recorded on Bruker Avance III 500 MHz system and analyzed with MestReNova (Mestrelab Research, Spain).

#### 3.3.2 ASZ and DAOY cell culture

ASZ murine BCC cells were cultured in M154 Calcium Free media supplemented with 2% fetal bovine serum “chelexed” by Chelex-100 (Bio-Rad), 1X pen/strep, and 0.05 mM CaCl<sub>2</sub>. Given ASZ

cell sensitivity to calcium, all maintenance of these cells including passaging was performed with this M154 2% serum media. DAOY cells were cultured in Eagle's Minimal Essential Media (ATCC) supplemented with 10% FBS, and 1X pen/strep.

### 3.3.3 Synthesis of NH<sub>3</sub>-PEG-*b*-PPS diblock copolymer

Cationic amine-functionalized PEG-*b*-PPS polymer material was synthesized as described in Karabin et al. 2018.<sup>22,190</sup> Briefly, heterobifunctional HO-PEG-*b*-PPS-Bz was prepared through the tosylation of hydroxyl PEG in the presence of silver oxide to favor the monofunctionalized HO-PEG-OTs product. Separately, PPS was initiated by benzyl mercaptan and end-capped with an excess of HO-PEG-OTs to form diblock copolymers of HO-PEG<sub>45</sub>-*b*-PPS<sub>20</sub>-Bz for micelles and HO-PEG<sub>17</sub>-*b*-PPS<sub>30</sub>-Bz for polymersomes. The hydroxyl terminal end of PEG was further modified with a mesylate functional group similar to the previously described protocol followed by azide functionalization by refluxing with sodium azide overnight. Finally, the azide was reduced to an amine with triphenylphosphine in a THF:water solvent system to yield the cationic NH<sub>3</sub>-PEG<sub>45</sub>-*b*-PPS<sub>20</sub>-Bz for micelles and NH<sub>3</sub>-PEG<sub>17</sub>-*b*-PPS<sub>30</sub>-Bz for polymersomes.

<sup>1</sup>H NMR (400 MHz, CDCl<sub>3</sub>): δ 7.34 – 7.31 (d, 4H), 3.67 – 3.63 (s, 4H/unit PEG), 2.99 – 2.84 (m, 2H/unit PPS), 2.66 – 2.54 (m, 1H/unit PPS), 1.42 – 1.35 (m, 3H/unit PPS). <sup>13</sup>C NMR (126 MHz, CDCl<sub>3</sub>): δ 138.2, 128.9, 128.5, 127.2, 70.6, 41.3, 38.4, 20.8.<sup>22</sup>

### 3.3.4 Assembly of cationic formulations

Charged polymer formulations were assembled as described previously using flash nanoprecipitation.<sup>29,150,160</sup> For each formulation, different proportions of methoxy-terminated PEG-*b*-PPS and amine-terminated PEG-*b*-PPS were mixed to a total of 20 mg (25%: 5 mg amine-terminated + 15 mg methoxy-terminated; 50%: 10 mg amine-terminated + 10 mg methoxy-terminated; 75%: 15 mg amine-terminated + 5 mg methoxy-terminated; 100%: 20 mg amine-terminated). These polymer mixes along with 0.0625% by weight of the hydrophilic DiI were solubilized in THF to 500  $\mu$ L total. This organic phase and 500  $\mu$ L of 1X phosphate buffered saline (PBS) as the aqueous phase were loaded into separate 1 mL syringes and anchored to a confined impingement jet (CIJ) block.<sup>187,188</sup> The phases were impinged together into the mixing chamber of the block once for MC formulations and directly into a 1.5 mL aqueous reservoir of 1X PBS. The polymersome formulation was impinged a total of three times before the final deposit into the 1.5 mL aqueous reservoir of 1X PBS. All formulations were desiccated overnight to remove residual THF and filtered through a gravity column packed with Sephadex LH-20 hydrophobic resin and a 1X PBS mobile phase to yield stable charged nanoparticle formulations.

### 3.3.5 Nanoparticle characterization: Size, polydispersity, and zeta potential

Nanostructure size distribution and polydispersity index (PDI) were measured by dynamic light scattering (DLS) using a Zetasizer Nano (Malvern Instruments) with a 4 mW He-Ne 633 nm laser. Each nanoparticle formulation was diluted 1:100 or 1:1000 into Milli-Q water and analyzed as two rounds of three runs ( $n = 6$ ). Zeta potential was measured by electrophoretic light scattering

(ELS) using the same Zetasizer (Malvern Instruments). Nanostructures were diluted 1:10 in ultrapure water prior to ELS for a 0.1X PBS background.

### 3.3.6 Uptake and confocal microscopy

DAOY and ASZ cells were plated at 50,000 cells/well in 500  $\mu$ L in fluorodishes and incubated overnight. Each well received nanoparticle treatments diluted 1:1000 into the final working volume and incubated for 24 hours. Cells were washed four times in PBS before adding fresh media and a drop of NucBlue stain (Invitrogen) in addition to the encapsulated Alexa488 for PEI and Dil for PEG-*b*-PPS nanoparticles. Cells were imaged within a humidified chamber using a 63x oil-immersion objective on a Lecia SP5 Scanning Confocal Microscope using HyD detectors and three lasers: 457 nm argon laser for NucBlue, 488 nm argon laser for Alexa488, and 633 nm red HeNe for Dil.

### 3.3.7 Cytotoxicity

The viability of DAOY and ASZ cells after treatment with charged micelle and polymersome formulations of 100% amine polymer composition were determined using the MTS assay. DAOY and ASZ cells were plated at 5,000 cells/well in a 96 well plate and grew to 70% confluency before treatment with each polymer concentration in triplicate. After incubating nanoparticles for 24 hours, 20  $\mu$ L of MTS reagent (Promega) was added to each well and incubated for another 1.5 hours. Then 70  $\mu$ L of the supernatant from each well was transferred to a new 96-well plate and absorbance was recorded at 490 nm using a Synergy H1M plate reader. The absorbance of the

nontreated controls was normalized to 100%, and all other conditions were calculated in reference to the nontreated controls. Data was analyzed for statistical significance with GraphPad Prism 8 using two-way ANOVA and Tukey's multiple comparison tests.

### 3.3.8 Flow cytometry

DAOY and ASZ cells were plated at 50,000 cells/well in 500  $\mu$ L in 12-well plates. Nanoparticle formulations were added to the cells for a final concentration of 0.25 mg/mL and repeated in triplicate. Cells were incubated with nanoparticles for 24 hours before collection for flow cytometry. Treated cells were lifted with trypsin, quenched with media, and rinsed with 1X PBS. Cells were stained for viability with Zombie Aqua (Biolegend) and incubated at 4°C for 10 minutes. The supernatant was discarded after gentle centrifugation and the samples were rinsed with 1X PBS before a final resuspension in 1:1 fixing/staining buffer (Biolegend). Cells stained with Zombie Aqua and encapsulated Dil were analyzed using an LSRFortessa SORP Cell Analyzer (BD Biosciences) using the 405 nm excitation laser and 450/50 filter set for Zombie Aqua and the 550 nm excitation laser and 582/15 filter set for Dil. The data was analyzed by Cytobank online software. Data was analyzed for statistical significance with GraphPad Prism 8 using two-way ANOVA and Tukey's multiple comparison tests.

### 3.4 Results and Discussion

#### 3.4.1 Initial uptake into DAOY and ASZ cell lines by morphology

PEG-*b*-PPS nanoparticles of micelle and polymersome morphologies were prepared for uptake experiments with the hydrophobic fluorophore DiI loaded into the hydrophobic micelle core or polymersome bilayer membrane. The characterization of these structures is shown in **Figure 3-3** as the expected parameters for each morphology: 15-30 nm for micelles and 70-100 nm for polymersomes. DiI-loaded micelle and polymersome formulations were added to ASZ and DAOY cells for confocal imaging studies for the cellular uptake. Polyethylenimine of molecular weight 25 kDa tagged with Alexa488 (Alexa488@25kDaPEI) was used as a positive control. Confocal imaging with DAPI and the corresponding loaded dyes is shown in **Figure 3-4**. The positive control of high molecular weight PEI is taken up readily by both cell lines while uptake for PEG-*b*-PPS nanostructures was more conservative. DAOY cells were able to internalize both

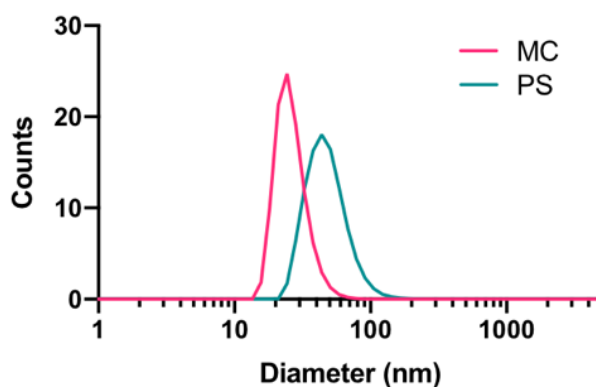


**Figure 3-3. Characterization of micelle and polymersome formulations.** The hydrodynamic diameter and polydispersity is shown in the DLS traces for these nanoparticle formulations loaded with DiI.

micelle and polymersome morphologies while ASZ cells were only able to take up a minimal number of micelles but no uptake is evident with polymersomes.

As expected, the uptake for these non-phagocytic cells lines was lower and more restricted than that of the APC uptake seen in immunoengineering applications into macrophages and dendritic cells.<sup>48,57,192</sup> Given that both micelles and polymersomes are a

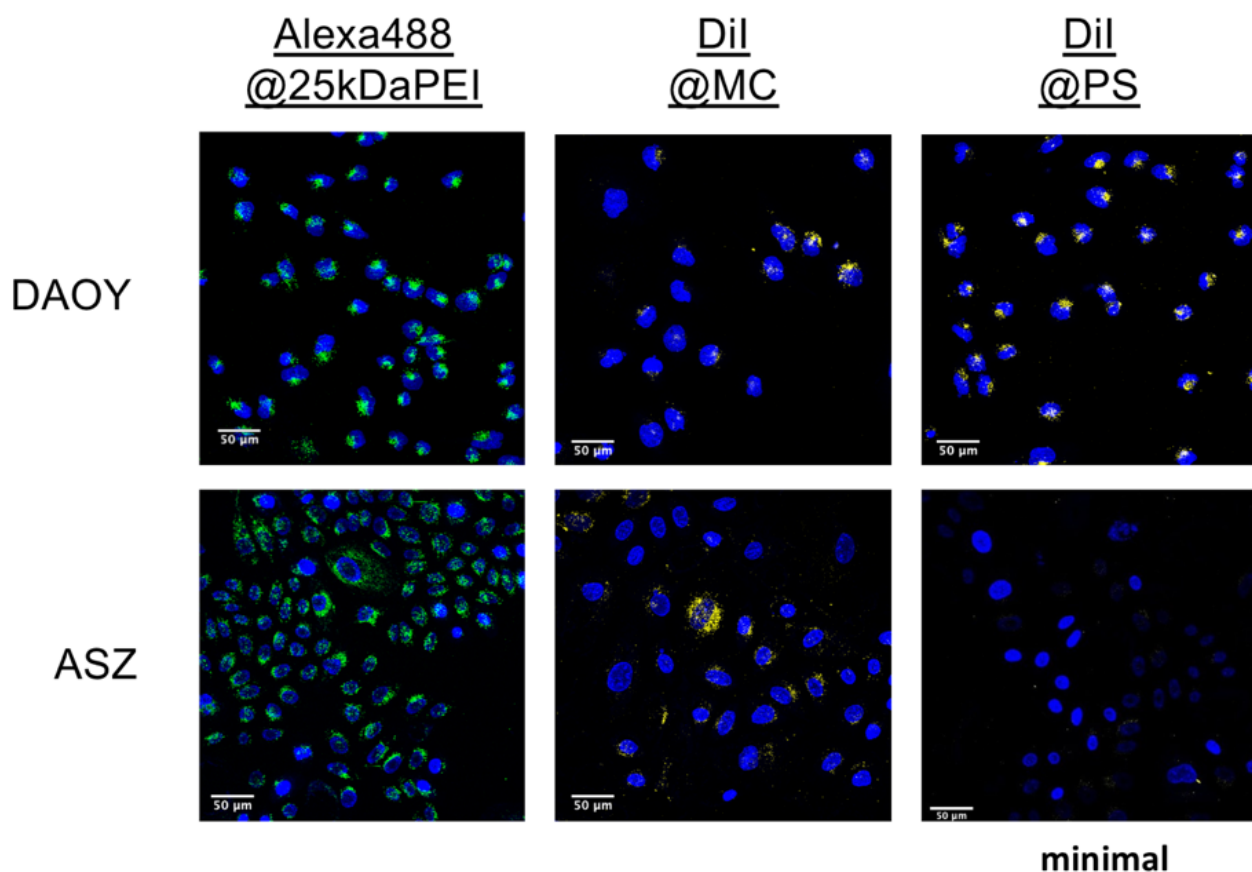


**Figure 3-4. Uptake of micelles and polymersomes into DAOY and ASZ cells.** Confocal microscopy images of micelles and polymersomes loaded with the hydrophobic Dil (Dil@MC, Dil@PS) compared to the positive control of cationic 25 kDa PEI with Alexa488 fluorescence (Alexa488@25kDaPEI). Blue staining for DAPI marks cell nuclei while green staining for Alexa488 and yellow staining for Dil represent nanoparticle uptake. Minimal nanoparticle staining was found for polymersome uptake in ASZ cells. The scale bar in these micrographs represents 50  $\mu\text{m}$ .

spherical shape with identical surface functionalization, the differences between uptake can be narrowed to the effects of nanoparticle size. From this pilot, there appears to be a size limitation for ASZ cells more than DAOY cells where micelles are internalized by both types, while polymersomes were too large for ASZ cells to readily take up. This is in accordance with previous work showing that ASZ cells were able to take up silica nanoparticles of 42 nm diameter but not of 75 nm or 200 nm, indicating an upper limit to the particle size tolerated by this cell line that matches the uptake of smaller micelles but not larger polymersomes.<sup>247</sup> In comparison, DAOY cells have shown to take up nanoparticles of diameters as high as 180 nm, which is fully inclusive of the larger polymersome morphology used in this work.<sup>207,252</sup>

### 3.4.2 Enhancing uptake into DAOY and ASZ cell lines with charged formulations

In an effort to enhance uptake, PEG-*b*-PPS formulations were made to cover a range of cationic surface charges. A positive surface charge is known to enhance internalization through several mechanisms discussed previously including an increase in passive association with the slightly negative cell membrane. The previous experiment used formulations of entirely methoxy-functionalized PEG chains which tend to be neutral or slightly negatively charged across the nanoparticle surface. To incorporate a cationic charge, amine-functionalized PEG-*b*-PPS was synthesized and mixed with the neutral methoxy polymer in controlled amounts before assembly via FNP. This strategy was applied to both micelle and polymersome constructs to create formulations of increasing cationic character for both morphologies.

These cationic formulations were prepared for administration to both DAOY and ASZ cell types in the same way as the initial uptake study with Dil. Given that both cell lines were able to take up micelles in the previous experiment, the charged micelle formulations were applied to evaluate any change in uptake. The cells were analyzed via flow cytometry as shown in **Figure 3-5** for DAOY and ASZ cell lines. The formulation surface charges and resulting uptake as quantified by median fluorescence intensity (MFI) is shown in **Figure 3-5a**. Both cell types show a dependence on charge as a more cationic character results in a higher uptake. In ASZ cells, all

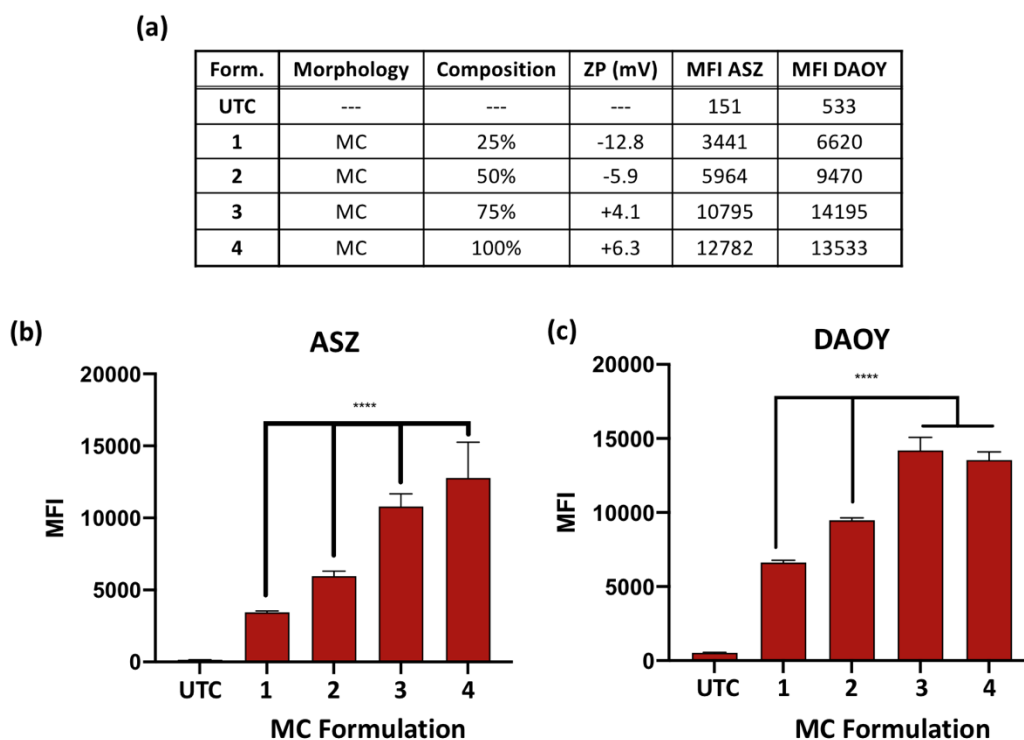


**Figure 3-5. Uptake of charged micelle formulations into ASZ and DAOY cells via flow cytometry.** (a) Charged micelle characteristics including zeta potential (ZP) for surface charge and resulting MFI as representative uptake in both cell lines. Untreated controls (UTC) are cells without any nanoparticle treatment. Composition refers to the percentage of cationic polymer in the formulation. Median fluorescence intensity (MFI) of charged micelle uptake into (b) ASZ cells and (c) DAOY cells with statistical significance determined by two-way ANOVA and Tukey's multiple comparison tests, \*\*\*\* $p < 0.0001$ .

four formulations are statistically significant for increasing uptake with increasing surface charge from -12.8 mV, -5.9 mV, +4.1 mV, and +5.9 mV. Specifically, the lowest to highest cationic micelle preparation in ASZ cells increased uptake nearly four-fold. For DAOY cells, a similar trend is seen for increasing uptake with increasing surface charge, however, the effect is leveled off for the highest surface charges of +4.1 mV and +5.9 mV. Between the lowest surface charges and the highest grouping, uptake increased about two-fold for DAOY cells.

For the charged micelle formulations, the increase in uptake between treatments was significant yet modest. This reflects the same modesty of the zeta potential differences between formulations as well, given that each of these four samples remains close to the neutral range. For example, nanoparticles can reach  $\pm 50$  mV or more depending on the material characteristics.<sup>209,252</sup> However, while this range is dramatically larger, it is likely that the extreme ends are not as compatible with these cell populations. As discussed, highly charged materials have the potential to disrupt membrane integrity and induce non-specific cell death across a population. Given that the goal for this initial work with non-phagocytic ASZ and DAOY cell lines is to increase uptake without increasing cytotoxicity, the modest range explored here is a reasonable starting point with promising results thus far.

For the polymersome morphology, only the DAOY cell line showed appreciable uptake in a preliminary run, so these charged polymersome formulations were only given to this cell line. The formulation zeta potentials and corresponding uptake quantification via flow cytometry is shown in **Figure 3-6**. This data also suggests an increase in cell uptake with an increased surface charge; however, there was not a distinct difference between the three lowest charges of +2.31

mV, +5.03 mV, and +10.8 mV. Only the final formulation of +12.4 mV had a significant increase in uptake compared to the first three charged polymersome formulations. The average of the lower charged group and this highest charge increased polymersome uptake into DAOY cells nearly four-fold.

Similar to the charged micelle formulations, the increased uptake for polymersomes is modest as is the difference in surface charge between the formulations. The results for this set of surface charges suggest overall that a cationic character may improve uptake into DAOY cells. However, the difference between the two highest values of +10.8 mV and +12.4 mV would typically be considered almost negligible but showed a significant improvement. This could be due to a certain threshold of cationic character to enhance surface associations but certainly suggests further investigation of these patterns in both cells lines. Another consideration for the

(a)

Form.	Morphology	Composition	ZP (mV)	MFI DAOY
UTC	---	---	---	1465
1	PS	25%	+2.31	15762
2	PS	50%	+5.03	6391
3	PS	75%	+10.8	19982
4	PS	100%	+12.4	55946

(b)

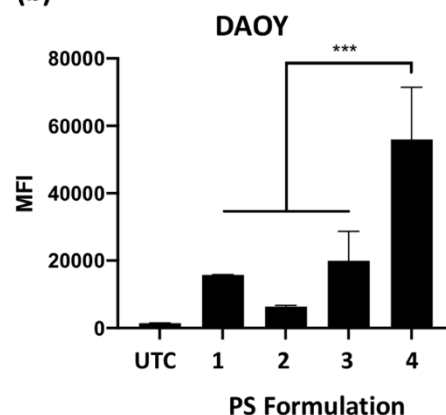


**Figure 3-6. Uptake of charged polymersome formulations into DAOY cells via flow cytometry.** (a) Charged polymersome characteristics including zeta potential (ZP) for surface charge and resulting MFI as representative uptake in DAOY cells. Untreated controls (UTC) are cells without any nanoparticle treatment. Composition refers to the percentage of cationic polymer in the formulation. (b) MFI of charged micelle uptake into DAOY cells with two-way ANOVA and Tukey's multiple comparison tests, \*\*\* $p < 0.001$ .

polymersomes in this size range is the influence of charge on the type of uptake into the cell. Previous work has shown that negatively charged and positively charged particles can be taken up through different routes into the same cell type.<sup>255,256</sup> Despite a relatively small range of surface charges, this consideration might contribute to the sudden increase in uptake seen for polymersomes in DAOY cells.

### 3.4.3 Cytotoxicity profile of charged formulations

As mentioned previously, changing the physiochemical characteristics of a material can change its effects in biological systems in both positive and negative ways. Each aspect of a given material can be modified to enhance the intended functionality but often reaches a point where the magnitude of effect has detrimental effects on the balance of the biological system. Theoretically, cationic charge used in this work to enhance uptake may often disrupt cell membranes and cause significant cytotoxicity at high levels. It was vital to assess the cell viability after treatment with these charged formulations, as increasing the cationic surface charge of these micelle and polymersome formulations may enhance uptake, but the effects are invalidated if the target cells do not survive. To address this, the formulations with the most cationic surface charges, +6.3 mV micelles and +12.4 mV polymersomes, were administered to cells and assessed for viability. As shown in **Figure 3-7**, the cationic formulations were non-toxic in RAW 264.7 macrophages with greater than 85% cell viability at all in-well concentrations tested, which fall well within the reasonable range for traditional, neutral charged PEG-*b*-PPS nanoparticles. Because this cytotoxicity data was performed using the phagocytic RAW cell line,

the enhanced uptake into these cells also represents a lack of cytotoxicity that may occur with off-target effects in an *in vivo* setting. Together, these results suggest that the increased cationic nature of these formulations remain within a safe range to use without modulating cytotoxicity.

### 3.5 Conclusion

This work with the uptake of PEG-*b*-PPS nanoparticles into the non-phagocytic ASZ and DAOY cell lines serves as a foundation for future experiments. As expected, both of these cell lines had limited internalization compared to what is seen in the phagocytic APC populations of macrophages and dendritic cells. The micelles were able to be taken up by both cell lines, perhaps due to their smaller diameter, as the other aspects of surface chemistry and spherical shape were identical between the formulations. The polymersomes were only visibly internalized by the DAOY cell line, however, which could be due to the larger diameter being more difficult to internalize by the non-phagocytic ASZ cell line.

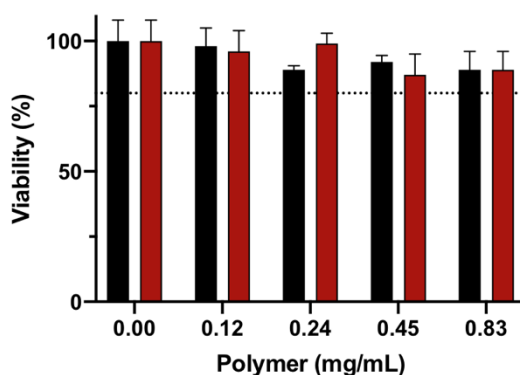


**Figure 3-7. Cytotoxicity of the two highest cationic micelle and polymersome formulations.** Treatments of +6.3 mV micelles (red) and +12.4 mV polymersomes (black) are shown across in-well concentrations up to 0.83 mg/mL in RAW 267.4 macrophages. The dotted line represents cell viability of 80% considered the minimal value for a non-cytotoxic outcome.

I prepared charged formulations to enhance uptake for cell lines that had an existing baseline uptake: micelles for both ASZ and DAOY cell lines, and polymersomes for DAOY cells. For all pairings, these charged preparations showed an increase in uptake as the surface charge became more cationic, increasing two-fold for micelles in DAOY cells and four-fold for micelles in ASZ cells and polymersomes in DAOY cells. While this effect is indeed modest, being able to enhance the uptake of a nanocarrier formulation by several-fold may allow for a marked increase in therapeutic effect and a decrease in  $IC_{50}$  of the loaded cargo. Any efforts toward this goal will significantly improve the clinical potential of a delivery system that requires less therapeutic to see a strong effect, especially when the drug is expensive, strong, and has many potential off-target side effects. Further investigation of these results that include a broader range of surface charges would clarify this effect for both micelle and polymersome morphologies in ASZ and DAOY cell lines.

An important consideration for charged particles is the potential to become cytotoxic if the effects are strong. Specifically, the highest cationic charges in the range used here were the most likely to have a toxic effect on cells. However, no decrease in cell viability was found even at fairly high polymer concentrations. This indicates that the cationic charge of the micelle and polymersome formulations fell into an ideal overlap of increasing internalization but not causing cell death. Falling on either side of this scale would produce a subpar nanoparticle product for this application that either would not increase uptake after the tedious amine-functionalized polymer synthesis, or that the charge would be high enough to cause cytotoxicity.

This result is also promising considering the third possibility of having no overlap between the two beneficial ends, with a formulation that induces cell death before any change in nanoparticle uptake. However, for both DAOY and ASZ cell lines, good evidence is provided for the ideal outcome of increased internalization without cytotoxic consequences. This suggests these cell lines are amenable to further work with PEG-*b*-PPS nanoparticle delivery systems, including refining the conditions that maximize uptake and continuing to load therapeutic drugs into the micelle and polymersome formulations for the given clinical applications.

### **3.6 Acknowledgements**

I would like to thank Meghan Ward for the critical role she had in the development and planning of this collaboration, her expertise in the biological context of this work and applications, maintaining cells, conducting *in vitro* experiments, and data analysis. I would like to thank Thomas Meade for the use of laboratory space and materials. I would like to acknowledge Mallika Modak for help conducting the flow cytometry experiments and subsequent data analysis.

### **3.7 Publication information**

The work in this chapter contributes to the foundation of several future projects with grant funding that utilize PEG-*b*-PPS nanocarriers for drug delivery into ASZ and DAOY cells lines to be completed over the coming years with a number of associated publications between the labs of Evan Scott and Thomas Meade.

## CHAPTER 4

# Development of FiVe-1-loaded nanocarriers for inhibiting vimentin

### 4.1 Abstract

The inflammasome is a vital component of the innate immune system with a powerful role in initiating and amplifying inflammation at the site of pathogenic threat. However, despite tight control on a number of regulatory levels, the inflammasome has been implicated in a number of severe morbidity and mortality outcomes after the initial infection. The intermediate filament vimentin has been shown to play an important role in the prevention of inflammasome-mediated tissue damage following pathogenic challenge, suggesting vimentin as a viable therapeutic target. In this work, the recently identified small molecule vimentin inhibitor FiVe1 was loaded into PEG-*b*-PPS micelle formulations to evaluate the compatibility of this nanocarrier delivery vehicle and the potential of Five1-loaded formulations to inhibit inflammasome activation via IL-1 $\beta$  production. The work in this chapter demonstrates the initial steps of optimizing and evaluating the *in vitro* performance of nanocarrier delivery systems. Additionally, the role of FiVe1 in vimentin inhibition and biological outcomes is discussed for future work with this construct.

## 4.2 Introduction

### 4.2.1 Inflammasome activation and regulation

The inflammasome is a specialized multiprotein complex found in activated immune cells that responds quickly and efficiently to perceived pathogenic threats as a vital part of the innate immune defense system. Upon detection of tissue distress, these components translocate and initiate a cascade of activation and cleavage to produce cytokines for immune cell recruitment to the site. This extremely powerful tool plays a vital role in the initiation of immune defenses based on the wide range of triggers and the proximity of components for the rapid and prolific generation of cytokines.

There are a number of known inflammasome systems, but the most extensively studied is the NLRP3 inflammasome which can respond to both pathogenic and non-pathogenic tissue damage.<sup>257</sup> In resting innate immune cells, the presence of pathogen- or damage-associated molecular patterns (PAMPs, DAMPs) initiates the transcriptional upregulation of inflammasome proteins including NLRP3, pro-IL-18, and pro-IL-1 $\beta$  via NF- $\kappa$ B and IRF3 (**Figure 4-1**).<sup>258</sup> This signal also causes the adaptor protein ASC to translocate into the cytosol from the nucleus to bridge NLRP3 and the inactive procaspase-1 through vimentin anchoring which forms the inflammasome.<sup>259</sup> In this assembled apparatus, procaspase-1 is cleaved and rearranged to the active form that in turn cleaves pro-IL-1 $\beta$  and pro-IL-18 cytokines to the active soluble form.<sup>260</sup> These potent cytokines are then secreted from the now active immune cells to recruit other immune components to the site of activation.

The inflammasome is a powerful tool vital to the organism's defense system that is able to respond to a wide range of triggers requiring tight control. One element of its regulation is the proposed two-signal requirement for (1) transcriptional regulation and (2) complex activation.<sup>261</sup> Known triggers of the first step include lipopolysaccharides (LPS), cytokines, and reactive oxygen species, while the second assembly step seems to be influenced by exposure to adenosine triphosphate (ATP), lysosomal rupture, or reactive oxygen species (ROS).<sup>262</sup> Regulation can also

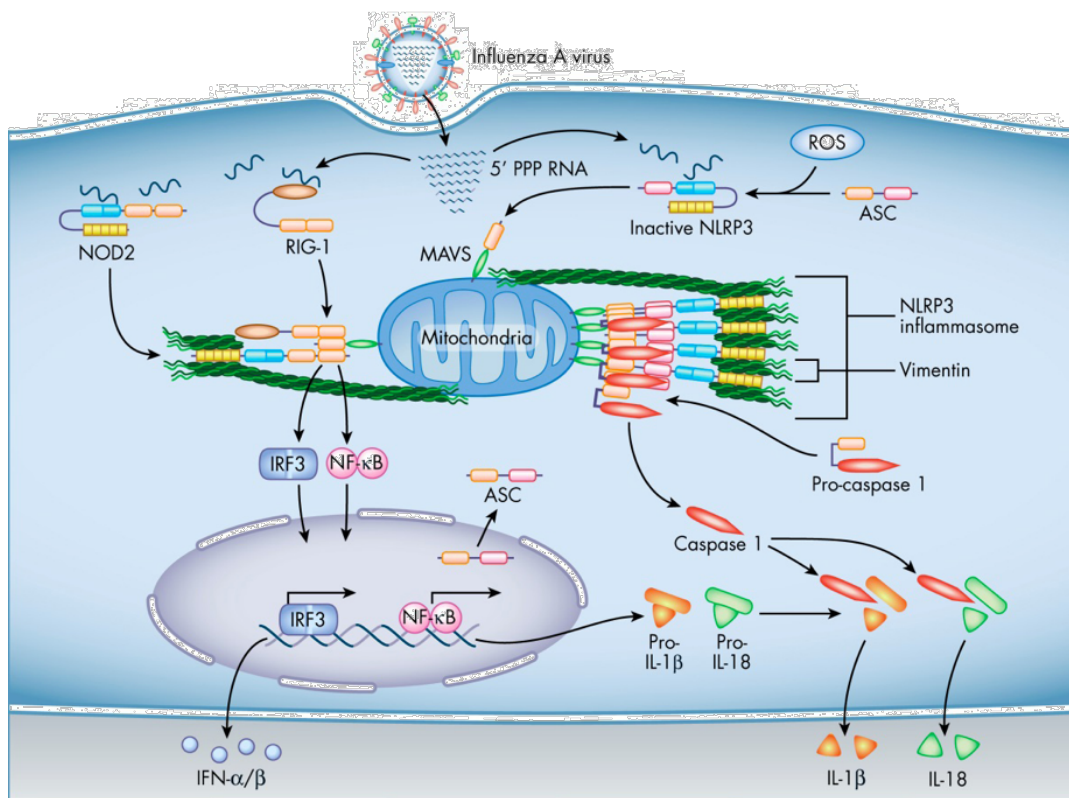


**Figure 4-1. Overview of the signaling cascade after pathogenic infiltration to form the NLRP3 inflammasome.** Entry of influenza A and release of viral RNA into resting innate immune cells triggers the transcriptional upregulation of inflammasome components and cytokines via IRF3 and NF- $\kappa$ B. ASC is translocated into the cytosol from the nucleus and recruits NLRP3. The association of NLRP3 with procaspase-1 via vimentin scaffolding forms the inflammasome. The assembled multiprotein inflammasome complex cleaves procaspase-1 to the active form which cleaves IL-1 $\beta$  and IL-18 to their active forms which are secreted to the extracellular environment. Figure reprinted with permission from Karen Ridge Lab.

be enforced at the step of adaptor protein ASC translocation to the cytosol, or through the immunosuppressive effects of type I interferons, for example.<sup>263</sup> However, despite these layers of control, the inflammasome has been implicated in several disease processes that damage host tissue after pathogenic insult.<sup>258</sup>

#### 4.2.2 Targeting vimentin to inhibit inflammasome-mediated damage

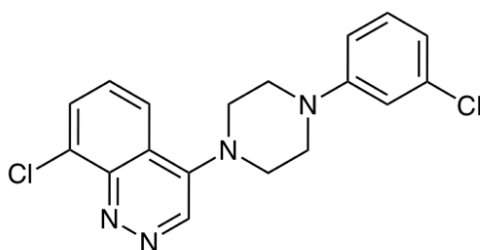
One potential target for inflammasome inhibition is the type-III intermediate filament vimentin. As a critical component of the cytoskeleton, vimentin plays a vital role in a number of cellular processes including cell motility, mitosis, and cell structure which have many relevant applications to disease processes involved in development, cancer, and the immune system.<sup>264</sup> As mentioned previously, one such role of vimentin is the mechanical assembly and scaffolding for inflammasome components. In addition to this physical role, vimentin has been shown to be a regulator of NOD2 activity.<sup>265</sup> NOD2 is involved upstream in the NLRP3 inflammasome cascade as a component that phosphorylates the IRF3 and NF- $\kappa$ B transcription factors that upregulate the production of inflammasome components in the first step of regulation.<sup>260</sup> Inhibition of vimentin would disrupt inflammasome assembly and prevent the cascade of steps that lead to cytokine production and inflammation seen to damage host tissue.

Work by dos Santos showed the dependence of the NLRP3 inflammasome on vimentin in a double knock out  $Vim^{-/-}$  mouse model that had improved morbidity and mortality after exposure to LPS, asbestos, and bleomycin.<sup>259</sup> These studies demonstrate improved survival rates of  $Vim^{-/-}$  mice after a lethal dose of LPS with a median survival of 138 hours compared to about

40 hours for wild type (WT) mice. After sub-lethal doses, several markers for acute lung injury were significantly improved in *Vim*<sup>-/-</sup> mice compared to WT mice including histology, wet-to-dry weight ratio, and bronchoalveolar lavage fluid protein content, each of which represent a breakdown of tissue barriers in the lung. Finally, to show the dependence of these outcomes on inflammasome activity, levels of caspase-1 and IL-1 $\beta$  were similar to that of the saline control in *Vim*<sup>-/-</sup> mice while WT values were significantly elevated. Overall, these results suggest that vimentin is an effective potential target for therapeutic intervention to prevent NLRP3 inflammasome-mediated tissue damage.

#### 4.2.3 Small molecule FiVe1 as a vimentin inhibitor for potential prevention of inflammasome-mediated damage

A recent screen of small molecules for cytotoxic activity against breast cancer cells that have undergone epithelial-mesenchymal transition (EMT) and soft tissue sarcomas identified the compound shown in **Figure 4-2**, later named FiVe1 (FOXC2-inhibiting Vimentin effector 1).<sup>266</sup> Since then, FiVe1 has been implicated in a number of works as a small molecule with high



**FiVe1:** FOXC2-inhibiting Vimentin effector 1

**Figure 4-2. Structure of the small molecule FiVe1 inhibitor of vimentin.** Named after the mechanistic role involving FOXC2 and vimentin, the chemical structure of FiVe1 is highly lipophilic based on the cinnoline ring.

potential for vimentin-related applications including cancer and infectious disease.<sup>267,268</sup> In work by Bollong, FiVe1 was extensively characterized to determine that the lethal and irreversible mechanism of action on FOXC2-transformed cells was tied to the inhibition of vimentin. Specifically, a marked increase was identified in the steady-state levels of vimentin phosphorylated at the S59 position after FiVe1 treatment. Mechanistically, FiVe1 was found to label the rod domain of vimentin through direct binding and induce the dose-dependent production of lower weight vimentin degradation products. This degradation was additionally found to be ubiquitin proteasome-mediated after FLAG-immunoprecipitation of ubiquitinated vimentin products.

The effects of vimentin phosphorylation at S59 and subsequent filament degradation included a number of phenotypic outcomes for EMT cells treated with this FiVe1. First, significant morphological collapse into a more epithelial presentation was seen through confocal microscopy as the VIM apparatus supporting the cell structure collapses. Cells treated with FiVe1 were unable to repair a monolayer scratch wound after 48 hours, indicating inhibition of cell motility. Additionally, mitotic failure was induced after FiVe1 treated cells failed to faithfully form the mitotic spindle and organize chromosomes during metaphase. Overall, these outcomes represent the disruption of vimentin-mediated cell processes, indicating that FiVe1 is a potent vimentin inhibitor in these cells. While these outcomes are not directly related to inflammasome activity, FiVe1 has a high potential for preventing tissue damage mediated through this inflammatory pathway.

An important consideration for the clinical application of this novel vimentin inhibitor is that the cinnoline-containing molecular structure makes FiVe1 quite hydrophobic. While direct application to cells with a DMSO vehicle can produce these therapeutic outcomes, it is unlikely to perform as well in the largely aqueous biological context as DMSO is untenable for biomedical applications and FiVe1 is unlikely to be bioavailable. Given the highly hydrophobic nature indicated by a calculated logP of 4.42 and the cytosolic location of its vimentin target, FiVe1 is an excellent candidate for loading and delivery using a nanoparticle vehicle.

#### 4.2.4 Chapter objectives

The work in this section explores the development of this construct as FiVe1-loaded PEG-*b*-PPS micelles and their use *in vitro* as a potential inhibitor of inflammasome-mediated tissue damage. Given that the initial identification and mechanistic analysis of this drug was directed toward cancer applications, this section also includes data relevant to the effects of free FiVe1 inhibition of vimentin as it relates to inflammasome activity.

These studies begin with developing a methodology to reliably load FiVe1 into PEG-*b*-PPS structures at therapeutically relevant concentrations. I hypothesize that the high logP and hydrophobic character of FiVe1 will enable high loading into micelles. Several assembly techniques are used to determine the highest efficiency approach to forming FiVe1-loaded micelles while maintaining a low polydispersity. A method to accurately purify and quantify FiVe1 loaded was also developed for this construct via HPLC.

For the initial *in vitro* evaluation of FiVe1-loaded micelles, bone marrow-derived macrophages (BMDMs) are prepared for an established enzyme-linked immunosorbent assay (ELISA) protocol of inducing inflammasome activation via LPS challenge and quantifying the secreted IL-1 $\beta$  in the supernatant. I hypothesize that blank micelles will not have an effect on inflammasome activation as inert controls, which will isolate any future effects on FiVe1-loaded particles to the presence of FiVe1 itself. I also expect both blank and loaded micelles to be non-toxic at all relevant concentrations in the BMDM cells. An important consideration for this inflammasome activation study is that the presence LPS may divert the finite cellular energy toward managing the pathogenic threat instead of the typical activities including phagocytosis. That is, the BMDMs exposed to LPS may have decreased uptake of particles and a lower therapeutic impact. I hypothesize that despite this potential decrease, cells exposed to LPS challenge will maintain a level of uptake sufficient to have a therapeutic level of FiVe1 delivered.

After establishing these baseline functions, BMDMs will be treated with both free and loaded FiVe1 to evaluate changes in IL-1 $\beta$  production. Previously found data for free FiVe1 IC<sub>50</sub> will be used to determine the therapeutically relevant doses for the FiVe1 treatments. This free drug range will be replicated and matched to the loaded micelle formulations with the expectation that FiVe1 loaded into micelles will have an equivalent, if not improved, effect of reducing IL-1 $\beta$  levels at lower doses of FiVe1.

## 4.3 Materials and Methods

### 4.3.1 Materials and Instrumentation

Unless indicated below, chemical reagents were purchased from Sigma-Aldrich (St Louis, MO, USA) and used as received. Methanol (MeOH), sodium chloride (NaCl, brine), ammonium chloride (NH<sub>4</sub>Cl), and Dil ((1,1'-dioctadecyl-3,3,3',3'-tetramethylindocarbocyanine perchlorate) were obtained from Fisher Science (Pittsburgh, PA, USA) and used as received. Propylene sulfide was obtained from TCI America (Boston, MA, USA) and used as received. <sup>1</sup>H NMR spectra were recorded on Bruker Avance III 500 MHz system and analyzed with MestReNova (Mestrelab Research, Spain).

### 4.3.2 Assembly and loading of PEG-*b*-PPS micelles

#### *Thin film rehydration*

Micelles were assembled via thin film hydration (TF) and flash nanoprecipitation (FNP) to load FiVe1. For TF as described previously<sup>192</sup> 10 mg of polymer along with 0.0625% by weight of the hydrophilic Dil and stock FiVe1 were dissolved in 1 mL of DCM. FiVe1 was added in amounts of 225 mg, 22.5 mg, and 2.25 mg with a 4.5 mg/mL stock in DCM. The organic phase was transferred to glass HPLC vials and slowly vacuum desiccated overnight to form a thin film on the glass surface of the HPLC vial (**Figure 5-6a**). The dry vials were filled with 1 mL of 1X PBS as the aqueous phase and agitated overnight on a tabletop shaker to form FiVe1-loaded micelles. The samples were filtered through a gravity column packed with Sephadex LH-20 hydrophobic resin and a 1X PBS

mobile phase to remove unloaded FiVe1 and yield stable nanoparticle formulations of blank and FiVe1-loaded micelles.

#### *Flash nanoprecipitation*

Polymer formulations were assembled as described previously using flash nanoprecipitation to form blank and FiVe1-loaded micelles.<sup>29,150,160</sup> For each formulation, 20 mg of each polymer along with 0.0625% by weight of the hydrophilic DiI and stock FiVe1 were solubilized in THF to 500  $\mu$ L total. FiVe1 was added in amounts of 225 mg, 22.5 mg, and 2.25 mg with a 4.5 mg/mL stock in THF. This organic phase and 500  $\mu$ L of 1X PBS as the aqueous phase were loaded into separate 1 mL syringes and anchored to a confined impingement jet (CIJ) block (**Figure 5-7a**).<sup>187,188</sup> The phases were impinged together into the mixing chamber of the block once and directly into a 1.5 mL aqueous reservoir of 1X PBS. All formulations were desiccated overnight to remove residual THF and filtered through a gravity column packed with Sephadex LH-20 hydrophobic resin and a 1X PBS mobile phase to remove unloaded FiVe1 and yield stable nanoparticle formulations of blank and FiVe1-loaded micelles.

#### 4.3.3 Nanoparticle characterization

Nanostructure size distribution and polydispersity index (PDI) were measured by dynamic light scattering (DLS) using a Zetasizer Nano (Malvern Instruments) with a 4 mW He-Ne 633 nm laser. Each nanoparticle formulation was diluted 1:100 or 1:1000 into Milli-Q water and analyzed as two rounds of three runs (n = 6).

#### 4.3.4 Quantification of FiVe1

Aliquots of filtered and unfiltered FiVe1-loaded micelles were frozen at  $-80^{\circ}\text{C}$  and lyophilized overnight. The salt pellet was vortexed with HPLC grade DMF and centrifuged at  $5000 \times g$  for 5 minutes to isolate the salt from the dissolved FiVe1. The supernatant was collected and injected into a Thermo Fisher Dionex UltiMate 3000 HPLC system using an Agilent Polypore  $7.5 \times 300$  mm column and an Agilent Polypore  $7.5 \times 50$  mm guard column housed at  $60^{\circ}\text{C}$ . HPLC grade DMF was used as the mobile solvent at a rate of  $0.5$  mL/min and FiVe1 was detected via UV at  $340$  nm. The resulting traces were analyzed by Chromeleon software (Thermo Scientific). Loading was quantified through relative comparison of filtered and unfiltered aliquots as well as absolute quantification using a standard curve of stock FiVe1.

#### 4.3.5 BMDM cell culture and differentiation

BMDMs were isolated from the marrow of mouse femurs and tibias as previously described.<sup>259</sup> Cells were purified through a Ficoll-Paque gradient and differentiated on charge-free plates in Dulbecco's Modified Eagle Medium with 20% endotoxin-reduced fetal bovine serum (Sigma) and 30% L929 cell supernatant for 5 days.

#### 4.3.6 Cytotoxicity (LDH assay)

Cell viability was assessed using a Cytotoxicity Detection Kit<sup>PLUS</sup> LDH kit (Sigma) and used according to manufacturer instructions. Prepared cells were treated with micelle formulations at final polymer concentrations of  $0.0625$ ,  $0.125$ ,  $0.250$ ,  $0.500$ , and  $1$  mg/mL and incubated for 24

hours before viability analysis. The percentage cell viability was calculated as  $\frac{\text{experimental value} - \text{low control}}{\text{high control} - \text{low control}} \times 100\%$ . Data was analyzed for statistical significance with GraphPad Prism 8 using two-way ANOVA and Tukey's multiple comparison tests.

#### 4.3.7 IL-1 $\beta$ quantification and flow cytometry

Secreted IL-1 $\beta$  was measured using the IL- $\beta$ 1 Ready-Set-GO ELISA (Ebioscience) according to the manufacturer's instructions. The supernatant of treated cells was used for IL-1 $\beta$  quantification while the cell pellet was prepared for flow cytometry. Cells were resuspended and stained with Ghost Dye Red780 viability dye (Tonbo Bioscience). Samples were analyzed on a 3C.A1 LSR Fortessa 1 Analyzer (RHLCCC) using a Cy3 filter for detection of DiI and gated on live cells. Data was analyzed for statistical significance with GraphPad Prism 8 using two-way ANOVA and Tukey's multiple comparison tests.

### 4.4 Results and Discussion

#### 4.4.1 FiVe1 loading into micelles

The drug of interest for this investigation of inflammasome inhibition is FiVe1, a small molecule hydrophobic compound with poor aqueous solubility. Using distribution coefficient logD as a measurement for lipophilicity of ionizable compounds, FiVe1 is calculated to be over 40 times more soluble in organic media compared to aqueous media at all pH levels above 6. This strong preference makes it an excellent candidate for loading into the hydrophobic core of micelles. A quantification method for free and loaded Five1 was developed with an HPLC protocol

and UV-detector for an improved limit of quantification using a standard curve, as shown in **Figure 4-3**. Two assembly techniques of thin film rehydration and flash nanoprecipitation were investigated for loading FiVe1 into PEG<sub>2000</sub>-*b*-PPS<sub>20</sub>-Bz micelle polymer as shown in **Figure 4-4a**. Thin film was able to load FiVe1 at a modest  $12.8\% \pm 3.6\%$  across four trials while FNP was able to load at a respectable  $39.8\% \pm 4.1\%$  across six attempts.

An important consideration for loading drugs into nanoparticles is ensuring that the presence of cargo does not disrupt the morphology of the structure due to the amount loaded or the characteristics of the drug itself. In **Figure 4-4b**, the DLS traces for blank micelles along with FiVe1-loaded micelles at three concentrations show no change in the diameter or dispersity

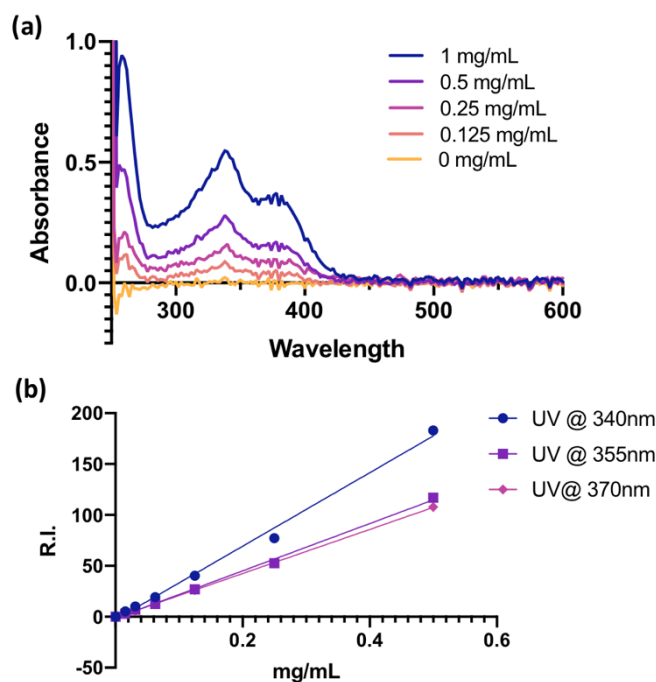


**Figure 4-3. HPLC quantification of free and loaded FiVe1 samples.** (a) The UV-Vis absorption spectrum of FiVe1 at concentrations serially diluted from 1 mg/mL of FiVe1. (b) The standard curve of FiVe1 stock concentrations at three relevant wavelengths of 340 nm, 355 nm, and 370 nm with a more sensitive limit of detection than UV-Vis.

of the nanoparticles with or without drug, which were both within range of previously observed diameters for the morphology.<sup>48</sup> These two analyses suggest that micelles are a suitable nanocarrier system for loading FiVe1.

Free FiVe1 was found to have an inhibitory effect on inflammasome activation with an  $IC_{50}$  of about 1  $\mu\text{M}$  based on the production of IL-1 $\beta$  after LPS stimulation of BMDMs. The aim was thus to load FiVe1 into micelles at concentrations near this relevant marker to evaluate the therapeutic effect at similar doses between free and loaded drug. As shown in **Figure 4-4b**, the formulations tested for diameter and polydispersity via DLS were 50  $\mu\text{M}$ , 5  $\mu\text{M}$ , and a dose too low to be quantified by the HPLC method. For each of these, a 1:10 serial dilution of the stock was added to dose, suggesting that the lowest unquantifiable formulation is near a 0.5  $\mu\text{M}$  loaded concentration. When diluted as a treatment for *in vitro* assays, the in-well concentration will be within a reasonable range based on the  $IC_{50}$  of 1  $\mu\text{M}$ .

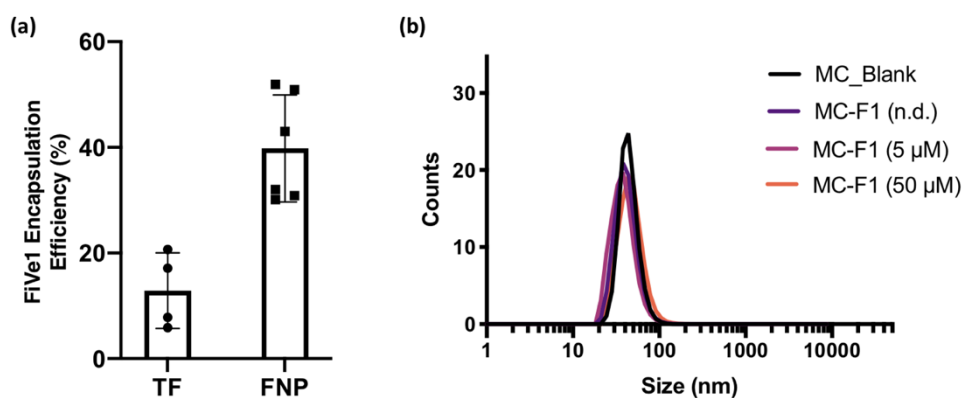


**Figure 4-4. Loading and characterization of micelle nanoparticles with FiVe1.** (a) Loading of FiVe1 as encapsulation efficiency into micelles (MC) via thin film rehydration (TF) and flash nanoprecipitation (FNP) at  $12.8\% \pm 3.6\%$  and  $39.8\% \pm 4.1\%$  respectively. (b) DLS characterization of blank and loaded micelles showing equivalent diameter and polydispersity across three FiVe1 concentrations compared to blank micelles. N.d. represents a concentration of FiVe1 that was a 1:10 dilution of the 5  $\mu\text{M}$  stock but was unable to be detected via HPLC.

#### 4.4.2 Establishing baseline *in vitro* conditions for FiVe1-loaded micelles

For these studies with inhibition of the inflammasome, it was important to show that the micelle formulations themselves do not elicit a response in the BMDM cell line used for these investigations. The metric to evaluate inflammasome activation is the secretion of IL-1 $\beta$  into the cell supernatant as one of the major outcomes of this pathway. This secretion could be stimulated by the PEG-*b*-PPS material itself, the quantity administered, the morphology of the particles, the size, the chemical features, or the surface charge. To evaluate the effects of the nanoparticles themselves, BMDMs were exposed to a dose of LPS to activate the inflammasome and treated with either blank micelles or DMSO as a negative control and analyzing the IL-1 $\beta$  produced. **Figure 4-5a** shows the outcome of treating prepared BMDMs with blank micelle

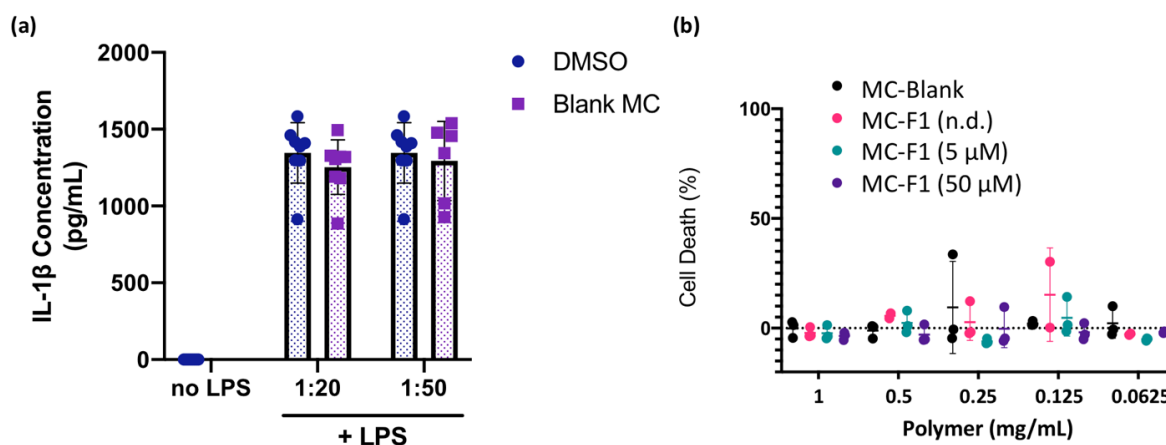


**Figure 4-5. *In vitro* baseline establishment of micelle inflammasome activation and cytotoxicity of all formulations.** (a) Blank micelle (MC) influence on IL-1 $\beta$  production via ELISA quantification after LPS challenge. No significant difference was found in IL-1 $\beta$  concentration for two different micelle concentrations compared to the DMSO positive control. These polymer dilutions are equivalent to 0.25 mg/mL for 1:20 and 0.1 mg/mL for 1:50. (a) LDH cytotoxicity of blank and FiVe1-loaded micelles across polymer concentrations up to 1 mg/mL. No significant cytotoxicity was found for blank or loaded micelle formulations. N.d. represents a concentration of FiVe1 that was a 1:10 dilution of the 5  $\mu$ M stock but was unable to be detected via HPLC.

formulations of two different concentrations. The presence of micelles did not affect the IL-1 $\beta$  production compared to DMSO for both concentrations, as expected. This establishes the nanoparticle vehicle as an inert part of the system such that any effect seen in the production of IL-1 $\beta$  as a measure of inflammasome activation or inhibition is likely due to the loaded FiVe1 cargo itself and not the nanoparticles.

The next consideration for these micelle formulations is that they remain non-cytotoxic at high doses. The nature of the IL-1 $\beta$  ELISA with a goal of signal reduction as it corresponds to inflammasome inhibition requires an additional confirmation that the reduction is due to inhibition of the pathway of interest. Another reason why the IL-1 $\beta$  production may be decreased after treatment is that the cells have not survived. In this way, an initial viability assessment is necessary not only before continuing this delivery strategy, but also pairing it with every inhibition assay for these studies. The results of an LDH cell viability assay are shown in **Figure 4-5b** for blank and FiVe1-loaded micelle formulations across a wide range of polymer concentrations from 0.0625 mg/mL to 1 mg/mL. Even at the high polymer concentration of 1 mg/mL, each of these formulations was found to be largely non-toxic to cells.

The final baseline to establish is evaluating the uptake of micelles into the BMDM cell line after LPS challenge. While this cell type as an antigen-presenting subset is likely to take up foreign materials such as nanoparticles, the presentation of a danger signal such as LPS may induce redirection of cellular resources toward responding to this threat. Given the finite amount of energy in a cell, the energy requirements of internalization may be too high to maintain a level of uptake for a therapeutic effect. To evaluate this potential outcome, BMDMs were treated with

blank micelles after an LPS challenge according to the typical ELISA conditions for stimulating inflammasome-mediated IL-1 $\beta$  production. Cellular uptake was quantified via flow cytometry with associated gating as shown in **Figure 4-6**. Despite this somewhat conservative gating strategy, about 14.5% of BMDMs take up nanoparticles strongly, while another percentage likely takes up a lower level of particles based on the overall peak shift. This level is sufficient for the therapeutic effect of cargo delivered via these micelle nanoparticles.

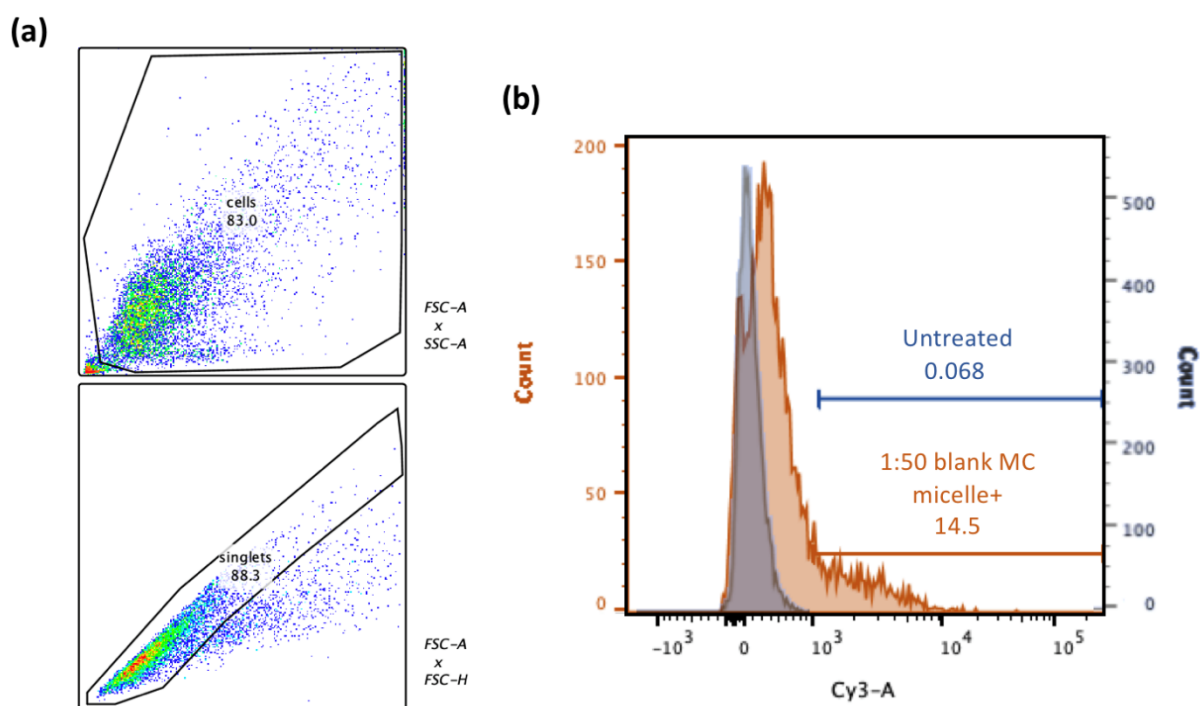


**Figure 4-6. Uptake of blank micelles in BMDMs after LPS challenge.** (a) The conservative gating strategy and (b) corresponding quantification of micelle-positive BMDMs show uptake of 14.5% and a general peak shift toward micelle-positive cells.

#### 4.4.3 Therapeutic effect of free FiVe1 on inflammasome inhibition

The purpose for developing this FiVe1-loaded micelle formulation was to induce inhibition of the inflammasome after LPS challenge. As a downstream product of inflammasome activation, the initial *in vitro* ELISAs evaluate the production of IL-1 $\beta$  with a high level corresponding to high inflammasome activity and a lower level indicating an amount of inhibition. The controls for this series of experiments included cells not challenged with LPS as a negative (minimal signal) control, cells challenged with LPS and no treatment as a positive (maximum signal) control, and the previously discussed vehicle controls of DMSO only and blank micelles.

After several rounds of these ELISAs to establish a pattern and further optimize conditions, a panel was created that included a free FiVe1 range of doses that mirrored the IC<sub>50</sub> conditions and matched loaded FiVe1 micelle doses. The results of IL-1 $\beta$  production are shown in **Figure 4-7** for free and loaded FiVe1 as normalized values according to the controls, where LPS only should represent the highest IL-1 $\beta$  signal with no inflammasome inhibition. The conditions were repeated across two plates for both sets of free and FiVe1-loaded micelles to reduce variance.

Beginning with free FiVe1 plates in **Figure 4-7a**, the first observation is the variance between the in-plate replicates for each treatment. While it is reassuring that no individual well produced zero signal, the values within each treatment extend above and below the normalized 1.0 that represents full inflammasome activation. This suggests that some administrations of the

free FiVe1 drug may modestly inhibit inflammasome activation, but many of them appear to enhance activation above LPS only as the positive control. It is difficult to consider any of these treatments as strong evidence toward a pattern of inhibition or otherwise with these measures of variance and the resulting high standard deviation.

Beyond high variance within treatments, the average IL-1 $\beta$  production is centered around the normalized 1.0 for LPS-only cells across the entire therapeutic range. These dilutions include the previously determined IC<sub>50</sub> value of 1  $\mu$ M along with several higher dosages that do not show any change in IL-1 $\beta$  production. Statistically, there is no significant difference in IL-1 $\beta$  production for any of the free FiVe1 treatments, either between them or in comparison to the untreated LPS-only cells.

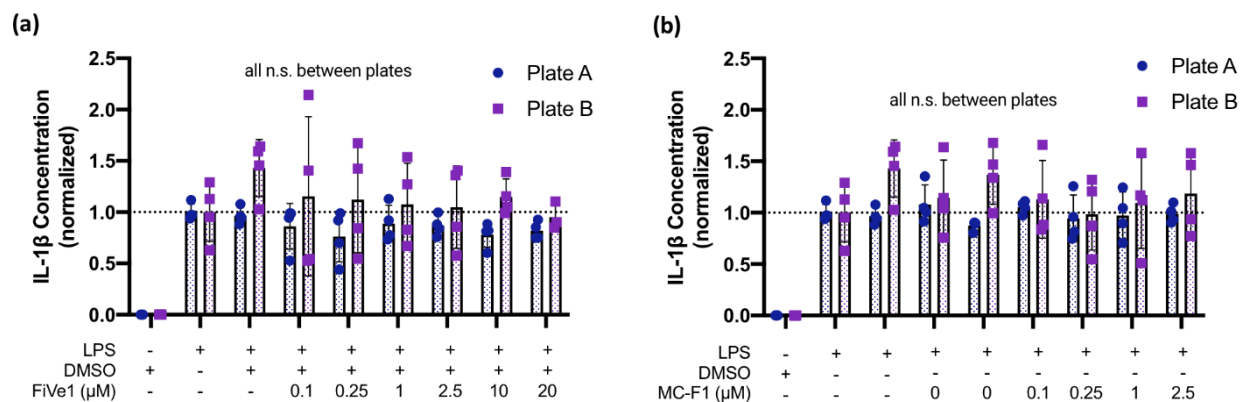


**Figure 4-7. Normalized ELISA quantification of IL-1 $\beta$  production in BMDM cells treated with matched FiVe1 concentrations after LPS challenge in two replicate plates.** Negative controls of the DMSO vehicle and positive controls of LPS only were used to normalize IL-1 $\beta$  values. (a) Free FiVe1 treatments showed no significant difference between plates or across the dose range compared to LPS-only wells. (b) Five1-loaded micelles with matched FiVe1 concentrations as free FiVe1 also showed no significant difference between plates or treatments compared to LPS-only wells.

Given that FiVe1 is a small molecule hydrophobic drug with poor aqueous solubility, it is reasonable to expect an overall lower therapeutic performance when administered directly to cells. This is one of the many reasons why a nanocarrier delivery vehicle system is a critically important consideration for these types of drugs, as it can enhance solubility, uptake, and lower the dose needed for a therapeutic effect. However, the  $IC_{50}$  of the free drug was not able to be replicated in these plates despite the same concentrations and experimental conditions. This suggests a more systemic concern about the efficacy of FiVe1 as a potential inflammasome inhibitor.

#### 4.4.4 Therapeutic effect of FiVe1-loaded micelles on inflammasome inhibition

As mentioned previously, a nanocarrier delivery vehicle for the hydrophobic FiVe1 could result in a significant increase in therapeutic potential. Using the FiVe1-loaded micelle formulations at several base concentrations, the FiVe1 doses were matched to the free drug treatments and administered to BMDMs using the same protocol. The expectation is that FiVe1 loaded into a nanoparticle delivery vehicle will show enhanced inflammasome inhibition and a decrease in IL-1 $\beta$  production compared to free FiVe1. The results of this ELISA for FiVe1-loaded micelles are shown in **Figure 4-7b** with matched concentrations to the free FiVe1 treatments, repeated across two plates and normalized to the positive control of LPS only without treatment.

For FiVe1-loaded micelles, the variance within replicates of treatments on the same plate is somewhat lower than that of the free FiVe1. This suggests that each treatment tends to converge onto a more specific outcome and adds more confidence to the results. However,

similar to the free FiVe1 plates, there appears to be little difference between treatments compared to the positive control of maximum inflammasome activation across the full range of tested values. Given that many of the doses average out to a value above what should be considered the maximum IL-1 $\beta$  production, this is a concerning outcome. Statistically, there is no difference in IL-1 $\beta$  production for any of the FiVe-loaded micelle formulations. This suggests that even FiVe1 is loaded into a nanocarrier delivery is not providing sufficient inflammasome inhibition to decrease IL-1 $\beta$  production under these conditions.

The preliminary experiments to establish *in vitro* baseline data give further insight into possible explanations for this outcome. First, the blank and loaded micelles are non-cytotoxic to the plated BMDM cell line at concentrations up to 1 mg/mL as shown in **Figure 4-5b**, which is much higher than the 0.10 to 0.25 mg/mL concentrations used for these experiments. Additionally, the presence of the micelle nanocarrier in this ELISA does not affect the resulting IL-1 $\beta$  production positively or negatively, as shown in **Figure 4-5a**. This provides evidence that the high IL-1 $\beta$  production seen in the FiVe1-loaded micelle treatments is not due to the micelle material causing a separate production of IL-1 $\beta$ , dependent on inflammasome activation or independent from it. Finally, the micelle uptake shown in **Figure 4-6** is sufficient for successful internalization into the BMDM cells after LPS challenge. A reasonable assumption is also that any loaded cargo would be released and effectively delivered for the therapeutic outcome, if any.

Together these investigations suggest that the FiVe1-loaded micelles are of sufficient dose, are non-cytotoxic, do not induce an independent release of IL-1 $\beta$ , and are internalized by BMDM cells subjected to the LPS assay conditions. Independent of the current application, this

data provides excellent evidence for micelles being a good nanocarrier load and deliver FiVe1, and that FiVe1-loaded micelles show high potential as a nanoparticle therapeutic. However, this specific application for inhibiting the assembly and activation of the inflammasome requires further investigation.

#### 4.4.5 Considerations of FiVe1 as a vimentin inhibitor

With these established baselines and the lack of significant change seen in free FiVe1 treatments, there is ample evidence to suggest that the lack of response based on IL-1 $\beta$  production is not due to a fault in the nanocarrier delivery system. Instead, a deeper evaluation of the mechanism of FiVe1 is required to fully understand why this early investigation has not resulted in the expected outcomes for inflammasome inhibition as measured by IL-1 $\beta$ . Moving forward, there are several distinct areas to explore for this application of FiVe1.

It is worthwhile to consider additional optimizations to the ELISA protocol. Several improvements were made for the organization of the 96-well plates for this assay to increase the number of replicates and include a skirt to reduce drying effects on the outside wells. Additional considerations include the use of an immortalized cell line to reduce the complexity of the biological system. Given the high variability of the results seen from harvested BMDMs, an immortalized line may offer a more concrete starting point for the IC<sub>50</sub> dose among other baseline assay conditions before moving back toward biological relevance. Some options include THP-1 cells as a human-derived cell line, or RAW macrophages as a well-understood murine cell line. Another option is to investigate the effect of reagent timing within the wells. In the current

protocol, LPS and FiVe1 treatments are added sequentially which may affect how the LPS affects the cells initially. Especially for the nanoparticle treatments which are known to adsorb compounds such as LPS to the surface, the level of LPS that the cells experience may be variable.<sup>269,270</sup> However, this is less likely given the similar outcomes of cells that are not treated with nanoparticles. Other considerations include increasing the LPS dose for a greater inflammasome response and a potentially more visible effect of FiVe1 inhibition, as well as increasing the incubation times to allow for the nanoparticles to be fully processed and release cargo. However, these considerations mainly only address the nanoparticle-based treatments while the lack of effect is seen for the free drug as well.

Beyond the experimental design and execution is the potential for the mechanism of FiVe1 to be different than expected. There are several vimentin inhibitors under clinical investigation that each affect a different aspect of vimentin function including transcriptional regulation,<sup>271</sup> filament distribution,<sup>272</sup> direct competition,<sup>273</sup> and filament degradation.<sup>274</sup> Beyond simply inhibiting vimentin, it is the specific mechanism that determines the type and extent of vimentin disruption and the resulting clinical uses.<sup>275</sup> While the mechanism of FiVe1 vimentin inhibition is not yet fully elucidated, it is understood that this compound mainly falls into the latter category of disruption via phosphorylation.<sup>266</sup> Instead of the more typical phosphorylation at C328 which is also the location of post-translational modifications, FiVe1 was found to phosphorylate at S56.<sup>276</sup> Previous work has shown that phosphorylation at this spot and the resulting production of vimentin degradation products is sufficient to interfere with cell morphology, wound healing, and mitotic failure.<sup>266</sup> However, there is not yet data showing the

specific ability to interfere with NLRP3 inflammasome assembly, as such is the goal of this current work. It is therefore a possibility that this S56 site of phosphorylation is not sufficient to prevent inflammasome activation and decrease the level of IL-1 $\beta$  as measured in these assays.

For example, both the C328 and S59 phosphorylation sites exist on the main rod domain of the protein and could reasonably be expected to have similar outcomes in treated cells. However, in comparison to the loss of migration for wound healing and collapsed morphology that were also seen in Withaferin A, a compound that phosphorylates at C328, the multinucleation effects were only apparent in the FiVe1 treated cells.<sup>266</sup> The outcomes were replicated with both inadequate and excessive phosphorylation which could indicate that FiVe1 acts on other sites within the vimentin structure. Additionally, while other vimentin inhibitors have been shown to interfere with the inflammasome assembly, none so far have been shown to induce mitotic failure as FiVe1 does.<sup>266,267</sup> While these examples are not directly applicable to this application of inflammasome inhibition, they serve as an example of the deep complexity of interactions between the delicate biological balance and the small molecule mechanism of interference. The fact that vimentin plays an integral role in the assembly and function of the inflammasome and that FiVe1 inhibits vimentin makes this drug an excellent candidate for investigation for this application does not guarantee that it will have this type of effect without further investigation.

## 4.5 Conclusion

Through the work in this section, I was able to develop a PEG-*b*-PPS micelle nanocarrier formulation for the loading and delivery of the small molecule hydrophobic FiVe1. This drug showed much potential as an inhibitor of the widely utilized intermediate filament vimentin that plays a number of critical roles in the cell. Given the high logP of this compound, it was able to load effectively and reliably into micelles via flash nanoprecipitation across a range of final concentrations, around 40%. The addition of this drug to the micelle construct across this range of concentrations did not affect the diameter or dispersity of the carrier.

The main assay for this section was the treatment of BMDMs with an LPS challenge to induce inflammasome activation along with any relevant treatments, followed by an ELISA to quantify the IL-1 $\beta$  secreted into the supernatant after several hours. I took a systematic approach to establish the *in vitro* baseline for this work that provided much insight into the interpretation of subsequent results. First, I checked that the micelle carriers themselves do not have an activating or inhibiting effect on the production of IL-1 $\beta$  as a measure of inflammasome activation. This ensured that any effects on the level of IL-1 $\beta$  are likely due to the treatment itself rather than the polymer vehicle. Next, I found that the PEG-*b*-PPS nanomaterial remains non-cytotoxic in these cells through polymer concentrations of 1 mg/mL for both blank and FiVe1-loaded formulations. Finally, I ensured that BMDMs subjected to an LPS challenge were still able to devote the energy resources to take up the micelle treatment. Flow cytometry showed a level

of uptake that should be sufficient for the administered treatments to effectively deliver enough cargo for a therapeutic effect.

Lastly, I investigated the effects of both free FiVe1 and FiVe1-loaded micelles on the resulting IL-1 $\beta$  production across a range of concentrations relevant to the previously found IC<sub>50</sub> of FiVe1. As discussed extensively, the results of this study did not produce the expected results of reduced IL-1 $\beta$  that indicates effective inflammasome inhibition. For both free and loaded treatments, no significant differences were found between groups and the positive control across several plates and experimental designs. Additionally, the original IC<sub>50</sub> of free FiVe1 could not be replicated. The evidence provided by the baseline studies suggests that the nanocarrier formulation is not responsible for the lack of expected response. These FiVe1-loaded micelles remain as an effective delivery system for this therapeutic. Instead, these results suggest future work investigating the specific molecular mechanism of FiVe1 inhibition of vimentin to evaluate if inflammasome inhibition is within the scope of its action or if this nanocarrier delivery system would be better suited for a different application of vimentin inhibition in the cell.

#### **4.6 Acknowledgements**

I would like to thank Alex Berr for her integral role in establishing and designing this collaboration, maintaining cells, conducting the *in vitro* experiments, and collecting data. Her expertise in this biological context were indispensable for the work in this chapter. I would like to thank Karen Ridge for the use of her laboratory space and materials. I would also like to thank Sean Allen for his advice interpreting data in this chapter.

#### 4.7 Publication information

The work in this chapter represents the initial development of PEG-*b*-PPS nanocarrier therapeutics for the application of reducing inflammasome-mediated damage in these models.

This funded work will continue across a number of publications between the labs of Evan Scott and Karen Ridge in the following years.

## CHAPTER 5

# Development of a self-assembling poly(amino acid)-*b*-PPS nanocarrier platform

### 5.1 Abstract

Due to the presence of anti-PEG antibodies in the general population, there is an increasing need for a broader diversity of surface chemistries in synthetic nanocarriers used for biomedical applications. This chapter explores the development of a novel biomimetic poly(amino acid)-*b*-poly(propylene sulfide) (PAA-*b*-PPS) block copolymer for self-assembling nanocarriers through the use of poly(sarcosine) (pSarc) as a minimally-complex pilot. Independently synthesized pSarc and PPS block lengths are paired via a rationally selected linker that takes advantage of both N-carboxyanhydride (NCA) and PPS chemistries. The resulting combinatorial library of paired pSarc-*b*-PPS diblock copolymers rapidly and efficiently extends through the relevant range of hydrophilic weight fractions. Stable aqueous formulations of micelle and vesicle morphologies at specific weight fraction ranges are assembled through flash nanoprecipitation (FNP) and validated via dynamic light scattering (DLS), negative stain transmission electron microscopy (nsTEM), and small angle x-ray scattering (SAXS). After validating this pSarc-*b*-PPS pilot, the PAA backbones are expanded to include amino acids with more functionality using poly(glutamic acid), poly(lysine), poly(tryptophan), and poly(tyrosine) which each demonstrate various levels of success as structural blocks in this copolymer system. Overall, this work demonstrates the

immense capability of an NCA-based PAA-*b*-PPS diblock copolymer system for self-assembling nanocarriers with a vast range of functionalization potential and surface chemistry variation.

## 5.2 Introduction

### 5.2.1 PEG disadvantages

Despite the overwhelming number of beneficial features offered by PEG to biomedical applications, there are a number of potential drawbacks worth consideration as increasingly more nanoparticles are developed for therapeutic use. Both the chemical considerations of the functionalization limits of this polymer along with the biological evidence of immune recognition and enhanced clearance are especially relevant as everyday exposure to PEG products increases (**Figure 5-1**). Each of these considerations offers a strong rationale to investigate a more diverse range of hydrophilic chemistries for nanoparticles.

Beginning with the chemical aspects, PEG is heavily limited by the fact that only its terminal ends can be functionalized (**Figure 5-1a**). Modifications to the ethylene glycol backbone may prevent the effective association with water molecules that form the protective hydration shell that gives PEG its highly desirable pharmacokinetic profile. The disruption of this hydration shell may reverse the reduced biofouling and increased circulation time are characteristic features of using PEG as a stealth material for biomedical applications.<sup>277</sup> As a result of this limitation, if one terminal end is used to conjugate to the therapeutic or nanocarrier, only one remains for functionalization. One solution is to increase the amount of conjugation sites by coupling additional amino acids or dendrimers onto the PEG.<sup>12,34</sup> However, these approaches are

synthetically challenging with expensive protocols and low yields.<sup>278</sup> Compared to other synthetic polymers with the capacity to incorporate a wide range of chemical modifications, PEG is severely limited in favor of its indispensable hydration shell.

The second chemical consideration of PEG is the distinct lack of biodegradation of its ethylene glycol chains (**Figure 5-1b**). One of the very first PEG medical products, an osmotic

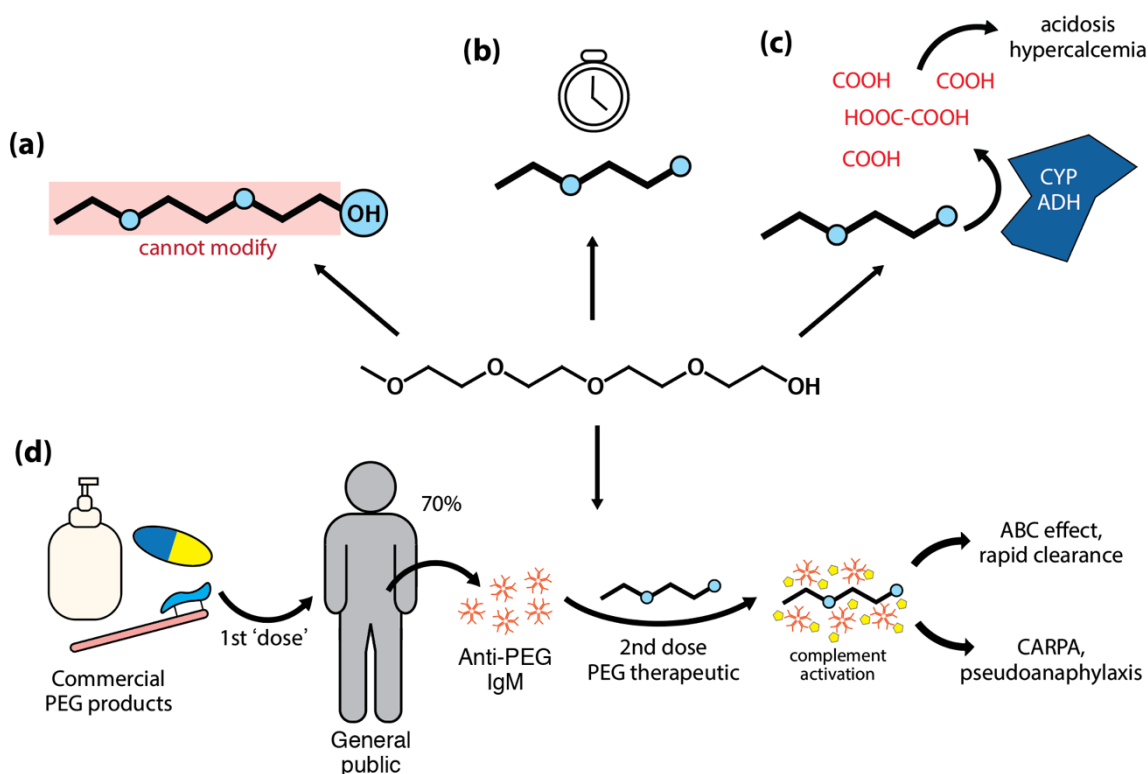


**Figure 5-1. Summary of PEG limitations and disadvantages.** (a) PEG functionalization is limited to the terminal hydroxyl group to preserve the formation of the protective hydration shell. (b) PEG is largely non-biodegradable, remaining in the body for long periods without efficient breakdown. (c) Low level enzymatic degradation by cytochrome P450 (CYP) and alcohol dehydrogenase (ADH) produces carboxylic and diacid metabolite that can cause acidosis and hypercalcemia. (d) Commercial PEG-containing products induces the production of anti-PEG IgM antibodies in about 70% of the general public without intentional exposure. A second dose of a PEG-based therapeutic activated complement which can trigger enhanced clearance through the ABC effect, or more critically, a potentially fatal pseudoanaphylaxis.

laxative, took advantage of this fact by utilizing PEG as a non-biodegradable solute to pull water into the intestine via osmosis and soften stool.<sup>279</sup> Biomedical applications also take advantage of this aspect as PEG-based products are resistant to enzymatic degradation and remain in circulation longer.<sup>34</sup> However, this is an important consideration for the resulting excretion from the body after administration. Ideally, an exogenous material should be fully cleared from the body via enzymatic degradation to non-toxic products to prevent tissue build up after multiple doses.<sup>34,38</sup> Instead, long chain PEG cannot be excreted through the urine or feces as is typical of shorter chains, and instead is known to accumulate in the liver and lysosome where it is at risk of causing macromolecular syndrome.<sup>11,12,280,281</sup> The other risk for these longer PEGs is the slow degradation by cytochrome P450 (CYP)<sup>140</sup> or alcohol dehydrogenase (ADH)<sup>141</sup> into carboxylic acids and diacids that can cause acidosis and hypercalcemia (**Figure 5-1c**).<sup>281</sup>

The biological perspective is unfortunately more severe. Over the last several decades, a series of studies have found anti-PEG antibodies in people who had previously never been exposed to PEG-based therapeutics (**Figure 5-1d**). There is strong evidence that the ubiquity of PEG even in commercial products is sufficient to induce an immune response in 70% of the general population.<sup>135</sup> Experts now recommend the pre-screening of any patient that is eligible for PEG-based therapeutics to undergo additional testing to verify if the therapeutic will both be tolerated by the immune system and have the chance for a therapeutic effect.<sup>282,283</sup> The complexity of this scenario is likely to increase significantly given the recent efforts to globally vaccinate against COVID-19 with multiple doses of a PEGylated mRNA nanocarrier.<sup>284</sup> This

deliberate exposure to a PEG-based therapeutic could have significant effect on the landscape of FDA-approved and future nanoparticle therapeutics.

The presence of anti-PEG antibodies plays out in a number of important ways. First, since as early as 2000, there has been strong evidence of the accelerated blood clearance (ABC) effect in PEG-based materials even after a single dose.<sup>285-287</sup> In this phenomenon, the subsequent doses of a therapeutic following the initial administration have a reduced circulation time and overall efficacy in the body. These effects have been demonstrated in a number of *in vivo* models including pigs<sup>288</sup> and beagle dogs<sup>289</sup> and have been correlated with dose and administration time to promote either this ABC effect or B cell anergy.<sup>290</sup> The currently understood mechanism for this ABC effect is the T cell-independent proliferation of B cells in the marginal zone of the spleen that produces IgM antibodies that initiate the typical opsonization cascade with complement activation and clearance by the mononuclear phagocyte system.<sup>291,292</sup> At a minimum, this suggests that many of the beneficial effects of PEG on the circulation time of therapeutic formulations are present for only the first dose and return to non-PEG levels afterward.

Another response to the development of anti-PEG antibodies is a severe hypersensitivity reaction (HSR). In comparison to the simple neutralization of PEG-based therapeutics via the ABC effect, hypersensitivity can have disastrous medical outcomes for the patients receiving treatment. Instead of opsonization and clearance, PEG-based materials trigger a complement activation-related pseudoallergy (CARPA) that culminates in a pseudoanaphylaxis that can often be fatal.<sup>283,293,294</sup> As with the ABC effect, these outcomes are dependent on the PEG dose, chain length, and administration schedule as recorded in human patients.<sup>144</sup> While further

investigation of these hypersensitivity responses is required, it remains a critically important consideration before administering any type of PEG-based therapeutic for clinical applications.

Given the drawbacks of PEG, it is well worth considering other hydrophilic polymers in an effort to expand the surface diversity of nanocarrier therapeutics.<sup>280,295</sup> Any potential alternative materials should both address these drawbacks of PEG but also closely replicate the advantages of PEG to enhance therapeutic pharmacokinetics. This seemingly monumental task begins with considering each aspect of PEG individually and in combination to initiate the development of new materials.

### 5.2.2 Poly(amino acids) as materials for biomedical applications

A number of poly(amino acids) (PAAs) and their derivatives have been investigated as potential alternatives for PEG-based materials, including poly(glutamic acid), poly(hydroxyethyl-L-asparagine), and poly(hydroxyethyl-L-glutamine).<sup>34,280,295</sup> These PAA examples are hydrophilic materials with enhanced biodegradation capacity, enhanced circulation time, and reduced incidents of ABC after several administrations.<sup>296,297</sup> Poly(glutamic acid) has already been approved by the FDA for use as a food thickener and cosmetic additive.<sup>298</sup> With these characteristics, several formulations using PAAs have made it through a number of clinical trials before ultimately falling short due to evidence of antigenicity and inconsistent results. However, these trials also showed reduced adverse effects related to tolerability, safety, and side effects, including only rare instances of mild hypersensitivity reactions.<sup>299</sup> Overall, the potential of PAA materials remains especially high given these promising results over several studies.

In addition to these PAA examples, amino acids as the monomer units of the peptide and protein polymers offer an unmatched degree of functionalization capacity that the single terminal end of PEG chains lack. Each residue has a side chain that carries any number of moieties that can be utilized in chemical or biological applications. The modular addition of residues to the peptide backbone allows for unrestricted combinations of units that carry a variety of charges, hydrophilic or hydrophobic character, fluorescence, conjugation sites, steric influences for secondary and tertiary assembly, and many more functionalities. PAA chains also have the potential to incorporate the same features that impart the stealth character of PEG, including a polar, uncharged surface, high chain flexibility, and water coordination sites, all of which contribute to a protein-resistant hydration shell.<sup>40,300</sup> While most often utilized as the bioactive therapeutic component, the development of a structural PAA that can incorporate these amino acid functionalities would offer a vast range of potential benefits to expand the surface diversity of nanoparticle therapeutics.

### 5.2.3 Poly(amino acid) synthesis via N-carboxyanhydride chemistry

An important consideration for the development of PAA materials is the mechanism for synthesis. The most well-established route for peptide generation is through solid phase peptide syntheses (SPPS) which is an extremely reliable and meticulous cycle of deprotection, addition, and extension. This technique prioritizes tight sequence control of residues as this carries the biological activity of the peptide of interest. However, this approach is not amenable to the scaled-up production of longer PAAs for nanoparticle structure given the required solvent

volumes, the incomplete deprotection and coupling that causes truncations and deletions,<sup>301</sup> and overall poor atom economy.<sup>302</sup> Instead, the lack of intended biological activity of these PAAs releases them from a dependence on tight sequence control and opens up the possibility for more rapid and mild synthetic routes.

One such solution is found in N-carboxyanhydride (NCA) chemistry which cyclizes amino acids into monomers for quick polymerization of chains up through hundreds of units long. In this strategy, a chemical compound with an arrangement of amine and carboxylic acid separated by one carbon can be reacted with phosgene to form a heterocyclic five-member ring called an NCA (**Figure 5-2**). This ring simultaneously protects the amine and activates the carboxylic acid to produce biomimetic peptide bonds with high atom efficiency.<sup>303</sup> They are susceptible to anionic ring opening polymerization (ROP) with a nucleophile, especially a primary amine, under mild, easily controlled conditions to yield polymer populations of reliable dispersity.<sup>304,305</sup> Through this same approach, long PAA chains comprised of multiple types of NCA monomers can be synthesized quickly and efficiently as a mixed copolymer material.

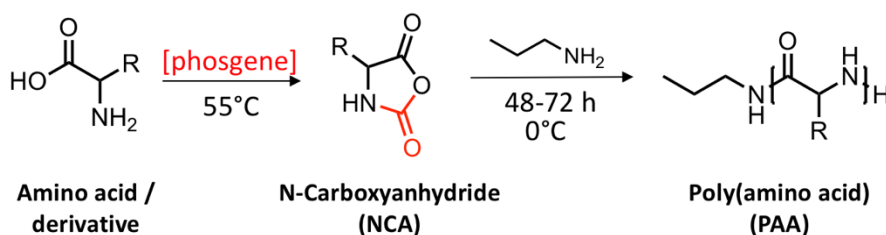


**Figure 5-2. General scheme of N-carboxyanhydride (NCA) polymer chemistry.** Amino acids or derivatives with this arrangement of carboxylic acid and amine moieties can be cyclized into a five-member heterocyclic ring in the presence of a phosgene source with gentle heating. These NCA monomers are polymerized with a primary amine initiator under mild conditions to create poly(amino acids) (PAAs) of reliable length and dispersity.

N-carboxyanhydrides, or Leuchs anhydrides, were first developed in the early 1900s by treating N-alkoxycarbonyl amino acids with halogenating agents.<sup>306</sup> Since then, the concept has been revived several times with significant developments in the chemical synthesis and overall applications. A major update to the synthesis of NCAs was in 1950 with the Fuchs-Farthing method of treating amino acids directly with phosgene.<sup>307,308</sup> The most recent wave of developments occurred almost 50 years later in 1997 when Deming used transition metal complexes to initiate the ROP of NCA monomers.<sup>309</sup> Since this publication, this chemistry has expanded significantly to optimize many aspects of NCA synthesis,<sup>310</sup> ROP initiation,<sup>311</sup> copolymers, non-linear structures, faster reaction kinetics,<sup>312</sup> unique monomers and hybrid solid phase NCA polymerization.<sup>303</sup> With these advancements, NCA-based materials are used widely in applications such as surface coatings,<sup>313</sup> solid core nanoparticle systems,<sup>314</sup> and polymeric carriers.<sup>315</sup>

With these properties, NCA chemistry holds substantial potential as the basis of a hydrophilic block that could diversify nanoparticle chemistry beyond that which is offered by PEG. Compared to the single terminal end of PEG, these chains offer a significant range of functionalization on every unit of the chain. They offer enhanced biodegradation and excretion compared to PEG while maintaining a level of increased circulation time. They are not as commercially prevalent with presumed lower rates of anti-PAA antibodies in the general population with less extreme ABC effects and HSR severity. Overall, PAA chains may address many of the downsides of PEG-based materials while maintaining many of the features that have

cemented its position in biomedical applications, making them a worthwhile investigation for a novel nanocarrier delivery system.

#### 5.2.4 Considerations for nanoparticle self-assembly

To establish any self-assembling polymer system, the exploration of a number of engineering principles must be conducted to fully understand the capabilities of the material. Compared to liposome formulations, nanocarriers made from synthetic polymers have an extensive potential for chemical modifications to adjust the size, morphology, internal architecture, permeability, and fluidity.<sup>316</sup> Polymers can be synthesized as linear chains of multiple blocks, brushes, and branches that can be symmetric or asymmetric across each component. A critical determinant of polymeric nanoparticle properties beyond these variations is the packing parameter of each polymer component as it coils in three-dimensional space.<sup>317</sup>

The packing parameter ( $P_c$ ), which is derived from the polymer length ( $l$ ), the hydrophilic area ( $a$ ), and the hydrophobic volume ( $v$ ) can be used to predict the supramolecular assembly of the polymeric structure as  $P_c = \frac{v}{a \times l}$  (**Figure 1-10b**). It is generally accepted that amphiphilic polymers with packing parameters that fall into specific ranges tend to form defined morphologies.<sup>316,318-320</sup> Values below  $1/3$  indicate a high volume-ratio of the external hydrophilic surface which results in the most extreme wedge angle and the formation of micelles with a hydrophobic core. For packing parameters between  $1/3$  and  $1/2$ , wormlike cylinders are likely to form, while polymers with values between  $1/2$  and  $1$  form vesicles with an aqueous core. Additionally, values near  $1$  indicate about equal volume contributions between hydrophilic and

hydrophobic blocks and tend to result in the assembly of bilayers, while values above 1 will be inverted morphologies as the hydrophobic contribution increases beyond what can be contained internally.

Within these variables of representing volume for each chain, it is critical to consider the contributing physiochemical properties and thermodynamic contributions of the polymer blocks in the material.<sup>321</sup> Among these, the hydrophilic chain will interact with water in unique ways based on the association sites of water molecules and the flexibility of the chains.<sup>319,320</sup> Specific charge distributions or surface chemistries may also contribute to the overall steric interactions between chains as they move throughout the system.<sup>322</sup> For the hydrophobic component, many nanostructures are stabilized by the hydrophobic effect and the reduced entropy of water molecules around these lipophilic chains.<sup>320</sup> These aspects among others make each copolymer pairing a unique system to be investigated independently based on the vast number of variables that contribute to the overall supramolecular arrangement of polymer chains.

### 5.2.5 Strategies to rapidly screen the self-assembly of novel materials

While synthetic polymer nanostructures often simplify the packing parameter to the hydrophilic weight fraction, this shortcut is not broadly applicable to all situations.<sup>323</sup> The variables associated with hydrophilic and hydrophobic volumes within the packing parameter calculation are dependent on the chemical composition of the amphiphile. Changing either of the polymer blocks could result in a very different set of ranges for each aggregate morphology based on the interactions with water, thermodynamic considerations, and steric effects among

others.<sup>318,319</sup> For this reason, the hydrophilic fraction ranges used to predict the resulting nanostructures are often material specific. The impact of these variables on the self-assembly process can be estimated through thermodynamic modeling and molecular dynamics simulations. However, these computational approaches are rarely capable of predicting the true final assembled aggregate morphology and its associated supramolecular properties.<sup>324</sup> Each new material intended for self-assembly must develop these ranges through experimental validation that explores a wide range of block length ratios.

Knowing the general hydrophilic weight fraction ranges that form micellar, vesicular, and more complex morphologies for PEG-*b*-PPS can offer initial conservative insight into the possible ranges for these PAA-*b*-PPS polymers. However, while these new materials maintain the hydrophobic block of PPS, the effects of the hydrophilic PPS block can have a significant influence on the overall packing parameter. The flexibility, steric bulk, solvation, and entropic considerations are likely to be very different between the repeating ethylene glycol units of PEG and the peptide bonds between units of the PAA. For this reason, the ideal first step in developing this novel material is to determine a representative backbone residue to fully understand the aggregate effects of these physiochemical properties within a copolymer with PPS. A pilot material would offer more accurate hydrophilic fraction ranges to base future PAA chains with a more diverse set of residues for each possible morphology. It is essential to explore the full scale of block ratios to first understand which morphologies are possible for each material as some may be more stable in aqueous conditions than others.

One of the most efficient approaches for exploring the full range of hydrophilic weight fractions for a novel copolymer system is through the development of a combinatorial library for a range of chain lengths (**Figure 5-3a**). That is, if two independent blocks can be paired through a rationally designed linker, long and short chains of each type can be matched to rapidly expand a copolymer library to cover all relevant hydrophilic fractions. This approach is especially attractive given the many safety and toxicity concerns of the phosgene reagent used to make the NCA monomers for this investigation. But more generally, it also offers much improved consistency between polymer blocks by extending the life of the same polymer batch for many copolymers. The system becomes more robust in this way with reduced variance between both

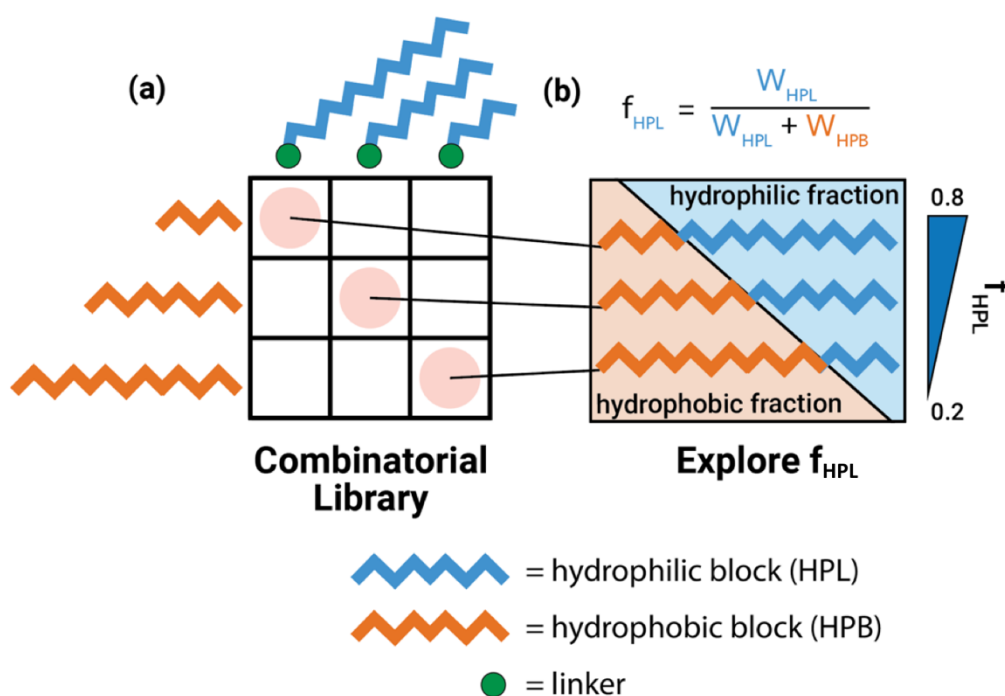


**Figure 5-3. Efficient strategy to assemble diverse diblock copolymers using a combinatorial library and rational linker.** (a) Independent synthesis of hydrophilic and hydrophobic blocks with a linker moiety enables full-quality analysis before unrestricted pairing of block lengths. (b) Diblock copolymers from this library rapidly expand to fill the relevant hydrophilic weight fraction range for potential nanostructure formation.

polymer chains that are susceptible to impurities and polydispersity between batches. With this strategy of combinatorial pairing, it is possible to rapidly scan the hydrophilic fraction space for the ranges that form certain morphologies the most reliably (**Figure 5-3b**).

### 5.2.6 Chapter objectives

This section outlines the development of a PAA-*b*-PPS copolymer material for self-assembling nanocarriers using NCA chemistry to replace the hydrophilic block with a biomimetic chain of highly functional amino acid modular units. The investigations begin with the selection of a minimally complex amino acid monomer to isolate the behavior of the peptide backbone within the PPS-based self-assembling system. I hypothesize that this approach will offer an efficient way to evaluate the potential of a PAA-*b*-PPS system while offering insight into the behavior that can be generalized to future PAA variations. This minimally complex amino acid should be sufficiently hydrophilic to maintain the chain interactions that stabilize the structure while remaining largely neutral, non-bulky. For synthetic simplicity, the block should also require no additional protection or purification steps. Each of these conditions should be met by simple amino acids such as glycine which I expect to function well as a backbone or spacer between more complex units in future chains.

The strategic approach to evaluating this new copolymer based on NCA chemistry is ideally one that is rapid and sufficient for full analysis but uses a minimal amount of material. In addition to reducing the time and financial burden of an unknown material, it is important to reduce the amount of NCA monomers used as their synthesis requires a high level of expertise.

Additionally, to probe the wide relevant range of hydrophilic fractions, many different polymer samples with varying lengths of both blocks must be prepared to mathematically meet the hydrophilic weight fraction parameter. The strategy that I expect to meet these requirements is one that independently synthesizes both hydrophilic and hydrophobic chains so that they can be combinatorially paired, thereby using each block length for multiple copolymer weight fractions. The feasibility of this approach relies heavily on finding or making a linker that can be used for both types of block chemistries: the anionic ROP or thiol chemistry of PPS and the amine-initiated ROP of NCAs. There are many such compounds that have the potential to reliably polymerize and conjugate these two blocks, and I hypothesize one that maintains the primary amine terminal end of the NCA chain and links the blocks via the disulfide-capable PPS thiolate will offer the best features of both systems.

Once the pilot PAA-*b*-PPS copolymer material is made, it must be assembled into nanostructures and remain stable in aqueous media. Given that there are a wide range of assembly techniques widely used in this field, I hypothesize that exploring several techniques with a range of mechanisms will produce nanoparticle populations that can be further analyzed for this prototype material. A sample of non-aggregating polymer in aqueous solution can be evaluated for the morphologies it contains by using multiple orthogonal techniques that analyze unique properties. I expect a combination of DLS for dispersity and diameter, negative stain transmission electron microscopy for visual identification of soft structures, and small-angle x-ray scattering to model the internal architecture will be sufficient to converge on a cohesive understanding of the possible formulation morphologies. Further, conducting this analysis on

formulations made from copolymers that span a number of hydrophilic weight fractions will reveal which ranges are likely capable of forming stable structures of potentially multiple morphologies. I hypothesize that the PAA-*b*-PPS is capable of forming micelles and vesicles for this pilot work and that the ranges will be similar to the PEG-*b*-PPS nanostructures given the influence of the mutual PPS block.

Finally, the prototype material must be non-toxic *in vitro* in order to have potential as a delivery vehicle for biomedical applications. It has previously been shown that PPS-based materials are non-toxic in biological systems through non-human primates, but the hydrophilic block switching from PEG in these studies to a PAA chain requires confirmation. I hypothesize that the pilot PAA-*b*-PPS that incorporates an intentionally simple and inert hydrophilic backbone will not show evidence of toxicity *in vitro*. While this type of analyses must be repeated for each variation in PAA block composition, validation of the minimally complex peptide backbone in combination with the morphologies that form will provide solid support for future work with these materials.

After the PAA-*b*-PPS prototype has been successfully synthesized, paired with a selected linker, assembled to form stable structures that are identified morphologies, and shown to be non-toxic, the PAA-*b*-PPS construct will be expanded to include more functional hydrophilic blocks. The strategy of evaluating a minimally complex pilot material is to provide insight into the behavior of similar polymer systems. I hypothesize that the PAA-*b*-PPS library of materials can be quickly expanded using the same linker and pairing chemistries for a wide range of NCA blocks. Several more complex amino acids with charges such as lysine and glutamic acid or more specific

functional units like the fluorescence of tryptophan and the unique capabilities of cysteine will be fed through the same synthesis, assembly, and analytical pipeline as the prototype. I hypothesize that several of these backbones will be able to form stable nanostructures in aqueous media, validating the pilot. The work in this chapter will set a strong foundation for the development of this novel PAA-*b*-PPS material for drug delivery in biomedical applications.

## 5.3 Materials and Methods

### 5.3.1 Materials and instrumentation

#### *Materials*

Unless indicated below, chemical reagents were purchased from Sigma-Aldrich (St Louis, MO, USA) and used as received. Hexanes, methanol (MeOH), ethyl eosin (EE), and DiI were purchased from Fisher Scientific (Pittsburgh, PA, USA). Propylene sulfide was purchased from TCI Chemicals (Boston, MA, USA).  $^1\text{H}$  NMR and  $^{13}\text{C}$  NMR spectra were recorded on Bruker Avance III 500 MHz system and analyzed with MestReNova (Mestrelab Research, Spain).

#### *General conditions*

Unless otherwise indicated, synthetic procedures were performed under inert conditions with freshly opened anhydrous solvents and a nitrogen atmosphere. After workup, products were used immediately or quickly transferred to vials kept under nitrogen and stored in the  $-20^\circ\text{C}$  freezer until use. Special care should be taken when preparing NCA derivatives given its extreme sensitivity to decomposition or ring opening.

### *Safety*

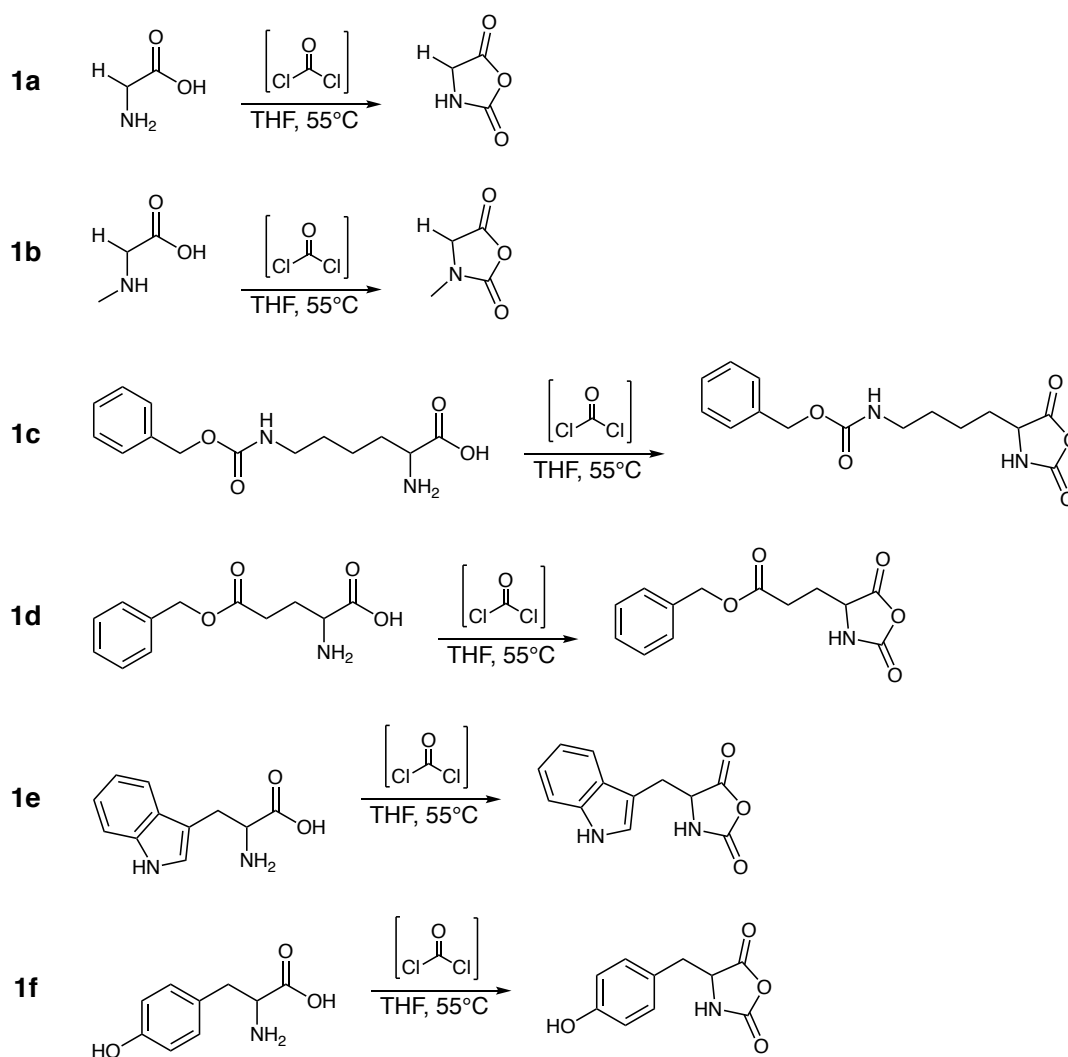
Phosgene and its derivatives are EXTREMELY HAZARDOUS to human health at any scale. Please take all appropriate safety measures into consideration when planning, handling, and disposing of these chemicals and any materials that have come into contact with them.

### 5.3.2 Preparation of Gly NCA, Sarc NCA, BzGlu NCA, LysZ NCA, Trp NCA, and Tyr NCA

#### *General synthesis of NCAs*

The synthesis of amino acid NCA monomers is shown in **Scheme 5-1**. Briefly, amino acid starting material was added to a round-bottom flask equipped with a reflux condenser and charged with a stir bar. Anhydrous THF was added to the flask at a concentration of 10 mL THF per 1 g of amino acid and the suspension was heated to reflux at 55°C. Diphosgene (0.6 eq) or triphosgene (0.4 eq) was added to the mixture while heating to reflux (written as “phosgene” inclusive of these derivatives, selected based on amount required for safe handling). The reaction was allowed to reflux under these conditions until the amino acid became soluble and the mixture turned clear, or after 4 hours total. The flask was cooled to room temperature and nitrogen was bubbled through the flask and across two gas scrubbers of 2 M NaOH for 3 hours to quench any remaining phosgene derivatives. THF was removed under reduced pressure and the solution was precipitated in excess ice-cold hexanes. The solid was collected via filtration after additional

cooling to enhance precipitation and filtered to recover the NCA product. The final product was stored carefully under an inert atmosphere at  $-80^{\circ}\text{C}$  and used within several days of synthesis.



**Scheme 5-1.** Preparation of amino acid NCA monomers from glycine, sarcosine, protected lysine, protected glutamic acid, tryptophan, and tyrosine. (1a) Gly NCA, (1b) Sarc NCA, (1c) LysZ NCA, (1d) BzGlu NCA, (1e) Trp NCA, (1f) Tyr NCA

Gly NCA (1a):  $^1\text{H}$  NMR (500 MHz, DMSO- $d_6$ ):  $\delta$  (ppm) = 4.32 (s, 2H), 8.84 (s, 1H).  $^{13}\text{C}$  NMR (126 MHz, DMSO- $d_6$ ):  $\delta$  (ppm) = 167.49, 153.03, 46.3.<sup>325</sup>

Sarc NCA (1b):  $^1\text{H}$  NMR (500 MHz, DMSO- $d_6$ ):  $\delta$  (ppm) = 4.22 (s, 2H), 2.86 (s, 3H).  $^{13}\text{C}$  NMR (126 MHz, DMSO- $d_6$ ):  $\delta$  (ppm) = 167.79, 153.04, 51.58, 30.27.<sup>326</sup>

LysZ NCA (1c):  $^1\text{H}$  NMR (500 MHz, DMSO- $d_6$ ):  $\delta$  (ppm) = 7.38-7.25 (m, 5H), 5.00 (s, 2H), 4.42 (t, 1H), 3.01 (q, 2H), 1.77-1.22 (m, 8H).  $^{13}\text{C}$  NMR (126 MHz, DMSO- $d_6$ ):  $\delta$  (ppm) = 171.5, 156.0, 151.8, 137.1, 128.2, 127.6, 65.0, 30.6, 28.7, 21.5.<sup>327</sup>

BzGlu NCA (1d):  $^1\text{H}$  NMR (500 MHz, DMSO- $d_6$ ):  $\delta$  (ppm) = 7.40-7.31 (m, 5H), 5.10 (s, 2H), 4.45 (dd, 1H), 2.52 (t, 2H), 2.10-1.87 (m, 2H).  $^{13}\text{C}$  NMR (126 MHz, DMSO- $d_6$ ):  $\delta$  (ppm) = 171.6, 171.2, 151.8, 135.9, 128.4, 127.9, 65.6, 56.1, 29.0.<sup>327</sup>

Trp NCA (1e):  $^1\text{H}$  NMR (500 MHz, DMSO- $d_6$ ):  $\delta$  (ppm) = 7.52 (d, 1H), 7.35 (d, 1H), 7.13 (d, 1H), 7.07 (m, 1H), 6.98 (m, 1H), 4.76 (t, 1H), 3.19-3.13 (dd, 2H).  $^{13}\text{C}$  NMR (126 MHz, DMSO- $d_6$ ):  $\delta$  (ppm) = 171.23, 151.83, 135.93, 127.15, 124.44, 121.05, 118.57, 118.39, 111.39, 106.98, 58.18, 26.42.<sup>328</sup>

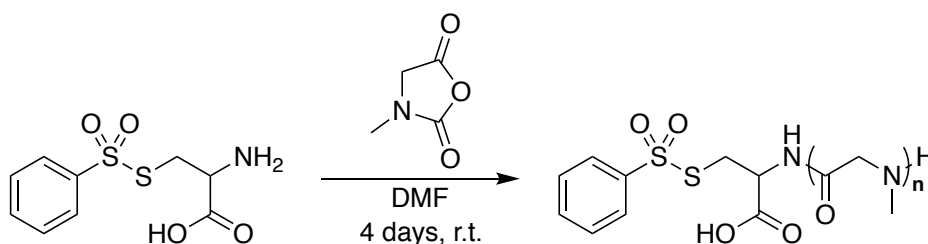
Tyr NCA (1f):  $^1\text{H}$  NMR (500 MHz, DMSO- $d_6$ ):  $\delta$  (ppm) = 9.33 (s, 1H), 9.02 (s, 1H), 6.95 (d, 1H), 6.69 (d, 2H), 4.69 (t, 1H), 2.9 ppm (d, 2H).  $^{13}\text{C}$  NMR (126 MHz, DMSO- $d_6$ ):  $\delta$  (ppm) = 172.03, 157.21, 153.04, 131.43, 125.10, 116.55, 35.64.<sup>329</sup>

### 5.3.3 Preparation of phenylthiosulfonyl cysteine (FTS-Cys)

The FTS-Cys initiator was prepared as previously described and shown in **Scheme 5-2**.<sup>330</sup> Briefly, cysteamine hydrochloride monohydrate (1.5 g, 8.5 mmol) was dissolved in ice-cold 2 M hydrochloric acid to a concentration of 1 M (8.5 mL). In a separate container, sodium nitrite (600

mg, 8.5 mmol) was dissolved in 5 mL ice-cold Milli-Q water and added dropwise to the stirring cysteine solution. Benzenesulfinic acid sodium salt (3.5 g, 21.3 mmol) was added to the red solution in two parts to form a solid precipitate, first after 1.5 hours (2.8 g, 17.1 mmol) and again after 2 hours (700 mg, 4.25 mmol). The reaction was stirred for an additional 2 hours and stored at 4°C overnight. The solid precipitate was collected via filtration, washed with ice-cold Milli-Q water (MQ), and recrystallized from water yielding off-white, fluffy, needle-like crystals (1.07 g, 47.8% yield).

$^1\text{H}$  NMR (500 MHz, DMSO- $d_6$  + TFA):  $\delta$  (ppm) = 7.96 (d, 2H), 7.71 (t, 1H), 7.80 (t, 2H), 4.22 (dd, 1H), 3.46 (dd, 2H).  $^{13}\text{C}$  NMR (126 MHz, DMSO- $d_6$  + TFA):  $\delta$  (ppm) = 169.01, 143.80, 135.09, 130.37, 127.22, 51.82, 35.04.



**Scheme 5-2. Preparation of phenylthiosulfonyl-cysteine (FTS-Cys).**

5.3.4 Preparation of FTS-poly(sarcosine) (FTS-pSarc), FTS-poly(tryptophan) (FTS-pTrp), FTS-poly(tyrosine) (FTS-pTyr), FTS-poly(glutamic acid) (FTS-pGlu), and FTS-poly(lysine) (FTS-pLys)

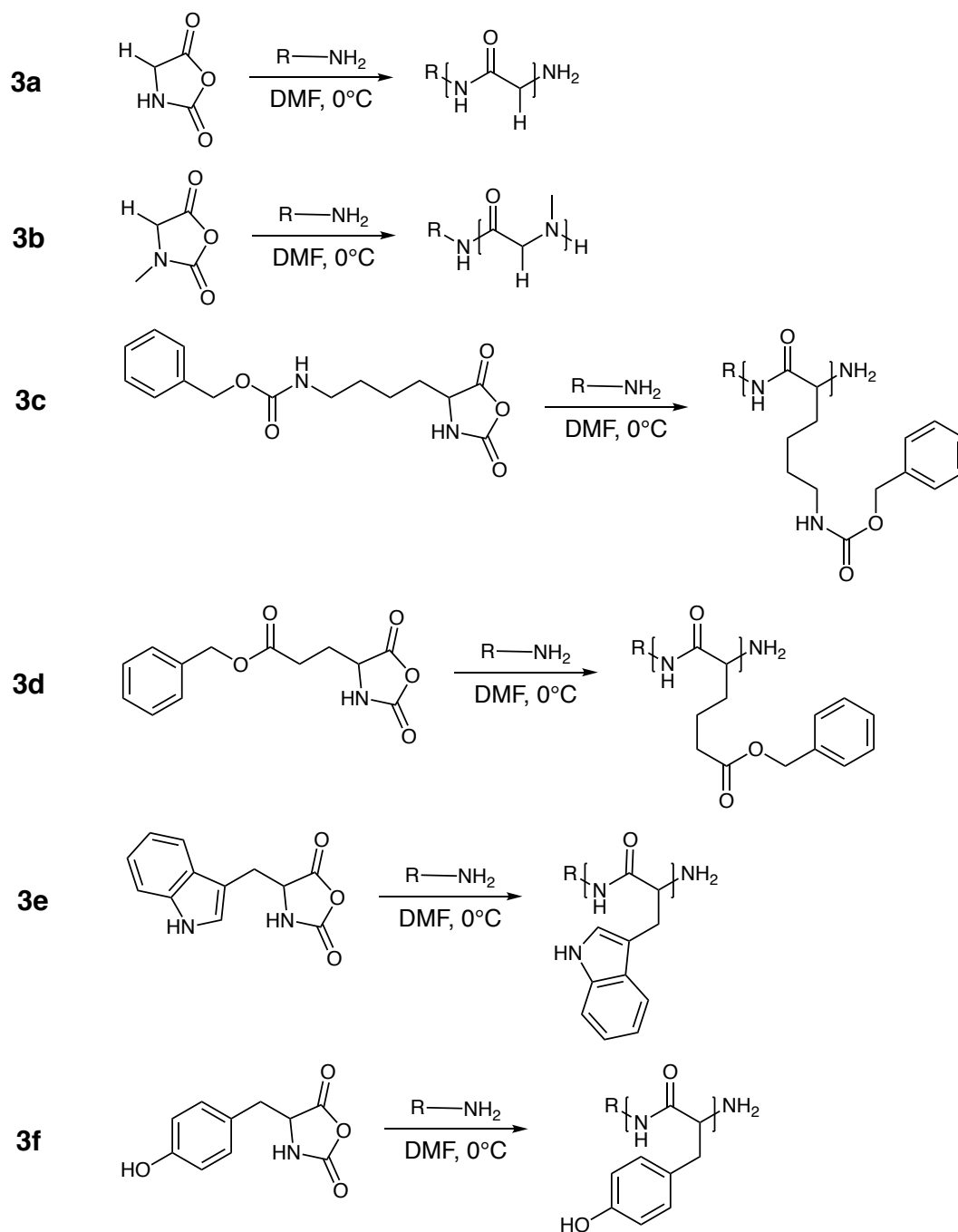
#### *General synthesis of FTS-PAA*s

The synthesis of FTS-PAA homopolymers is shown in **Scheme 5-3**. FTS-Cys was aliquoted into separate vials for each polymer length and suspended in anhydrous DMF. The NCA monomer was added in the corresponding number of equivalents for each length and the vials were placed on a horizontal shaker. The FTS-Cys solubilized into solution as the ROP began, within 30 minutes, and the vials were shaken vigorously for 4 days until gas no longer built up within the container. Polymer samples were precipitated into diethyl ether, collected via filtration, and dried in vacuo to yield the final FTS-PAA polymers.

FTS-pSarc (3b):  $^1\text{H}$  NMR (500 MHz, DMSO- $d_6$ ):  $\delta$  (ppm) = 7.93 (d, 2H), 7.81 (t, 1H), 7.61 (t, 2H), 4.45-3.86 (m, 2H/unit), 3.10-2.71 (m, 3H/unit).

FTS-pLysZ (3c):  $^1\text{H}$  NMR (500 MHz, DMSO- $d_6$ ):  $\delta$  (ppm) = 7.94 (d, 2H), 7.79 (t, 1H), 7.62 (t, 2H), 7.33-7.22 (m, 5H), 4.99 (s, 2H/unit), 4.13 (t, 1H/unit), 1.61-1.32 (m, 8H/unit).

FTS-pBzGlu (3d):  $^1\text{H}$  NMR (500 MHz, DMSO- $d_6$ ):  $\delta$  (ppm) = 7.94 (d, 2H), 7.83 (t, 1H), 7.62 (t, 2H), 7.34 (m, 5H/unit), 5.07 (m, 2H/unit), 4.28 (m, 1H/unit), 1.94 (m, 2H/unit), 1.20 (m, 2H/unit).



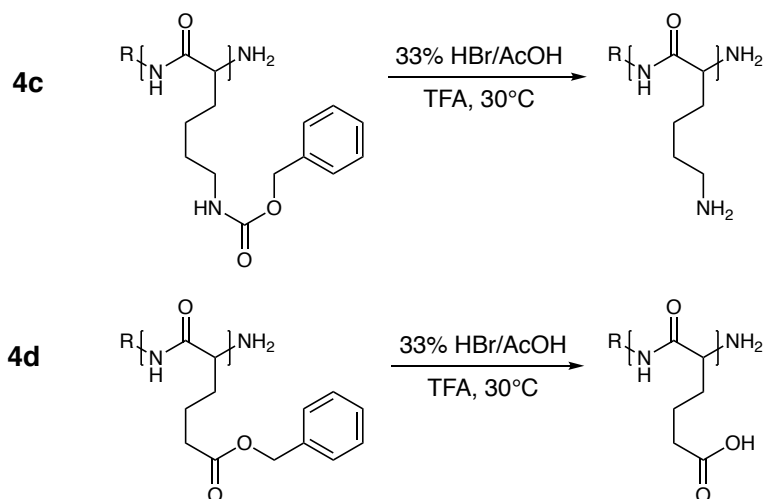
**Scheme 5-3. Preparation of poly(amino acids) from glycine, sarcosine, protected lysine, protected glutamic acid, tryptophan, and tyrosine. (3a) pGly, (3b) pSarc, (3c) pLysZ, (3d) pBzGlu, (3e) pTrp, (3f) pTyr.**

FTS-pTrp (3e):  $^1\text{H}$  NMR (500 MHz, DMSO- $d_6$ ):  $\delta$  (ppm) = 7.89 (m, 3H), 7.79 (t, 1H), 7.75 (s, 1H/unit) 7.58 (t, 2H), 7.35 (d, 1H/unit), 7.13 (d, 1H/unit), 7.05 (m, 1H/unit), 6.96 (m, 1H/unit), 3.93 (t, 1H/unit).

FTS-pTyr (3f):  $^1\text{H}$  NMR (500 MHz, DMSO- $d_6$ ):  $\delta$  (ppm) = 7.90 (d, 2H), 7.80 (t, 1H), 7.63 (t, 2H), 7.05 (m, 1H/unit), 6.70 (m, 2H/unit), 4.46 (m, 1H/unit), 2.88 (m, 2H/unit).

#### *Deprotection of FTS-BzGlu and FTS-LysZ*

The deprotection of pBzGlu and pLysZ is shown in **Scheme 5-4**. pBzGlu and pLysZ deprotection was conducted in 1:1 TFA/33% HBr in AcOH. The reactions were gently heated to 30°C and reacted until the mixture became a milky consistency, about 30 minutes. The deprotected polymers were precipitated in hexanes three times until the supernatant became clear. The light red solids were collected and dried in vacuo to yield the final deprotected polymers.



**Scheme 5-4. Preparation of deprotected poly(amino acids) from lysine and glutamic acid.** (4c) pLys, (4d) pGlu.

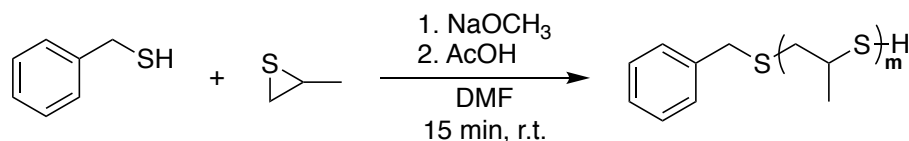
FTS-pLys (4c):  $^1\text{H}$  NMR (500 MHz,  $\text{DMSO-d}_6$ ):  $\delta$  (ppm) = 7.88 (d, 2H), 7.80 (t, 1H), 7.58 (t, 2H), 1.65-1.28 (m, 8H/unit).

FTS-pGlu (4d):  $^1\text{H}$  NMR (500 MHz,  $\text{DMSO-d}_6$ ):  $\delta$  (ppm) = 7.93 (d, 2H), 7.78 (t, 1H), 7.57 (t, 2H), 4.03 (t, 1H/unit), 2.25 (m, 2H/unit), 1.90 (m, 2H/unit).

### 5.3.3 Preparation of PPS homopolymer

Small molecule-initiated PPS homopolymer polymerization was performed as described previously with slight modifications as shown in **Scheme 5-5**.<sup>22</sup> Briefly, benzyl mercaptan (13.46  $\mu\text{L}$ , 0.115 mmol) was added to 1 mL anhydrous DMF and 0.5 M sodium methoxide in methanol (253  $\mu\text{L}$ , 0.123 mmol) in a water bath. After stirring for 5 minutes, propylene sulfide was added in a single rapid injection according to the intended polymer chain length (25 units: 180  $\mu\text{L}$ , 2.3 mmol; 35 units: 288  $\mu\text{L}$ , 3.7 mmol; 62 units: 450  $\mu\text{L}$ , 5.7 mmol). After 15 minutes of polymerization, acetic acid (66  $\mu\text{L}$ , 1.15 mmol) was added to end the reaction. The solution was precipitated in cold methanol, collected, and dried in vacuo to yield a straw-colored, viscous liquid (25 units: 155 mg, 70%; 35 units: 217 mg, 70%; 62 units: 358 mg, 67%).

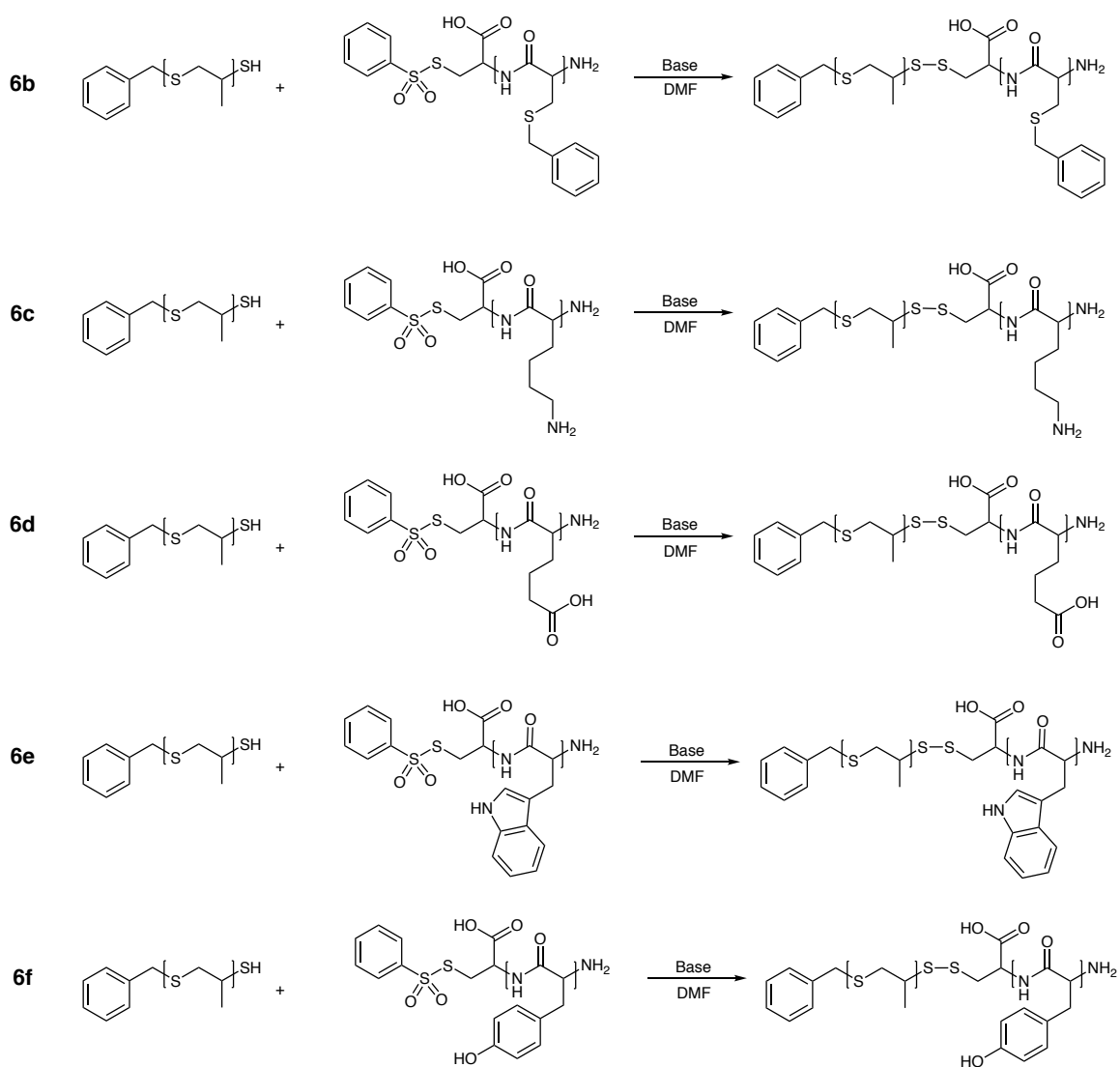
$^1\text{H}$  NMR (500 MHz,  $\text{CDCl}_3$ ):  $\delta$  (ppm) = 7.27 (d, 4H), 2.90 – 2.76 (m, 2H/unit), 2.60 – 2.51 (m, 1H/unit), 1.34 – 1.23 (m, 3H/unit).



**Scheme 5-5. Preparation of poly(propylene sulfide) homopolymer.**

5.3.6 Synthesis of PAA-*b*-PPS copolymers*General synthesis of PAA-*b*-PPS copolymers*

The combinatorial library was created using the following general procedure, substituting polymers of varying lengths for each chain as shown in **Scheme 5-6**. Briefly, the PPS chains were



**Scheme 5-6.** Preparation of PAA-*b*-PPS copolymers from sarcosine, lysine, glutamic acid, tryptophan, and tyrosine. (6b) pSarc-*b*-PPS, (6c) pLys-*b*-PPS, (6d) pGlu-*b*-PPS, (6e) pTrp-*b*-PPS, (6f) pTyr-*b*-PPS.

dissolved into a stock anhydrous DMF and aliquoted out into 1.1 eq. portions for each library entry along with 1.1 eq. of base to deprotonate to the thiolate ion. The PAA chains were dissolved into a stock anhydrous DMF and aliquoted out into 1 eq. portions across the PPS vials. The mixtures were shaken vigorously overnight and precipitated into diethyl ether to yield the final PAA-*b*-PPS copolymers.

pSarc-*b*-PPS (6b):  $^1\text{H}$  NMR (500 MHz, DMSO- $d_6$ ):  $\delta$  (ppm) = 4.44-3.85 (m, 2H/unit pSarc), 2.68-2.59 (m, 1H/unit PPS), 1.37-1.20 (m, 3H/unit PPS).

pLys-*b*-PPS (6c):  $^1\text{H}$  NMR (500 MHz, DMSO- $d_6$ ):  $\delta$  (ppm) = 7.88 (d, 2H), 7.80 (t, 1H), 7.58 (t, 2H), 2.68-2.59 (m, 1H/unit PPS), 1.37-1.20 (m, 3H/unit PPS), 1.65-1.28 (m, 8H/unit Lys).

pGlu-*b*-PPS (6d):  $^1\text{H}$  NMR (500 MHz, DMSO- $d_6$ ):  $\delta$  (ppm) = 7.93 (d, 2H), 7.78 (t, 1H), 7.57 (t, 2H), 4.03 (t, 1H/unit Glu), 2.68-2.59 (m, 1H/unit PPS), 1.37-1.20 (m, 3H/unit PPS), 2.25 (m, 2H/unit Glu), 1.90 (m, 2H/unit Glu).

pTrp-*b*-PPS (6e):  $^1\text{H}$  NMR (500 MHz, DMSO- $d_6$ ):  $\delta$  (ppm) = 7.89 (m, 3H), 7.79 (t, 1H), 7.75 (s, 1H/unit Trp), 7.58 (t, 2H), 7.35 (d, 1H/unit Trp), 7.13 (d, 1H/unit Trp), 7.05 (m, 1H/unit Trp), 6.96 (m, 1H/unit Trp), 3.93 (t, 1H/unit Trp), 2.68-2.59 (m, 1H/unit PPS), 1.37-1.20 (m, 3H/unit PPS).

pTyr-*b*-PPS (6f):  $^1\text{H}$  NMR (500 MHz, DMSO- $d_6$ ):  $\delta$  (ppm) = 7.90 (d, 2H), 7.80 (t, 1H), 7.63 (t, 2H), 6.87 (m, 1H/unit Tyr), 6.66 (m, 2H/unit Tyr), 4.61 (m, 1H/unit Tyr), 2.88 (m, 2H/unit Tyr), 2.68-2.59 (m, 1H/unit PPS), 1.37-1.20 (m, 3H/unit PPS).

### 5.3.7 Assembly of PAA-*b*-PPS copolymers

#### *Thin film rehydration (TF)*

Polymer formulations were assembled via TF as described previously.<sup>192</sup> For each formulation, 10 mg of PAA-*b*-PPS diblock copolymer along with either 0.0625% by weight of the hydrophilic Dil or 0.25% ethyl eosin were dissolved into 1 mL of DCM. The organic phase was transferred to glass HPLC vials and slowly vacuum desiccated overnight to form a thin film on the glass surface of the HPLC vial. The dry vials were filled with 1 mL of 1X phosphate buffered saline (PBS) or Milli-Q water (MQ) as the aqueous phase and agitated overnight on a tabletop shaker to form PAA-*b*-PPS nanostructures. The samples were filtered through a gravity column packed with Sepharose 6B-CL size-exclusion resin and a 1X PBS mobile phase to yield stable nanoparticle formulations.

#### *Flash nanoprecipitation (FNP)*

Polymer formulations were assembled as described previously using flash nanoprecipitation.<sup>29,150,160</sup> For each formulation, 20 mg of each polymer along with either 0.0625% by weight of the hydrophilic Dil or 0.25% ethyl eosin were solubilized in THF or DMF to 500  $\mu$ L total. This organic phase and 500  $\mu$ L of either 1X PBS or Milli-Q water as the aqueous phase were loaded into separate 1 mL syringes and anchored to a confined impingement jet (CIJ) block.<sup>187,188</sup> The phases were impinged together into the mixing chamber of the block five times before the final deposit into the 1.5 mL aqueous reservoir. All formulations were desiccated overnight to remove residual organic solvent and filtered through a gravity column packed with

Sepharose 6B-CL size-exclusion resin and a 1X PBS mobile phase to yield stable nanoparticle formulations.

### 5.3.8 Characterization of PAA-*b*-PPS copolymers

#### *Size, polydispersity, and zeta potential*

Nanostructure size distribution and polydispersity index (PDI) were measured by dynamic light scattering (DLS) using a Zetasizer Nano (Malvern Instruments) with a 4 mW He-Ne 633 nm laser. Each nanoparticle formulation was diluted 1:100 or 1:1000 into Milli-Q water and analyzed as two rounds of three runs ( $n = 6$ ). Zeta potential was measured by electrophoretic light scattering (ELS) using the same Zetasizer (Malvern Instruments). Nanostructures were diluted 1:10 in ultrapure water prior to ELS for a 0.1X PBS background.

#### *Transmission electron microscopy (TEM)*

The 1.5% uranyl formate (UF) negative stain was prepared in ultrapure water. Potassium hydroxide (10 N) was used to adjust the pH to 4.5. Formvar carbon film copper grids (400 mesh; Electron Microscopy Sciences, Inc.) were glow discharged (25 W, 10 sec). A volume of 3  $\mu\text{L}$  of PAA-*b*-PPS nanostructure formulation was applied to glow discharged grids. Grids were gently blotted, passaged through two 30  $\mu\text{L}$  volumes of ultrapure water, and were negatively stained by two passages through 30  $\mu\text{L}$  volumes of 1.5% UF stain. Excess stain was removed by gentle blotting. This procedure resulted in  $\sim 0.5$   $\mu\text{L}$  of stain on the grid. The activity was  $2.55 \times 10^{-5}$   $\mu\text{Ci}/\text{grid}$ . A JOEL 1400 Transmission Electron Microscope operating at 120 kV was used to acquire images of each PAA-*b*-PPS formulation.

### *Small-angle x-ray scattering (SAXS) data acquisition and analysis*

Small-angle x-ray scattering (SAXS) experiments were performed using synchrotron radiation at the DuPont-Northwestern-Dow Collaborative Access Team (DND-CAT) beamline at Argonne National Laboratory's Advanced Photon Source (Argonne, IL, USA) with 10 keV (wavelength  $\lambda = 1.24 \text{ \AA}$ ) collimated X-rays. Polymersome formulations were analyzed in the  $q$ -range ( $0.001\text{--}0.5 \text{ \AA}^{-1}$ ) with a sample-to-detector distance of approximately 7.5 m and an exposure time of 1 s. The diffraction patterns of silver behenate were utilized to calibrate the  $q$ -range from 0.001 to  $0.5 \text{ \AA}^{-1}$ . The momentum transfer vector  $q$  is defined as  $q = 4\pi \sin\theta/\lambda$ , where  $\theta$  is the scattering angle. Data reduction, consisting of the removal of solvent/buffer scattering from the acquired sample scattering, was completed using the PRIMUS 2.8.2 software while model fitting was completed using the SASView 4.0.1 software package (<http://www.sasview.org/>).

Further data analysis was performed using the core-shell sphere ([http://www.sasview.org/docs/user/models/core\\_shell\\_sphere.html](http://www.sasview.org/docs/user/models/core_shell_sphere.html)) and vesicle model fits (<http://www.sasview.org/docs/user/models/vesicle.html>). The fitting formulae for these models is described below

*Core-shell model:*

Calculates 1D and 2D scattering as the following:

$$P(q) = \frac{\text{scale}}{V} F^2(q) + \text{background}$$

where

$$F(q) = \frac{3}{V_s} \left[ V_c(\rho_c - \rho_s) \frac{\sin(qr_c) - qr_c \cos(qr_c)}{(qr_c)^3} + V_s(\rho_s - \rho_{\text{solv}}) \frac{\sin(qr_s) - qr_s \cos(qr_s)}{(qr_s)^3} \right]$$

where

$V_s$  = volume of the whole particle

$V_c$  = volume of the core

$r_s$  (radius + thickness) = radius of the particle, effective radius for  $S(Q)$  when  $P(Q) \cdot S(Q)P(Q) \cdot S(Q)$

$r_c$  = radius of the core

$\rho_c$  = scattering length density of the core

$\rho_s$  = scattering length density of the shell

$\rho_{\text{solv}}$  = scattering length density of the solvent

*Vesicle model:*

Calculates 1D and 2D scattering as the following:

$$P(q) = \frac{\phi}{V_{\text{shell}}} \left[ \frac{3V_{\text{core}}(\rho_{\text{solvent}} - \rho_{\text{shell}})j_1(qR_{\text{core}})}{qR_{\text{core}}} + \frac{3V_{\text{tot}}(\rho_{\text{shell}} - \rho_{\text{solvent}})j_1(qR_{\text{tot}})}{qR_{\text{tot}}} \right]^2 + \text{background}$$

where

$\Phi$  = volume fraction of shell material

$V_{\text{shell}}$  = is the volume of the shell

$V_{\text{cor}}$  = is the volume of the core

$V_{\text{tot}}$  = is the total volume

$R_{\text{core}}$  = is the radius of the core

$R_{\text{tot}}$  = is the outer radius of the shell, effective radius for  $S(Q)$  when  $P(Q) \cdot S(Q)$

$\rho_{\text{solvent}}$  = scattering length density of the solvent, same as core

$\rho_{\text{scale}}$  = scattering length density of the shell

background = flat background level (incoherent scattering in the case of neutrons)

$j_1$  = spherical bessel function,  $j_1 = (\sin(x) - x \cos(x)) / x^2$

### 5.3.9 RAW 264.7 cell culture

RAW 264.7 cells (murine macrophage cell line) were acquired from American Type Culture Collection (ATCC, Rockville, MD, USA). Cells were cultured in Dulbecco's Modified Eagle's Medium (DMEM) supplemented with 10% fetal bovine serum (FBS), penicillin (100 IU/mL) and streptomycin (100  $\mu\text{g}/\text{mL}$ ) at 37 °C in the presence of air (95%) and CO<sub>2</sub> (5%).

### 5.3.10 Cytotoxicity

The viability of RAW 264.7 macrophages in the presence of pSarc-*b*-PPS nanostructures was determined using the MTT (3-(4,5-dimethylthiazolyl-2)-2,5-diphenyltetrazolium bromide) assay. RAW 264.7 cells ( $3 \times 10^5$  cells/mL, 100  $\mu$ L) were transferred into each well of a 96-well plate and left overnight in the incubator for adherence. The adhered cells were treated with micelle and vesicle nanostructure formulations to attain a final polymeric concentration in each well at 0.125, 0.25, and 0.5 mg/mL and incubated for 24 hours. After 24 hours, all wells were added with MTT (5 mg/mL in PBS, 10  $\mu$ L) and further incubated for 4 hours. The resultant formazan crystal deposition in each well was dissolved in DMSO (200  $\mu$ L) and the absorbance was measured at 570 nm. All the samples were analyzed in quadruplicates. The percentage cell viability was calculated as  $\left( \frac{OD \text{ of treated sample}}{OD \text{ of untreated sample}} \right) \times 100\%$  %. Data was analyzed for statistical significance with GraphPad Prism 8 using two-way ANOVA and Tukey's multiple comparison tests.

## 5.4 Results and Discussion

### 5.4.1 A note on phosgene safety

The work in this section uses phosgene derivatives to prepare the NCA monomers. Despite the improved handling of the diphosgene and phosgene derivatives as liquid and solid forms respectively, *significant* caution should be used for phosgene in all forms.<sup>331</sup> The utility of these reagents to produce a wide range of chemical intermediates for synthetic applications does not alleviate the caution that should be taken for its handling and storage. All three phosgene

reagents can induce severe respiratory complications as derivatives and after decomposition to a highly toxic colorless and odorless gas.<sup>332</sup> The highest caution should be exercised for all reactions and workups that involve this reagent, including effective PPE, proper handling and measuring, minimal stoichiometric amounts used, close tracing of all glassware and surfaces in contact with the reagents, maintenance of the reaction barrier within the refluxing system, complete quenching of any excess reagent, effective purification, and proper waste disposal. Additionally, consider alternative synthetic routes for the desired compounds if possible.<sup>333-335</sup> Guidance for these areas can be found in a number of published resources including The National Institute for Occupational Safety and Health (NIOSH), the U.S. Environmental Protection Agency (EPA), and others.

#### 5.4.2 Finding a suitable pilot backbone

##### *Glycine*

As the simplest amino acid, glycine (Gly) and its single proton side chain was an appropriate starting point for the investigation of PAA applications as nanocarriers. Polymers of this amino acid are essentially long chains of pure peptide bonds and would offer insight into the self-assembling characteristics of PAAs before introducing more complex moieties.

The NCA cyclization reaction was straightforward as there is no additional side chain protection to consider. Glycine NCA (Gly NCA) monomer was formed in reliable yields with minor modifications to previous protocols<sup>325,336</sup> by reacting with phosgene in THF heated to 55°C and precipitated in cold hexanes as shown in **Scheme 5-1a**. The polymerization of Gly NCA into

poly(glycine) (pGly) was also straightforward. Given the considerations further described below, pure chains of pGly are rarely synthesized in the literature and instead are synthesized as part of a larger copolymer construct.<sup>337,338</sup> However, this approach to pGly polymerization was based on the general protocol of NCA polymerization, speaking to the translational capability of this chemistry regardless of most monomer features. In this way, a suspension of Gly NCA monomer was initiated with a small molecule primary amine until complete dissolution and a small release of CO<sub>2</sub> gas as the rings open (**Scheme 5-3a**).

Unfortunately, while this pGly product was fully soluble in the DMF solvent for polymerization, it was no longer able to enter solution again after the polymer was collected and dried. I attempted to enhance pGly solubility using a number of organic solvents including the “magic mixture” of equal parts DMF:DMSO:NMP.<sup>339</sup> I also attempted to solubilize pGly in aqueous solvents with the full range of pH values, temperatures up to 50°C, and many chaotropic salts<sup>340</sup> including lithium bromide, lithium chloride, and potassium thiocyanate. Despite previous work finding mild success in solubilizing short pGly chains using difluoroacetic acid and trifluoroacetic acid<sup>341</sup> or lithium salts,<sup>342</sup> the lengths of pGly needed for this diblock copolymer were likely too long as homopolymer chains longer than 9 units were found to adopt the polyglycine II conformation and irreversibly aggregate.<sup>343</sup> These conditions are also unlikely to be compatible with the subsequent synthetic or assembly steps. It was thus impossible to analyze via NMR or use it for any future experiments. More specifically, the insolubility of pGly is likely due to a known property of pGly polymers to align in layers that maximize hydrogen bonding between chains.<sup>343</sup> As a pure chain of peptide bonds, pGly does not have a side group to sterically

or electrostatically disrupt any intra-chain bonding, meaning that every single Gly unit is able to interact directly with a Gly unit on a separate chain through hydrogen bonding and CO-CO dipolar associations (**Figure 5-4a**). Favoring these interactions between pGly chains instead of between a pGly chain and water results in this seemingly irreversible aggregation.<sup>344</sup> Interestingly, it is this interaction between glycine-rich chains that helps provide the strength and toughness of spider silk.<sup>337,345</sup> In these systems, alanine-rich polymer chains have an even more significant chain association strength as the methyl side chain creates a hydrophobic domain within the void space that is entirely impenetrable to water.<sup>346</sup> This effectively rules out alanine as a pilot NCA backbone for this material.

This ability to form immensely stable hydrogen bonds suggests that while a pGly polymer is the simplest PAA backbone, it is likely a significant outlier in its physiochemical properties and cannot be used to make any broader conclusions about a potential nanomaterial. Gly units may be quite useful as a component of a PAA chain of many different types of monomers, perhaps as

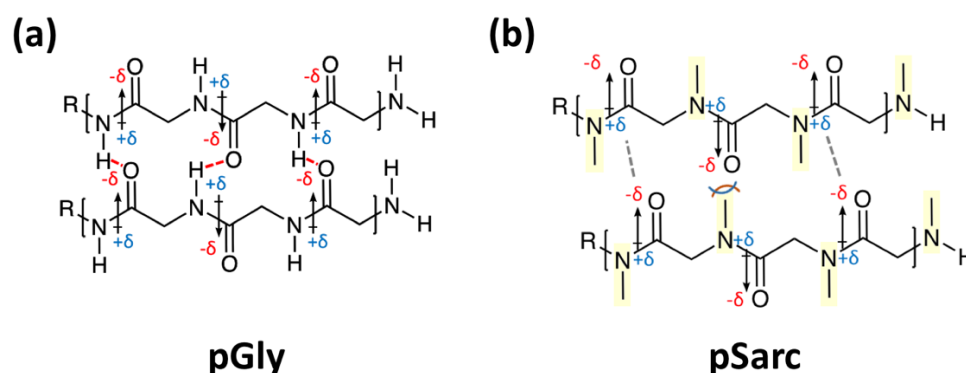


**Figure 5-4. Intermolecular associations between poly(glycine) and poly(sarcosine) chains.** (a) pGly chains show primarily carbonyl dipole-dipole (red/blue) forces and hydrogen bonding while (b) pSarc chains have reduced carbonyl dipole-dipole forces and eliminated hydrogen bonding due to N-methylation, as highlighted in yellow.

a spacer or to modify chain flexibility, but likely not as a pure pGly chain. However, the simplicity of Gly cyclization into an NCA monomer and subsequent polymerization without need for additional protection groups remains an advantage for this amino acid.

### *Sarcosine*

Sarcosine (Sarc), or N-methylglycine, is a peptoid molecule with a single proton side chain and an N-methylation of the amino group. In addition to altering several aspects of the polymerization kinetics, a polymer made from this monomer would not be able to form the excessive number of between-chain associations as seen with pGly.<sup>347</sup> Instead, the methylation of the amine portion of the peptide bond fully removes the N-H proton that otherwise would hydrogen bond with the carbonyl group of another chain (**Figure 5-4b**). I expected this derivative to be a sufficient balance between incorporating a more substantial side chain and further modifying the monomer unit to be no longer useful as a simple pilot for a self-assembling copolymer system. Additionally, poly(sarcosine) has also previously been shown to resist protein adsorption similarly to PEG<sup>313 348</sup> and effectively shield charges on liposomes.<sup>349</sup>

Cyclization to the sarcosine NCA (Sarc NCA) monomer was also straightforward as another molecule without need for side chain protection. The reaction improved with additional drying of the commercially supplied sarcosine starting material as heated on a stir plate with full vacuum overnight. The insoluble peptoid slowly solubilized in THF heated to 55°C upon the presence of phosgene after several hours, as previously reported (**Scheme 5-1b**).<sup>350</sup> Polymerization of the Sarc NCA to the polypeptoid poly(sarcosine) (pSarc) was accomplished with similar conditions to Gly NCA polymerization with a primary amine in DMF (**Scheme 5-3b**) despite the propagation

proceeding with a secondary amine active chain end.<sup>351</sup> The similar results of this polymerization confirm the density functional theory (DFT) computational analysis of NCA polymerization with primary and secondary amine initiators.<sup>347</sup> While the rate-limiting step of the three-part reaction pathway is nucleophilic addition, the energy barrier of the secondary amine initiator is lower than the primary amine. This indicates that N-methylated peptoids like Sarc can initiate and propagate just as quickly if not faster than the primary amine of standard amino acids. The NMR spectra of pSarc chains confirms a successful polymerization via this mechanism as a promising backbone for initial self-assembly studies.

#### 5.4.3 Finding a suitable NCA/PPS linker

A critical component of this strategy is the selection of a protected linker between the blocks that enables unrestricted pairing of distinct chain lengths of pSarc and PPS. This will maximize the utility of each synthesized polymer and minimize the mass of material needed to conduct the screen. I began exploring potential heterobifunctional linkers beginning with small molecules that could potentially initiate one or both of these chains.

For the PAA portion, NCA monomers are capable of “living” ROP with the introduction of a primary amine under mild conditions. Conversely, PPS is formed through the initiation of commercially available propylene sulfide by a small-molecule thiolate ion. The resulting terminal thiolate ion can be temporarily neutralized to a thiol for future functionalization, covalently capped with an alkyl halide, or added directly to a thiol-disulfide exchange. A linker would have to have both a primary amine and either a thiolate or disulfide moiety to covalently attach both

polymer blocks. However, complexities quickly arose after exploring a variety of potential linkers that would have ROP capabilities for one or both of these chains. The character of both thiolate ions and amines as nucleophiles would non-specifically initiate off both ends of the linker unless a protection strategy was utilized.

Unfortunately, a large number of these linker candidates failed to adequately isolate the nucleophilic requirements of amines and thiolates and limit ROP to only one end of the polymer at a time. The investigation of linkers and temporary protecting groups posed a separate collection of concerns related to the stability, oxidation and acidic sensitivity, and nucleophilic activity of the protecting group. These trials are listed in **Table 5-1** that display the potential PPS link (red), NCA link (blue), and identified reason for failure (pink) if applicable.

First, I began with the simplest cysteine and cysteamine compounds (entries 1 and 2) as a direct attachment of blocks via the thiol for PPS blocks and the amine for the NCA blocks. However, this arrangement did not account for the overlap in initiation chemistries of these monomer rings as nucleophiles. I hypothesized that in some cases the nucleophilic character of amines and thiolate anions could initiate polymerization of both NCAs and propylene sulfide, rendering these linker candidates ineffective. To test this, I used cystine to initiate NCA monomers of the amine end in a separate reaction and performed a complete workup. I used this homopolymer to attempt to initiate propylene sulfide of the presumed intact thiolate end of the cystine linker. However, this second polymerization failed to produce a copolymer in this NCA-to-PPS case, as well as the reverse order of PPS polymerization first followed by NCA polymerization for both cysteine and cysteamine. This indicates that the initial polymerization of

Table 5-1. Potential linker strategies for unrestricted pairing of PAA and PPS polymer blocks and chemical considerations.

	Linker	Considerations
1	 Cysteamine	Unintended NCA and PPS polymerization from both ends
2	 Cysteine	
3	 Pyr-Cysteamine	Unintended NCA ring opening with pyridyl nitrogen (pink)
4	 Pyr-Cysteine	
5	 Trt-Cysteamine	Instability to acidic deprotection conditions (pink)
6	 Trt-Cysteine	
7	 N-Acetylhomocysteine thiolactone	No independent block validation
8	 Bromoethylamine	
9	 N-allyloxycarbonyl glycine NCA	NCA instability (pink)
10	 FTS-Cysteamine	Synthetic difficulties
11	 FTS-Cysteine	Success

Red text: PPS link; blue text: PPA link; pink text: problem areas

PPS or NCA polymers occurred on both ends of the cysteine and cysteamine without distinction. In other words, the nucleophilic character of both the amine and the thiol ends of these initiators is sufficient to polymerize both chemistries at once, requiring a protecting strategy in order to preserve the other end of the initiator.

To protect the thiol moiety on these compounds, 2,2'-dipyridyl disulfide was reacted with the thiol on cysteine and cysteamine to form a disulfide bridge (entries 3 and 4). Unfortunately, these linkers were insufficient in two ways. First, the nitrogen in the pyridyl ring was nucleophilic enough to interfere with NCA polymerization, resulting in the double-end polymerization seen in the unprotected initiators. Second, the disulfide bridge protection was susceptible to exchange by the propagating primary amine on the NCA chain to both end up as two connected NCA homopolymers. Both of these cases resulted in a failed protection of the pyridyl disulfide group for these polymerization chemistries.

The next protecting group for the cysteine and cysteamine was the trityl group. This bulky acid-labile protecting group is often used in the SPPS strategies as it is easily removed in mild conditions. While these trityl-protected linkers are theoretically able to maintain thiol protection during NCA polymerization and can be easily deprotected, the acidic conditions required introduce several complications that will limit the strategic implementation in future PAA-*b*-PPS copolymers. First, the trityl group is removed under mild acidic conditions that would not be stable to the deprotection of amino acid derivatives that require a harsher acidic environment, including *N*<sub>6</sub>-carbobenzyloxy-L-lysine (LysZ) and glutamic acid  $\gamma$ -benzyl ester (BzGlu) used extensively in future chapters. The use of this linker would instead be limited to use with the few

NCA monomers that do not require any protection or ones that are protected by Alloc and Fmoc groups.<sup>352</sup> The other consideration with the acid-lability of the trityl group is that despite the mild deprotection conditions, the acidity required is too high to be withstood by the PPS chain that is specifically selected for its sensitivity to oxidative and acidic environments.<sup>153</sup>

A brief investigation of thiolactone compounds was conducted as potential linker applied as a cap to the NCA chain. Thiolactones are used in a number of one-pot syntheses as a heterocyclic molecule that is susceptible to nucleophilic ring opening with an amine to reveal a free thiol moiety.<sup>353,354</sup> The strategy for this potential linker in PAA-*b*-PPS constructs was to first polymerize the NCA chain and cap the primary amine terminal end with a thiolactone group to open into a thiolate ion for PPS propagation. The downside of this approach is the inability of this linker to allow for a combinatorial approach. While the thiolactone chemistry is amenable to simply making NCA chains connected to PPS chains, the end cap-initiator mechanism can only be applied to single linear syntheses without independent block formation and cross-chain pairing. For the purposes of this current work, the thiolactone and its derivatives are not sufficient for this combinatorial approach without further modifications.

Additionally, the use of a linker that would attach to the amine end of the NCA polymer would eliminate an extremely useful moiety for future conjugation. A linker that is able to initiate an NCA chain out from the center would result in a terminal amine that interfaces with the external environment of the formed nanoparticles. As one of the most commonly modified moieties in bioactive conjugations such as peptide coupling and chemical modifications as a nucleophile, having a primary amine would offer a vast range of tunability for targeting, cross-

linking, and functionalizing of nanoparticles made from PAA-*b*-PPS materials. While not a vitally important component of linker selection, this is a worthwhile consideration that makes a thiolactone a less preferred linker option.

Next, the simple bromoethylamine linker was investigated. In this strategy, a PPS chain would be initiated independently and capped with the bromoethylamine as an alkyl halide to functionalize the end of the PPS chain with an amine. This amine would be able to initiate NCA polymerization off the end of PPS directly. However, for the same reason as the previously discussed thiolactone, this linear approach is not ideal for creating a combinatorial library with independent hydrophilic and hydrophobic blocks. For this reason, bromoethylamine was not pursued further for this application.

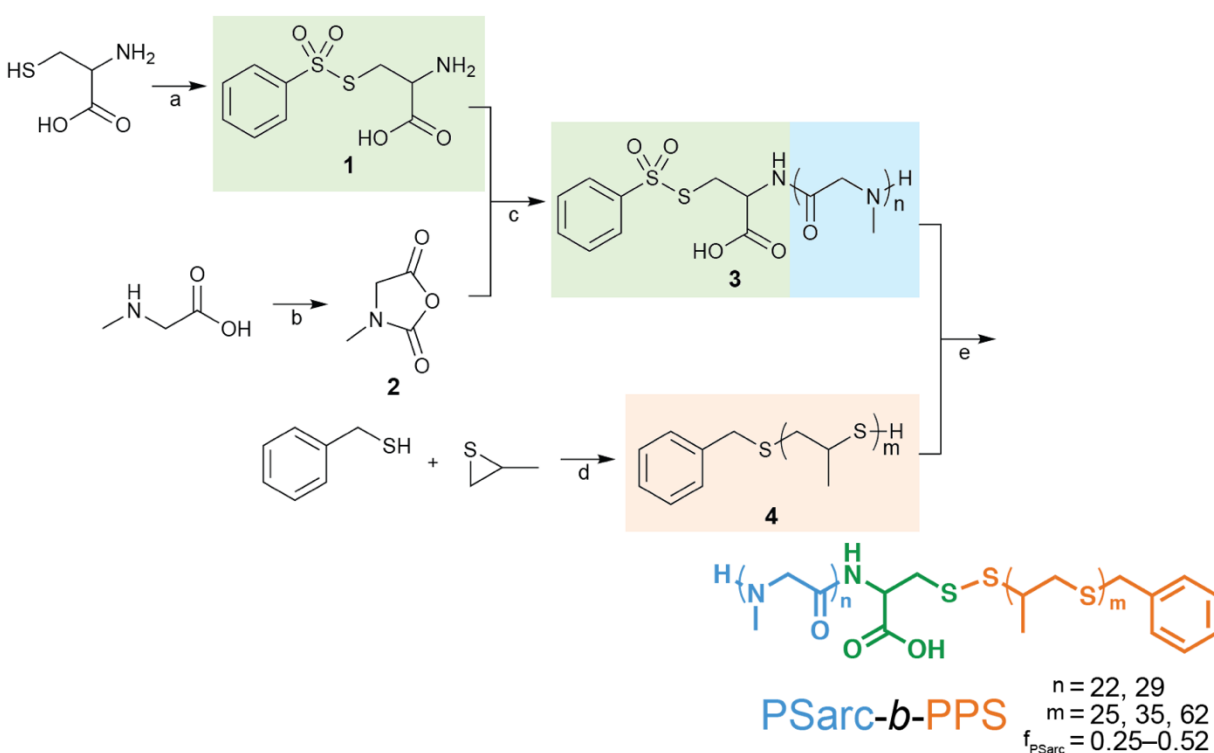
In the spirit of using NCA monomers as chemical linkers directly for chemical syntheses, I attempted to make an NCA linker with an allyl side chain for a Michael-type addition with the PPS thiolate active end.<sup>355</sup> For this strategy, the NCA chain would be capped with a unit of N-allyloxycarbonyl glycine and analyzed independently. PPS would also be polymerized separately after capping with acetic acid to protonate the thiolate ion to a thiol. The independent chains of PAA and PPS could be paired freely through the allyl-thiol bond in appropriate conditions to yield a complete diblock copolymer. Unfortunately, along with the lower preference of a linker that does not maintain the primary amine of the NCA chain, this NCA linker was not sufficiently stable as a monomer and could not be isolated for further use. Deeper investigation of this NCA to identify the source of instability would be a worthwhile pursuit as a potential monomer unit for mixed PAA chains beyond that of a linker, but was not sufficient for the investigation here.

#### 5.4.4 Synthesis of pSarc-*b*-PPS copolymers

With these considerations in mind, a return to the strategy of a primary amine combined with a disulfide protected thiol was the most ideal choice. The phenylthiosulfonyl (FTS) group is a unique option for protecting a thiol moiety as the disulfide formed is specific to thiol-disulfide exchanges and resistant to reactions with primary amines, as seen in the pyridyl disulfide protection previously described.<sup>330,356</sup> Initial synthesis of this type of linker was for the simpler cysteamine but the reaction failed to produce the desired product, and indeed this type of compound has not been reported in known literature. Instead, only cysteine was amenable to this protection with this phenylthiosulfonyl group protection to make FTS-protected cysteine (FTS-Cys) as the linker (**Scheme 5-2**). This strategy allows for the initiation of the NCA chain off the primary amine and maintenance of the amine terminal end of the PAA chain. The protected disulfide group prevents cross-reactivity and turns the PAA chain into a type of cap for the end of the PPS chain. This allows for the independent synthesis and analysis of each polymer block with unrestricted combinatorial pairing to generate many diblock copolymers with minimal material. In this way, the FTS-Cys linker is the ideal option for this approach.

The three components of linker, PAA, and PPS were incorporated as shown in **Scheme 5-7** beginning with the synthesis of the FTS-Cys initiator. The preparation was straightforward with the development of a light pink precipitate as a marker of reaction progress. After purification, the recrystallized needle-like product was stable for many months and used for each of the following PAA-*b*-PPS syntheses. Separately, the Sarc NCA was prepared via phosgenation to the

heterocyclic N-carboxyanhydride monomer form (**Scheme 5-1b**). Chains of pSarc were initiated by FTS-Cys to create multiple hydrophilic blocks within a reasonable mass range for the potential copolymers, shown here as 22, 29, 50, 60, and 80 units of pSarc (**Scheme 5-3b**). These FTS-pSarc blocks were analyzed via NMR (**Figure 5-5.3b**) and stored as the hydrophilic dimension of the copolymer library. The PPS blocks were initiated by the small molecule benzyl mercaptan and



**Scheme 5-7. Preparation of pSarc-*b*-PPS using the FTS-Cys linker for combinatorial block pairing.** The FTS-Cys linker (1, green) is prepared from cysteine and used to initiate previously synthesized Sarc NCA (2) to form the hydrophilic FTS-pSarc block (3, blue). Separately, PPS (4, orange) is prepared with a benzyl mercaptan initiator to form the hydrophobic block. For combinatorial pairing, specific lengths of FTS-pSarc and PPS blocks are conjugated via a thiol-disulfide exchange off the FTS linker to form pSarc-*b*-PPS diblock copolymers of various lengths. The representative copolymers for this work have pSarc block lengths of 22 and 29 with PPS block lengths of 25, 35, and 62. The resulting  $f_{\text{pSarc}}$  values fall between 0.25 and 0.52. *Conditions:* (a) sodium nitrite, water, 0°C, 1.5 h; benzenesulfonic acid sodium salt, 0°C to r.t., 4 h. (b) diphosgene, THF, 55-60°C, 4 h. (c) DMF, r.t., 96 h. (d) NaOMe, DMF, 20°C, 15 min; AcOH, r.t., 2 min. (e) base, MeOH, r.t., o/n.

capped with a proton to form the more stable thiol of lengths 14, 25, 35, and 62 units. (Scheme 5-5). These chains were also analyzed via NMR (Figure 5-5.6b) and stored carefully as the more sensitive hydrophobic dimension of the copolymer library. Both the pSarc and PPS polymer block properties are summarized in Table 5-2.

The lengths of these chains were selected to fully explore the range of hydrophilic weight fractions, with long and short variants of both blocks. Realistically, testable weight fraction ranges fall in a narrower range than the theoretical 0.00 to 1.00 as those would represent homopolymers of hydrophobic and hydrophilic blocks respectively. An efficient approach must find a balance between a comprehensive examination of the reasonable values in order to include all possible outcomes but also focus on the ranges that are most likely to form the desired morphologies and transitional areas in order to extract the most useful information. In the case of this work, I hypothesized that this new PAA-*b*-PPS material could form micelles at a minimum, with the potential for vesicles. For diblock copolymers that use PPS, specifically PEG-*b*-PPS, micelles form

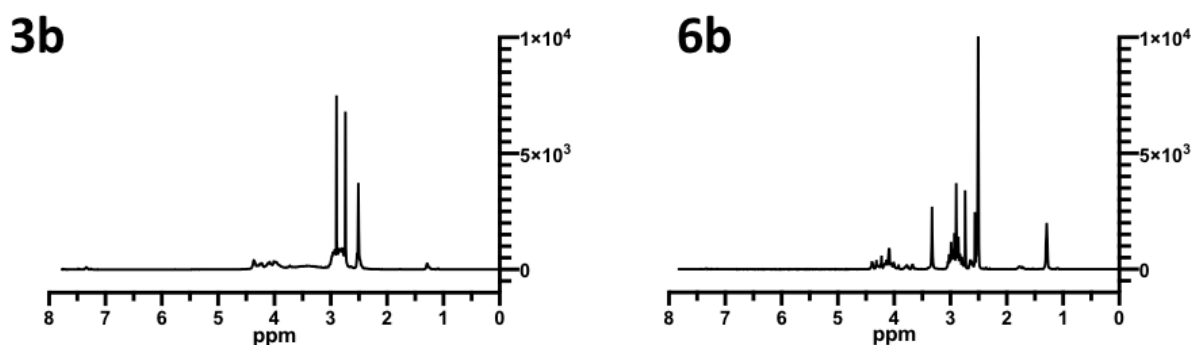


**Figure 5-5.**  $^1\text{H}$  NMR of FTS-pSarc homopolymer and pSarc-*b*-PPS diblock copolymer. NMR spectra of (3b) FTS-pSarc and (6b) pSarc-*b*-PPS are labeled to match the assignments in Scheme 5-3 and Scheme 5-6. Chemical shifts for each of these compounds are listed in the materials section after each synthetic procedure. Large peaks represent excess

reliably around 0.50 and above, filomicelles at 0.38, polymersomes between 0.25 and 0.30, and bicontinuous nanospheres at around 0.12.<sup>96,160,184</sup> PPS lengths were maintained between 20-75 units to ensure retention of oxidation-responsive characteristics that have been validated in prior work for controlled delivery applications (**Figure 1-11**).<sup>22,81,96,180</sup> Previous work from other labs has demonstrated a considerable range in hydrophilic weight fraction of pSarc ( $f_{\text{pSarc}}$ ) for forming the same morphology. A key difference between the polymers generated in this previous work are the hydrophobic blocks which were of different sizes, monomers, and therefore

**Table 5-2. Library of pSarc-*b*-PPS copolymers after FTS-Cys linker-mediated combinatorial pairing.**

	pSarc	MW <sub>pSarc</sub>	PPS	MW <sub>PPS</sub>	f	MW <sub>pSarc-<i>b</i>-PPS</sub>	Mass	Yield
1	60	4381	14	1127	0.80	5508	34.8	64%
2	50	3671	14	1127	0.77	4798	33.5	80%
3	80	5801	25	1941	0.75	7742	40.7	74%
4	80	5801	35	2681	0.68	8482	40.5	61%
5	50	3671	25	1941	0.65	5612	31.9	65%
6	50	3671	35	2681	0.58	6352	34.4	62%
7	80	5801	62	4679	0.55	10480	38.1	43%
8	29	2180	25	1941	0.52	4121	60.1	73%
9	22	1683	25	1941	0.46	3624	41.7	58%
10	29	2180	35	2681	0.45	4861	60.4	62%
11	50	3671	62	4679	0.44	8350	31.9	42%
12	22	1683	35	2681	0.38	4364	40.6	47%
13	29	2180	62	4679	0.31	6859	73.4	53%
14	22	1683	62	4679	0.25	6362	46.7	36%

pSarc: number of pSarc block units; MW<sub>pSarc</sub>: molecular weight of pSarc chain in Da; PPS: number of PPS block units; MW<sub>PPS</sub>: molecular weight of PPS chain in Da; f:  $f_{\text{pSarc}}$ ; mass: weight of product in mg; yield: experimental mass compared to theoretical mass.

hydrophobicity.<sup>94-96</sup> More broadly, these examples suggest that the hydrophilic weight fraction ranges for nanoparticles made with pSarc are highly dependent on the character of the hydrophobic block, emphasizing the importance of mapping the relevant weight fraction range for all new materials. In this way, pSarc coupled with PPS blocks will offer a unique contribution to the understanding of pSarc as a material.

After these considerations, the diblock copolymers of pSarc-*b*-PPS were formed through a one-step thiol disulfide exchange in mild basic conditions (**Scheme 5-6b**). As mentioned previously, the FTS disulfide bridge on the cysteine side chain is susceptible only to thiols on the PPS chains and not to the amines on the terminal end of each pSarc chain. Using a linker without this specificity would introduce the possibility of forming pSarc-(ss-pSarc) chains that could theoretically link end-to-end as exceptionally long homopolymers. Instead, this reaction runs safely overnight to form pSarc-*b*-PPS copolymers in good yields after an ether precipitation to remove any unreacted pSarc.

The library of pSarc-*b*-PPS diblock copolymers formed from this selection of hydrophilic and hydrophobic chain lengths is shown in **Table 5-2** along with the associated physical parameters. The entries in the table are organized from highest to lowest hydrophilic weight fraction in part to demonstrate the vast range of ratios possible from a comparatively small set of individual blocks. Indeed, this list of 14 copolymers shows this extensive coverage from 0.80 to 0.25 without pairing all possible options. Based on the considerations above of previous work with PPS- and pSarc-based copolymers, I decided to narrow in on copolymer chains with

hydrophilic fractions between 0.25 and 0.52 for distinguishing between micellar, vesicular, and potentially worm-like nanostructures (**Figure 1-10c**).

#### 5.4.5 Assembly of pSarc-*b*-PPS copolymers

After forming the diblock copolymers, a critical component of nanocarrier assembly is the method of self-assembly. A given copolymer can form aggregates of varying stability, size, and morphology based on the technique used to introduce them to the final aqueous media. Copolymers of PEG-*b*-PPS have been broadly assembled via thin film rehydration, hot water suspension, cosolvent dispersion, and flash nanoprecipitation.<sup>160,183,184</sup> Within these examples, identical polymers can form separate morphologies from different techniques, while other morphologies have only been shown to form from specific techniques as seen with bicontinuous nanospheres via FNP and filomicelles via TF.<sup>63,73,81</sup> When evaluating a new copolymer system, it is therefore of vital importance to assess particle formation using multiple techniques, as a single approach will offer an incomplete picture. This is especially important if the selected approach is unable to form stable suspensions and the material is prematurely abandoned.

##### Thin film rehydration

For these pSarc-*b*-PPS copolymers, the first assembly technique was thin-film rehydration, a well-understood strategy widely employed for nanoparticle self-assembly. For this technique, the organic components including the polymer itself and any hydrophobic cargo or dyes are solubilized in DCM or another volatile solvent and added to a glass vial (**Figure 5-6a**). The organic solvent is slowly removed via desiccation or rotary evaporation to leave a thin film

on the surface of the glass. The aqueous layer with any hydrophilic cargo or dyes are added to the glass vial and the vessel is agitated overnight. Through this process, the polymer will bud off from the edges of the glass as nanostructures and encapsulate any of the hydrophilic or hydrophobic cargo. For vesicular nanostructures, this technique often results in nanostructures of high polydispersity in size and requires a post-processing step of extrusion or sonication to increase homogeneity.<sup>357,358</sup>

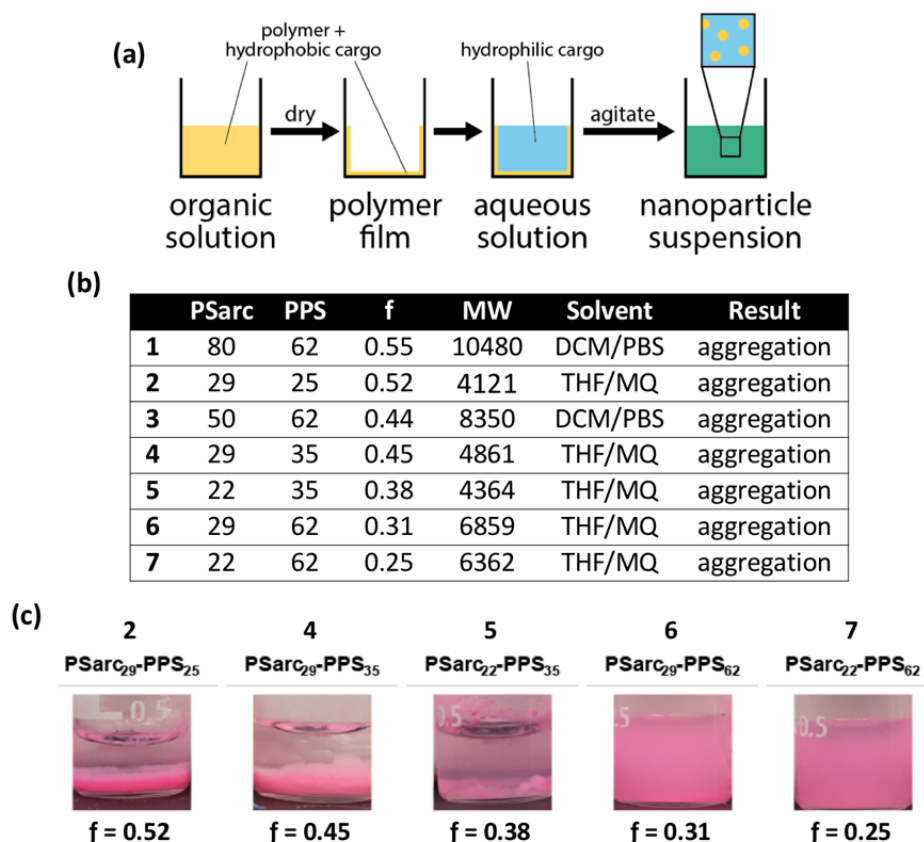


**Figure 5-6. Overview of pSarc-*b*-PPS diblock copolymer assembly via thin-film rehydration.** (a) Schematic of TF rehydration of pSarc-*b*-PPS copolymers highlighting the organic components (yellow), aqueous components (blue), and the final nanoparticle suspension (green). (b) Thin-film assembly conditions and outcomes for seven copolymer entries via DCM/PBS or THF/MQ, arranged by descending hydrophilic weight fraction. (c) Visualization of the aggregation outcomes of five copolymers after attempted TF with the corresponding hydrophilic weight fractions.

The results of the TF assembly of this copolymer are shown in **Figure 5-6b** with each polymer and the hydrophobic dye Dil for visualization. Organic components were solubilized in THF to make the thin film and Milli-Q water was the aqueous solvent for agitation. Unfortunately, all five representative polymers were unable to form stable nanostructures through this method and resulted in extensive aggregation along the sides and bottoms of the vial (**Figure 5-6c**).

### Flash nanoprecipitation

The second approach was assembling via flash nanoprecipitation, a technique recently adapted to use with PEG-*b*-PPS polymer.<sup>160,186</sup> Compared to thin-film rehydration, FNP is a high-energy regime of multiple impingements capable of reaching extremely high Reynolds numbers during turbulent mixing<sup>188</sup> The supersaturation of the polymer triggers nucleation and rapid precipitation to form the aggregate structures. Multiple rounds of impingement mixing can narrow the polydispersity of the nanoparticles samples if necessary before diluting in the aqueous phase to finalize the final supramolecular assembly.<sup>160,186</sup> In FNP, the organic and aqueous phases are loaded into separate syringes and mounted on a block with strictly defined internal dimensions (**Figure 5-7a**). The syringes are impinged into the block and turbulent mixing initiates the nucleation and precipitation of aggregate structures in the supersaturated mixture. These solvent identities and ratios along with the number of impingements and reservoir volume are variables that can prevent or promote stable nanocarrier assembly and should be explored fully in the case of aggregation.

For solvent selection, it is vital that the organic phase is miscible with water to allow for efficient mixing of all components within both phases. THF is typically the solvent of choice for

FNP, but this but this strategy is also amenable to DMF, DMSO, and others.<sup>160,186,359</sup> THF is the preferred organic solvent because of its enhanced solvency for many polymer and cargo components, its non-ideal liquid-vapor equilibria with water, and its higher volatility than water.<sup>360</sup> To the latter point, this means that THF can be removed from the final reservoir in a

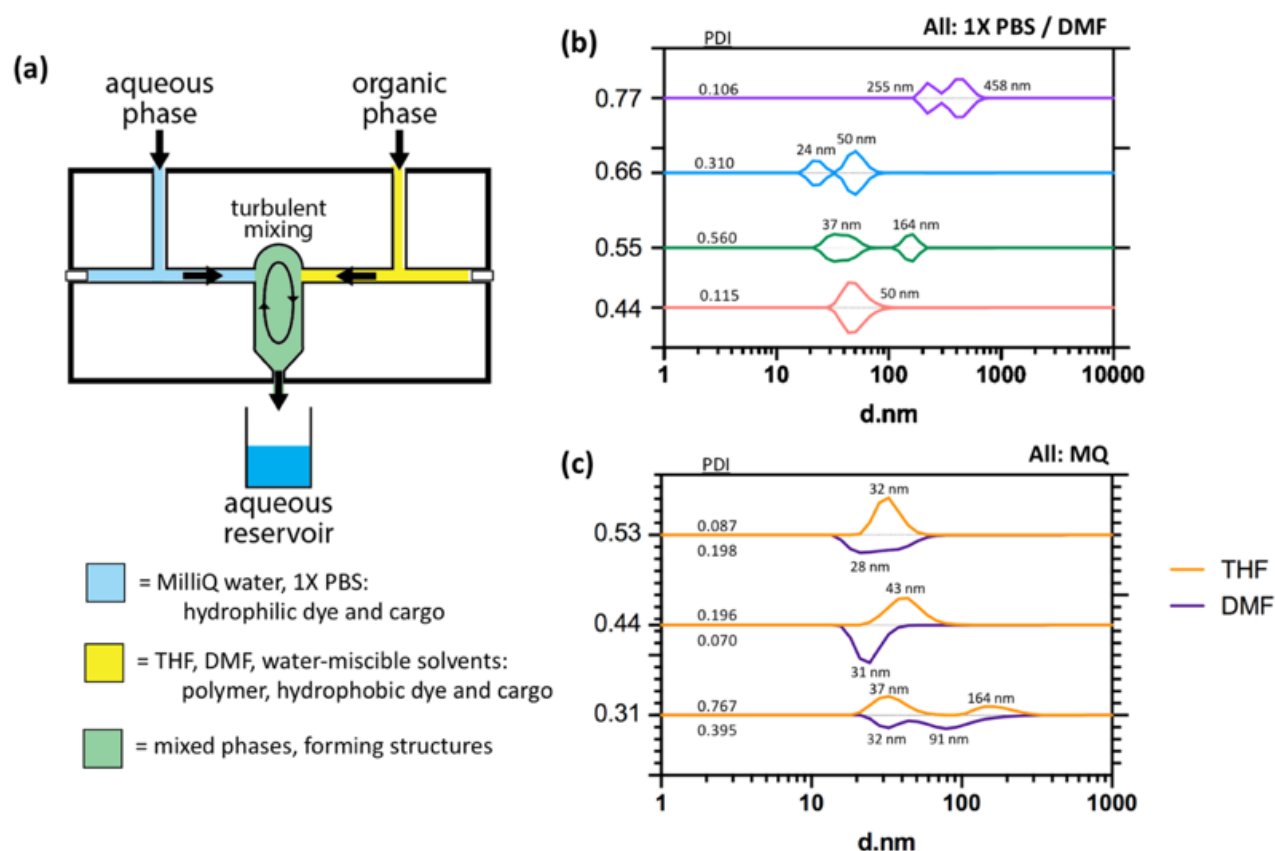


**Figure 5-7. Overview of pSarc-*b*-PPS diblock copolymer assembly via flash nanoprecipitation.** (a) Schematic of flash nanoprecipitation demonstrating the two-phase impingement system of aqueous (blue) and organic (yellow) phases into the mixing chamber (green) and deposit into the aqueous reservoir. (b) DLS results of pSarc-*b*-PPS formulations of weight fraction 0.77, 0.66, 0.55, and 0.44 assembled via FNP with DMF and 1X PBS. Peak diameter is listed next to each major population along with overall sample PDI listed on the right. (c) DLS results of pSarc-*b*-PPS formulations of weight fraction 0.53, 0.44, and 0.31 assembled via FNP in two ways: with MQ and THF (top, orange) or with MQ and DMF (bottom, purple). Peak diameter is listed next to each major population along with overall sample PDI listed on the right.

slow, controlled way through overnight vacuum desiccation, while other solvents require dialysis or lyophilization.<sup>359,361</sup> As for the aqueous solvent, phosphate-buffered saline (PBS) is preferred given the similarity to the biological conditions that the nanoparticle formulations will be introduced into; however, this approach is only possible if the presence of salt does not interfere with the solubility of the cargo.<sup>362</sup> Previous work has also demonstrated that some morphologies form more consistently and homogeneously in different aqueous solutions, including Milli-Q water (MQ)<sup>78</sup>

For these pSarc-*b*-PPS copolymers, I performed FNP on the higher weight fractions using PBS and DMF. Given the longer lengths of the pSarc chains in these polymers, it was difficult to achieve full solubility in the standard THF organic phase so the solvent was switched to DMF. Formulations made with this regime were comprised of pSarc blocks of 50 and 80 units and PPS blocks of 14, 25, and 35 units. The resulting copolymers had hydrophilic weight fractions of 0.77, 0.66, 0.55, and 0.44 in **(Figure 5-7b)**. Unfortunately, they were largely inconsistent and only partially stable in aqueous solutions, further indicated by multiple populations at intermediate diameters and high PDI values **(Figure 5-7c)**. Following these initial trials, Milli-Q water was used as the aqueous phase for all subsequent attempts to reduce aggregation.

The next set of polymer samples were more intermediate weight fractions using pSarc chains of length 29 and PPS chains of lengths 25, 35, and 62. For these, I first used Milli-Q water for the aqueous phase and DMF for the organic phase, assuming similar solubility issues with the previous batch. These formulations are shown in **Figure 5-7c** as more monodisperse populations for the higher weight fractions of 0.52 and 0.44 and a mixed population for 0.31. A second

attempt at FNP assembly was conducted with Milli-Q water and THF after confirming that the shorter pSarc lengths are more soluble in this organic solvent. The size distribution for FNP assembly of these copolymers via both DMF/MQ and THF/MQ solvent systems are shown in Figure 5-7c as asymmetric violin plots. Both of these approaches produced stable nanoparticle suspensions in aqueous media and were very promising for pSarc-*b*-PPS as a novel self-assembling material.

Moving forward, FNP with a MQ/THF solvent system was selected for the final formulations based on the previously discussed considerations for both phases and the comparison between the different systems. Based on these initial rounds, five representative polymers were selected for further refinement of assembly conditions. For these polymers, the hydrophilic fraction range most likely to form micelles and vesicles is between 0.52 and 0.25. A full characterization comprised of three orthogonal techniques was performed on all five formulations to fully elucidate the nanoparticle populations contained within the samples.

#### 5.4.6 Characterization of pSarc-*b*-PPS copolymers

The first characterization technique has been discussed briefly for the initial screen of pSarc-*b*-PPS copolymers as dynamic light scattering (DLS) which shows the distribution of particle sizes within a sample. The results of this technique are listed in **Table 5-3** and displayed in **Figure 5-8** for each of the five formulations. Overall, two patterns emerge across the formulations. First, all five samples have a smaller diameter peak between 32 and 43 nm which might represent a more compact micelle morphology with a hydrophobic core. Second, the lower weight fractions

**Table 5-3. Optimization and characterization of pSarc-*b*-PPS formulations assembled via FNP.**

	pSarc	PPS	f	MW	Solvent	d.nm	PDI	EE	Dil
1	50	14	0.77	4798	PBS/DMF	365	0.106	yes	yes
2	50	25	0.66	5612	PBS/DMF	42.9	0.310	yes	yes
3	80	62	0.55	10480	PBS/DMF	78.7	0.560	yes	yes
4	29	25	0.52	4121	MQ/THF	33.5	0.087	---	yes
5	29	25	0.52	4121	MQ/DMF	30.5	0.198	---	yes
6	22	25	0.46	3624	MQ/THF	276	0.225	---	yes
7	50	62	0.44	8350	PBS/DMF	51.7	0.115	yes	yes
8	29	35	0.45	4861	MQ/THF	44.7	0.196	---	yes
9	29	35	0.45	4861	MQ/DMF	24.7	0.070	---	yes
10	22	35	0.38	4364	MQ/THF	85.9	0.492	---	yes
11	29	62	0.31	6859	MQ/THF	80.9	0.767	---	yes
12	29	62	0.31	6859	MQ/DMF	74.5	0.395	---	yes
13	22	62	0.25	6362	MQ/THF	60.8	0.432	---	yes

pSarc: number of pSarc block units; PPS: number of PPS block units; f:  $f_{\text{pSarc}}$ ; MW: molecular weight of pSarc-*b*-PPS copolymers in Da; solvent: aqueous and organic phases used for FNP; d.nm: diameter of pSarc-*b*-PPS formulations in nm via DLS; PDI: polydispersity index of pSarc-*b*-PPS formulations via DLS; EE: loading of ethyl eosin; Dil: loading of Dil.

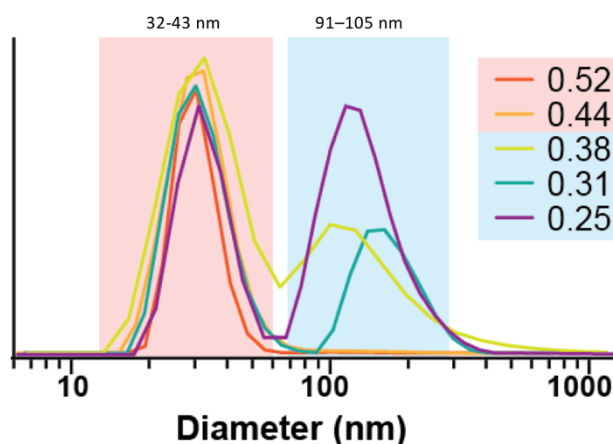


**Figure 5-8. DLS results for optimized pSarc-*b*-PPS formulations.** pSarc-*b*-PPS formulations of all  $f_{\text{pSarc}}$  had a population from 32 to 43 nanometers, similar to the expected range for micelles (red). pSarc-*b*-PPS formulations of lower  $f_{\text{pSarc}}$  at 0.38, 0.31, and 0.25 had an additional population at 91 to 105 nm, similar to the expected range for vesicles (blue).

of 0.38, 0.31, and 0.25 have an additional second peak between 91 and 105 nm which has the potential to represent a second morphology within the sample.

The number-weighted DLS metrics associated with these traces are calculated as diameter, PDI, major population peaks, and zeta potential. The hydrodynamic diameters match closely to the peaks seen on the spectra along with the major peaks in the sample. The PDI for the higher weight fractions of 0.52 and 0.44 are low at 0.087 and 0.196 respectively, representing a tight distribution of nanoparticles with very similar diameters. PDI values below 0.300 are considered high-quality, homogenous formulations.<sup>186,359,363</sup> The PDI for the remaining three weight fractions of 0.38, 0.31, and 0.25 are much higher at 0.432, 0.767, and 0.492, as they numerically describe samples with two distinct populations. It is important to pair the calculated values with the peak traces directly, as the concept of polydispersity can be defined in distinct ways. While the PDI for these samples is high given multiple nanoparticle populations, the shape of the peaks seen in the traces are good quality when assessed individually. In other words, formulations containing multiple formulations have high PDI values even if each population is itself relatively homogeneous. Additionally, each formulation was measured for zeta potential which is a metric of surface charge. All formulations had a slightly negative zeta potential which is ideal for resisting aggregation and maintaining stability in complex *in vivo* environments.

The next analysis of these formulations was negative stain transmission electron microscopy (nsTEM). Compared to the population-level assessment of nanoparticle diameter in DLS, nsTEM offers the ability to directly visualize individual nanostructures. This is an indispensable tool for understanding the physical characteristics of multiple or unknown

morphologies in a sample. Representative micrographs of the pSarc-*b*-PPS formulations are shown in **Figure 5-9**. The initial assessment of each formulation can begin with matching diameters of the populations seen in DLS for each sample: a smaller one at 32 to 43 nm for all formulations and a larger one from 91 to 105 nm for the 0.38, 0.31, and 0.25 formulations. Each of the major peaks in DLS are indeed accounted for in the nsTEM micrographs, indicating agreement between two entirely orthogonal techniques.

Further analysis of the nsTEM results can be divided into two sections based on visual clues for each potential morphology. The internal architecture of different morphologies will respond in distinct ways to the grid preparation process that tends to desiccate the samples and cause the negative stain dye to pool in unique ways. First, a micellar morphology has a

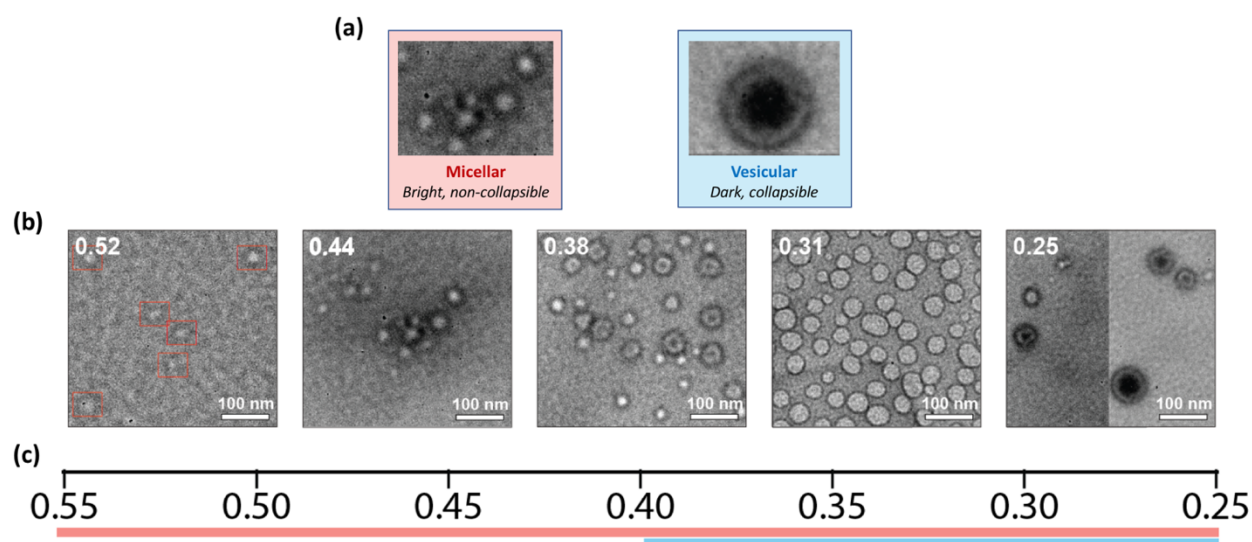


**Figure 5-9. Negative stain TEM of pSarc-*b*-PPS formulations.** Representative examples of non-collapsible micelle-like morphologies (red) and collapsible vesicular-like morphologies (blue) are shown in (a). Micrographs of each pSarc-*b*-PPS formulation are shown in (b) in order of descending hydrophilic weight fraction with the below scale (c) marking which morphologies were identified at each range, micellar (red) and vesicular (blue).

hydrophobic core made entirely of the hydrophobic polymer chains. Along with being too compact to change shape as freely, they also do not respond significantly to desiccation that would remove water from the structure, as there is no water in the micelle interior. As a result, the negative stain pools around the outside edge of a sphere with a bright non-compressible center (**Figure 5-9a**, left). Conversely, vesicles are much larger structures with a bilayer membrane protecting an aqueous core. These structures respond to the desiccation process that tends to shrink and collapse their cores, creating a bowl shape that can pool negative stain (**Figure 5-9a**, right). In addition to the negative stain outlining the edges of the sphere, vesicles can appear as compressible structures with a dark center filled with negative stain that indicates an aqueous core.

Taking this into account, all five formulations contained examples of the small non-compressible centers with bright white cores that fell within the 32 to 43 nm diameter range seen in DLS. These are highly suggestive of micelles. For the lower weight fraction samples, there are additional structures with larger diameters and dark, dye-pooling centers representing compressible cores, which is highly suggestive of a vesicular morphology as polymersomes. Overall, these two analytical techniques suggest the presence of micellar spheres in all five formulations along with a potentially vesicular morphology in the lower hydrophilic weight fractions, as summarized in **Figure 5-9c**.

The third technique is small-angle x-ray scattering (SAXS) which is an extremely powerful tool to elucidate the internal architecture of a nanoparticle suspension. The scattering pattern of the beamline passing through the sample can be compared to core-shell and vesicle models to

provide strong morphological evidence on a population level. That is, the scattering will tend to conform to the majority structure in the sample. For these formulations, calculated radii match what is expected from both DLS and nsTEM for all samples (**Table 5-4**). The scattering pattern for the higher weight fractions of 0.52, 0.44, and 0.38 conform to the core-shell sphere model which is indicative of micelles (**Figure 5-10a**). In this case, the SAXS modeling for 0.38 adds substantial clarity to a sample with two unresolved populations on DLS and the presence of less orthodox soft structures on nsTEM. Here, SAXS modeling clarified this morphological ambiguity, with a good fit between the obtained scattering profile and a spherical vesicle model. For the remaining lower weight fraction formulations of 0.31 and 0.25, the scattering profile conforms to the vesicle

**Table 5-4. Characterization of pSarc-*b*-PPS formulations via DLS, nsTEM, and SAXS.**

	<i>f</i>	$M_n^a$	DLS/ELS			$d_{peak}^b$	TEM	SAXS <sup>d</sup>		
			<i>d</i>	<i>PDI</i>	<i>ZP</i>			<i>ID</i> <sup>c</sup>	$r_{core}$	$r_{shell}$
PSarc <sub>29</sub> - <i>b</i> -PPS <sub>25</sub>	0.52	3909	33.5	0.087	-8.37	32	MC	14.9	5.1	cs
PSarc <sub>29</sub> - <i>b</i> -PPS <sub>35</sub>	0.44	4649	44.7	0.196	-8.34	43	MC	19.4	4.5	cs
PSarc <sub>22</sub> - <i>b</i> -PPS <sub>35</sub>	0.38	4125	60.8	0.432	-6.90	37	MC	17.9	6.8	cs
						91	PS	---	---	---
PSarc <sub>29</sub> - <i>b</i> -PPS <sub>62</sub>	0.31	6647	80.9	0.767	-3.82	37	MC	---	---	---
						105	PS	54.9	7.5	v
PSarc <sub>22</sub> - <i>b</i> -PPS <sub>62</sub>	0.25	6150	85.9	0.492	-7.48	32	MC	---	---	---
						105	PS	55.1	8.2	v

<sup>a</sup> $M_n$  calculated by <sup>1</sup>H-NMR. <sup>b</sup> $d_{peak}$  is the diameter (*d*) of detected population peak(s) ( $d_{peak}$ , nm). <sup>c</sup>Micelle (MC) or Polymersome (PS) identification by TEM. <sup>d</sup>SAXS scattering (majority population);  $\chi^2$  denotes best fit model (cs, core-shell; v, vesicle). Labels: diameter (*d*, nm); polydispersity index (*PDI*); zeta potential (*ZP*, mV); core radius ( $r_{core}$ , nm); shell radius ( $r_{shell}$ , nm).

model which is indicative of polymersomes (**Figure 5-10b**). For each of these modeling calculations, the overall measure of fit of  $\chi^2$  being less than 1 is a good indicator of conformation to that model.

Together, these orthogonal analyses converge on a cohesive morphological description of the pSarc-*b*-PPS copolymer samples (**Figure 5-11**). Prototype polymer formulations with a  $f_{\text{pSarc}}$  above 0.38 resulted in a single monodisperse population of micelles, while formulations with a  $f_{\text{pSarc}}$  below 0.38 result in a second majority population of polymersomes. The polymers of  $f_{\text{pSarc}} = 0.38$  appeared to exist at the border of the two morphologies, as the DLS and nsTEM profiles matched those of the polymersome samples, but the SAXS scattering profile best fit the core-shell model of the micelle samples. Overall, this work highlights the innate differences across the

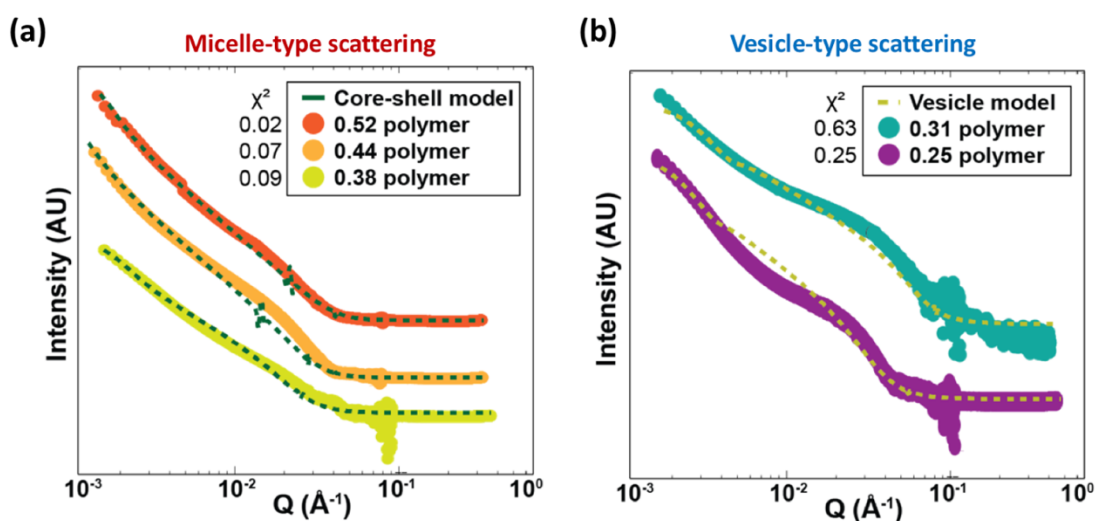


**Figure 5-10. SAXS scattering and model fits for pSarc-*b*-PPS formulations.** (a) Higher weight fraction formulations are shown with the core-shell micelle model while (b) lower weight fraction formulations are shown with the vesicle model. For each formulation, the  $\chi^2$  statistic as a measure of fit to the model is shown next to each legend entry with a value  $< 1$  considered a good match.

analytical methods as DLS and SAXS average across the population, while the visualization of nsTEM is able to focus on the distinct morphological characteristics of even minor subpopulations. These nanostructures were also able to encapsulate the hydrophobic dyes ethyl eosin and DiI, which confirms the presence of a defined hydrophobic space to stably retain the cargo (**Table 5-3**).

The final investigation of these pSarc-*b*-PPS nanoparticles is ensuring low cytotoxicity. Regardless of the morphologies, stability, and loading, if the nanomaterial is not compatible with cell viability, the material cannot be used for biomedical applications. All five pSarc-*b*-PPS formulations were applied to murine-derived macrophages at a range of concentrations with

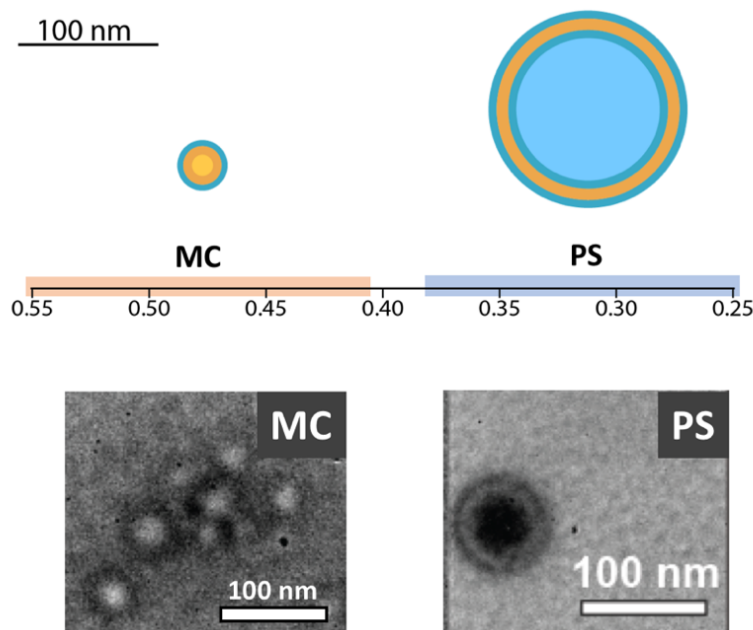
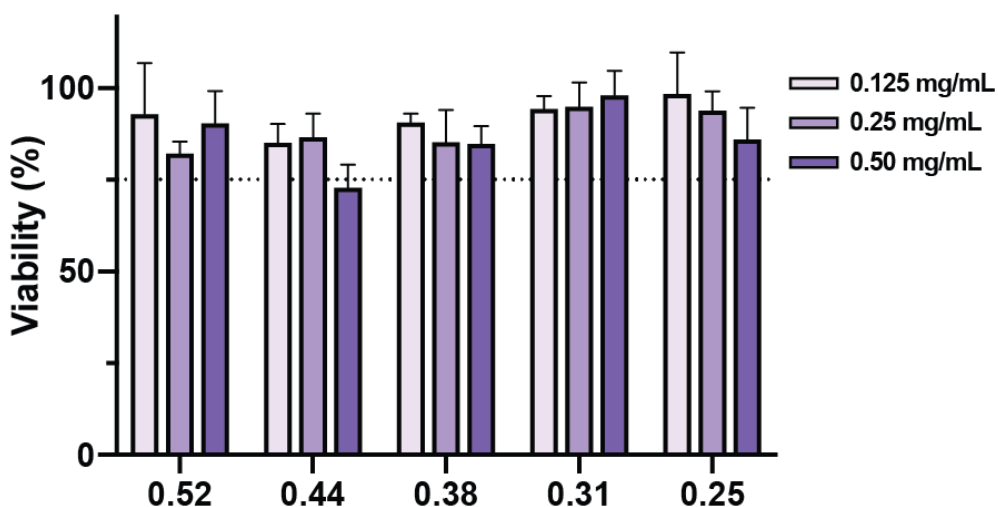


**Figure 5-11. Schematic of pSarc-*b*-PPS micelle and vesicle morphology ranges on the scale of hydrophilic weight fraction.** The orthogonal analyses of DLS, nsTEM, and SAXS provide strong evidence that pSarc-*b*-PPS of weight fractions between 0.25 and 0.35 form polymersome vesicles (PS) while weight fractions between 0.38 and 0.55 form micelles (MS). Representative nsTEM images of both morphologies are shown below.

minimal cytotoxicity (**Figure 5-12**). The lack of toxicity in this phagocytic cell line that is capable of extensive nanoparticle endocytosis is encouraging for biomedical applications of these nanoparticles as micelles and vesicles. Overall, the success of these pSarc-*b*-PPS nanostructures as prototype drug delivery vehicles is exceedingly promising and warrants much deeper investigations to develop their use with more functionalized NCA backbones.

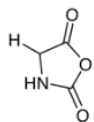
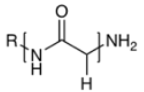
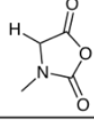
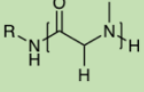
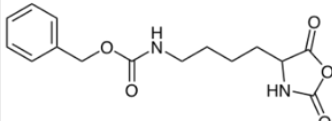
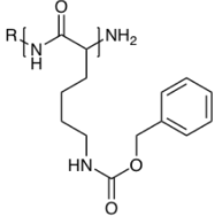
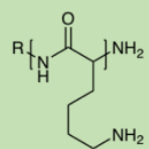
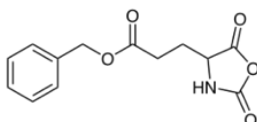
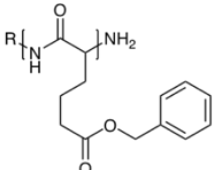
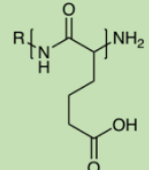
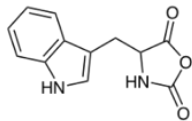
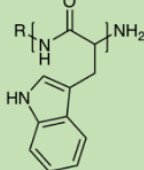
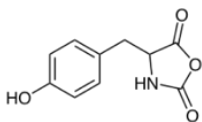
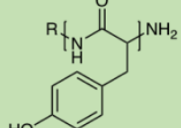
#### 5.4.7 Synthesis of NCA monomers for expanded PAA-*b*-PPS backbones

The next step for the development of this novel PAA-*b*-PPS nanoparticle system is expanding the backbone beyond that of the pilot pSarc. Sarcosine was selected as a unit with a simple structure to minimize side-chain complexities that would otherwise make it difficult to generalize the results of pSarc-*b*-PPS to other PAA chains. Here, I explore a number of amino



**Figure 5-12. Cytotoxicity of representative pSarc-*b*-PPS formulations.** Polymer concentrations of 0.125, 0.25, and 0.50 mg/mL were added to RAW 264.7 cells and assessed for viability. The dotted line marks 75% viability as a reasonable minimum for a non-toxic result, which was largely achieved by all formulations at all concentrations.

acids with high potential for chemical or biological functionalities to incorporate into the structural component of the nanoparticle. The monomers and derivatives synthesized are shown in **Figure 5-13**.

	NCA (1)		Polymer (3)		Deprotect (4)	
<b>Glycine</b> (a)		Y		Y	N/A	
<b>Sarcosine</b> (b)		Y		Y	N/A	
<b>Lysine(Z)</b> (c)		Y		Y		Y
<b>Bz Glutamic Acid</b> (d)		Y		Y		Y
<b>Tryptophan</b> (e)		Y		Y	N/A	
<b>Tyrosine</b> (f)				Y	N/A	

**Figure 5-13. Structures of amino acid monomers and polymers synthesized for this chapter.** Each compound is assigned a letter (a – h) and can be identified throughout figures and schemes as (1) for NCA monomers, (3) for polymers, and (4) for deprotected polymers as applicable. Green color PAA polymers were paired with PPS as pilot or expanded backbones for novel PAA-*b*-PPS materials.

## Lysine

Lysine (Lys) was one of the first functionalized amino acids worth exploring for incorporation into a mixed PAA chain as its side chain is both a cation at physiologic pH and an amine moiety with significant chemical modification potential. The nucleophilic amine of Lys is utilized nearly ubiquitously in classical protein modifications including amide formation with activated esters, sulfonamides with sulfonyl chlorides, reductive amination with aldehydes, and urea with isocyanates formation.<sup>364,365</sup> In addition, the long side chain length of Lys plays a critical role in the energetics of conformation-dependent stabilizing interactions that can be employed within a mixed PAA copolymer with those applications.<sup>366</sup>

Preparation of Lys for NCA cyclization required an initial protection of the side-chain amine to prevent side reactions with phosgene to make larger rings or polymerize any formed monomers within the flask. Of the several available commercial preparations of  $\epsilon$ -protected Lys, I selected N<sub>6</sub>-Carbobenzyloxy-L-lysine (LysZ) as the Z protection on the amine side chain is stable to both NCA cyclization and polymerization reactions and can be deprotected in acidic conditions with hydrogen bromide and trifluoroacetic acid.<sup>327</sup> The NCA preparation of LysZ proceeded smoothly with this side-chain protection using the same protocol of phosgene in THF at 55°C (**Scheme 5-1c**).

The polymerization of LysZ NCA was accomplished in the same manner with a primary amine over several days (**Scheme 5-3c, Figure 5-14.3c**). Precipitation of the formed poly(LysZ) (pLysZ) was based on the solubility parameters of the protected side chains with bulky Z groups. NMR analysis was used to calculate the average chain length before deprotecting the side chain

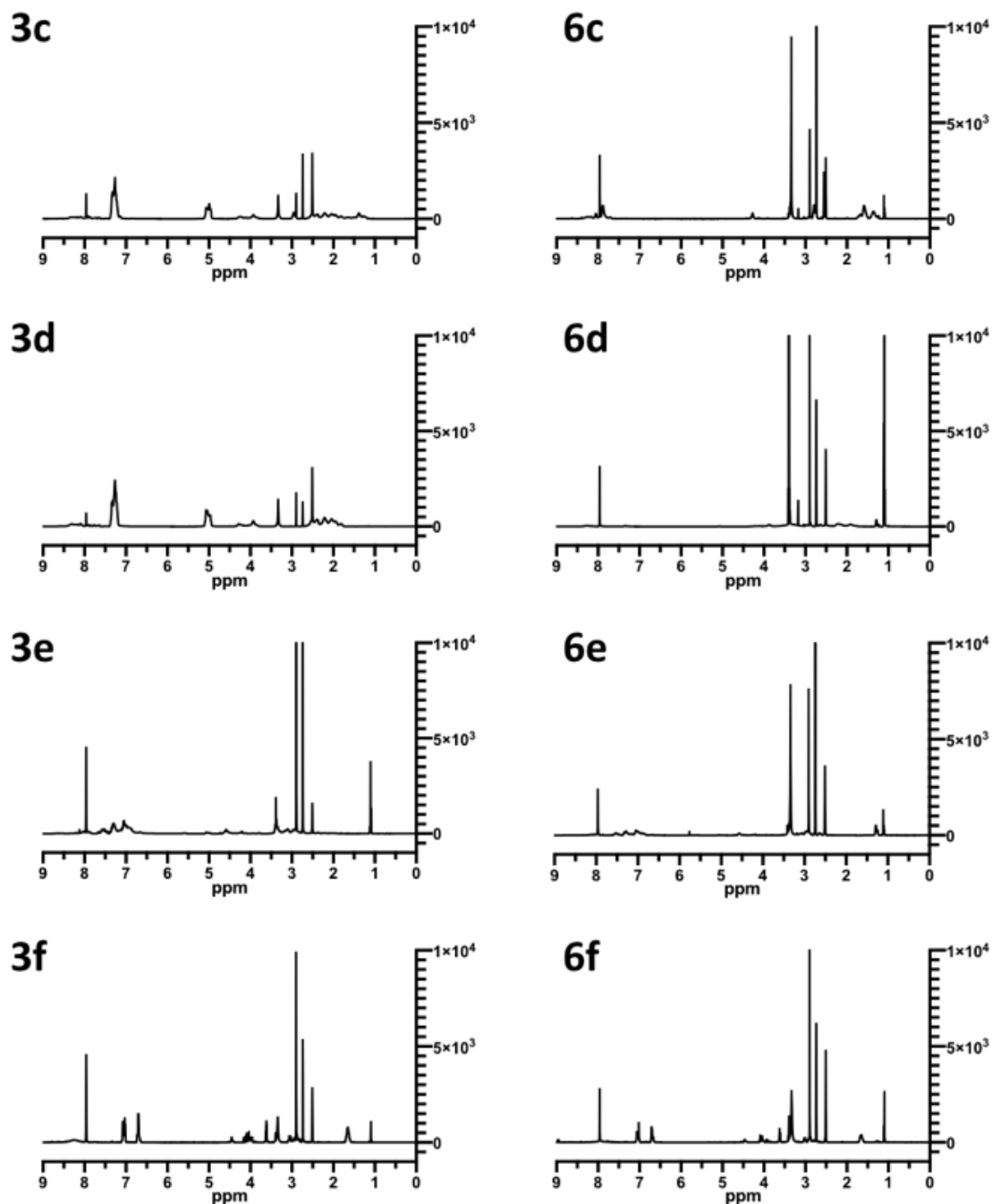


**Figure 5-14.**  $^1\text{H}$  NMR of FTS-PAA expanded chains of pLysZ, pBzGlu, pTrp, and pTyr. Spectra of (3c) FTS-pLysZ, (3d) FTS-pBzGlu, (3e) FTS-pTrp, (3f) FTS-pTyr, and PAA-*b*-PPS chains (6c) pLys-*b*-PPS, (6d) pGlu-*b*-PPS, (6e) pTrp-*b*-PPS, (6f) pTyr-*b*-PPS are labeled to match the assignments in Scheme 5-3 and Scheme 5-6. Chemical shifts for each of these compounds are listed in the materials section after each synthetic procedure. Large peaks represent excess solvent in the DMSO- $d_6$  environment as DMF (7.95 ppm, 2.90 ppm, and 2.73 ppm), DMSO (2.50 ppm), water (3.33 ppm), and diethyl ether (3.38 ppm and 1.09 ppm).

amine groups. With slight modifications to previously published work, protected pLysZ was solubilized in TFA and subjected to 33% HBr in acetic acid in slight excess over gentle heating to 30°C until the reaction mixture turned cloudy, about 30 minutes, indicating a shift in solubility as the Z group is removed (**Scheme 5-4c**).<sup>367</sup> The deprotected poly(Lys) (pLys) polymer was analyzed one final time via NMR to quantify the completeness of protection group removal based on the disappearance of its associated peaks. The pLys was fully deprotected under these acidic conditions after a short reaction length without noticeable chain cleavage. The straightforward and successful synthesis of pLys through the employment of a Z protecting group makes this a worthy cationic addition to the growing NCA/PAA library.

#### *Glutamic acid*

In addition to the cationic Lys for mixed PAA chains, glutamic acid (Glu) is an amino acid with a carboxylic acid side chain that is anionic at physiological pH. Similar to Lys, the functional utility of the carboxylic acid as a versatile reactive group makes its protection vital to successful NCA cyclization and reduction of side products. Of the commercial options, I settled on using L-glutamic acid  $\gamma$ -benzyl ester (BzGlu) as a simple benzyl protection of the side chain carboxylic acid. As with previous methods, the BzGlu starting material was cyclized in the presence of phosgene in THF at 55°C over several hours, resulting in a clear solution of BzGlu NCA monomer (**Scheme 5-1d**).<sup>327</sup>

As with the Z-group protection of Lys, BzGlu was effectively maintained throughout the polymerization to poly(BzGlu) (pBzGlu) with the addition of a primary amine (**Scheme 5-3d**, **Figure 5-14.3d**). Similar still is the bulky, hydrophobic protecting group that alters the workup

conditions compared to the final unprotected polymer properties. NMR was used to calculate the average chain length after purification. With the same slight modifications to previous protocols, the Bz protection was removed efficiently under the same acidic conditions with TFA and 33% hydrogen bromide in acetic acid under gentle heating (**Scheme 5-4d**).<sup>368</sup> The same conditions for deprotection of both the pLysZ and pBzGlu makes it especially convenient for copolymers with both cationic and anionic requirements to be prepared in a single step.<sup>369</sup> This type of zwitterion could have strong potential for imparting a stealth character by reducing protein adsorption upon exposure to biological fluids.<sup>104</sup>

### *Tryptophan*

Tryptophan (Trp) was another interesting amino acid to attempt NCA formation and polymerization with as it has a measurable level of intrinsic fluorescence. Along with tyrosine and phenylalanine, the aromatic properties of tryptophan give it a fluorescence-excitation spectrum in the UV range (280/346 nm) that can be useful for tracking and quantifying nanomaterials during preparation.<sup>370</sup> In this way, Trp is an example of an amino acid monomer that can be broadly added to many types of mixed PAA chains to impart a functionality that improves the development and quality of a material without any additional synthetic strategies. That is, the Trp NCA monomer can simply be added into the mixture of monomers that comprise the rest of the PAA chain.

As with the previous NCA monomers, the most disruptive size chains that require protection before cyclization with phosgene are nucleophiles. While Trp has an available nitrogen in its side chain, the delocalization of its electron pair into the rest of the indole ring makes it an

extremely weak nucleophile and likely unable to interfere with the forming NCA monomers in solution.<sup>371</sup> For this reason, the synthesis of Trp NCA was conducted on the standard amino acid as a starting material without protection. The monomer was formed as the others and in previously reported work, with phosgene in THF heated to 55°C until the reaction mixture became clear (**Scheme 5-1e**).<sup>328</sup> While not as common in the literature for pure poly(Trp) (pTrp),<sup>372</sup> this polymer was synthesized through initiation via a small molecule primary amine under mild conditions (**Scheme 5-3e**).<sup>373</sup> NMR analysis was used to calculate the average chain length of the pTrp polymers (**Figure 5-14.3e**).

In addition to the synthesis of pTrp homopolymer, the intrinsic fluorescence of this amino acid made it useful to immediately test as a minor component of a non-fluorescent PAA chain. I hypothesized that one to two equivalents of Trp NCA added to a polymerizing reaction of BzGlu NCA or pSarc NCA would be a sufficient fluorescent signal to track and quantify the copolymers. The resulting pSarc and pBzGlu chains with and without randomly inserted Trp residues were analyzed with UV-Vis spectroscopy at 280/350 nm (**Figure 5-15**). From these results, it seems that only a handful of Trp residues in a longer PAA chain are able to significantly enhance fluorescence of the material without major changes to the physiochemical properties of the chain. Using Trp as an example, this strategy of random copolymerization for functional residues that are not dependent on a specific sequence will be immensely useful for this type of PAA material.

### *Tyrosine*

Tyrosine (Tyr) is an aromatic polar amino acid known as a precursor to the catecholamines that can influence the synthesis of epinephrine and norepinephrine in the brain.<sup>374</sup> The ability of

the aromatic side chains to  $\pi$ - $\pi$  stack can be utilized to stabilize a structure,<sup>374</sup> modify NP self-assembly,<sup>375</sup> or associate more closely with aromatic cargo.<sup>376</sup> Additionally, tyrosine homopolymers have been found to be versatile materials for assembling hydrogels and aggregates with unique supramolecular arrangements.<sup>329,377-379</sup> These examples make tyrosine an interesting NCA monomer for this library in both short and longer stretches of this residue.

For protecting group considerations, the Tyr phenolate is an oxygen-containing ionizable side chain with a number of resonance states that is susceptible to both nucleophilic and electrophilic attacks.<sup>380</sup> Many protocols for the cyclization to Tyr NCA begin with the O-protected Tyr with benzyl or t-butyl groups to prevent any nucleophilic side reactions.<sup>328,381,382</sup> However, compared to nitrogen-containing side chains and given the  $pK_a$  of the tyrosine phenolate around 10.1, the side chain of this residue should remain protonated and weakly nucleophilic in all

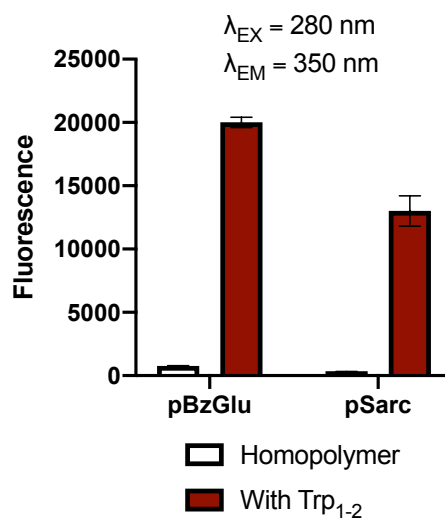


**Figure 5-15. Fluorescence of pBzGlu and pSarc polymers with and without Trp.** All samples were evaluated via UV-Vis at an excitation wavelength of 280 nm and emission wavelength of 350 nm to show a clear impact of one to two Trp units on the fluorescence of PAA chains.

reaction conditions for cyclization and polymerization.<sup>383</sup> For this reason, Tyr NCA was formed from the standard Tyr amino acid as supported by previous work.<sup>329,379</sup> As before, Tyr was cyclized in the presence of phosgene in THF at 55°C to Tyr NCA (**Scheme 5-1f**). Polymerization of Tyr NCA to poly(Tyr) (pTyr) was accomplished after initiation by a small molecule primary amine as shown in **Scheme 5-3f**.<sup>377,378</sup>

#### 5.4.8 Synthesis, assembly, and characterization of expanded PAA-*b*-PPS backbones

Each of these successfully polymerized chains of Tyr, Trp, Glu, and Lys were initiated with the same FTS-Cys linker as the previous pSarc-*b*-PPS copolymers (**Scheme 5-3d-f**). With this chemistry, the same combinatorial strategy is possible for a wide range of PAA-*b*-PPS polymers. FTS-homopolymers of these four amino acid NCAs were made to be paired with PPS<sub>27</sub> to form diblock copolymers with a hydrophilic weight fraction between 0.61 to 0.67 (**Scheme 5-6d-f**, **Figure 5-16a**) as a likely range for simple micellar structures. The PAA homopolymers were taken through the same pairing via thiol exchange with the PPS block to form the copolymers pTrp<sub>23</sub>-*b*-PPS<sub>27</sub>, pTyr<sub>26</sub>-*b*-PPS<sub>27</sub>, pGlu<sub>26</sub>-*b*-PPS<sub>27</sub>, and pLys<sub>27</sub>-*b*-PPS<sub>27</sub>.

The four copolymers were assembled via the same FNP method in MQ/THF with the hydrophobic Dil as for pSarc-*b*-PPS (**Figure 5-16b**). From these images, all four formulations are stable in aqueous conditions but have varying levels of turbidity. As seen in PEG-*b*-PPS and pSarc-*b*-PPS formulations, this cloudiness often indicates particle sizes as being large enough to interfere with light passing cleanly through the sample. In these copolymer systems, micelles with diameters around 20 nm are small enough to remain clear solutions while filomicelles that

have a similar diameter as micelles, but a length of several microns, are translucent. For larger particles, polymersomes at 70 to 120 nm appear cloudy and BCNs at 200 to 400 nm are nearly opaque solutions of a consistency similar to milk. Additionally, mixes of different morphologies often appear as cloudy in solution. Each of these are distinct from aggregates as unstable clumps of polymer that often stick to the walls or bottom of the vial.

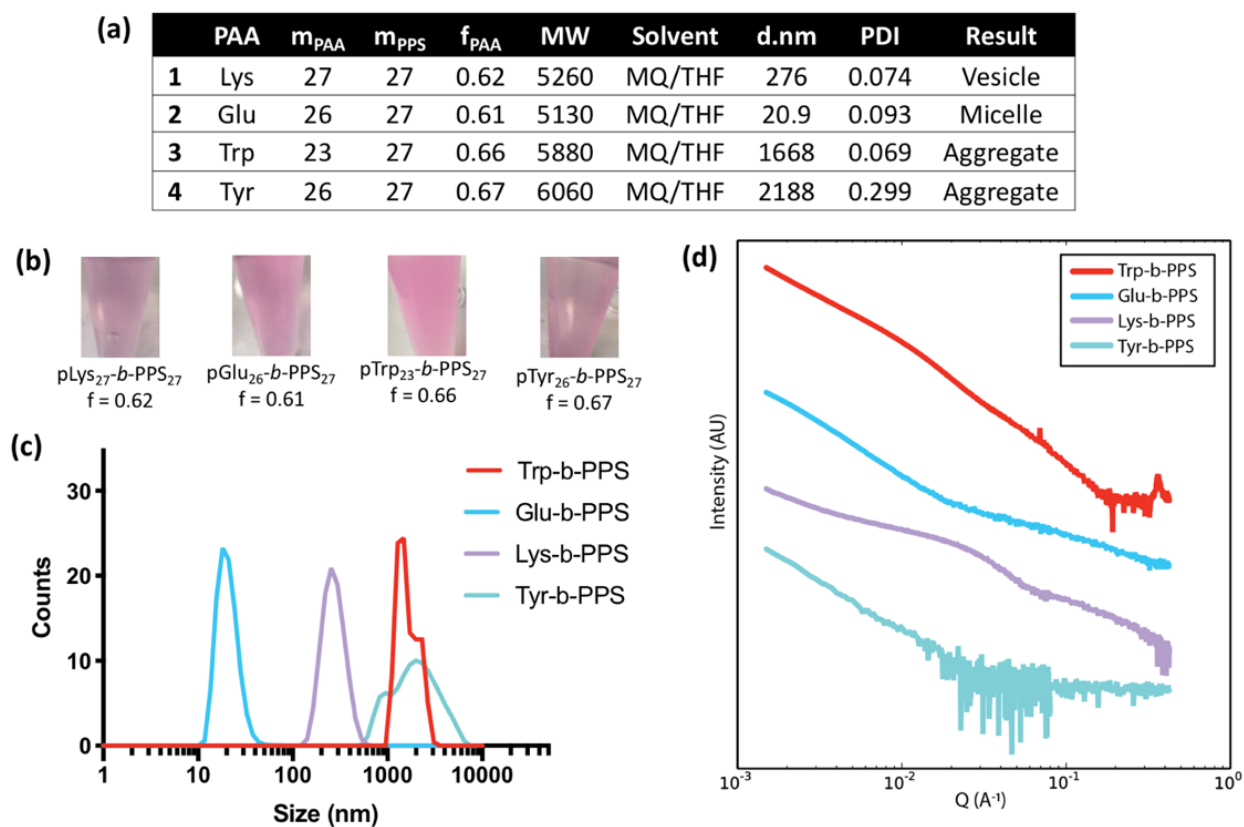


**Figure 5-16. Synthesis and assembly of expanded PAA-*b*-PPS copolymer backbones.** (a) Table of copolymer properties and FNP assembly solvents for Lys, Glu, Trp, and Tyr backbones. (b) Visualizations of nanostructures assembled via FNP and suspended in the aqueous reservoir. (c) DLS traces for pTrp-*b*-PPS (red), pGlu-*b*-PPS (blue), pLys-*b*-PPS (purple), and pTyr-*b*-PPS (green) formulations. Values for peak diameters and PDI are listed in table (a). (d) SAXS traces for pTrp-*b*-PPS (red), pGlu-*b*-PPS (blue), pLys-*b*-PPS (purple), and pTyr-*b*-PPS (green) formulations.

Of the four samples, pTrp-*b*-PPS and pTyr-*b*-PPS appear the cloudiest while pLys-*b*-PPS is more translucent, and pGlu-*b*-PPS is the clearest. Despite these visual clues, the only conclusion without deeper characterization is that the formulations are not immediately unstable. Analysis on these formulations was conducted with DLS for diameter and polydispersity along with SAXS for internal architecture. These traces are shown in **Figure 5-16c** and the diameter and PDI values are listed in **Figure 5-16a**.

The four PAA-*b*-PPS copolymers all formed particles measurable by DLS. The pGlu-*b*-PPS particles were the smallest diameter at 20.9 nm with a very good PDI of 0.093. This initial analysis shows a very uniform, monodisperse population of nanoparticles that are within the expected range for micelles. pLys-*b*-PPS particles had a diameter of 276 nm with an excellent PDI of 0.074. This formulation is much larger than what is expected for micelles and larger than the vesicles that would be expected from PEG-*b*-PPS which are around 70 to 120 nm and from pSarc-*b*-PPS which were near 91 to 108 nm. However, it should be noted that much larger polymer vesicles tens of microns in diameter have been made from other materials and assembly techniques, making this a potential outcome for pLys-*b*-PPS nanostructures.<sup>384</sup> Additionally, these DLS results show a high level of monodispersity that suggests a uniform, stable morphology from the cationic copolymer.

The two remaining formulations had less clear DLS readings through this assembly method. For pTyr-*b*-PPS, the diameter shifted significantly higher to 2188 nm with an acceptable PDI of 0.299. Along with being technically outside of the nanoparticle range, this formulation shows two overlapping large peaks which collectively suggest an aggregation of these particles

in solution. For pTrp-*b*-PPS, the diameter is again shifted higher to 1688 nm with an excellent PDI of 0.069. Similarly to pTyr-*b*-PPS, these structures are not within the nanoparticle range and the peak shape suggests an unstable or aggregated assembly. The low PDIs for these last two formulations with pTyr and pTrp can be explained by the derivation of PDI as  $\left(\frac{\sigma}{d}\right)^2$  where higher diameters (*d*) can tolerate higher standard deviations ( $\sigma$ ) as they scale within this fraction. For this reason, it is essential to incorporate the results of other analytical techniques to get a clear picture of these formulations.

SAXS scattering was also collected for these four samples and is shown in **Figure 5-16d**. For pGlu-*b*-PPS particles, the scattering shape is similar to what would be seen for micellar nanoparticles using the core-shell model. The pLys-*b*-PPS formulation showed a characteristic scattering that aligns with the expected pattern for a vesicle. Given that the DLS results for pLys-*b*-PPS show a monodisperse population of a diameter larger than what is typical for PEG-*b*-PPS vesicles, this SAXS scattering provides further insight into the potential morphology of this sample. Additional analysis would include direct visualization via nSTEM and loading of a hydrophilic dye to verify a legitimate internal aqueous space for hydrophilic cargo. However, these analyses provide strong evidence that these two PAA-*b*-PPS blocks of pLys and pGlu are able to form stable nanostructures in aqueous environments despite the significant increase in backbone complexity compared to the initial pSarc-*b*-PPS investigations.

As expected from the DLS results, the scattering for pTrp-*b*-PPS and pTyr-*b*-PPS was not similar to any of the typical models used for micelles, vesicles, filomicelles, or BCNs. It is likely with these two formulations that the nanostructures were not stable enough to hold a consistent

morphology, forming large multi-peak traces on DLS and undefined scattering patterns for SAXS. This outcome was not unexpected for these two amino acid residues as they are more hydrophobic than the previous sarcosine, glutamic acid, and lysine. While they were unable to form stable nanoparticle suspensions through the FNP technique with a MQ/THF solvent system, it may be worth exploring other variations of FNP along with other techniques such as thin-film and cosolvent dispersion. A less turbulent regime than FNP may allow for the supramolecular assembly of more stable aggregate structures.

Additionally, in these pilot backbone expansion trials, it is important to consider the final application. PAA-*b*-PPS nanoparticles are unlikely to be made from a pure homopolymer of these amino acids and instead are more likely to be used in a mixed system with a majority of spacer residues or other functionalities. For example, the fluorescent properties of Trp are highly apparent at a very small ratio of monomer compared to the length of the chain. However, the exploration of these residues demonstrates the robustness of the PAA-*b*-PPS system to form unique particles with complex backbones. Overall, this work shows the significant potential of the PAA-*b*-PPS diblock copolymer material as a self-assembling delivery system capable of forming multiple morphologies with a vast range of monomer functionalities.

## 5.5 Conclusion

Through this work, I was able to develop and optimize a screening workflow for the synthesis and characterization of a number of PAA-*b*-PPS copolymers. Extensive efforts were invested in the identification of the FTS-Cys linker that takes advantage of both NCA and PPS

chemistries with high efficiency and low generation of homopolymer byproducts. Independent synthesis of each polymer block allowed for pairing of known lengths to quickly develop copolymers that cover the full hydrophilic weight fraction range. This strategy not only reduces the materials needed to make the copolymer library, but it also drastically reduces variance associated with using multiple polymer batches, instead using the same homopolymer batch for many copolymers. This was especially useful given the safety and toxicity concerns of monomer syntheses as well as avoiding a significant investment of time and resources on a completely new copolymer without any evidence for stable self-assembly. This strategy is amenable to adaptations for other diblock copolymer systems that seek to connect blocks of similar nucleophilic susceptibility.

By subjecting these copolymers to both thin film and FNP with a variety of solvent systems, I was able to find a set of conditions that formed stable pSarc-*b*-PPS nanostructures in aqueous media. Initially, the more conventional strategy of thin film rehydration resulted in the aggregation of all five samples. This outcome was surprising but not discouraging, as the yet unknown physiochemical properties of this new material may simply be more suited to form supramolecular assemblies using other combinations of energy, turbulent mixing, and solvent exchanges. Also, while somewhat surprising, this result mirrors what was seen for BCN-forming PEG-*b*-PPS polymers when initially found.<sup>78</sup> Even within the next attempt with FNP, the solvent system between 1X PBS or Milli-Q water and DMF or THF produced different results as these solvents interact with each other and the two blocks of the copolymer in specific ways. Overall, the MQ/THF system resulted in stable nanoparticle formulations the most reliably. The formation

of stable nanostructures under these conditions and the observed failure under TF might suggest a requirement for the high Reynolds number and impingement pressures achieved through this type of mixing system. This application of FNP to assemble PPS-based materials that incorporate a hydrophilic block other than PEG provides evidence that PPS is the key component of copolymers that can self-assemble into advanced architectures using FNP.

Based on the three orthogonal characterization techniques of DLS, nsTEM, and SAXS, I found that the five pSarc-*b*-PPS nanoparticle formulations contained both micelles and polymersome morphologies. Pure micelle populations are formed most reliably at higher hydrophilic weight fractions, here at 0.52 and 0.44, while the second population of polymersome vesicles begin to appear most reliably for the 0.31 and 0.25 formulations. These results are similar to what is seen with PEG-*b*-PPS with micelles typically made from polymers of 0.57 and vesicles of 0.25 weight fractions (**Figure 1-10c**). This suggests that the overall packing parameter of these two copolymers remain similar despite vastly different hydrophilic blocks. However, future PAA-*b*-PPS materials will consist of more complex chains that can shift these ranges quite drastically. Additionally, the presence of micelle populations in all five samples indicates that this pilot investigation can be optimized to narrow the copolymer and formed nanostructure distributions. Overall, I found that the combination of these characterization techniques provided strong evidence toward confirming each type of morphology within the formulations as being able to form multiple stable nanostructures.

The significance of a material being able to form multiple stable morphologies cannot be understated. While many amphiphilic materials can make micelles that are excellent vehicles for

hydrophobic cargo, the additional vesicular structure increases the utility of the delivery system several fold. Aside from the ability to load hydrophilic cargo, there are also options for loading multiple cargos at once given the larger stable diameter and multiple cargo spaces. It would also offer aspect ratio and degree of curvature for tuning interactions with biological systems. A larger vesicle would have an increased surface area for anchoring ligands, targeting moieties, or imaging agents for different *in vivo* biodistribution. Finally, this capability to form stable bilayers indicates the potential to develop other stable morphologies beyond spheres.

I next found that these pSarc-*b*-PPS nanocarriers of both morphologies are non-toxic to murine-derived macrophages. As a phagocytic cell type, macrophages would be capable of extensive uptake compared to non-immune cell types and would be the most likely to show toxic effects. Beyond this simple viability assay, it was important to establish these NCA-based PAA polymers as non-cytotoxic given the terminal amine moiety on each polymer chain that could have induced cationic-dependent membrane disruption. By incorporating the negative surface charge measured by zeta potential for each formulation, it is possible that the positive charge of the terminal amine at neutral pH is balanced and partially overcome by the carboxylic acid of the original FTS-Cys linker that is negative at neutral pH. The resulting overall negative charge and evidence of no toxicity to macrophages suggests that these particles are safe to use in biomedical applications.

After this extensive investigation of the pilot pSarc-*b*-PPS nanoparticles, I expanded the same linker strategy to the PAA hydrophilic blocks of Trp, Tyr, Glu, and Lys to make nanostructures with more complex backbones. Having successfully formed NCA monomers of

these four amino acids with protection on the side chains of Lys and Glu, I found that the FTS-Cys linker worked exactly as anticipated for diverse NCA polymers. This is due to the design of the selected linker being sufficiently protected from primary amine exchanges, stable to the polymerization and deprotection conditions, and dependent on the amine ROP of the NCA monomers as a whole instead of for the original pSarc alone. While a cysteine NCA monomer could not be reliably formed, these four examples provided an excellent start to the expansion of PAA-*b*-PPS materials into more functional hydrophilic blocks.

Synthesis and assembly of these four PAA-*b*-PPS copolymers at hydrophilic weight fractions between 0.61 and 0.67 offered a new perspective compared to the pilot with pSarc. Instead of scanning the hydrophilic range with one polymer system, I looked at the morphologies formed at the same fraction across copolymers with a range of physiochemical properties. I found that the more hydrophilic blocks of Lys and Glu were able to form micelle- and vesicle-like structures while the more hydrophobic Tyr and Trp backbones appeared to form aggregates. Given the emphasis on expanding the backbone to four different amino acids, additional investigation into a more optimized set of assembly conditions could show these backbones to be capable of forming stable structures as well. Overall, these Lys, Glu, Tyr, and Trp PAA chains offered strong evidence to the robustness of this novel PAA-*b*-PPS system to accommodate side chains with more functional uses in chemical and biological applications.

The work I accomplished in this chapter represents the first synthesis and assembly of the diblock copolymer pSarc-*b*-PPS as a novel self-assembling nanocarrier delivery system. Inspired by the increasingly urgent need to develop more diverse nanoparticle materials beyond the

ubiquity of PEG, the PAA strategy offers a vast range of monomer functionalities that can be incorporated into the structural component of the nanoparticle-forming micelle and vesicle morphologies. These morphologies alone can be utilized for a vast array of biomedical applications as a delivery vehicle but could be further expanded to incorporate the unique physiochemical features of amino acid residues. Expanding the backbone further to incorporate functional residues would offer an unmatched level of tuning and customization to the specific application, limited only by the creativity of the researcher.

## **5.6 Acknowledgements**

I would like to thank Sharan Bobbala and Michael Vincent for their vital role in the acquisition and interpretation of characterization data for these nanostructures. In particular, Sharan provided data analysis and modeling of the SAXS scattering along with assistance in cytotoxicity studies. Michael conducted and interpreted the negative stain TEM images, and provided insight into the overall convergence of each technique on the nanoparticle morphologies. I would also like to acknowledge the assistance of Rajan Burt, a masters student working with me on these NCA projects. Finally, I would like to acknowledge Sean Allen for his enthusiasm and endless ideas for the application of NCA materials to our nanocarrier platform.

## **5.7 Publication information**

Portions of the work in this chapter has been previously published with the following citation information:

Frey M, Vincent M, Bobbala S, Burt R & Scott EA. Mapping the supramolecular assembly space of poly(sarcosine)-*b*-poly(propylene sulfide) using a combinatorial copolymer library. *Chem Comm* 56, 6644-6647 (2020). doi: 10.1039/D0CC00925C.

## CHAPTER 6

# Implementing general sequence control over the NCA copolymerization of protected lysine and glutamic acid

### 6.1 Abstract

The sequence of monomers within a copolymer system has a significant impact on the physiochemical properties of that material and must be implemented with a controlled synthesis. In contrast to the tight sequence control of solid-phase peptide synthesis, poly(amino acid) (PAA) chains without bioactivity can take advantage of approaches that offer a faster and cheaper synthesis while maintaining general sequence control. Poly(LysZ-co-BzGlu) with a random sequence is synthesized with this type of general control via NCA chemistry and a specific application of the foundational principles of copolymer kinetics. A combination of the Markov terminal monomer model and the Fineman-Ross approach is used to computationally determine the reactivity ratios of LysZ and BzGlu NCA monomers after using the values from initial homopolymer and copolymer synthesis trials. The reactivity ratios are used to determine the ideal monomer feed ratio to ensure an equal probability of cross- and self-propagation of monomers to result in a random sequence as analyzed by NMR over time. Finally, the idea of compositional drift with monomer consumption is addressed by the addition of a specific monomer mass at a specific reaction time, as calculated by these models. From this reciprocal incorporation of both computation and experimental outcomes, a copolymer of LysZ and BzGlu is synthesized with equal incorporation of both monomers through high fractional conversions.

This approach sets a foundation for applying these methods to a range of NCA copolymer systems to impart general sequence control.

## 6.2 Introduction

### 6.2.1 Bioactive peptide synthesis and specific sequence control

In all living organisms, significant cellular effort is devoted to elaborate mechanisms that maintain extremely tight sequence control during mRNA translation to peptides. The coordination of ribosomes, tRNA, and three-base pair codons control the specific addition of a single amino acid at a time to propagate the growing peptide chain with exceptional accuracy. The sequence of residues in a peptide chain is what imparts the biological function as the peptide folds into specific secondary, tertiary, and quaternary structures based on intermolecular forces between side chains and specific physiochemical properties.<sup>385</sup> Only correctly folded proteins will have the necessary physical alignment of residues to interact with the biological target and perform their specific cellular role. Indeed, single DNA point mutations that alter the amino acid sequence are responsible for a vast number of human diseases, as the affected proteins are unable to perform their function in often disastrous ways.<sup>386</sup>

Solid phase peptide synthesis (SPPS) has become an indispensable tool for the production of therapeutic and commercial products given its highly controlled pattern elongation on a solid support. Peptides are synthesized via a sequence of steps including the reversible deprotection of the resin-anchored peptide terminal end and coupling to the next protected amino acid.<sup>387</sup> When the peptide is fully synthesized, it can be purified and cleaved from the solid support

without complicated isolations or purifications. The stepwise addition of residues to create a highly controlled sequence is further enhanced by the ability to automate this process using specifically designed synthesizers with fluid handling and amino acid reservoirs. In fact, many non-peptide applications have been developed using this strategy to make highly specialized materials.<sup>388,389</sup>

This technology that has been developing since the early-to-mid 1900s has been an indispensable tool for the large-scale production of sensitive bioactive peptides, but it is not without downsides.<sup>390</sup> Recent concerns have focused on the cost, sustainability, and environmental impacts of SPPS as it utilizes high volumes of hazardous solvents such as DMF to perform each synthetic step.<sup>303,391</sup> Additionally, the coupling and deprotection steps do not always reach full completion which can result in skipped residues and truncations that may completely inactivate the bioactivity of the resulting product.<sup>301,332</sup> Another important consideration is that SPPS is significantly less able to synthesize peptides with “difficult sequences,” as those that have strong associative forces which can form aggregates.<sup>340</sup> These difficult amino acids include hydrophobic residues or residues that form stable alpha helices and beta sheets such as glycine, leucine, isoleucine, valine, and phenylalanine.<sup>393</sup> Finally, while the strategy is highly specialized for these functions of tight control, the number of applications for developing other materials or polymers is narrow.<sup>394</sup> That is, the disadvantages listed here, among others, are a product of maintaining the ability to produce very specific peptide materials at the expense of other aspects. It is therefore largely unreasonable to consider this strategy for

amino acid-based materials that do not need such tight sequence control and another approach can be implemented.

### 6.2.2 Structural poly(amino acids) and general sequence control

Shifting away from the typical perspective of amino acids and peptides, the core of this chemistry is that amino acid monomers are connected via peptide bonds to create a poly(amino acid) (PAA) polymer. While the usual function of these polymers is biological activity, this monomer/polymer angle also suggests a much broader role as a structural material independent of a specific biological target. For these applications without a strong dependence on residue sequence, alternative synthesis strategies may be utilized without the previously mentioned drawbacks of SPPS. In this way, a balance between efficiency and general sequence control can be found based on the requirements of the material application.

As discussed in depth in Chapter 5, NCA chemistry offers a range of benefits to the bulk production of PAAs under mild and controllable conditions through the anionic ring-opening polymerization (ROP) of NCA monomers. While the previous work explored mainly PAA homopolymers, one of the main benefits of NCA chemistry is the ability to make mixed polymers of many amino acid monomers using the exact same conditions as a homopolymer. Adding NCA monomers in specific ratios will create a chain with the same stoichiometric composition after full conversion. The peptide bonds that form between amino acid monomers are identical to the endogenously formed peptide bonds from mRNA translation and from peptides made via SPPS. After removal of any protecting groups, the final PAA is ready for further use.

Many times, the order of amino acids within a mixed PAA chain is not particularly important, such as in the example of adding one to two equivalents of tryptophan NCA to chains of poly(sarcosine) and poly(BzGlu) as demonstrated in Chapter 5. However, between the case of no control at all and the tight control from SPPS, there are many cases where having general sequence control is critical to the material properties. One such example explored in this chapter is a copolymer of lysine and glutamic acid which are charged residues at neutral pH. This type of copolymer has the possibility of containing zwitterionic character as a highly hydrophilic charged material with overall electroneutrality and is shown to be capable of resisting protein adsorption and enhancing the material biological half-life in a similar way as poly(ethylene glycol) (PEG).<sup>395</sup> While typical zwitterion polymers have a positive and negative charge on each unit, a PAA of lysine and glutamic acid with the correct general sequence could impart the same function by individually contributing positive and negative charges, respectively. This will only be the case if the sequence of lysine and glutamic acid residues are such that the charge is equal across the length of the chain (**Figure 6-1**).<sup>396</sup> In essence, general sequence control will determine if this material is a functional zwitterion or not.

### 6.2.3 General polymer sequence types

There are three general types of polymer sequences discussed here that cover a range of organizations (**Figure 6-2**). One type that is heavily utilized in amphiphilic nanomaterials is a block copolymer. Examples of block copolymers include poly(ethylene glycol)-block-poly(propylene sulfide) (PEG-*b*-PPS) discussed in Chapters 2-4 and poly(amino acid)-block-poly(propylene

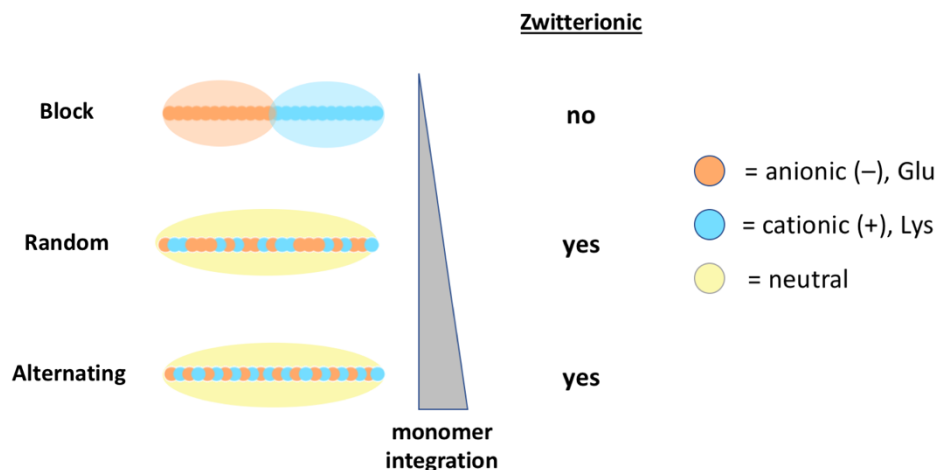


**Figure 6-1. Integration of charged monomers in a copolymer chain to produce a zwitterionic material.** For equal monomer amounts, when anionic Glu (orange) and cationic Lys (blue) residues are integrated poorly, there is a distribution of charge across the length of the copolymer chain. However, for sufficiently integrated Glu and Lys monomers, the opposite charges are effective neutral across the length of the copolymer chain, resulting in a zwitterionic material.

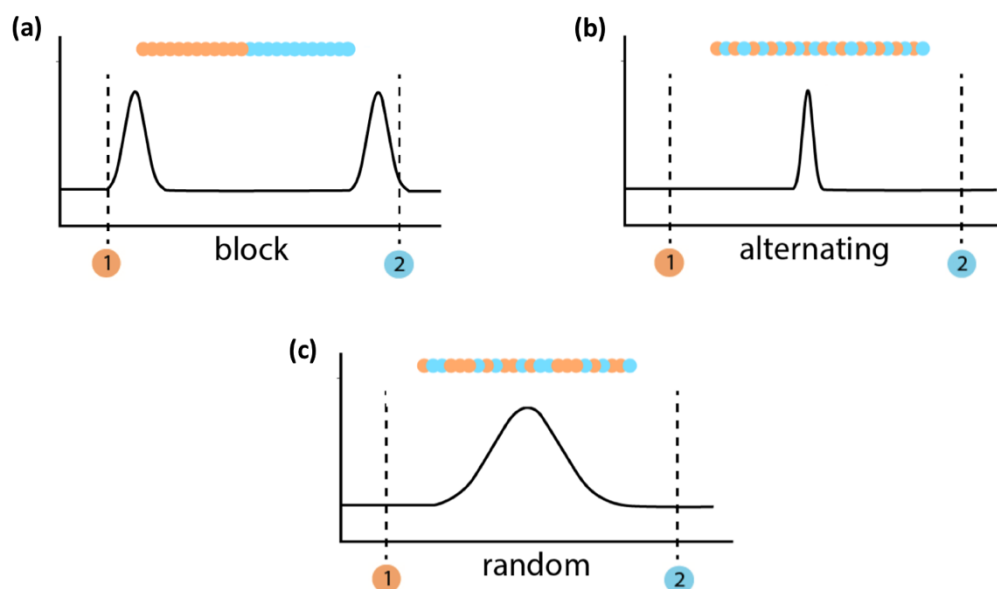


**Figure 6-2. Three types of general copolymer sequences for two-monomer systems.** (a) Block copolymers have a clear dedicated section of pure blocks. (b) Alternating has a repeating AB unit made from strict sequence control for a fully integrated character across the chain. (c) Random has monomers equally likely to insert at every position of the growing chain that averages out both monomer characters overall.

sulfide) (PAA-*b*-PPS) introduced in Chapter 5. In this block sequence, the two monomer types are completely separated into pure blocks attached at the center. This type of control can be implemented in a number of ways depending on the chemistry of the system. For PEG-*b*-PPS, the formed PEG block is used as a macroinitiator for the PPS block, while in the PAA-*b*-PPS materials, the blocks were formed independently before coupling via disulfide bonds. Another option for a pure NCA polymer is simply adding only one monomer at a time and allowing the chain to fully extend before adding the next monomer. These block polymers have many uses for materials that require distinct functional regions that are separated along the length.

Another type of polymer sequence is alternating, which is comprised of an ABAB-ordering of monomers within the chain. This is the most controlled of the three types mentioned here as each unit position must cross-propagate and switch monomers based on the previous position. This may also be considered an ideal arrangement for many materials that must have multiple fully integrated monomers for a uniform physiochemical character across the entire length.<sup>397</sup> Examples of applications for alternating copolymers include electron donor-acceptor pairs and Lewis acid complexes which each have a strong dependence on maintaining an exact distance within and between units as pairs or otherwise. However, the relatively tight control for this sequence may be difficult to achieve and verify for many polymerization strategies. There have been several models developed to address the unique concerns and features of alternating copolymers.<sup>398</sup>

The final type of general polymer sequence discussed here is a random arrangement. As a balance between the fully decoupled block and meticulously controlled alternating sequences,

a random polymerization can offer similar benefits as alternating without tight control. In contrast to the more colloquial definition of 'random,' in polymer chemistry, a random sequence indicates that any given position in the polymer chain is equally as likely to be any of the monomers in solution, without influence from adjacent units.<sup>399</sup> A statistically random copolymer of sufficient length should maintain the same broad physiochemical properties across the length without the more intensive pattern of cross-propagation at each position. Random copolymers are used ubiquitously throughout material applications in pharmaceuticals and industry including rubbers, polyurethanes, and poly(vinyl alcohol), among many others.<sup>400</sup>

Considering these options in the context of a lysine and glutamic acid copolymer for potential zwitterionic character, each option offers distinct advantages or disadvantages. A block copolymer of lysine and glutamic acid would not be zwitterionic as the charges are intentionally separated between two blocks. One end of the polymer would be extremely cationic while the other would be extremely anionic. Avoiding this type of sequence is critical for this material application. An alternating sequence would mimic the zwitterionic polymers with a positive and negative charge on each unit.<sup>396</sup> As mentioned previously, this is the most ideal arrangement, but it requires extensive monomer control, perhaps through adding single monomers at a time until they are fully added to the growing chain before adding the next monomer in the sequence. However, this also introduces complexities given the lack of stepwise protection that is offered by SPPS. Without this controlled sequence of protection and deprotection, monomers may be added multiple times to some chains and not added at all to other chains. Instead, the random sequence is an option that should accomplish the goals of an integrated copolymer zwitterion

without the drawbacks of the alternating sequence. In this chapter, I explore the development of a random poly(LysZ-co-BzGlu) polymer formed through the general sequence control of NCA chemistry using the protected lysine and glutamic acid NCA monomers described in Chapter 5.

#### 6.2.4 Monomer reactivity ratios as critical determinants of copolymer sequence

General sequence control of NCA polymerization can be implemented through the application of classical polymer chemistry concepts and equations. Instead of temporally controlling the addition of monomers for block and alternating sequences, adjusting the kinetics of monomers added to a propagating chain would enable a more self-sufficient approach to bulk polymer synthesis. The critical component of this strategy is the concept of monomer reactivity rates and reactivity ratios for multiple monomer systems. That is, how quickly will a monomer add to the active terminal end of the growing chain in comparison to the other monomers in solution? The approach to determining these reactivity ratios is especially complex; decades of studies have rarely converged on a single reliable strategy.<sup>401</sup> For this reason, a significant portion of this chapter is dedicated to the foundational aspects of these concepts and potential approaches to determine these reactivity ratios. The validity of the selected approach will be shown in part by the experimental results for the poly(LysZ-co-BzGlu) copolymer. For simplicity, the two monomers will be labeled 1 and 2 throughout the following schematics and equations but can be considered as Glu (1) and Lys (2) for the copolymer explored in this chapter.

To simplify a complex copolymerization system, the traditional Markov approach to copolymer kinetics considers only the active terminal ends.<sup>402,403</sup> While this model has

disadvantages compared to other models that incorporate the effects of monomers previous to the active terminal end, these more involved models also carry a level of complexity that outweighs their utility for this investigation. According to the Markov terminal approach, a system of two monomers has four deterministic outcomes for either of the two monomers adding to the growing chain (**Figure 6-3**). For a chain with an active terminal end of monomer 1 (M1), either another M1 can be added (11) or a monomer 2 (M2) can be added (12). For a chain with an active terminal end of M2, either M1 can add (21) or another M2 can add (22). Each of these four outcomes has a specific rate that depends on the chemistry of the terminal end and the monomer to be added. The rates are defined with similar nomenclature here as  $k_{11}$ , representing active end M1 reacting with another M1, and the same for  $k_{12}$ ,  $k_{21}$ , and  $k_{22}$ .

Given that the self-propagation rates of  $k_{11}$  and  $k_{22}$  are independent of the second monomer in the system, these values can be found by conducting initial homopolymerization studies. To do this, we must first consider the dependencies of the polymerization rate in the

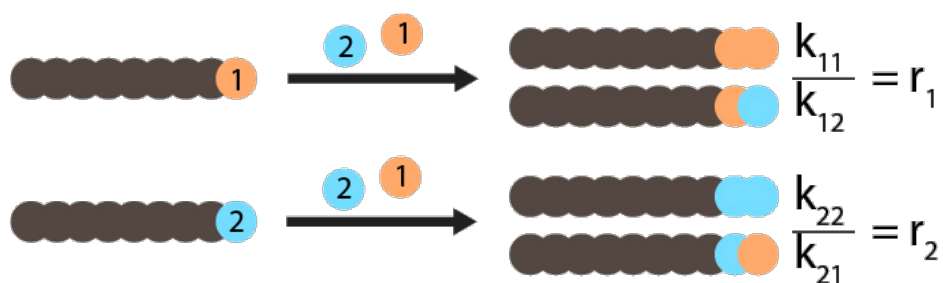


**Figure 6-3. The four deterministic (Markov) outcomes and corresponding reactivity ratios of a two-monomer system based on the active terminal end.** For active terminal ends of M1, self-propagation with M1 happens at a rate  $k_{11}$  while cross-propagation with M2 happens at a rate  $k_{12}$ . The ratio of these rates yields the reactivity ratio  $r_1$  as being dependent on both homopolymerization ( $k_{11}$ ) as well as the competing chemistries specific to the monomers in the system ( $k_{12}$ ). The case is the same for chains with an active terminal end of M2 for  $k_{22}$ ,  $k_{21}$ , and  $r_2$ .

system. Aside from the rate constant itself, a system will polymerize faster if there is a higher number of chains actively growing as well as a higher amount of monomer available to react and add to those chains. Mathematically, the polymerization rate ( $R_p$ ) of an anionic system is equal to the product of  $k_p[P^*][M]$  where  $k_p$  is the kinetic equilibrium constant,  $[P^*]$  is the concentration of active terminal ends as reactive intermediates, and  $[M]$  is the monomer concentration.<sup>403</sup> For this derivation, we can replace the concentration of reactive intermediates with the concentration of the initiator  $[I]$ , assuming that all initiator molecules can begin a chain and that chain terminations are minimal. Additionally, the polymerization rate is the functional equivalent of the rate of monomer being used up in the propagation as a derivative with respect to time, yielding **Equation 1**.

$$-\frac{d[M]}{dt} = K_p[I][M] \quad (6.1)$$

Solving this differential to **Equation 2** and incorporating  $[M]/[M_0]$  as the inverse of the degree of polymerization ( $DP_n$ ) yields **Equation 3**. This derivation yields a tool that can calculate  $k_{11}$  and  $k_{22}$  in a homopolymer synthesis with a known initiator concentration that tracks  $DP_n$  with respect to reaction time.<sup>404</sup> These values can be fed back into the computation to solve for other key polymerization parameters.

$$[M] = [M_0]e^{-k_p[I]t} \quad (6.2)$$

$$\ln\left(\frac{1}{DP_n}\right) = -k_p[I]t \quad (6.3)$$

To find the reactivity ratio, the most critical component of future calculations, the four deterministic outcomes can give a numerical value to how likely one monomer will add to a given terminal end in comparison to the other.<sup>405</sup> The reactivity ratios are thus dependent on the active terminal end, and this dependence is reflected in the abbreviated nomenclature for the  $k$  rates. The reactivity ratio of M1 ( $r_1$ ) describes the case of an active terminal end of M1, as the rate that another M1 will add ( $k_{11}$ ) divided by the rate that the other M2 will add ( $k_{12}$ ). The same is true for finding the reactivity ratio of M2 ( $r_2$ ) with an active terminal end of M2 as the rate another M2 will add ( $k_{22}$ ) over the rate that M1 will add ( $k_{21}$ ). Given these conditions, both  $r_1$  and  $r_2$  describe the proportional likelihood that the same type of monomer will add to the chain (self-propagation) compared to adding the other type of monomer (cross-propagation). A high reactivity ratio means that a terminal end is more likely to self-propagate, while a low reactivity ratio is when a terminal end is more likely to cross-propagate. A reactivity ratio of 1 means that either monomer would add with equal rates. In this way, the reactivity ratios of each monomer in the system are independent from each other but dependent on the system itself. That is, each combination of monomers will have a unique  $k_{12}$  and  $k_{21}$  as they are dependent on the identity of that second monomer.

Returning to the types of general polymer sequences, the reactivity ratios can be applied in this context as well (**Figure 6-4**).<sup>401</sup> A block copolymer that is not synthesized temporally (adding different monomers at different times) or spatially (polymerizing chains separately) could also be formed from two monomers with very high reactivity ratios. Whichever current terminal end begins the chain will continue to add monomers of the same type until there are few

remaining, at which point the other monomer will add and form the other block. An alternating copolymer could be formed by using monomers with reactivity ratios that are very low or zero.<sup>398</sup> In this situation, any given active terminal end is more likely to add the other type of monomer instead of the same type, resulting in a 1212 pattern. Finally, a random copolymer can be formed from an equal mixture of two monomers that have reactivity ratios equal to 1. For any given active terminal end, either monomer type is likely to add to the chain, resulting in a random assembly across the length of the chain.

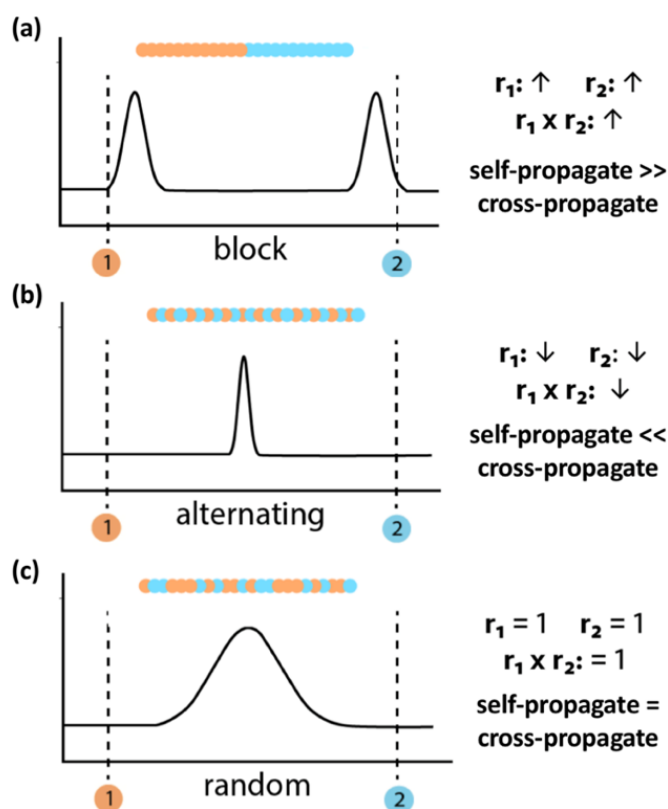


**Figure 6-4. Three general copolymer sequences with the associated relationship to reactivity ratios.** (a) Block copolymers have a very high  $r_1$  and  $r_2$  as more likely to self-propagate until that monomer is consumed. (b) Alternating copolymers have a very low  $r_1$  and  $r_2$  that are more likely to cross-propagate at each unit. (c) Random copolymers have  $r_1$  and  $r_2$  equal to 1 as equally likely to add either monomer to the next position (50%).

### 6.2.5 Determining reactivity ratios

Placing reactivity ratios in the practical context of a growing copolymer enables the determination of its value for each monomer in the system. According to the pivotal Mayo-Lewis equation shown below (**Equation 4**), the overall copolymer composition ( $F_1$ ) is dependent on both the reactivity ratios of the monomers ( $r_1$  and  $r_2$ ) as well as the monomer feed composition ( $f_1$  and  $f_2$ ).<sup>405</sup> Among these three types of variables, the monomer feed composition is determined experimentally as the amount of monomer physically added to the flask, while the overall copolymer composition can be found through NMR analysis of product. In this way, the reactivity ratios can be solved for experimentally using the known values for monomer and polymer composition.

$$F_1 = \frac{r_1 f_1^2 + f_1 f_2}{r_1 f_1^2 + 2 f_1 f_2 + r_2 f_2^2} \quad (6.4)$$

Rearranging the Mayo-Lewis equation through a number of in-depth steps highlighted elsewhere<sup>402</sup> yields two linear functions for determining the reactivity ratios known as the Fineman-Ross<sup>406</sup> and Kelen-Tudos<sup>407</sup> approaches. Shown below is the Fineman-Ross equation that is utilized for this work, with  $x$  representing  $f_1/f_2$  and  $y$  representing  $F_1/F_2$  (**Equation 5**). Transforming the experimental copolymerization results of feed composition and copolymer composition to fit this pattern yields a meaningful slope and y-intercept used to solve for the reactivity ratios.<sup>408</sup> This experimental and mathematical approach can be used to determine the reactivity ratios of any copolymer system of interest.

$$\frac{x(y-1)}{y} = r_1 \left( \frac{x^2}{y} \right) - r_2 \quad (6.5)$$

### 6.2.6 General sequence control using applied reactivity ratios

Thus far, monomer reactivity ratios have been established as a critical parameter in predicting the type of copolymer that forms from an equal mixture of monomers. However, since these ratios are based on the individual monomer and active terminal end chemistries, they are values that describe the monomers in that specific system and cannot be altered. In order to manipulate the type of copolymer that forms from a given monomer system, other practical factors must be considered beyond chemistries and rates. Instead, we can incorporate the monomer and terminal end concentrations in the context of overall polymer composition.

These variables assemble in **Figure 6-5** as a continuation of the four deterministic outcomes. The expanded deterministic outcomes are shown with the previous rates of  $k_{11}$ ,  $k_{12}$ ,  $k_{22}$ , and  $k_{21}$  along with the concentration of the relevant terminal ends ( $P_1$  or  $P_2$ ) and the monomer being added ( $M_1$  and  $M_2$ ). Conceptually, this implies that the overall probability of an outcome that a certain monomer adds to a given terminal end is dependent on the relative amount of each the monomer and the terminal end present in the reaction mixture. Even if  $k_{12}$  is very high, having a low level of  $M_1$  terminal ends or  $M_2$  available to add to the chain will result in a low probability of that outcome. In this way, differences in reaction rates from the target for

a polymer sequence can be compensated for by adjusting these values experimentally. Specifically, the type of polymer sequence can be controlled by altering the monomer concentration, otherwise known as the feed composition.

The overall probability of each outcome happening can be found by incorporating these expressions as the general form  $p(\text{specific outcome}) / p(\text{all outcomes})$ . For the terminal model that divides the outcomes by the active terminal end, that simplifies to  $p(\text{M1M1}) / p(\text{M1M1 OR M1M2})$ . The corresponding equations for each outcome are shown as pulled directly from those listed in **Figure 6-5 (Equations 6 – 9)**. Further reorganization of these equations to couple the  $k_{xy}$  variables allows for substitution of the reactivity ratios and the generation of the set of copolymer probability equations.

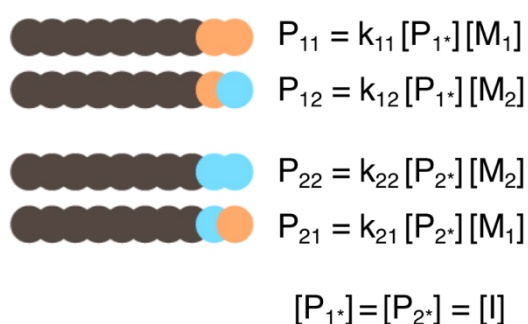


**Figure 6-5. The four deterministic outcomes based on the terminal Markov model.** This approach is used to calculate the probability of each outcome happening ( $P_{11}$ ,  $P_{12}$ ,  $P_{22}$ , and  $P_{21}$ ). These probabilities depend on the rates of self- and cross-propagation ( $k$ ), the concentration of active terminal ends of that type ( $P^*$ ), and the concentration of available monomer of that type ( $M$ ). Given that the active terminal polymer ends in solution cannot be directly calculated, we can assume that these variables are equal to the concentration of initiator added to the reaction with complete initiation of chains and minimal early terminations.

$$P_{11} = \frac{1}{r_1 + \frac{1-f_1}{f_1}} \quad (6.6)$$

$$P_{12} = \frac{1}{1 + r_1 \frac{f_1}{1-f_1}} \quad (6.7)$$

$$P_{21} = \frac{1}{1 + r_2 \frac{1-f_1}{f_1}} \quad (6.8)$$

$$P_{22} = \frac{1}{r_2 + \frac{f_1}{1-f_1}} \quad (6.9)$$

These equations can then be used to model the possible outcomes of a two-monomer system for copolymerization as a function of the feed composition to account for differences in reactivity ratios. Conceptually, a higher reactivity ratio can be balanced by a lower monomer composition so that all outcomes for both monomers are equally likely and will add in a random sequence. These principles are applied further to the Lys and Glu system explored in this chapter to calculate the ideal initial monomer feed composition to build a copolymer that has an equal chance to add either monomer.

### 6.2.7 Accounting for monomer feed consumption

A practical consideration of critical importance is the idea that monomer is used up over the course of polymer propagation as they are added to the polymer chain. In this way, the initial monomer feed composition changes over time and drifts away from the initial ideal monomer ratio. This indicates that the growing polymer chain will no longer have a balanced probability to add either monomer unit and will drift away from the intended random sequence paradigm. Even as soon as 5% conversion may show a drift significant enough to change the physiochemical properties of the system. Many early copolymerization studies addressed this concern by the only forming copolymers at low conversion, which is highly inefficient and wasteful of often precious material.<sup>409</sup> It is therefore essential to consider how to address the consumed monomer throughout the polymerization to maintain the ideal feed composition at high fractional conversions.

One such solution is the periodic supplementation of fresh monomer to the system. Adding a specific amount of monomer to the system after a certain amount of time to offset the monomer consumed in that time should be a sufficient strategy. As long as the drift within that frame is within the acceptable window for the application, the supplementation interval can be as frequent or infrequent as allowed by the physical constraints in the laboratory. While an automated approach of continuously adding fresh monomer to the stirring solution would offer an extremely tight and hands-off approach,<sup>410</sup> this chapter explores this manual interval and compositional variance within a reasonable timeframe. The moving parts of this time interval,

the acceptable drift away from the ideal composition, and the rate at which monomer is consumed all play a role in determining how much monomer to add to the system. A reasonable approach to this aspect of copolymerization is explored in this chapter to maintain the random sequence as the chain grows.

### 6.2.8 Chapter objectives

In this chapter, these copolymerization principles are used to develop a strategy to impart general sequence control over a random NCA copolymer of lysine and glutamic acid. These amino acids are of particular interest as they are cationic and anionic at neutral pH. A correctly controlled random sequence of these residues should result in a zwitterionic polymer with equal charge distribution across the length of the polymer chain that is effectively neutral. Previous studies exploring these two monomers, including the specific protecting groups utilized here, both suggest this to be a worthwhile pursuit and offer a modest foundation of background information to best inform these copolymerization studies. Lysine and glutamic acid will serve as the initial model for understanding NCA polymerization kinetics as they relate to a mixed PAA system in a way that can be expanded to other monomer pairings.

This chapter is intended to directly couple the conceptual elements of polymer chemistry with the experimental outcomes of copolymer synthesis. Initial understanding of homopolymer kinetics will provide rate values for the monomer system that can be used to solve for the complex copolymerization outcomes. As these computationally derived parameters are applied to copolymerization experiments, the resulting analysis of those chains will provide evidence that

validates the computational approach. This reciprocal approach is often overlooked once a novel system has been fully established but remains a critical source of guidance and deeper understanding of the system especially exploring new variations.

The main goal of the work in this chapter is ultimately the synthesis of a poly(LysZ-co-BzGlu) copolymer with a random sequence. Few experiments take into account the differences in reactivity ratios between monomers in a mixed copolymer system, instead assuming that an equal monomer feed will result in an equal monomer distribution.<sup>328,369</sup> However, if the reactivity ratios are not initially equal, this approach will instead produce a largely uncontrolled copolymer sequence dependent entirely on the rates that each active terminal end will add the same or opposite monomer. I hypothesize this to be shown in the case of poly(LysZ-co-BzGlu) which is comprised of LysZ and BzGlu NCA monomers that are expected to have unequal reactivity ratios. In this case, copolymerization with an equal monomer feed composition will produce a sequence similar to a block copolymer instead of a random sequence. These reactivity ratios can be determined through kinetic analysis of homopolymer synthesis and copolymer synthesis using different monomer ratios and applying the Fineman-Ross approach. I hypothesize that these controlled syntheses with varying amounts of LysZ and BzGlu NCA monomers will produce values that can be used to estimate the reactivity ratios of the system.

The derived equations stemming from the four deterministic outcomes of the terminal Markov approach and the Mayo-Lewis equation suggest that monomers with different reactivity ratios can be balanced by adjusting the monomer feed ratio. This adjusted feed composition should account for the propensity of each monomer to self-propagate or cross-propagate such

that the chance of either monomer adding to the chain is equal at 50%. This value of 50% for a two-monomer system suggests a random general sequence as either unit has the same chance of existing at any given position in the chain, resulting in the intended random sequence. I hypothesize that adjusting the monomer feed for LysZ and BzGlu NCA monomers will result in a copolymer with a chain composition much closer to 0.50, indicating that the monomers are adding at equal rates and therefore with equal likelihood to add to the chain.

The final consideration for this section is that the monomers in the reaction flask are physically used up as they add to the chain, thus changing the feed composition over time and therefore the probability that a monomer will add to the chain. This compositional drift will result in a non-random sequence as the monomer feed shifts concentrations and the copolymer is no longer of equal character along the length. I expect this to be demonstrated at later timepoints and higher fractional conversion of the LysZ and BzGlu copolymer systems with a drop in copolymer composition from the initial 0.50. The drift can be addressed by supplementing the reaction with fresh monomer at defined intervals. The rate of monomer consumption is proportional to the fractional conversion of the growing polymer at each time point, and the necessary moles to supplement monomer composition drift can be calculated according to this principle. I expect the experimental values of LysZ and BzGlu homopolymers and copolymer trials to provide accurate values for these monomer consumption calculations. While the initial calculated feed ratio will correct for the initial copolymer composition, this feed ratio must be maintained to ensure a complete random sequence throughout the length of the copolymer. I hypothesize that semi-batch additions of the LysZ or BzGlu NCA monomers according to these

calculations will maintain the 0.50 copolymer composition over time, indicating a maintenance of the equal monomer addition rates as a random sequence. In the case of an unprotected poly(Lys-*co*-Glu) copolymer with charged residues, this random sequence throughout the length will allow for the development and maintenance of a zwitterionic character across the entire chain.

The work in this chapter represents an effective reciprocal relationship between experimental and computational approaches. The experimental results of polymerization kinetics will provide data for computational analysis to calculate the reactivity ratios and determine the ideal monomer feed composition for equal monomer addition and supplementation. Applying these calculated values to the experimental protocol will validate all previous steps of data collection and computational modeling. Compared to many other studies that largely ignore these copolymer kinetic principles, this work will show that general sequence control can be implemented on a system of monomers that react at different rates. The pipeline to obtain the experimental and modeling values outlined in this chapter can be applied to any number of future PAA-based copolymer systems.

## 6.3 Materials and Methods

### 6.3.1 Materials and instrumentation

#### *Materials*

Unless indicated below, chemical reagents were purchased from Sigma-Aldrich (St Louis, MO, USA) and used as received. Hexanes and methanol were purchased from Fisher Scientific

(Pittsburgh, PA, USA).  $^1\text{H}$  NMR were recorded on Bruker Avance III 500 MHz system and analyzed with MestReNova (Mestrelab Research, Spain).

### *General conditions*

Unless otherwise indicated, synthetic procedures were performed under inert conditions, with freshly opened anhydrous solvents and a nitrogen atmosphere. After workup, products were used immediately or quickly transferred to vials kept under nitrogen and stored in the  $-20^\circ\text{C}$  freezer until use. Special care should be taken when preparing NCA derivatives given their extreme sensitivity to decomposition or ring opening.

### *Safety*

Phosgene and its derivatives are EXTREMELY HAZARDOUS to human health at any scale. Please take all appropriate safety measures into consideration when planning, handling, and disposing of these chemicals and any materials that have come into contact with them.

### 6.3.2 BzGlu and LysZ homopolymer kinetic studies

BzGlu and LysZ NCA monomers were prepared as described in Chapter 5 and used shortly after synthesis. For homopolymer kinetic studies, anhydrous DMF (5 mL) and hexylamine initiator (0.227 mmol, 1 eq.) were added to a prepared Schlenk flask under inert atmosphere. NCA monomer (11.35 mmol, 50 eq.) was added to the respective flasks and allowed to react through the timepoints of 0.5 hours, 4 hours, 24 hours, and 48 hours. At these times, aliquots were

precipitated in excess 1M HCl and shaken to dissolve excess monomer. The solid was collected and dried in vacuo to yield the homopolymer product for NMR analysis of chain length.

pLysZ:  $^1\text{H}$  NMR (500 MHz, DMSO- $d_6$ ):  $\delta$  (ppm) = 7.33-7.22 (m, 5H/unit), 4.99 (s, 2H/unit), 4.13 (t, 1H/unit), 1.61-1.32 (m, 8H/unit), 1.50-1.40 (m, 6H), 0.85 (t, 3H).

pBzGlu:  $^1\text{H}$  NMR (500 MHz, DMSO- $d_6$ ):  $\delta$  (ppm) = 7.34 (m, 5H/unit), 5.07 (m, 2H/unit), 4.28 (m, 1H/unit), 1.94 (m, 2H/unit), 1.20 (m, 2H/unit), 1.50-1.40 (m, 6H), 0.85 (t, 3H).

### 6.3.3 Preparation of poly(LysZ-co-BzGlu) copolymer with defined feed ratios

Copolymerization reactions were set up in broadly the same way as described for homopolymerization except that both monomers were added to the flask. Briefly, for the  $f_1$  of 0.50 condition, anhydrous DMF (10 mL) and hexylamine (0.0454 mmol, 1 eq.) were added to a prepared Schlenk flask under inert atmosphere. BzGlu NCA ( $f_1 = 0.50$ : 1.135 mmol, 25 eq.;  $f_1 = 0.35$ : 0.795 mmol, 17.5 eq.) and LysZ NCA monomer ( $f_1 = 0.50$ : 1.135 mmol, 25 eq.;  $f_1 = 0.35$ : 1.47 mmol, 32.5 eq.) were added to the flask at the same time and allowed to react through the timepoints of 4 hours, 24 hours, and 120 hours. At these times, aliquots were precipitated in excess 1M HCl and shaken to dissolve excess monomer. The solid was collected and dried in vacuo to yield the copolymer product for NMR analysis of chain length.

Poly(LysZ-co-BzGlu):  $^1\text{H}$  NMR (500 MHz, DMSO- $d_6$ ):  $\delta$  (ppm) = 7.34-7.22 (m, 5 H/LysZ or BzGlu unit), 5.07 (m, 2H/BzGlu unit), 4.99 (s, 2H/LysZ unit), 4.28-4.13 (m, 1H/LysZ or BzGlu unit), 1.61-1.32 (m, 8H/unit), 1.50-1.40 (m, 6H), 0.85 (t, 3H).

### 6.3.4 Drift correction protocol for extended poly(LysZ-co-BzGlu) copolymer

Copolymerization for drift correction was set up in an identical way to the previous adjusted  $f_1$  experiments but with an additional supplement of BzGlu NCA monomer added to one flask. Briefly, for the  $f_1$  of 0.50 condition, anhydrous DMF (10 mL) and hexylamine (0.0454 mmol, 1 eq.) were added to a prepared Schlenk flask under inert atmosphere. BzGlu NCA ( $f_1 = 0.50$ : 1.135 mmol, 25 eq.;  $f_1 = 0.35$ : 0.795 mmol, 17.5 eq.) and LysZ NCA monomer ( $f_1 = 0.50$ : 1.135 mmol, 25 eq.;  $f_1 = 0.35$ : 1.47 mmol, 32.5 eq.) were added to the flask at the same time and allowed to react through the timepoints of 24 hours, 48 hours, and 72 hours. At these times, aliquots were precipitated in excess 1M HCl and shaken to dissolve excess monomer. The solid was collected and dried in vacuo to yield the copolymer product for NMR analysis of chain length.

A third reaction for the  $f_1$  of 0.35 was set up in parallel under identical conditions. Briefly, anhydrous DMF (10 mL) and hexylamine (0.0454 mmol, 1 eq.) were added to a prepared Schlenk flask under inert atmosphere. BzGlu NCA (0.795 mmol, 17.5 eq.) and LysZ NCA monomer (1.47 mmol, 32.5 eq.) were added to the flask at the same time and allowed to react through the timepoints of 24 hours and 48 hours. At 53 hours, BzGlu NCA (0.087 mmol, 1.92 eq.) was added to the flask and continued to polymerize. An additional aliquot was taken at 72 hours. At these times, aliquots were precipitated in excess 1M HCl and shaken to dissolve excess monomer. The solid was collected and dried in vacuo to yield the copolymer product for NMR analysis of chain length.

Poly(LysZ-co-BzGlu):  $^1\text{H}$  NMR (500 MHz, DMSO- $d_6$ ):  $\delta$  (ppm) = 7.34-7.22 (m, 5 H/LysZ or BzGlu unit), 5.07 (m, 2H/BzGlu unit), 4.99 (s, 2H/LysZ unit), 4.28-4.13 (m, 1H/LysZ or BzGlu unit), 1.61-1.32 (m, 8H/unit), 1.50-1.40 (m, 6H), 0.85 (t, 3H).

### 6.3.5 Experimental analysis of copolymers

$^1\text{H}$  NMR integration of key peaks was sufficient to deconvolute the similar signals for BzGlu and LysZ residues. Specifically, the shift corresponding to the protecting group of BzGlu is near 5.07 ppm while the associated shift for the protecting group of LysZ is near 5.01 ppm. This difference was enough to reliably resolve the peaks associated with both units and calculate degree of polymerization ( $\text{DP}_n$ ) and copolymer composition according to the established approaches.

### 6.3.7 Computation and modeling

Any computational analysis or reaction modeling not described in this chapter can be found with extensive depth and justification in reference 411. Please see this document as supplemental reading for this chapter as necessary.

## 6.4 Results and Discussion

### 6.4.1 Quenching for fractional conversion analysis

Before any polymerization experiments, an effective quenching and workup method must ensure complete reaction termination and reliable purification of the formed polymer chains from the remaining NCA monomers. This is especially important for the reactions that were

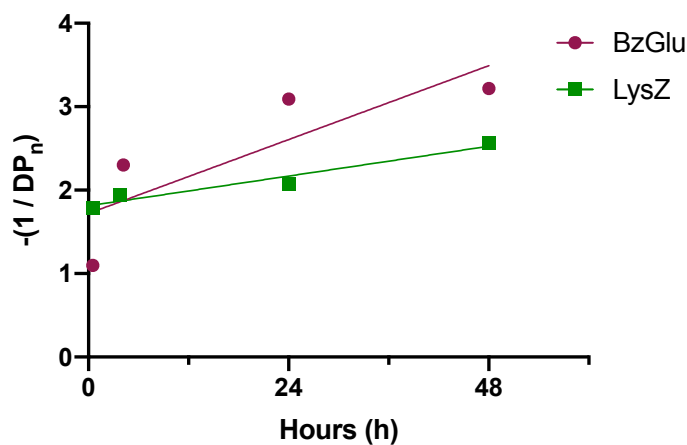
stopped at low fractional conversion as these will contain a vast majority of unreacted NCA monomers compared to the shorter copolymer chain. Both of these quenching and purification tasks were accomplished at once with a precipitation in 1M HCl. The reaction is stopped as any remaining NCA monomer is hydrolyzed to the non-reactive amino acid form. The mixture is purified as the quenched amino acid monomers are soluble in the aqueous solution while the copolymer chain crashes out. Vigorous shaking of the precipitation tubes shows a transition from cloudy to clear as the monomer rings are opened and the solid copolymer associates with the sides of the tube. A quick centrifuging of these tubes leads to effective separation of the copolymer chains from the free amino acids as a pellet.

#### 6.4.2 Homopolymer kinetics to find reactivity ratios

For these experiments, BzGlu NCA and LysZ NCA monomers were prepared as described previously in Chapter 5 from commercially protected starting materials (**Scheme 5-1c**, **Scheme 5-1d**).<sup>310,330</sup> The pBzGlu and pLysZ homopolymers were initiated with hexylamine as a simple primary amine with a unique NMR peak shift at 0.83 ppm for reliable composition quantification (**Scheme 5-3c**, **Scheme 5-3d**). Homopolymerizations were setup in parallel using equal molar amounts of the hexylamine initiator (0.227 mmol) and NCA monomers (11.35 mmol) for a monomer-to-initiator ratio of 50 equivalents. Aliquots of the growing chain were quenched and purified for NMR analysis at timepoints of 30 minutes, 4 hours, 24 hours, and 48 hours. From the corresponding NMR integration of the representative peaks for the BzGlu and LysZ units compared to the hexylamine initiator, the chain length was recorded in terms of  $DP_n$ . These

values were manipulated according to **Equation 3** and plotted as the negative natural log of the inverse  $DP_n$  at each timepoint (**Figure 6-6**).

A linear regression of these two lines for the individual homopolymers result in a slope that represents the product of the self-propagation rate constant and the initiator concentration. Since the amount of initiator was identical between the reactions, the visualization of slopes was representative of their overall reaction rates. The rate of BzGlu ( $k_{11}$ ) was  $8.12 \text{ M}^{-1}\text{h}^{-1}$  and the rate of LysZ ( $k_{22}$ ) was  $3.28 \text{ M}^{-1}\text{h}^{-1}$ , indicating that BzGlu self-propagates about 2.48 times faster than LysZ. From this homopolymerization, we've acquired both the values for  $k_{11}$  and  $k_{22}$  along with



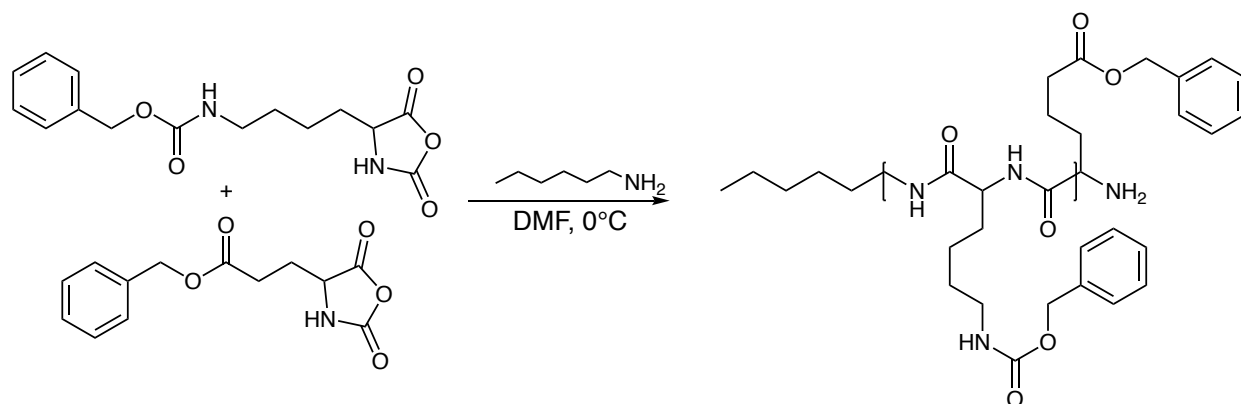
Polymer	[I] (M)	Slope	$k_{11}$ or $k_{22}$
pBzGlu	0.00454	0.03690	8.12
pLysZ	0.00454	0.01488	3.28

**Figure 6-6. Homopolymer kinetics to solve for the homopolymerization rates of  $k_{11}$  for BzGlu and  $k_{22}$  for LysZ.**

This graph represents the negative inverse of the natural log of the degree of polymerization as an analogue for fractional conversion with respect to time for each monomer. The  $DP_n$  was determined by NMR integration of samples taken at each timepoint through 48 hours. The slope of these transformed axes is equal to the product of the rate  $k$  and the initiator concentration, with the initiator concentration being known experimentally.

the understanding that the NCA polymerization of BzGlu and LysZ have significant kinetic differences that must be addressed by adjusting the feed composition for copolymer syntheses. Given that BzGlu reacts several-fold faster than LysZ, it is expected that the subsequent calculations that the amount of BzGlu in the monomer feed will be less than LysZ to offset this kinetic advantage.

The reactivity rates of the two monomers in this system can be found with additional experiments synthesizing copolymers at a range of initial monomer feed ratios (**Scheme 6-1**). The reactions are terminated at early fractional conversion to maintain the effects of the monomer feed before significant compositional drift affects the polymer chains. To illustrate this approach, the 3.5-hour timepoints of the copolymer reactions with  $f_1$  values of 0.50 and 0.35 were retroactively used for the calculation of  $r_1$  and  $r_2$  using the Fineman-Ross model (**Equation 5** above). The resulting parameters are shown in **Figure 6-7** with the slope ( $r_1$ ) and intercept ( $r_2$ ) of



**Scheme 6-1.** Copolymerization of LysZ NCA and BzGlu NCA with a hexylamine initiator.

the line between the two points. From this analysis, the BzGlu-defined  $r_1$  was found to be 0.666 and the LysZ-defined  $r_2$  was 0.303.

Compared to the literature values of these same NCA monomers of 1.86 for  $r_1$  and 0.52 for  $r_2$ , these results represent considerable deviation.<sup>412</sup> First, these literature values used the Kelen-Tudos model which weights each data point equally across the range of monomer feeds. Additionally, this demonstration used only two monomer feeds instead of a more extensive set that explores an extended range that includes having more LysZ than BzGlu. Another important consideration is the relatively late time point of 24 hours for fractional conversion which is much later than the usual reaction time which tends to be limited to about an hour. It is likely that these copolymers are much further beyond the 5% fractional conversion and are therefore affected by consumption of monomer and compositional drift. Each of these factors can

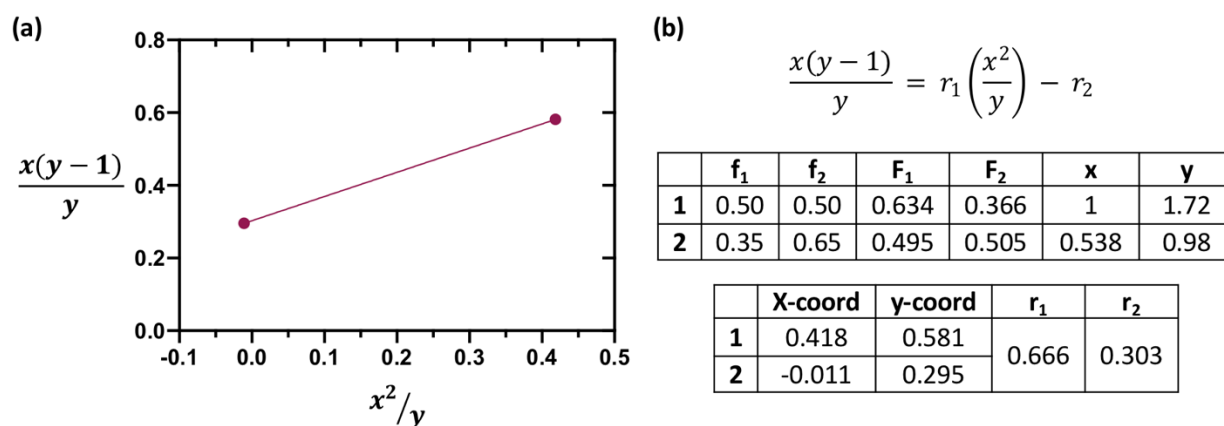


**Figure 6-7. The Fineman-Ross approach to solving for reactivity ratios for BzGlu and LysZ NCA monomers.** This approach is based on the copolymer composition ( $F_1$  and  $F_2$ ) and the monomer feed composition ( $f_1$  and  $f_2$ ). The values of  $f$  correspond to the amount of monomer added to the reaction flask while the  $F$  values are found through NMR integration after an earlier fractional conversion. In (a), the calculated values of  $x$  and  $y$  are plotted according to this approach to yield a linear regression with a slope representing  $r_1$  and a  $y$ -intercept representing negative  $r_2$ . The Fineman-Ross equation and table of calculated values is shown in (b) for the two copolymer systems.

influence the results of this work to deviate from a more accurate estimation but were included to demonstrate this approach. Additional experiments with defined monomer feed ratios would be conducted in exactly the same way, with algebraic reorganization to yield plotted points that are summarized by a linear regression. The slope of this regression represents  $r_1$  while the x-intercept represents  $r_2$ . It is also suggested that future applications utilize earlier timepoints for these studies, as a longer fractional conversion will bias the copolymer chain lower toward the initial monomer feed as monomers are used instead of isolating the effects of reactivity ratios. For the subsequent work, the literature values of  $r_1$  and  $r_2$  are used for enhanced computational and experimental accuracy.

#### 6.4.3 Identifying the ideal monomer feed composition

To determine the monomer feed composition to offset the reactivity ratios, the four probability equations for each  $P_{11}$ ,  $P_{12}$ ,  $P_{21}$ , and  $P_{22}$  are required. Given the goals of this material to minimize the likelihood that any given section of the copolymer has a presence of one monomer over the other, we can prioritize the likelihood of cross-propagation over self-propagation. The translation of this to the four outcomes and probabilities is to maximize the chance for  $P_{12}$  and  $P_{21}$  as the outcomes that represent cross-propagation. Setting these probabilities equal to each other represents that the monomers are equally as likely to switch from BzGlu to LysZ as they are to switch from LysZ to BzGlu, so that no particular weight toward one monomer over the other is found. Additionally, since the feed composition ratio and reactivity ratio are proportionately inverse, adjusting the monomer feed to increase cross-

propagation in one direction will decrease the cross-propagation in the opposite way. Therefore, the ideal values for both  $P_{12}$  and  $P_{21}$  are when the monomer cross-propagation rates are weighted equally.

Moving forward with this conceptual understanding, setting  $P_{12}$  equal to  $P_{21}$  and inserting the literature values for  $r_1$  and  $r_2$ , the  $f_1$  monomer feed composition of BzGlu can be found unambiguously. The quadratic expression yields an  $f_1$  value of 0.356 which represents the proportion of the feed that is comprised of BzGlu NCA, while the remaining 0.654 of the 100% total composition represents LysZ NCA. Coincidentally, the values for  $P_{12}$  and  $P_{21}$  using these reactivity ratios and feed compositions are fairly close to 50% probability. Using other reactivity ratios or feed compositions would result in other values for  $P_{12}$  and  $P_{21}$  but should still yield a copolymer of the intended general sequence. This calculated  $f_1$  value, rounded to 0.35 for BzGlu monomer, was utilized as the 'adjusted' condition for the subsequent experimental syntheses.

#### 6.4.4 Copolymerization with adjusted and unadjusted feed composition

To validate the computational results for the monomer feed composition, two reactions were prepared side-by-side with all conditions equal except for the monomer feed ratio. Representing the typical condition that assumes an equal monomer feed will produce a random sequence is the reaction with an  $f_1$  of 0.50. This condition along with the  $f_1$  of 0.35 were polymerized as before with hexylamine and periodic collection of aliquots for analysis of copolymer composition over time via NMR. The results of this comparison are shown in **Figure 6-8** as a visualization of both LysZ versus BzGlu composition and an inset of fractional

conversion over time. The initial timepoints for each  $f_1$  condition at  $t = 0$  assume the copolymer composition to be equal to the monomer composition of either 0.35 or 0.50.

Broadly, the coloration of the graphs between green for LysZ and red for BzGlu indicates significant differences in copolymer composition. For the  $f_1 = 0.50$  condition, the initial timepoint of 3.5 hours shows a drastic jump to an  $F_1$  of 0.634, representing BzGlu being incorporated into the chain. Given the higher kinetic rate constant ( $k_{11}$ ) at 8.12 and higher reactivity ratio ( $r_1$ ) at 1.86, not only does BzGlu NCA monomer add to the growing chain faster, it is more likely to self-propagate once it becomes the active terminal end. It is likely that chains polymerized with an  $f_1$  of 0.50 have longer blocks of BzGlu before adding LysZ units when the monomer feed is not adjusted. In contrast, the  $f_1$  of 0.35 reaction shows a copolymer composition of 0.495 at the first timepoint, which is an excellent outcome for a target of 0.50 for a random or alternating polymer

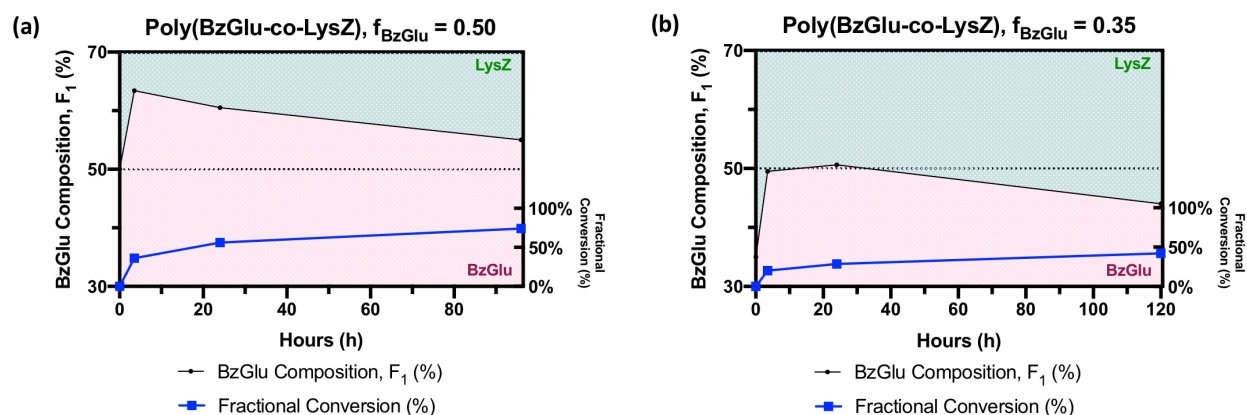


**Figure 6-8. Copolymerization of poly(LysZ-co-BzGlu) chains with monomer feed adjustment.** Reactions of an (a) unadjusted  $f_1$  value of 0.50 and (b) adjusted  $f_1$  value of 0.35 with respect to BzGlu NCA were prepared. Copolymer composition of BzGlu at timepoints through 120 hours is represented by the plotted points on the left x-axis and the red shading beneath the curve, while LysZ is represented in the remainder of the graph shaded green. The horizontal dotted line at 50% represents the target copolymer composition. The inset on both (a) and (b) is the fractional conversion at each timepoint and plotted on the right x-axis.

sequence. This suggests that the theoretically calculated feed ratio based on the reactivity ratios does indeed counteract the propensity of BzGlu to add in an uncontrolled manner to the copolymer chain.

An additional observation to be made is the fractional conversion for each  $f_1$  reaction. Given that BzGlu has the higher  $k_{11}$  compared to  $k_{22}$  as being nearly 2.5 times faster to polymerize, the same timepoints show a marked difference in fractional composition. The difference indicates that the uncontrolled addition of BzGlu NCA monomers in the  $f_1 = 0.50$  reaction represents a larger proportion of the chain that adds much faster than LysZ as seen in the  $f_1 = 0.35$  reaction. Overall, this is strong evidence to support that the computational approach to this two-monomer system is accurate in producing copolymers of nearly equal incorporation of both monomers.

A final observation for these reactions is that the later timepoints show a drifting back toward the initial monomer feed composition. All copolymer systems that reach the full theoretical fractional conversion will also reach the polymer composition that matches the initial monomer composition. That is, if every monomer is added to the chain and converted to polymer units, there is a conservation of mass such that the final composition will be the same as the ratio of monomers that were added at the beginning. The compositional drift seen in these reactions is a demonstration of the monomer in the feed being consumed disproportionately and the system returning to unbalance. Since BzGlu adds faster, the drift toward LysZ indicates that the monomer feed is lacking BzGlu monomers and is biased toward adding many LysZ monomers as the more abundant species. While the adjusted polymer chains with an initial  $f_1$  of 0.35 started

with an equal incorporation of both monomers, the later stages of the chain are distinctly biased toward LysZ as the only remaining monomer. For the unadjusted chains of  $f_1 = 0.50$ , there will be a more block-like distribution as the BzGlu is added at the beginning and the LysZ is added almost exclusively at the end. This represents the exact need for monomer supplementation to maintain the copolymer general sequence.

#### 6.4.5 Drift correction with monomer supplementation

The first step for addressing composition drift that occurs as the chain grows and monomer is consumed is defining the window of acceptable composition imbalance for the application. For cases where the sequence is not as important to the function, the system can tolerate less frequent batch additions of monomer while the more dependent applications will need more frequent synthetic attention. From the previous studies exploring the effects of an adjusted feed ratio, it can be determined that the resulting compositional drift does not have a significant impact until the final timepoint taken at 5 days. Assuming a linear decrease as shown by default in connecting the individual data points, even up through 60 hours the polymer appears to stay within a few percentage points of the target 0.50 composition. This indicates that the monomers are likely still adding equally to the growing chain as the fractional conversion increases. For this reason, I hypothesized that a more tolerant approach to monomer supplementation would be sufficient, though many two-monomer systems and material applications may require more frequent attention.

Since the monomers are adding in equal amounts based on the adjustment for reactivity ratios, the consumption of the entire monomer pool will slowly shift the monomer composition as the denominator drops. That is, an initial 35/65 combination as 35% will become 31.5% at 25/55 and 25% at 15/45. This shift is no longer sufficiently adjusting for the reactivity ratios as concentration of BzGlu NCA is falling below the target 0.35. When supplementing monomer, only this BzGlu needs to be added to the reaction to restore the  $f_1$  to 0.35.

To calculate the timing of monomer supplementation and the amount needed to restore the monomer composition, we must return to the foundational equations derived previously. While it may be possible to estimate the amount of monomer to supplement using estimations based on fractional conversion, assumed equal monomer addition, and a series of approximations to restore the balance, a more nuanced modeling approach was used. To determine the amount of BzGlu monomer needed to supplement the adjusted copolymer reaction and the correct timing, a Runge-Kutta method was applied to a derivation of **Equation 1** as the consumption of M1 over time. This iterative computational approach was used to solve the resulting non-linear differential equation that is both coupled and first order. The previously found values for  $k_{11}$  and  $k_{22}$  from the homopolymerization studies, the reactivity ratios  $r_1$  and  $r_2$  from the literature, and the initiator and monomer concentrations from the physical reaction were used to solve this system as detailed in reference 411. The results of this computational modeling to estimate monomer consumption indicated the addition of nearly 2 equivalents of BzGlu NCA at 53 hours into the reaction.

For the experimental validation of this drift correction, three reactions were set up as before with one at  $f_1 = 0.50$  and one at  $f_1 = 0.35$ . In addition to these two as compared for the previous section is that a variation of the  $f_1 = 0.35$  had additional drift correction via batch supplementation of BzGlu. The  $F_1$  copolymer composition of BzGlu is shown in **Figure 6-9**. As before, aliquots were taken from each reaction at specific timepoints and quenched for NMR analysis to monitor copolymer composition throughout propagation. The timepoints for this were 24 hours, 48 hours, and 72 hours with monomer supplementation at 53 hours as marked by the vertical magenta line in the graph.

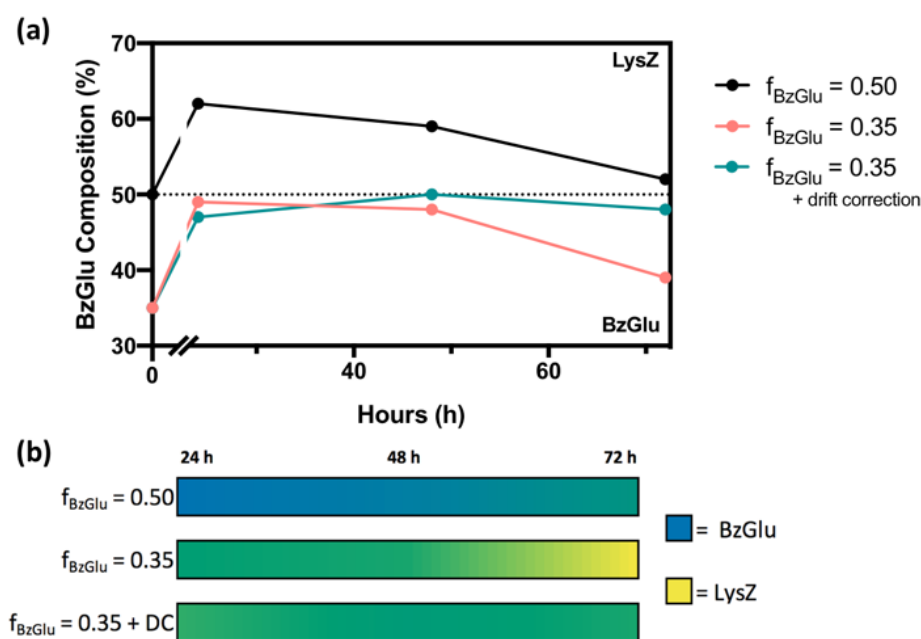


**Figure 6-9. Copolymerization of poly(LysZ-co-BzGlu) chains with semi-batch drift correction.** Three conditions are compared: the unadjusted  $f_1$  of 0.50, the adjusted  $f_1$  of 0.35, and the adjusted  $f_1$  of 0.35 with drift correction via additional BzGlu NCA. The copolymer composition over 72 hours in (a) is in terms of BzGlu with the target marked by the horizontal dotted line at 50%. Additional monomer is added at 53 hours to the  $f_1$  of 0.35 with drift correction as indicated by the vertical maroon dotted line. This is also represented with colors (b) as the majority character across time. BzGlu is blue while LysZ is yellow, with an even 50/50 mix being shown as a green color

For these reactions, the same initial jump to  $F_1 = 0.62$  for  $f_1 = 0.50$  and  $F_1 = 0.49$  for both  $f_1 = 0.35$  reactions is seen at the first 24 hour timepoint as successfully balanced reactivity ratios. Further, the same compositional drift is seen in the  $f_1 = 0.50$  and  $f_1 = 0.35$  without supplemental BzGlu, dropping to 0.52 and 0.39 respectively at the final 72 hour timepoint. These will ultimately drop until they match the initial monomer feed as every monomer eventually adds to the chain. However, in the  $f_1 = 0.35$  with drift correction at 53 hours, the  $F_1$  continues to hover around 0.48 at the 72 hour timepoint. In comparison to the exact same polymerization reaction which falls to an  $F_1$  of 0.39, this is a significant improvement on maintaining copolymer composition over time. The same trend is shown in color in **Figure 6-9b**, with BzGlu composition represented by blue, LysZ composition represented by yellow, and an equal mix of both residues appearing as green. The non-drift corrected reactions both show a fade to the more yellow color, with  $f_1 = 0.50$  beginning much more blue and becoming green while  $f_1 = 0.35$  starts green but shifts to yellow representing LysZ. In contrast, the supplemented  $f_1 = 0.35$  remains fully green. These side-by-side comparisons of both monomer feed adjustment from 0.50 to 0.35 along with the drift correction between the two reactions of 0.35 are strong evidence supporting general sequence control of an NCA copolymer for BzGlu and LysZ.

## 6.5 Conclusion

In this work, I used BzGlu and LysZ NCA monomers to demonstrate the practical application of fundamental polymerization concepts to impart general sequence control over copolymer synthesis. These two monomers with their respective protecting groups are fairly well

understood in the literature and served as a strong foundation for the exploration of these concepts and applications. The experimental values and computational solutions could be cross-checked against each other and with similar studies conducted in the literature to effectively produce a random copolymer despite different reactivities between the monomers. Additionally, these two unprotected residues are charged at neutral pH giving them the unique potential to form a zwitterionic copolymer that can be incorporated more broadly into the mixed PAA chains that I developed in the previous chapter.

I first studied the homopolymerization kinetics of the BzGlu NCA and LysZ NCA monomers separately to evaluate the reaction rates of each. I found that BzGlu polymerizes almost 2.5 times as fast as LysZ, confirming the need address the other parameters of polymerization to account for this difference in chemical reactivity. The values obtained for this portion as  $k_{11}$  and  $k_{22}$  were used in the computational approaches for both finding the reactivity ratios of monomers with respect to each other as well as the modeling for determining the rate of BzGlu consumption for batch supplementation. Both of these parameters were evaluated with respect to the existing work in the literature and found to deviate predictably given the conditions in our lab. However, this work set the foundation for the evaluation of future NCA copolymers of interest that use experimental and computational approaches in tandem for a robust understanding of the system.

Specifically, the Mayo-Lewis equation and the deterministic outcome terminal model provided a route to offset the different reactivity ratios of the monomers by changing their initial feed composition. Broadly, a monomer like BzGlu that is more likely to self-propagate instead of

cross-propagate as represented by a high reactivity ratio should have a lower monomer concentration. The general sequence control over the copolymerization depends on the adjustment of these critical parameters to ensure that any given position of the chain has an equally likely chance to add either monomer, yielding a random sequence. This concept was solved computationally as an ideal  $f_1$  feed composition of 0.35 for BzGlu. I found that the application of this value to the reaction preparation did indeed yield a copolymer with an  $F_1$  polymer composition near 0.50 compared to the unadjusted  $f_1$  that had an imbalanced  $F_1$  from the beginning. The computational approach was therefore validated by the experimental outcome for this section, as the calculations appropriately corrected for unequal monomer kinetic rates to yield a 0.50 copolymer composition.

After the application of the initial feed composition to the experimental polymerization conditions, I noticed the compositional drift of the copolymer as the reaction progressed to a higher fractional conversion. This is representative of the monomers being consumed as they are added to the chain, causing a shift in the monomer composition  $f_1$  but also in reducing the monomer concentration as being physically unable to interact with the active terminal end. This drift was corrected by adding more BzGlu NCA monomer as a supplement to restore the ideal  $f_1$  for random copolymerization. A modeling approach that utilized the experimentally found values for  $k_{11}$  and  $k_{22}$ , the reactivity ratios  $r_1$  and  $r_2$ , and the concentrations of initiator and monomer added to the reaction flask yielded values for monomer consumption. The resulting quantities for supplementing additional BzGlu monomer and the timepoint to add it were both accurate

and effective in maintaining the  $F_1$  BzGlu copolymer composition even after a high fractional conversion over many days.

Overall, this chapter represents an extension of the mixed PAA systems developed in the previous chapter as a more nuanced understanding of copolymerization kinetics in the implementation of general sequence control. Using BzGlu and LysZ for this pilot system, the data shown here provides excellent evidence that the fundamental kinetic parameters of the monomer systems can be found experimentally, fed back into the computational equations, and yield the ideal conditions to produce a copolymer with an equal incorporation of both monomers. This approach can be applied to any monomers of any identity to ensure random copolymerization that is maintained throughout the copolymer length with the correct monomer feed composition and drift correction with monomer supplementation. Importantly, since this approach is derived from the fundamental equations underlying polymer kinetics, it can be easily applied to the general control of copolymer systems with other target sequences aside from random.

## 6.6 Acknowledgements

I would like to acknowledge Rajan Burt for the role he played in conceptual framework and development of the work featured in this chapter. Rajan's enthusiasm for applying NCA materials to his interests and foundational knowledge of biomaterials and polymer kinetics were indispensable. I would like to thank Rajan for his role in experimental design, conducting kinetics studies, and the modeling/computational work that is also featured in this MS thesis. I would like

to acknowledge John Torkelson for his advice on these experimental designs and expertise in polymer chemical engineering and material science.

## 6.7 Publication information

Portions of the work in this chapter is in preparation for publication with the following citation information:

Burt RA\*, Frey MA\*, Torkelson JM, Scott EA. Kinetic Analysis Reveals General Sequence Control Capability of NCA Copolymerization with Implications for Zwitterionic Poly(amino acid) Biomaterials. (2021).

Further details on the computational approach and simulations described in this chapter can be found with the following citation information:

Burt, RA. Stealth Polyamino-acid Biomaterials: Chemical Synthesis, Polymer Design & Nanomedicine Applications. (Northwestern University, 2019).

## CHAPTER 7

# Concluding Remarks and Future Directions

### 7.1 Concluding remarks

The focus of this work was to advance the state of nanocarrier therapeutics by optimizing the development highly functionalized self-assembling polymer nanomaterials. I accomplished this goal in two parts, beginning with the improved synthesis of PEG-*b*-PPS and two demonstrations of its versatility toward biological applications. Second, I developed a new biomimetic PAA-*b*-PPS material for highly functional self-assembling nanocarriers and demonstrated an approach for exerting general sequence control over copolymerization.

#### 7.1.1 PEG-*b*-PPS optimizations

Previous protocols for the synthesis of PEG-*b*-PPS material have been inconsistent and largely inefficient with low yields and long workup procedures. While these approaches did successfully produce the desired copolymer in good quality, the discrepancies listed above along with the required higher-level chemistry knowledge led to a steep learning curve and poor outcomes, creating a consequential barrier for those wishing to utilize this material for unique applications. I found that several aspects of the reaction conditions and workup protocols for all three synthetic steps could be significantly improved. The resulting optimized, and in many ways simplified, synthesis has a drastically reduced requirement for time, materials, and cost along with an exceptionally improved yield and purity. The material made from the reevaluated

protocol was able to form three representative nanostructure morphologies, demonstrating equivalent polymer quality despite the modifications. This new protocol will allow for the widespread and scaled-up utilization of PEG-*b*-PPS as a material for nanocarrier therapeutics with much improved reliability.

### 7.1.2 Tuning PEG-*b*-PPS nanocarriers for uptake and therapeutic potential

Drug delivery vehicles impart a number of benefits to enhance drug targeting and uptake by modifying their size, charge, and morphology to best suit the preferences of the target cell type. I demonstrated this tunability of PEG-*b*-PPS nanoparticles to increase uptake into the non-phagocytic cell lines ASZ (basal cell carcinoma) and DAOY (medulloblastoma). I first looked at baseline nanocarrier uptake of micelle and polymersome morphologies as spherical particles with a sizable difference in diameter. DAOY cells were able to take up both the smaller micelles and the larger polymersomes while ASZ cells were only able to internalize micelles. To enhance this uptake, I made four cationic polymer mixtures with increasing positive surface charge for both micelles and polymersomes. The charged nanoparticles increased uptake in both cell lines in a modest dose-dependent manner: cationic micelles and polymersomes in DAOY cells, and cationic micelles in ASZ cells. Further, these cationic formulations were able to increase uptake without an additional increase in cytotoxicity, which is an important consideration for all cationic materials. This work sets a strong foundation for the development of PEG-*b*-PPS nanocarriers for these non-phagocytic cell lines with enhanced uptake.

Nanocarriers are ideal solutions for delivering hydrophobic small molecule therapeutics that are insoluble in aqueous media and have poor bioavailability. One such example is the vimentin inhibitor FiVe1 as a potential therapeutic for inhibiting inflammasome-mediated tissue injury. I developed a nanocarrier formulation of FiVe1-loaded micelles via flash nanoprecipitation with reliable loading at three dose levels as quantified by a customized HPLC protocol. These formulations were non-cytotoxic to the BMDM cell line with controls showing minimal impact on the inflammasome activation as measured by IL-1 $\beta$  and sufficient cell uptake after LPS challenge. However, the comparison of matched doses of free FiVe1 and FiVe1-loaded micelles produced no significant difference in IL-1 $\beta$  production from the negative control. Beyond the outcome of the nanocarrier treatments, I was unable to replicate the IC<sub>50</sub> of the free drug in this assay. This suggests FiVe1 vimentin inhibition may be a separate mechanism that is independent from that which is required for preventing inflammasome activation. Despite this outcome, the FiVe1-loaded micelle formulations were successfully developed as a therapeutic delivery system for this drug, and this work will serve as a baseline to future studies investigating diverse applications of this promising small molecule vimentin inhibitor.

### 7.1.3 Development of NCA-based nanocarriers

Despite the many advantages of PEG-based materials for biomedical applications, this material suffers from a number of drawbacks that range from the inconvenient limited functionalization to the more concerning development of adverse reactions of anti-PEG antibodies present in the general population. With this in mind, I sought to develop a novel

nanocarrier material comprised of poly(amino acid) blocks and PPS that can replicate the beneficial features of PEG without the associated disadvantages. I first developed a strategy to rapidly produce and evaluate diblock copolymers with minimal material using a combinatorial approach that incorporates a protective linker for unrestricted pairing. I used poly(sarcosine) as a minimally complex prototype material to evaluate the potential of PAA-*b*-PPS materials to assemble into aqueous-stable formulations. Using the FTP linker, I synthesized five representative copolymers of NCA and PPS chemistries with hydrophilic weight fractions between 0.25 and 0.52. I optimized nanostructure assembly via flash nanoprecipitation and characterized the morphologies via DLS, nsTEM, and SAXS modeling. I found that this pSarc-*b*-PPS material is capable of forming micelles and polymersome vesicles at predictable ranges.

To demonstrate robustness of this assembly strategy toward more complex and functional backbones, I expanded the library of PAA-*b*-PPS materials to include polymer blocks of lysine, glutamic acid, tryptophan, and tyrosine using the same pipeline. I assembled representative diblock copolymers of each material with similar hydrophilic weight fractions, between 0.62 and 0.67. Each of the PAA-*b*-PPS materials formed supramolecular assemblies with a diversity of morphologies and variability in hydrophilic weight fraction ranges that mirror the physiochemical properties of the amino acid side chains. This work represents a significant effort in the development of a biomimetic PAA-*b*-PPS material with the benefits of modular amino acid functionalities and the PPS oxidation sensitivity for triggered release, endosomal escape, and effective clearance.

#### 7.1.4 General sequence control of NCA-based functional materials

In contrast to the general assumption that a copolymer will be a random sequence if monomers are added to the reaction at the same time, the order of units instead depends on the kinetic properties of each monomer. I used these fundamental principles and equations to demonstrate the ability to impart general sequence control over an NCA copolymer of protected lysine and glutamic acid. For this strategy, I used experimental data to evaluate synthetic outcomes in conjunction with a modeling computational approach. I implemented the resulting theoretical estimations for the adjusted monomer feed composition and semi-batch maintenance into the synthetic protocol. These values were successfully able to maintain the statistically random incorporation of NCA monomers into the copolymer chain even through high fractional conversions as a demonstration of general sequence control. This combined approach of experimental and computational analysis can be used to produce mixed PAA copolymers with nuanced physiochemical properties for a wide range of applications.

#### 7.2 Future directions

The work in this dissertation represents a step toward the development of diverse, highly functional polymer nanocarriers comprised of the well-established PEG-*b*-PPS and the novel PAA-*b*-PPS for biological applications. My efforts toward these goals were heavily motivated by the incredible potential of these polymers to be significantly modified toward a vast range of therapeutic goals and clinical applications. I consider my work in these chapters to establish a foundation for further understanding of these materials and future investigations to fully explore

their capabilities without hesitation. To catalyze these efforts, I describe a number of worthwhile future directions for both PEG-*b*-PPS and PAA-*b*-PPS polymers that build off of the work demonstrated in this dissertation.

### 7.2.1 Further development of PEG-*b*-PPS synthesis for scaling up and improving the assembly of unique morphologies

My optimization of the PEG-*b*-PPS polymer synthesis addressed a number of disadvantages that would have made this material difficult to further develop for large-scale biological studies or dissemination to diverse research groups. After streamlining both the materials required and physical procedures to synthesize and purify the material, the next step in advancing this material is scaling up to industrial levels. In particular, the third step of PPS polymerization remains a sensitive and highly variable reaction that is limited by the exothermic nature of the polymerization that can damage the growing chains as they form. For this reason, using amounts of propylene sulfide monomer higher than 1-2 mL will produce enough heat that the reaction cannot be effectively cooled in a water bath. A number of chemical and engineering controls can be implemented to improve even cooling of this polymerization step that are worth exploring. For example, one simple approach would be to add the monomer in smaller, more frequent batches that can dissipate the produced heat without impairing equal monomer for all chains. The glassware setup of the PPS polymerization may also have potential for modification by utilizing a shape with higher surface area for more efficient cooling or a tangential flow system to improve the rate of cooling. Each of these could offer a strategy to scale up the production of

any PPS-based material, reducing variance between smaller batches and eliminating confounding factors on large-scale *in vivo* studies.

While this work largely demonstrated the synthesis and assembly of the more conventional spherical micelle and polymersome morphologies, PEG-*b*-PPS is capable of forming more specialized structures. Unfortunately, many of these new morphologies such as BCNs and filomicelles (FMs) are especially difficult to synthesize and assemble reliably due to longer PPS lengths and delicate temporary supramolecular chain associations. Specific efforts towards improving the chances of forming these morphologies would allow for the further exploration of their unique features as therapeutic delivery vehicles. For example, FMs are known to have a low assembly success rate despite the polymer meeting known analytical and quality benchmarks. Preliminary evidence suggests that PPS homopolymer can act as an impurity in the final product that interferes with FM assembly into the delicate worm-like filaments. This can be prevented from two simultaneous angles: preventing the formation of PPS homopolymer and removing any PPS homopolymer from the final product. The reduction of sodium methoxide equivalents in my optimized synthesis can address this first approach as this base is certainly a strong enough nucleophile to initiate PPS chains independently. For the purification approach, a second precipitation of the final product into cold ether will effectively remove PPS homopolymer and PEG-*b*-PPS with longer PPS blocks as these compounds remain soluble. This second approach should also result in a more accurate NMR estimation of PPS length and a narrower distribution of polymer chains in the final material. Very early work suggests that FM polymer can be 'rescued' in this way to form FM structures from previously failed attempts. Improving the success of these

nuanced morphologies would represent a significant step forward in their development toward exciting biomedical applications.

### 7.2.2 Applications for the uptake of PEG-*b*-PPS nanocarriers into ASZ and DAOY cell lines

In Chapter 3, I describe the effective enhancement of PEG-*b*-PPS nanocarrier uptake into the non-phagocytic ASZ and DAOY cell lines with a rational selection of morphology/size and surface charge. Additional work can be done to further enhance the modest uptake seen in this work by increased surface charge until the limit of cytotoxicity or other surface modifications of targeting ligands to enhance internalization that is cell-type specific. A more extensive investigation of the ideal nanoparticle size and morphology can also be completed. Uptake can be improved through nanoparticle tuning approaches until the therapeutic potential is achieved in each cell type, which requires a combined approach once the therapeutic outcome is selected.

With these baseline preferences established, several future directions for the targeting of these cell lines are based on their clinical sources: ASZ as basal cell carcinoma and DAOY as medulloblastoma. Specifically, the Meade Lab is interested in loading a number of therapeutics that inhibit Gli as a part of the hedgehog pathway that is affected in both of these cell lines and disease processes. Hydrophobic drugs such as GANT61 and imiquimod can be effectively loaded into either micelles or polymersomes for both cell lines. Hydrophilic drugs or larger diameter complexes can be loaded into polymersomes. As with nearly all applications of nanoparticle therapeutics, the addition of a delivery vehicle for a poorly bioavailable drug or targeting of non-

phagocytic cell populations can greatly enhance the therapeutic effect while reducing off-target toxicities.

### 7.2.3 Optimization of FiVe1-loaded micelles for vimentin inhibition and other therapeutics for inflammasome modulation

While the work in Chapter 4 to develop a FiVe1-loaded micelle construct to reduce inflammasome activation had an unexpected outcome, work to understand and overcome these barriers is far from over. Two major routes for future directions can be built from the successful development of this nanoparticle therapeutic. The first of these is work that pertains to the troubleshooting of the FiVe1-loaded micelle construct. A number of follow-up studies to further investigate the mechanism of vimentin inhibition by FiVe1 would offer insight into any disconnects between the loaded dose and the therapeutic outcome. The results of this work would either offer reasonable approaches to using FiVe1 for this application of inflammasome inhibition, or it would suggest unique applications of the exact same micelle construct to impart other therapeutic effects. As described previously in Chapter 4, vimentin is an integral part of many cellular functions related to important disease states including cancer proliferation, organism development, cell motility, and many more. In this way, the work toward developing these FiVe1-loaded micelle formations would be easily transferred to these other therapeutic applications without significant additional effort.

The other major route for the development of this work is using the same micelle delivery vehicle that has shown effective uptake, minimal cytotoxicity, and the loading of different

therapeutics that may inhibit inflammasome activation. In addition to FiVe1, The Ridge Lab has identified a number of other therapeutics with this potential including Withaferin A<sup>266,413</sup> and the most well-understood MCC950.<sup>259,414</sup> Each of these small molecules would benefit from the same advantages of a nanocarrier delivery vehicle, such as the micelles used for FiVe1. Additionally, Withaferin A has a similar hydrophobic character as FiVe1 with a calculated log P between 3 and 4, suggesting that it would also load similarly into micelles. My preliminary work with this compound also appears to support this comparison. Changing the loaded therapeutic would not only maintain a similar PEG-*b*-PPS nanocarrier construct but could also be carried through the pipeline established by the Ridge Lab for this inflammasome disease model of acute lung injury. These studies would be well worth the effort to understand both FiVe1 and vimentin inhibition with other compounds, given the initial work I have presented in this dissertation.

#### 7.2.4 Expanding the library of functional NCA monomers for structural and therapeutic applications

Throughout my thesis work, the incredible range of functionality introduced by NCA monomers was a major motivation toward the development of structural polymers that feature this chemistry. The potential of these monomers is as deep as the creativity of the researcher, with features that can address nearly every aspect of the nanocarrier platform as a structural component or as a therapeutic itself. I have attempted to summarize several of these future applications in broader categories but emphasize that these are an exceedingly small fraction of the nearly infinite possibilities in NCA chemistry.

As previously described, nearly any compound with an arrangement of carboxyl and amine moieties that mirrors an amino acid has the potential to be made into an NCA monomer and polymerized with appropriate side chain protection. There are a number of reviews that focus extensively on the NCA monomers that have been made in the literature from amino acid derivatives and fully synthetic molecules. Of these, several would have a direct functional impact on the structural component of PAA-*b*-PPS as I demonstrated for the fluorescent tryptophan residue. For natural amino acids, a cysteine moiety would enable cross linking between polymer chains for enhanced stability, perhaps to withstand the harsh conditions of the GI tract in oral delivery. Cysteine would also offer the ability to make PPS brush polymers that could form unique morphologies. Histidine could be used to add a polyhistidine-tag at the end of the chain for purification and detection. Lysine, glutamic acid, and aspartic acid could be used for a charged component, to enhance amine-based conjugation, enhance charged cargo encapsulation, or to chelate metals for detection and quantification. Amino acids such as proline may impact the packing of copolymer chains and subsequent supramolecular assembly. Hydrophobic amino acids could also offer unique capabilities when incorporated into mixed monomer chains. Expanding to unnatural or exotic amino acids offers a near infinite number of options, including linkers for click chemistry, stimuli-responsive moieties, robust fluorescent signals, and many more. Considering patterns of multiple moieties as oligopeptide sequences, NCA monomers could be added in ratios that enhance degradation via enzyme cleavage sites, cell penetration, and targeting to specific intracellular compartments, which can all be influenced by short motifs 2 to 4 units in length.<sup>415,416</sup>

Another angle for future work with NCA-based materials is the development of therapeutics. Many amino acid derivatives or metabolites play critical roles in the many intersecting feedback loops of biological systems. Considering the bioactivity likely resides in the presence of individual molecules that can interact freely with the target, the peptide bonds between units of PAA chains would function as a type of pro-drug. The slow peptide hydrolysis could have PAA chains act as a sustained depot or be modified with the cleavage sites mentioned previously to alter degradation kinetics and effective dosing. One such example as a pair of derivatives acting on either side of the indoleamine 2,3-dioxygenase (IDO) pathway which regulates immune function through tryptophan metabolism.<sup>417</sup> Inhibition of this pathway is induced by the presence of 1-methyl tryptophan (1-MT) as a competitive inhibitor, which has been shown to suppress proliferation of several cancer types which induce immune tolerance.<sup>418,419</sup> On the other end, exogenous supplementation of kynurenine (Kyn) as the metabolic product of IDO has been shown to induce anti-inflammatory effects for neuroprotection in a number of diseases.<sup>420,421</sup> Both of these 1-MT and Kyn mediators of IDO maintain the amine and carboxylate moieties so that they can easily pass through the NCA pipeline to produce polymer therapeutics that can be loaded and delivered to tissues. Conveniently, 1-MT does not need additional side chain protection and could be directly cyclized into an NCA monomer while Kyn may require selective protection of the aniline group before NCA preparation.<sup>422</sup> This strategy of identifying amino acid derivatives and metabolites with biological activity would offer a wide range of potential therapeutic NCA-based materials.

A unique therapeutic that seems perfectly suited for NCA chemistry is the random copolymer therapeutic glatiramer acetate (GA) for the treatment of multiple sclerosis (MS). This formulation is a random mixture of alanine, glutamic acid, lysine, and tyrosine in chains of molecular mass 5000 to 9000 Da.<sup>423</sup> This copolymer was developed to mimic the myelin basic protein which is an autoantigen responsible for the pathophysiology of MS.<sup>424</sup> I have easily synthesized all four of these amino acid NCAs, with my work in Chapter 5 detailing the synthesis for 3 out of the 4 listed here. While not included in this work in favor of glycine and sarcosine, alanine NCA is made easily under identical conditions as glycine NCA. The lack of sequence control of residues in this therapeutic along with the modest chain lengths are perfectly suited for NCA chemistry that can easily synthesize these copolymers in a one-pot procedure under mild conditions. The NCA approach for the synthesis of GA would enable rapid production for a fraction of the commercial price and could be modified to incorporate this peptide into a structural component or to enhance delivery. While this type of random copolymer nonbiological complex drug appears to be the only one of its type thus far in the literature, there is ongoing active research of its clinical effects as an FDA-approved therapeutic that may promote the discovery of other examples that would be suited for NCA adaptation.

### 7.2.5 Development of the PAA-*b*-PPS platform for drug delivery and biological applications

My work in Chapter 5 to develop the first of a novel class of self-assembling PAA-*b*-PPS nanocarriers offers many biological applications for future directions. As a new material, there is

a wealth of basic information that can be obtained about its material properties, including a more complete understanding of the potential stable morphologies and the corresponding hydrophilic weight fraction ranges. The stability of this material over time and in harsh conditions of temperature or pH, its ability to load diverse cargo of different physiochemical properties, the release kinetics of this cargo including potential membrane permeability, and many other aspects can also be evaluated.

Additionally, there are many directions for understanding the behavior of this copolymer *in vivo*. As a prototype material intended to mirror many of the advantages of PEG-*b*-PPS nanocarriers, a direct comparison of protein adsorption and biodistribution between otherwise identical formulations would be a valuable initial set of studies. As mentioned in Chapter 5, previous work has shown the ability of pSarc to reduce protein adsorption similarly to PEG. Other comparisons of circulation half-life, uptake into a range of basic cell types and organs, clearance mechanisms, and immunogenicity would be vital investigations of this pSarc-*b*-PPS material as a capable nanocarrier. After establishing this type of baseline, these studies could be repeated for the variations of PAA backbone that are more suited to the application.

Combining the future directions of the previous section of broader NCA capabilities, using any of these other NCA monomers for the production of a highly functional mixed copolymer will change the physiochemical properties of the material. This was demonstrated to a more extreme degree in Chapter 5 as pure blocks of tryptophan-, tyrosine-, lysine-, and glutamic acid-PPS copolymers showed significant shifts in the aggregate assembly at the same hydrophilic weight fraction. Each of these variations to add fluorescence, surface charge, intrachain interactions,

and any other functionality can be explored for unique capabilities as materials and as nanocarriers. Continuing to expand the backbone to residues including glycine and alanine as spaces, or residues such as serine to more closely model the ethylene glycol, are only a handful of the vast range of possibilities.

#### 7.2.6 Incorporating general sequence control for biologically relevant motifs

The work presented in Chapter 6 demonstrated an efficient and reliable approach to exerting general sequence control over the polymerization of two NCA monomers to generate copolymers with a statistically random sequence. To continue this work with the lysine and glutamic acid derivatives directly, the next studies would assess the biological outcomes of the target zwitterion in being able to reduce protein adsorption *in vitro*. An effectively randomized sequence of lysine and glutamic acid would have an evenly distributed charge across its surface to reduce adsorption while an improperly sequenced copolymer would increase adsorption and corresponding circulation time *in vivo*. After this confirmation, a future direction could include the evaluation of the minimum number of random units needed to impart this biological effect. In this way, the Lys/Glu random pairing could be considered a motif that can be added to the terminal end of any mixed PAA copolymer for a stealth effect.

Other motifs with a loose dependence on sequence could be developed through this general sequence control pipeline. A wide range of randomized peptide motifs have been identified that impact cellular processes including protease cleavage, localization, and endosomal escape, among many others.<sup>415</sup> Non-biological effects of motifs can also be considered for

manipulating the secondary and tertiary structure of larger PAA-*b*-PPS constructs for unique supramolecular assemblies of the polymer chains.<sup>416</sup> Each of these monomer combinations can be evaluated using the same structural framework as Lys/Glu for monomer kinetics and computational adjustments to maintain general sequence control. A library of useful monomer pairings can be rapidly developed using the work in Chapter 6 as a blueprint and incorporated into future PAA-materials.

## References

1. Hopkins, A. L. & Groom, C. R. The druggable genome. *Nat Rev Drug Discov* **1**, 727–730 (2002).
2. Kalepu, S. & Nekkanti, V. Insoluble drug delivery strategies: review of recent advances and business prospects. *Acta Pharm Sin B* **5**, 442–453 (2015).
3. Hodgson, J. ADMET—turning chemicals into drugs. *Nat Biotechnol* **19**, 722–726 (2001).
4. Jang, G. R., Harris, R. Z. & Lau, D. T. Pharmacokinetics and its role in small molecule drug discovery research. *Med Res Rev* **21**, 382–396 (2001).
5. Patra, J. K. *et al.* Nano based drug delivery systems: recent developments and future prospects. *J Nanobiotechnol* **16**, 71 (2018).
6. Lee, A. C.-L., Harris, J. L., Khanna, K. K. & Hong, J.-H. A Comprehensive Review on Current Advances in Peptide Drug Development and Design. *Int J Mol Sci* **20**, (2019).
7. Fojtu, M. *et al.* Reduction of Doxorubicin-Induced Cardiotoxicity Using Nanocarriers: A Review. *Curr Drug Metab* **18**, 237–263 (2017).
8. Yoo, J.-W., Chambers, E. & Mitragotri, S. Factors that Control the Circulation Time of Nanoparticles in Blood: Challenges, Solutions and Future Prospects. *Curr Pharm Design* **16**, 2298–2307 (2010).
9. Passirani, C., Barratt, G., Devissaguet, J. P. & Labarre, D. Long-circulating nanoparticles bearing heparin or dextran covalently bound to poly(methyl methacrylate). *Pharmaceut Res* **15**, 1046–1050 (1998).
10. Roberts, M. J., Bentley, M. D. & Harris, J. M. Chemistry for peptide and protein PEGylation. *Adv Drug Deliv Rev* **54**, 459–476 (2002).
11. D'souza, A. A. & Shegokar, R. Polyethylene glycol (PEG): a versatile polymer for pharmaceutical applications. *Expert Opin Drug Deliv* **13**, 1257–1275 (2016).
12. Veronese, F. M. & Pasut, G. PEGylation, successful approach to drug delivery. *Drug Discovery Today* **10**, 1451–1458 (2005).

13. Harris, J. M. & Chess, R. B. Effect of pegylation on pharmaceuticals. *Nat Rev Drug Discov* **2**, 214–221 (2003).
14. Yoshioka, Y., Tsunoda, S.-I. & Tsutsumi, Y. Development of a novel DDS for site-specific PEGylated proteins. *Chem Cent J* **5**, 25 (2011).
15. Bailon, P. *et al.* Rational design of a potent, long-lasting form of interferon: a 40 kDa branched polyethylene glycol-conjugated interferon alpha-2a for the treatment of hepatitis C. *Bioconjugate Chem* **12**, 195–202 (2001).
16. Hamidi, M., Azadi, A. & Rafiei, P. Pharmacokinetic consequences of pegylation. *Drug Deliv* **13**, 399–409 (2006).
17. Mitchell, M. J. *et al.* Engineering precision nanoparticles for drug delivery. *Nat Rev Drug Discov* **20**, 101–124 (2021).
18. Merisko-Liversidge, E. M. & Liversidge, G. G. Drug nanoparticles: formulating poorly water-soluble compounds. *Toxicol Pathol* **36**, 43–48 (2008).
19. Wang, Y., Luan, Z., Zhao, C., Bai, C. & Yang, K. Target delivery selective CSF-1R inhibitor to tumor-associated macrophages via erythrocyte-cancer cell hybrid membrane camouflaged pH-responsive copolymer micelle for cancer immunotherapy. *Eur J Pharm Sci* **142**, 105136 (2020).
20. Li, H.-J. *et al.* Stimuli-responsive clustered nanoparticles for improved tumor penetration and therapeutic efficacy. *Proc Natl Acad Sci U S A* **113**, 4164–4169 (2016).
21. Tong, R. & Cheng, J. Paclitaxel-initiated, controlled polymerization of lactide for the formulation of polymeric nanoparticulate delivery vehicles. *Angew Chem Int* **47**, 4830–4834 (2008).
22. Karabin, N. B. *et al.* Sustained micellar delivery via inducible transitions in nanostructure morphology. *Nat Commun* **9**, 624 (2018).
23. Hu, S.-H. *et al.* Core-shell nanocapsules stabilized by single-component polymer and nanoparticles for magneto-chemotherapy/hyperthermia with multiple drugs. *Adv Mater* **24**, 3627–3632 (2012).
24. Chen, W., Cheng, C.-A., Xiang, D. & Zink, J. I. Expanding nanoparticle multifunctionality: size-selected cargo release and multiple logic operations. *Nanoscale* **13**, 5497–5506 (2021).

25. Nguyen, T. L., Cha, B. G., Choi, Y., Im, J. & Kim, J. Injectable dual-scale mesoporous silica cancer vaccine enabling efficient delivery of antigen/adjuvant-loaded nanoparticles to dendritic cells recruited in local macroporous scaffold. *Biomaterials* **239**, 119859 (2020).
26. Toy, R. *et al.* TLR7 and RIG-I dual-adjuvant loaded nanoparticles drive broadened and synergistic responses in dendritic cells *in vitro* and generate unique cellular immune responses in influenza vaccination. *J Control Release* **330**, 866–877 (2021).
27. Irvine, D. J., Hanson, M. C., Rakhra, K. & Tokatlian, T. Synthetic Nanoparticles for Vaccines and Immunotherapy. *Chem Rev* **115**, 11109–11146 (2015).
28. Allen, S., Liu, Y.-G. & Scott, E. Engineering nanomaterials to address cell-mediated inflammation in atherosclerosis. *Regen Eng Transl Med* **2**, 37–50 (2016).
29. Allen, S. D., Bobbala, S., Karabin, N. B., Modak, M. & Scott, E. A. Benchmarking Bicontinuous Nanospheres against Polymersomes for *in vivo* Biodistribution and Dual Intracellular Delivery of Lipophilic and Water-Soluble Payloads. *ACS Appl Mater Interfaces* **10**, 33857–33866 (2018).
30. Matsumura, Y. & Maeda, H. A new concept for macromolecular therapeutics in cancer chemotherapy: mechanism of tumorotropic accumulation of proteins and the antitumor agent smancs. *Cancer Res* **46**, 6387–92 (1986).
31. Alexis, F., Pridgen, E., Molnar, L. K. & Farokhzad, O. C. Factors Affecting the Clearance and Biodistribution of Polymeric Nanoparticles. *Mol Pharmaceutics* **5**, 505–515 (2008).
32. Hussain, K. A. & Yi, P. Heteroaggregation of Neutral and Charged Nanoparticles: A Potential Method of Making Core–Shell Nanohybrids through Self-Assembly. *J Phys Chem C* **124**, 19282–19288 (2020).
33. Fratoddi, I. Hydrophobic and Hydrophilic Au and Ag Nanoparticles. Breakthroughs and Perspectives. *Nanomaterials (Basel)* **8**, (2017).
34. Knop, K., Hoogenboom, R., Fischer, D. & Schubert, U. S. Poly(ethylene glycol) in Drug Delivery: Pros and Cons as Well as Potential Alternatives. *Angew Chem Int* **49**, 6288–6308 (2010).
35. Bragonzi, A. *et al.* Comparison between cationic polymers and lipids in mediating systemic gene delivery to the lungs. *Gene Ther* **6**, 1995–2004 (1999).

36. Dobrovolskaia, M. A., Aggarwal, P., Hall, J. B. & McNeil, S. E. Preclinical Studies To Understand Nanoparticle Interaction with the Immune System and Its Potential Effects on Nanoparticle Biodistribution. *Mol Pharmaceutics* **5**, 487–495 (2008).
37. Graña-Suárez, L., Verboom, W. & Huskens, J. Fluorescent supramolecular nanoparticles signal the loading of electrostatically charged cargo. *Chem. Commun.* **52**, 2597–2600 (2016).
38. Su, C. *et al.* Absorption, distribution, metabolism and excretion of the biomaterials used in Nanocarrier drug delivery systems. *Adv Drug Deliv Rev* **143**, 97–114 (2019).
39. Frey, M., Bobbala, S., Karabin, N. & Scott, E. Influences of nanocarrier morphology on therapeutic immunomodulation. *Nanomedicine* **13**, 142 (2018).
40. Richtering, W., Alberg, I. & Zentel, R. Nanoparticles in the Biological Context: Surface Morphology and Protein Corona Formation. *Small* **16**, e2002162 (2020).
41. da-Silva-Freitas, D., Boldrini-França, J. & Arantes, E. PEGylation: a successful approach to improve the biopharmaceutical potential of snake venom thrombin-like serine protease. *Protein Peptide Lett* **22**, 1133–1139 (2015).
42. Kulkarni, S. A. & Feng, S.-S. Effects of particle size and surface modification on cellular uptake and biodistribution of polymeric nanoparticles for drug delivery. *Pharmaceut Res* **30**, 2512–2522 (2013).
43. Blanco, E., Shen, H. & Ferrari, M. Principles of nanoparticle design for overcoming biological barriers to drug delivery. *Nat Biotechnol* **33**, 941–951 (2015).
44. McCright, J. C. & Maisel, K. Engineering drug delivery systems to overcome mucosal barriers for immunotherapy and vaccination. *Tissue Barriers* **8**, 1695476 (2020).
45. Saraiva, C. *et al.* Nanoparticle-mediated brain drug delivery: Overcoming blood-brain barrier to treat neurodegenerative diseases. *J Control Release* **235**, 34–47 (2016).
46. Owens, D. E. & Peppas, N. A. Opsonization, biodistribution, and pharmacokinetics of polymeric nanoparticles. *Int J Pharmaceut* **307**, 93–102 (2006).
47. Sarin, H. *et al.* Physiologic upper limit of pore size in the blood-tumor barrier of malignant solid tumors. *J Transl Med* **7**, 1–13 (2009).

48. Yi, S. *et al.* Tailoring Nanostructure Morphology for Enhanced Targeting of Dendritic Cells in Atherosclerosis. *ACS Nano* **10**, 11290–11303 (2016).
49. Elci, S. G. *et al.* Surface Charge Controls the Suborgan Biodistributions of Gold Nanoparticles. *ACS Nano* **10**, 5536–5542 (2016).
50. Ishiwata, H., Suzuki, N., Ando, S., Kikuchi, H. & Kitagawa, T. Characteristics and biodistribution of cationic liposomes and their DNA complexes. *J Control Release* **69**, 139–148 (2000).
51. He, C., Hu, Y., Yin, L., Tang, C. & Yin, C. Effects of particle size and surface charge on cellular uptake and biodistribution of polymeric nanoparticles. *Biomaterials* **31**, 3657–3666 (2010).
52. Sonavane, G., Tomoda, K. & Makino, K. Biodistribution of colloidal gold nanoparticles after intravenous administration: effect of particle size. *Colloids Surf B* **66**, 274–280 (2008).
53. Talamini, L. *et al.* Influence of Size and Shape on the Anatomical Distribution of Endotoxin-Free Gold Nanoparticles. *ACS Nano* **11**, 5519–5529 (2017).
54. Huang, X., Teng, X., Chen, D., Tang, F. & He, J. The effect of the shape of mesoporous silica nanoparticles on cellular uptake and cell function. *Biomaterials* **31**, 438–448 (2010).
55. Geng, Y. *et al.* Shape effects of filaments versus spherical particles in flow and drug delivery. *Nat Nanotechnol* **2**, 249–255 (2007).
56. Kim, T. H. *et al.* Filamentous, mixed micelles of triblock copolymers enhance tumor localization of indocyanine green in a murine xenograft model. *Mol Pharmaceutics* **9**, 135–143 (2012).
57. Dowling, D. J. *et al.* Toll-like receptor 8 agonist nanoparticles mimic immunomodulating effects of the live BCG vaccine and enhance neonatal innate and adaptive immune responses. *J Allergy Clin Immunol* **140**, 1339–1350 (2017).
58. Dreaden, E. C., Austin, L. A., Mackey, M. A. & El-Sayed, M. A. Size matters: gold nanoparticles in targeted cancer drug delivery. *Ther Deliv* **3**, 457–478 (2012).
59. Zuckerman, J. E., Choi, C. H. J., Han, H. & Davis, M. E. Polycation-siRNA nanoparticles can disassemble at the kidney glomerular basement membrane. *Proc Natl Acad Sci U S A* **109**, 3137–3142 (2012).

60. Longmire, M., Choyke, P. L. & Kobayashi, H. Clearance properties of nano-sized particles and molecules as imaging agents: considerations and caveats. *Nanomedicine (Lond)* **3**, 703–717 (2008).
61. de Barros, A. B., Tsourkas, A., Saboury, B., Cardoso, V. N. & Alavi, A. Emerging role of radiolabeled nanoparticles as an effective diagnostic technique. *EJNMMI Res* **2**, 39 (2012).
62. Perrault, S. D., Walkey, C., Jennings, T., Fischer, H. C. & Chan, W. C. W. Mediating tumor targeting efficiency of nanoparticles through design. *Nano Lett* **9**, 1909–1915 (2009).
63. Moghimi, S. M., Hunter, A. C. & Andresen, T. L. Factors controlling nanoparticle pharmacokinetics: an integrated analysis and perspective. *Annu Rev Pharmacol Toxicol* **52**, 481–503 (2012).
64. Kou, L. *et al.* Transporter-Guided Delivery of Nanoparticles to Improve Drug Permeation across Cellular Barriers and Drug Exposure to Selective Cell Types. *Front Pharmacol* **0**, (2018).
65. Li, S.-D. & Huang, L. Pharmacokinetics and biodistribution of nanoparticles. *Mol Pharmaceutics* **5**, 496–504 (2008).
66. Xiao, K. *et al.* The effect of surface charge on *in vivo* biodistribution of PEG-oligocholeic acid based micellar nanoparticles. *Biomaterials* **32**, 3435–3446 (2011).
67. Levchenko, T. S., Rammohan, R., Lukyanov, A. N., Whiteman, K. R. & Torchilin, V. P. Liposome clearance in mice: the effect of a separate and combined presence of surface charge and polymer coating. *Int J Pharmaceut* **240**, 95–102 (2002).
68. Park, J.-H. *et al.* Systematic surface engineering of magnetic nanoworms for *in vivo* tumor targeting. *Small* **5**, 694–700 (2009).
69. Li, Y. *et al.* Hollow Mesoporous Silica Nanoparticles with Tunable Structures for Controlled Drug Delivery. *ACS Appl Mater Interfaces* **9**, 2123–2129 (2017).
70. Yang, J., Hu, Y., Wang, R. & Xie, D. Nanoparticle encapsulation in vesicles formed by amphiphilic diblock copolymers. *Soft Matter* **13**, 7840–7847 (2017).
71. Albarki, M. A. & Donovan, M. D. Bigger or Smaller? Size and Loading Effects on Nanoparticle Uptake Efficiency in the Nasal Mucosa. *AAPS PharmSciTech* **21**, 1–8 (2020).

72. Hu, Q.-D. *et al.* Cationic supramolecular nanoparticles for co-delivery of gene and anticancer drug. *Chem. Commun.* **47**, 5572–5574 (2011).
73. Ozpolat, B., Sood, A. K. & Lopez-Berestein, G. Liposomal siRNA nanocarriers for cancer therapy. *Adv Drug Deliv Rev* **66**, 110–116 (2014).
74. Palmerston Mendes, L., Pan, J. & Torchilin, V. P. Dendrimers as Nanocarriers for Nucleic Acid and Drug Delivery in Cancer Therapy. *Molecules* **22**, (2017).
75. Patel, S., Ryals, R. C., Weller, K. K., Pennesi, M. E. & Sahay, G. Lipid nanoparticles for delivery of messenger RNA to the back of the eye. *J Control Release* **303**, 91–100 (2019).
76. Vhora, I., Lalani, R., Bhatt, P., Patil, S. & Misra, A. Lipid-nucleic acid nanoparticles of novel ionizable lipids for systemic BMP-9 gene delivery to bone-marrow mesenchymal stem cells for osteoinduction. *Int J Pharmaceut* **563**, 324–336 (2019).
77. Makita-Chingombe, F., Kutscher, H. L., DiTursi, S. L., Morse, G. D. & Maponga, C. C. Poly(lactic-co-glycolic) Acid-Chitosan Dual Loaded Nanoparticles for Antiretroviral Nanoformulations. *J Drug Deliv* **2016**, 3810175 (2016).
78. Bobbala, S., Allen, S. D. & Scott, E. A. Flash nanoprecipitation permits versatile assembly and loading of polymeric bicontinuous cubic nanospheres. *Nanoscale* **10**, 5078–5088 (2018).
79. Hutanu, D., Mark, D. F., Lihong, G. & Costel, C. D. Recent Applications of Polyethylene Glycols (PEGs) and PEG Derivatives. *Mod Chem Appl* **2**, (2014).
80. Oldenborg, P. A. *et al.* Role of CD47 as a marker of self on red blood cells. *Science* **288**, 2051–2054 (2000).
81. Yi, S. *et al.* Surface Engineered Polymersomes for Enhanced Modulation of Dendritic Cells During Cardiovascular Immunotherapy. *Adv Funct Mater* **29**, 1904399 (2019).
82. Stack, T. *et al.* Enhancing subcutaneous injection and target tissue accumulation of nanoparticles via co-administration with macropinocytosis inhibitory nanoparticles (MiNP). *Nanoscale Horiz* **6**, 393–400 (2021).
83. Cherukula, K., Nurunnabi, M., Jeong, Y. Y., Lee, Y.-K. & Park, I.-K. A targeted graphene nanoplatfom carrying histamine dihydrochloride for effective inhibition of leukemia-induced immunosuppression. *J Biomater Sci Polym Ed* **153**, 1–16 (2017).

84. Han, Q. *et al.* CpG loaded MoS<sub>2</sub> nanosheets as multifunctional agents for photothermal enhanced cancer immunotherapy. *Nanoscale* **9**, 5927–5934 (2017).
85. Zhang, H. *et al.* Graphene oxide-chitosan nanocomposites for intracellular delivery of immunostimulatory CpG oligodeoxynucleotides. *Mater Sci Eng C Mater Biol Appl* **73**, 144–151 (2017).
86. Brewer, M. G. *et al.* Nanoparticles decorated with viral antigens are more immunogenic at low surface density. *Vaccine* **35**, 774–781 (2017).
87. Lee, E. J. *et al.* Nanocage-Therapeutics Prevailing Phagocytosis and Immunogenic Cell Death Awakens Immunity against Cancer. *Adv Mater* **30**, (2018).
88. Yamazaki, Y. *et al.* Immune activation with peptide assemblies carrying Lewis y tumor-associated carbohydrate antigen. *J Pept Sci* **23**, 189–197 (2016).
89. Yang, J. *et al.* Poly- $\gamma$ -glutamic acid/chitosan nanogel greatly enhances the efficacy and heterosubtypic cross-reactivity of H1N1 pandemic influenza vaccine. *Sci Rep* **7**, 44839 (2017).
90. Thambi, T., Li, Y. & Lee, D. S. Injectable hydrogels for sustained release of therapeutic agents. *J Control Release* **267**, 57–66 (2017).
91. Ahmed, E. M. Hydrogel: Preparation, characterization, and applications: A review. *J Adv Res* **6**, 105–121 (2015).
92. Wang, K. *et al.* Functional Hydrogels and Their Application in Drug Delivery, Biosensors, and Tissue Engineering. *Int J Polym Sci* **2019**, 1–14 (2019).
93. Xie, H. *et al.* A unique thermo-induced gel-to-gel transition in a pH-sensitive small-molecule hydrogel. *Sci Rep* **7**, 8459 (2017).
94. Allen, S. D., Bobbala, S., Karabin, N. B. & Scott, E. A. On the advancement of polymeric bicontinuous nanospheres toward biomedical applications. *Nanoscale Horiz* **4**, 258–272 (2019).
95. Rizwan, S. B. *et al.* Cubosomes containing the adjuvants imiquimod and monophosphoryl lipid A stimulate robust cellular and humoral immune responses. *J Control Release* **165**, 16–21 (2013).

96. Bobbala, S. *et al.* Employing bicontinuous-to-micellar transitions in nanostructure morphology for on-demand photo-oxidation responsive cytosolic delivery and off-on cytotoxicity. *Nanoscale* **12**, 5332–5340 (2020).
97. Chemelli, A., Maurer, M., Geier, R. & Glatter, O. Optimized loading and sustained release of hydrophilic proteins from internally nanostructured particles. *Langmuir* **28**, 16788–16797 (2012).
98. Roser, M., Fischer, D. & Kissel, T. Surface-modified biodegradable albumin nano- and microspheres. II: effect of surface charges on *in vitro* phagocytosis and biodistribution in rats. *Eur J Pharm Biopharm* **46**, 255–263 (1998).
99. Yoon, J.-Y., Kim, J.-H. & Kim, W.-S. Interpretation of protein adsorption phenomena onto functional microspheres. *Colloids Surf B* **12**, 15–22 (1998).
100. Gessner, A. *et al.* Nanoparticles with decreasing surface hydrophobicities: influence on plasma protein adsorption. *Int J Pharmaceut* **196**, 245–249 (2000).
101. Salvati, A. *et al.* Transferrin-functionalized nanoparticles lose their targeting capabilities when a biomolecule corona adsorbs on the surface. *Nat Nanotechnol* **8**, 137–143 (2013).
102. Tenzer, S. *et al.* Rapid formation of plasma protein corona critically affects nanoparticle pathophysiology. *Nat Nanotechnol* **8**, 772–781 (2013).
103. Vincent, M. P. *et al.* Surface chemistry-mediated modulation of adsorbed albumin folding state specifies nanocarrier clearance by distinct macrophage subsets. *Nat Commun* **12**, 1–18 (2021).
104. Vonarbourg, A., Passirani, C., Saulnier, P. & Benoit, J.-P. Parameters influencing the stealthiness of colloidal drug delivery systems. *Biomaterials* **27**, 4356–4373 (2006).
105. Dunkelberger, J. R. & Song, W.-C. Complement and its role in innate and adaptive immune responses. *Cell Res* **20**, 34–50 (2010).
106. Janeway, C. A., Jr, Travers, P., Walport, M. & Shlomchik, M. J. *Immunobiology*. (Garland Science, 2001).
107. Moghimi, S. M., Hunter, A. C. & Murray, J. C. Long-circulating and target-specific nanoparticles: theory to practice. *Pharmacol Rev* **53**, 283–318 (2001).

108. Braet, F. *et al.* Contribution of high-resolution correlative imaging techniques in the study of the liver sieve in three-dimensions. *Microsc Res Techniq* **70**, 230–242 (2007).
109. Walkey, C. D., Olsen, J. B., Guo, H., Emili, A. & Chan, W. C. W. Nanoparticle Size and Surface Chemistry Determine Serum Protein Adsorption and Macrophage Uptake. *J Am Chem Soc* **134**, 2139–2147 (2012).
110. Papini, E., Tavano, R. & Mancin, F. Opsonins and Dysopsonins of Nanoparticles: Facts, Concepts, and Methodological Guidelines. *Front Immunol* **11**, 567365 (2020).
111. Bae, Y. H. & Park, K. Targeted drug delivery to tumors: myths, reality and possibility. *J Control Release* **153**, 198–205 (2011).
112. Hillaireau, H. & Couvreur, P. Nanocarriers' entry into the cell: relevance to drug delivery. *Cell Mol Life Sci* **66**, 2873–2896 (2009).
113. Otsuka, H., Nagasaki, Y. & Kataoka, K. PEGylated nanoparticles for biological and pharmaceutical applications. *Adv Drug Deliv Rev* **55**, 403–419 (2003).
114. Suk, J. S., Xu, Q., Kim, N., Hanes, J. & Ensign, L. M. PEGylation as a strategy for improving nanoparticle-based drug and gene delivery. *Adv Drug Deliv Rev* **99**, 28–51 (2016).
115. Kwon, G. S. & Kataoka, K. Block copolymer micelles as long-circulating drug vehicles. *Adv Drug Deliv Rev* **16**, 295–309 (1995).
116. Kabanov, A. V. *et al.* The neuroleptic activity of haloperidol increases after its solubilization in surfactant micelles. *Febs Lett* **258**, 343–345 (1989).
117. Xiao, X.-F., Jiang, X.-Q. & Zhou, L.-J. Surface Modification of Poly Ethylene Glycol to Resist Nonspecific Adsorption of Proteins. *Chinese J Anal Chem* **41**, 445–453 (2013).
118. Chen, W.-Y. *et al.* Kosmotrope-like Hydration Behavior of Polyethylene Glycol from Microcalorimetry and Binding Isotherm Measurements. *Langmuir* **29**, 4229–4265 (2013).
119. Jaiswal, A. K., Srivastava, R., Pandey, P. & Bandyopadhyay, P. Microscopic picture of water-ethylene glycol interaction near a model DNA by computer simulation: Concentration dependence, structure, and localized thermodynamics. *PLOS ONE* **13**, e0206359 (2018).
120. Wu, J. & Chen, S. Investigation of the hydration of nonfouling material poly(ethylene glycol) by low-field nuclear magnetic resonance. *Langmuir* **28**, 2137–2144 (2012).

121. Muralidharan, P., Mallory, E., Malapit, M., Hayes, D. & Mansour, H. M. Inhalable PEGylated Phospholipid Nanocarriers and PEGylated Therapeutics for Respiratory Delivery as Aerosolized Colloidal Dispersions and Dry Powder Inhalers. *Pharm* **6**, 333–353 (2014).
122. Suggs, L. J., West, J. L. & Mikos, A. G. Platelet adhesion on a bioresorbable poly(propylene fumarate-co-ethylene glycol) copolymer. *Biomaterials* **20**, 683–690 (1999).
123. Lee, G. K., Maheshri, N., Kaspar, B. & Schaffer, D. V. PEG conjugation moderately protects adeno-associated viral vectors against antibody neutralization. *Biotechnol Bioeng* **92**, 24–34 (2005).
124. Klibanov, A. L., Maruyama, K., Torchilin, V. P. & Huang, L. Amphipathic polyethyleneglycols effectively prolong the circulation time of liposomes. *Febs Lett* **268**, 235–237 (1990).
125. Gref, R. *et al.* ‘Stealth’ corona-core nanoparticles surface modified by polyethylene glycol (PEG): influences of the corona (PEG chain length and surface density) and of the core composition on phagocytic uptake and plasma protein adsorption. *Colloids Surf B* **18**, 301–313 (2000).
126. Desai, N. P., Hossainy, S. F. & Hubbell, J. A. Surface-immobilized polyethylene oxide for bacterial repellence. *Biomaterials* **13**, 417–420 (1992).
127. Freire Haddad, H., Burke, J. A., Scott, E. A. & Ameer, G. A. Clinical Relevance of Pre-Existing and Treatment-Induced Anti-Poly(Ethylene Glycol) Antibodies. *Regen Eng Transl Med* 1–11 (2021). doi:10.1007/s40883-021-00198-y
128. Jang, H.-J., Shin, C. Y. & Kim, K.-B. Safety Evaluation of Polyethylene Glycol (PEG) Compounds for Cosmetic Use. *Toxicol Res* **31**, 105–136 (2015).
129. Pasut, G. & Veronese, F. M. State of the art in PEGylation: the great versatility achieved after forty years of research. *J Control Release* **161**, 461–472 (2012).
130. Miteva, M. *et al.* Tuning PEGylation of mixed micelles to overcome intracellular and systemic siRNA delivery barriers. *Biomaterials* **38**, 97–107 (2015).
131. Mori, A., Klibanov, A. L., Torchilin, V. P. & Huang, L. Influence of the steric barrier activity of amphipathic poly(ethyleneglycol) and ganglioside GM1 on the circulation time of liposomes and on the target binding of immunoliposomes *in vivo*. *Febs Lett* **284**, 263–266 (1991).

132. Fee, C. J. & Van Alstine, J. M. Prediction of the viscosity radius and the size exclusion chromatography behavior of PEGylated proteins. *Bioconjugate Chem* **15**, 1304–1313 (2004).
133. Yang, Q. *et al.* Evading Immune Cell Uptake and Clearance Requires PEG Grafting at Densities Substantially Exceeding the Minimum for Brush Conformation. *Mol Pharmaceutics* **11**, 1250–1258 (2014).
134. Peracchia, M. T. *et al.* Stealth PEGylated polycyanoacrylate nanoparticles for intravenous administration and splenic targeting. *J Control Release* **60**, 121–128 (1999).
135. Yang, Q. & Lai, S. K. Anti-PEG immunity: emergence, characteristics, and unaddressed questions. *Wiley Interdiscip Rev Nanomed Nanobiotechnol* **7**, 655–677 (2015).
136. Perry, J. L. *et al.* PEGylated PRINT nanoparticles: the impact of PEG density on protein binding, macrophage association, biodistribution, and pharmacokinetics. *Nano Lett* **12**, 5304–5310 (2012).
137. Jeon, S. I., Lee, J. H., Andrade, J. D. & De Gennes, P. G. Protein—surface interactions in the presence of polyethylene oxide: I. Simplified theory. *J Colloid Interface Sci* **142**, 149–158 (1991).
138. Tabata, Y. & Ikada, Y. Protein Precoating of Polylactide Microspheres Containing a Lipophilic Immunopotentiator for Enhancement of Macrophage Phagocytosis and Activation. *Pharmaceut Res* **6**, 296–301 (1989).
139. Torchilin, V. P. *et al.* Poly(ethylene glycol) on the liposome surface: on the mechanism of polymer-coated liposome longevity. *Biochim Biophys Acta* **1195**, 11–20 (1994).
140. Friman, S., Rådberg, G. & Svanvik, J. Hepatic Clearance of Polyethylene Glycol 900 and Mannitol in the Pig. *Digestion* **39**, 172–180 (1988).
141. Kawai, F. *Biodegradation of Polyethers (Polyethylene Glycol, Polypropylene Glycol, Polytetramethylene glycol, and Others)*. (Biopolymers Online, 2005). doi:10.1002/3527600035.bpol9012
142. Milla, P., Dosio, F. & Cattell, L. PEGylation of proteins and liposomes: a powerful and flexible strategy to improve the drug delivery. *Curr Drug Metab* **13**, 105–119 (2012).
143. Parveen, S. & Sahoo, S. K. Long circulating chitosan/PEG blended PLGA nanoparticle for tumor drug delivery. *Eur J Pharmacol* **670**, 372–383 (2011).

144. Kozma, G., Shimizu, T., Ishida, T. & Szebeni, J. Anti-PEG antibodies: Properties, formation and role in adverse immune reactions to PEGylated nano-biopharmaceuticals. *Adv Drug Deliv Rev* **154-155**, 163–175 (2020).
145. Pasut, G., Guiotto, A. & Veronese, F. M. Protein, peptide and non-peptide drug PEGylation for therapeutic application. *Expert Opin Ther Pat* **14**, 859–894 (2005).
146. Langer, C. J. CT-2103: a novel macromolecular taxane with potential advantages compared with conventional taxanes. *Clin Lung Cancer* **6 Suppl 2**, S85–8 (2004).
147. Visentin, R., Pasut, G., Veronese, F. M. & Mazzi, U. Highly efficient technetium-99m labeling procedure based on the conjugation of N-[N-(3-diphenylphosphinopropionyl)glycyl]cysteine ligand with poly(ethylene glycol). *Bioconjugate Chem* **15**, 1046–1054 (2004).
148. Caliceti, P., Schiavon, O., Sartore, L., Monfardini, C. & Veronese, F. M. Active Site Protection of Proteolytic Enzymes by Poly(ethylene glycol) Surface Modification: *J Bioact Compat Polym* **8**, 41–50 (1993).
149. Burke, J. A. *et al.* Subcutaneous nanotherapy repurposes the immunosuppressive mechanism of rapamycin to enhance allogeneic islet graft viability. *Biorxiv* 2020.09.03.281923 (2020).
150. Allen, S. D. *et al.* Polymersomes scalably fabricated via flash nanoprecipitation are non-toxic in non-human primates and associate with leukocytes in the spleen and kidney following intravenous administration. *Nano Res* **11**, 5689–5703 (2018).
151. Nicol, E., Nicolai, T. & Durand, D. Dynamics of Poly(propylene sulfide) Studied by Dynamic Mechanical Measurements and Dielectric Spectroscopy. *Macromolecules* **32**, 7530–7536 (1999).
152. Rumyantsev, M. Living polymerizations of propylene sulfide initiated with potassium xanthates characterized by unprecedentedly high propagation rates. *Polym Chem* **12**, 1298–1309 (2021).
153. Napoli, A., Valentini, M., Tirelli, N., Müller, M. & Hubbell, J. A. Oxidation-responsive polymeric vesicles. *Nat Mater* **3**, 183–189 (2004).
154. Schillén, K., Bryskhe, K. & Mel'nikova, Y. S. Vesicles Formed from a Poly(ethylene oxide)–Poly(propylene oxide)–Poly(ethylene oxide) Triblock Copolymer in Dilute Aqueous Solution. *Macromolecules* **32**, 6885–6888 (1999).

155. Dumas, P. H. & Sigwalt, P. Living enantiosymmetric and enantioasymmetric polymerization of methylthiirane in homogeneous phase. *Chirality* **3**, 484–491 (1991).
156. Rehor, A., N Tirelli & Hubbell, J. A. A New Living Emulsion Polymerization Mechanism: Episulfide Anionic Polymerization. *Macromolecules* **35**, 8688–8693 (2002).
157. Reddy, S. T., Rehor, A., Schmoekel, H. G., Hubbell, J. A. & Swartz, M. A. *In vivo* targeting of dendritic cells in lymph nodes with poly(propylene sulfide) nanoparticles. *J Control Release* **112**, 26–34 (2006).
158. Napoli, A., Tirelli, N., Wehrli, E. & Hubbell, J. A. Lyotropic Behavior in Water of Amphiphilic ABA Triblock Copolymers Based on Poly(propylene sulfide) and Poly(ethylene glycol). *Langmuir* **18**, 8324–8329 (2002).
159. A Napoli, N Tirelli, G Kilcher, A. & Hubbell, J. A. New Synthetic Methodologies for Amphiphilic Multiblock Copolymers of Ethylene Glycol and Propylene Sulfide. *Macromolecules* **34**, 8913–8917 (2001).
160. Allen, S., Osorio, O., Liu, Y.-G. & Scott, E. Facile assembly and loading of theranostic polymersomes via multi-impingement flash nanoprecipitation. *J Control Release* **262**, 91–103 (2017).
161. Frey, M., Vincent, M., Bobbala, S., Burt, R. & Scott, E. Mapping the supramolecular assembly space of poly(sarcosine)-*b*-poly(propylene sulfide) using a combinatorial copolymer library. *Chem. Commun.* **56**, 6644–6647 (2020).
162. Halliwell, B., Clement, M. V. & Long, L. H. Hydrogen peroxide in the human body. *Febs Lett* **486**, 10–13 (2000).
163. Ohshima, H., Tatemichi, M. & Sawa, T. Chemical basis of inflammation-induced carcinogenesis. *Arch Biochem Biophys* **417**, 3–11 (2003).
164. Austin, C. D. *et al.* Oxidizing potential of endosomes and lysosomes limits intracellular cleavage of disulfide-based antibody-drug conjugates. *Proc National Acad Sci* **102**, 17987–17992 (2005).
165. Cerritelli, S., Velluto, D. & Hubbell, J. A. PEG-SS-PPS: reduction-sensitive disulfide block copolymer vesicles for intracellular drug delivery. *Biomacromolecules* **8**, 1966–1972 (2007).

166. Scott, E. A. *et al.* Dendritic cell activation and T cell priming with adjuvant- and antigen-loaded oxidation-sensitive polymersomes. *Biomaterials* **33**, 6211–6219 (2012).
167. Grindel, J. M., Jaworski, T., Piraner, O., Emanuele, R. M. & Balasubramanian, M. Distribution, metabolism, and excretion of a novel surface-active agent, purified poloxamer 188, in rats, dogs, and humans. *J Pharm Sci* **91**, 1936–1947 (2002).
168. Yamaoka, T., Tabata, Y. & Ikada, Y. Distribution and tissue uptake of poly(ethylene glycol) with different molecular weights after intravenous administration to mice. *J Pharm Sci* **83**, 601–606 (1994).
169. Zagorski, J., Debelak, J., Gellar, M., Watts, J. A. & Kline, J. A. Chemokines Accumulate in the Lungs of Rats with Severe Pulmonary Embolism Induced by Polystyrene Microspheres. *J Immunol* **171**, 5529–5536 (2003).
170. Wu, X. A., Choi, C. H. J., Zhang, C., Hao, L. & Mirkin, C. A. Intracellular fate of spherical nucleic acid nanoparticle conjugates. *J Am Chem Soc* **136**, 7726–7733 (2014).
171. Smith, S. A., Selby, L. I., Johnston, A. P. R. & Such, G. K. The Endosomal Escape of Nanoparticles: Toward More Efficient Cellular Delivery. *Bioconjugate Chem* **30**, 263–272 (2019).
172. He, Z. *et al.* Reactive oxygen species (ROS): utilizing injectable antioxidative hydrogels and ROS-producing therapies to manage the double-edged sword. *J Mater Chem B* (2021). doi:10.1039/d1tb00728a
173. Chen, W. & Li, D. Reactive Oxygen Species (ROS)-Responsive Nanomedicine for Solving Ischemia-Reperfusion Injury. *Front Chem* **8**, 732 (2020).
174. Zhu, S. *et al.* Accelerated wound healing by injectable star poly(ethylene glycol)-*b*-poly(propylene sulfide) scaffolds loaded with poorly water-soluble drugs. *J Control Release* **282**, 156–165 (2018).
175. Poole, K. M. *et al.* ROS-responsive microspheres for on demand antioxidant therapy in a model of diabetic peripheral arterial disease. *Biomaterials* **41**, 166–175 (2015).
176. Mohtadi, El, F. *et al.* ‘Tandem’ Nanomedicine Approach against Osteoclastogenesis: Polysulfide Micelles Synergically Scavenge ROS and Release Rapamycin. *Biomacromolecules* **21**, 305–318 (2020).

177. Ford, C. A. *et al.* Diflunisal-loaded poly(propylene sulfide) nanoparticles decrease *S. aureus*-mediated bone destruction during osteomyelitis. *J Orthop Res* **39**, 426–437 (2021).
178. Deng, H. *et al.* Targeted scavenging of extracellular ROS relieves suppressive immunogenic cell death. *Nat Commun* **11**, 4951 (2020).
179. Geven, M. *et al.* Sulfur-based oxidation-responsive polymers. Chemistry, (chemically selective) responsiveness and biomedical applications. *Eur Polym J* **149**, 110387 (2021).
180. Du, F., Liu, Y.-G. & Scott, E. A. Immunotheranostic Polymersomes Modularly Assembled from Tetrablock and Diblock Copolymers with Oxidation-Responsive Fluorescence. *Cell Mol Bioeng* **10**, 357–370 (2017).
181. Woghiren, C., Sharma, B. & Stein, S. Protected thiol-polyethylene glycol: a new activated polymer for reversible protein modification. *Bioconjugate Chem* **4**, 314–318 (1993).
182. Lawrence, P. B. & Price, J. L. How PEGylation influences protein conformational stability. *Curr Opin Chem Biol* **34**, 88–94 (2016).
183. Velluto, D., Demurtas, D. & Hubbell, J. A. PEG-*b*-PPS Diblock Copolymer Aggregates for Hydrophobic Drug Solubilization and Release: Cyclosporin A as an Example. *Mol Pharmaceutics* **5**, 632–642 (2008).
184. Cerritelli, S. *et al.* Aggregation behavior of poly(ethylene glycol-*bl*-propylene sulfide) di- and triblock copolymers in aqueous solution. *Langmuir* **25**, 11328–11335 (2009).
185. Vasdekis, A. E., Scott, E. A., O’Neil, C. P., Psaltis, D. & Hubbell, J. A. Precision Intracellular Delivery Based on Optofluidic Polymersome Rupture. *ACS Nano* **6**, 7850–7857 (2012).
186. Allen, S., Vincent, M. & Scott, E. Rapid, Scalable Assembly and Loading of Bioactive Proteins and Immunostimulants into Diverse Synthetic Nanocarriers Via Flash Nanoprecipitation. *J Vis Exp* **138**, e57793 (2018).
187. Han, J. *et al.* A simple confined impingement jets mixer for flash nanoprecipitation. *J Pharm Sci* **101**, 4018–4023 (2012).
188. Johnson, B. K. & Prud’homme, R. K. Chemical processing and micromixing in confined impinging jets. *AIChE Journal* **49**, 2264–2282 (2006).

189. Olivito, F. *et al.* Efficient synthesis of organic thioacetates in water. *Org Biomol Chem* **16**, 7753–7759 (2018).
190. Mahou, R. & Wandrey, C. Versatile Route to Synthesize Heterobifunctional Poly(ethylene glycol) of Variable Functionality for Subsequent Pegylation. *Polymers* **4**, 561–589 (2012).
191. Goswami, L. N., Houston, Z. H., Sarma, S. J., Jalisatgi, S. S. & Hawthorne, M. F. Efficient synthesis of diverse heterobifunctionalized clickable oligo(ethylene glycol) linkers: potential applications in bioconjugation and targeted drug delivery. *Org Biomol Chem* **11**, 1116–1126 (2013).
192. Allen, S. D. *et al.* Celastrol-loaded PEG- b -PPS nanocarriers as an anti-inflammatory treatment for atherosclerosis. *Biomater Sci* **7**, 657–668 (2019).
193. Foroozandeh, P. & Aziz, A. A. Insight into Cellular Uptake and Intracellular Trafficking of Nanoparticles. *Nanoscale Res Lett* **13**, 1–12 (2018).
194. Rejman, J., Oberle, V., Zuhorn, I. S. & Hoekstra, D. Size-dependent internalization of particles via the pathways of clathrin- and caveolae-mediated endocytosis. *Biochem J* **377**, 159–169 (2004).
195. Rappoport, J. Z. Focusing on clathrin-mediated endocytosis. *Biochem J* **412**, 415–423 (2008).
196. Conner, S. D. & Schmid, S. L. Regulated portals of entry into the cell. *Nature* **422**, 37–44 (2003).
197. Lim, J. P. & Gleeson, P. A. Macropinocytosis: an endocytic pathway for internalising large gulps. *Immunol Cell Biol* **89**, 836–843 (2011).
198. Aderem, A. & Underhill, D. M. Mechanisms of phagocytosis in macrophages. *Annu Rev Immunol* **17**, 593–623 (1999).
199. Parton, R. G. & Simons, K. The multiple faces of caveolae. *Nat Rev Mol Cell Biol* **8**, 185–194 (2007).
200. Elsabahy, M. & Wooley, K. L. Design of polymeric nanoparticles for biomedical delivery applications. *Chem Soc Rev* **41**, 2545–2561 (2012).
201. Zhao, F. *et al.* Cellular Uptake, Intracellular Trafficking, and Cytotoxicity of Nanomaterials. *Small* **7**, 1322–1337 (2011).

202. Chou, L. Y. T., Ming, K. & Chan, W. C. W. Strategies for the intracellular delivery of nanoparticles. *Chem Soc Rev* **40**, 233–245 (2010).
203. Yuan, H., Li, J., Bao, G. & Zhang, S. Variable nanoparticle-cell adhesion strength regulates cellular uptake. *Phys Rev Lett* **105**, 138101 (2010).
204. Zhang, S., Li, J., Lykotrafitis, G., Bao, G. & Suresh, S. Size-Dependent Endocytosis of Nanoparticles. *Adv Mater* **21**, 419–424 (2009).
205. Hoshyar, N., Gray, S., Han, H. & Bao, G. The effect of nanoparticle size on *in vivo* pharmacokinetics and cellular interaction. *Nanomedicine (Lond)* **11**, 673–692 (2016).
206. Zhu, M. *et al.* Physicochemical properties determine nanomaterial cellular uptake, transport, and fate. *Acc Chem Res* **46**, 622–631 (2013).
207. Meng, W., Garnett, M. C., Walker, D. A. & Parker, T. L. Penetration and intracellular uptake of poly(glycerol-adipate) nanoparticles into three-dimensional brain tumour cell culture models. *Exp Biol Med (Maywood)* **241**, 466–477 (2016).
208. Li, Y. & Gu, N. Thermodynamics of charged nanoparticle adsorption on charge-neutral membranes: a simulation study. *J Phys Chem B* **114**, 2749–2754 (2010).
209. Wang, H. X. *et al.* Surface charge critically affects tumor penetration and therapeutic efficacy of cancer nanomedicines. *Nano Today* **11**, 133–144 (2016).
210. Ma, Y., Poole, K., Goyette, J. & Gaus, K. Introducing Membrane Charge and Membrane Potential to T Cell Signaling. *Front Immunol* **8**, 1513 (2017).
211. Liu, X., Huang, N., Li, H., Jin, Q. & Ji, J. Surface and size effects on cell interaction of gold nanoparticles with both phagocytic and nonphagocytic cells. *Langmuir* **29**, 9138–9148 (2013).
212. Jiang, Y. *et al.* The Interplay of Size and Surface Functionality on the Cellular Uptake of Sub-10 nm Gold Nanoparticles. *ACS Nano* **9**, 9986–9993 (2015).
213. Chen, L. *et al.* Morphological and mechanical determinants of cellular uptake of deformable nanoparticles. *Nanoscale* **10**, 11969–11979 (2018).
214. Gratton, S. E. A. *et al.* The effect of particle design on cellular internalization pathways. *Proc Natl Acad Sci U S A* **105**, 11613–11618 (2008).

215. Barua, S. *et al.* Particle shape enhances specificity of antibody-displaying nanoparticles. *Proc National Acad Sci* **110**, 3270–3275 (2013).
216. Agarwal, R. *et al.* Mammalian cells preferentially internalize hydrogel nanodiscs over nanorods and use shape-specific uptake mechanisms. *Proc Natl Acad Sci U S A* **110**, 17247–17252 (2013).
217. Aldossari, A. A., Shannahan, J. H., Podila, R. & Brown, J. M. Influence of physicochemical properties of silver nanoparticles on mast cell activation and degranulation. *Toxicol In vitro* **29**, 195–203 (2015).
218. Huo, S. *et al.* Ultrasmall gold nanoparticles as carriers for nucleus-based gene therapy due to size-dependent nuclear entry. *ACS Nano* **8**, 5852–5862 (2014).
219. Pan, Y. *et al.* Size-dependent cytotoxicity of gold nanoparticles. *Small* **3**, 1941–1949 (2007).
220. Zhao, Y. *et al.* Interaction of mesoporous silica nanoparticles with human red blood cell membranes: size and surface effects. *ACS Nano* **5**, 1366–1375 (2011).
221. Xia, T., Kovochich, M., Liong, M., Zink, J. I. & Nel, A. E. Cationic polystyrene nanosphere toxicity depends on cell-specific endocytic and mitochondrial injury pathways. *ACS Nano* **2**, 85–96 (2008).
222. Jiang, Y.-N. *et al.* Caveolin-1 sensitizes rat pituitary adenoma GH3 cells to bromocriptine induced apoptosis. *Cancer Cell Int* **7**, 1 (2007).
223. Wei, X. *et al.* Cationic nanocarriers induce cell necrosis through impairment of Na(+)/K(+)-ATPase and cause subsequent inflammatory response. *Cell Res* **25**, 237–253 (2015).
224. Zhanataev, A. K. *et al.* Genotoxicity of cationic lipopeptide nanoparticles. *Toxicol Lett* **328**, 1–6 (2020).
225. Akinc, A., Thomas, M., Klibanov, A. M. & Langer, R. Exploring polyethylenimine-mediated DNA transfection and the proton sponge hypothesis. *J Gene Med* **7**, 657–663 (2005).
226. Hong, S. *et al.* Interaction of polycationic polymers with supported lipid bilayers and cells: nanoscale hole formation and enhanced membrane permeability. *Bioconjugate Chem* **17**, 728–734 (2006).

227. Kim, J.-S., He, L. & Lemasters, J. J. Mitochondrial permeability transition: a common pathway to necrosis and apoptosis. *Biochem Biophys Res Commun* **304**, 463–470 (2003).
228. Halestrap, A. P., McStay, G. P. & Clarke, S. J. The permeability transition pore complex: another view. *Biochimie* **84**, 153–166 (2002).
229. Peterson, T. E. *et al.* Caveolin-1 can regulate vascular smooth muscle cell fate by switching platelet-derived growth factor signaling from a proliferative to an apoptotic pathway. *Arterioscler Thromb Vasc Biol* **23**, 1521–1527 (2003).
230. Chen, D., Song, M., Mohamad, O. & Yu, S. P. Inhibition of Na<sup>+</sup>/K<sup>+</sup>-ATPase induces hybrid cell death and enhanced sensitivity to chemotherapy in human glioblastoma cells. *BMC Cancer* **14**, 716 (2014).
231. Zhang, Q. *et al.* Circulating mitochondrial DAMPs cause inflammatory responses to injury. *Nature* **464**, 104–107 (2010).
232. Knudsen, K. B. *et al.* *In vivo* toxicity of cationic micelles and liposomes. *Nanomedicine* **11**, 467–477 (2015).
233. Arvizo, R. R. *et al.* Effect of nanoparticle surface charge at the plasma membrane and beyond. *Nano Lett* **10**, 2543–2548 (2010).
234. Yu, T., Greish, K., McGill, L. D., Ray, A. & Ghandehari, H. Influence of geometry, porosity, and surface characteristics of silica nanoparticles on acute toxicity: their vasculature effect and tolerance threshold. *ACS Nano* **6**, 2289–2301 (2012).
235. Zhu, W. *et al.* Nanomechanical mechanism for lipid bilayer damage induced by carbon nanotubes confined in intracellular vesicles. *Proc Natl Acad Sci U S A* **113**, 12374–12379 (2016).
236. Baranov, M. V., Kumar, M., Sacanna, S., Thutupalli, S. & van den Bogaart, G. Modulation of Immune Responses by Particle Size and Shape. *Front Immunol* **11**, 607945 (2020).
237. Verma, A. *et al.* Surface-structure-regulated cell-membrane penetration by monolayer-protected nanoparticles. *Nat Mater* **7**, 588–595 (2008).
238. Murphy, F. A. *et al.* Length-dependent retention of carbon nanotubes in the pleural space of mice initiates sustained inflammation and progressive fibrosis on the parietal pleura. *Am J Pathol* **178**, 2587–2600 (2011).

239. Mularski, A., Marie-Anaïs, F., Mazzolini, J. & Niedergang, F. Observing Frustrated Phagocytosis and Phagosome Formation and Closure Using Total Internal Reflection Fluorescence Microscopy (TIRFM). *Methods Mol Biol* **1784**, 165–175 (2018).
240. Boyles, M. S. P. *et al.* Multi-walled carbon nanotube induced frustrated phagocytosis, cytotoxicity and pro-inflammatory conditions in macrophages are length dependent and greater than that of asbestos. *Toxicol In vitro* **29**, 1513–1528 (2015).
241. Aszterbaum, M. *et al.* Ultraviolet and ionizing radiation enhance the growth of BCCs and trichoblastomas in patched heterozygous knockout mice. *Nat Med* **5**, 1285–1291 (1999).
242. Tilley, C. *et al.* Silibinin and its 2,3-dehydro-derivative inhibit basal cell carcinoma growth via suppression of mitogenic signaling and transcription factors activation. *Mol Carcinog* **55**, 3–14 (2016).
243. Lucena, S. R. *et al.* Characterisation of resistance mechanisms developed by basal cell carcinoma cells in response to repeated cycles of Photodynamic Therapy. *Sci Rep* **9**, 4835 (2019).
244. Alonso, L. & Fuchs, E. Stem cells of the skin epithelium. *Proc National Acad Sci* **100 Suppl 1**, 11830–11835 (2003).
245. Mirza, A. N. *et al.* Combined inhibition of atypical PKC and histone deacetylase 1 is cooperative in basal cell carcinoma treatment. *JCI Insight* **2**, (2017).
246. Tang, J. Y. *et al.* Vitamin D3 inhibits hedgehog signaling and proliferation in murine Basal cell carcinomas. *Cancer Prev Res (Phila)* **4**, 744–751 (2011).
247. Vogt, A. *et al.* Interaction of dermatologically relevant nanoparticles with skin cells and skin. *Beilstein J Nanotechnol* **5**, 2363–2373 (2014).
248. Li, Y. & Monteiro-Riviere, N. A. Mechanisms of cell uptake, inflammatory potential and protein corona effects with gold nanoparticles. *Nanomedicine (Lond)* **11**, 3185–3203 (2016).
249. Li, J. *et al.* Topical Lyophilized Targeted Lipid Nanoparticles in the Restoration of Skin Barrier Function following Burn Wound. *Mol Ther* **26**, 2178–2188 (2018).
250. Jacobsen, P. F., Jenkyn, D. J. & Papadimitriou, J. M. Establishment of a human medulloblastoma cell line and its heterotransplantation into nude mice. *J Neuropathol Exp Neurol* **44**, 472–485 (1985).

251. Bar, E. E., Chaudhry, A., Farah, M. H. & Eberhart, C. G. Hedgehog signaling promotes medulloblastoma survival via Bc/II. *Am J Pathol* **170**, 347–355 (2007).
252. Meng, W. *et al.* Uptake and metabolism of novel biodegradable poly (glycerol-adipate) nanoparticles in DAOY monolayer. *J Control Release* **116**, 314–321 (2006).
253. Tchoryk, A. *et al.* Penetration and Uptake of Nanoparticles in 3D Tumor Spheroids. *Bioconjugate Chem* **30**, 1371–1384 (2019).
254. Madala, H. R., Punganuru, S. R., Ali-Osman, F., Zhang, R. & Srivenugopal, K. S. Brain- and brain tumor-penetrating disulfiram nanoparticles: Sequence of cytotoxic events and efficacy in human glioma cell lines and intracranial xenografts. *Oncotarget* **9**, 3459–3482 (2017).
255. Dausend, J. *et al.* Uptake mechanism of oppositely charged fluorescent nanoparticles in HeLa cells. *Macromol Biosci* **8**, 1135–1143 (2008).
256. Brandenberger, C. *et al.* Quantitative evaluation of cellular uptake and trafficking of plain and polyethylene glycol-coated gold nanoparticles. *Small* **6**, 1669–1678 (2010).
257. Rubartelli, A., Gattorno, M., Netea, M. G. & Dinarello, C. A. Interplay between redox status and inflammasome activation. *Trends Immunol* **32**, 559–566 (2011).
258. Santos, dos, G., Kutuzov, M. A. & Ridge, K. M. The inflammasome in lung diseases. *Am J Physiol Lung Cell Mol Physiol* **303**, L627–33 (2012).
259. Santos, dos, G. *et al.* Vimentin regulates activation of the NLRP3 inflammasome. *Nat Commun* **6**, 1–13 (2015).
260. Swanson, K. V., Deng, M. & Ting, J. P. Y. The NLRP3 inflammasome: molecular activation and regulation to therapeutics. *Nat Rev Immunol* **19**, 477–489 (2019).
261. Kelley, N., Jeltama, D., Duan, Y. & He, Y. The NLRP3 Inflammasome: An Overview of Mechanisms of Activation and Regulation. *Int J Mol Sci* **20**, (2019).
262. Zheng, D., Liwinski, T. & Elinav, E. Inflammasome activation and regulation: toward a better understanding of complex mechanisms. *Cell Discov* **6**, 1–22 (2020).
263. Guarda, G. *et al.* Type I interferon inhibits interleukin-1 production and inflammasome activation. *Immunity* **34**, 213–223 (2011).

264. Battaglia, R. A., Delic, S., Herrmann, H. & Snider, N. T. Vimentin on the move: new developments in cell migration. *F1000Res* **7**, (2018).
265. Stevens, C. *et al.* The intermediate filament protein, vimentin, is a regulator of NOD2 activity. *Gut* **62**, 695–707 (2013).
266. Bollong, M. J. *et al.* A vimentin binding small molecule leads to mitotic disruption in mesenchymal cancers. *Proc Natl Acad Sci U S A* **114**, E9903–E9912 (2017).
267. Strouhalova, K. *et al.* Vimentin Intermediate Filaments as Potential Target for Cancer Treatment. *Cancers* **12**, (2020).
268. Li, Z., Paulin, D., Lacolley, P., Coletti, D. & Agbulut, O. Vimentin as a target for the treatment of COVID-19. *BMJ Open Respir Res* **7**, (2020).
269. Razdan, S., Wang, J.-C. & Barua, S. PolyBall: A new adsorbent for the efficient removal of endotoxin from biopharmaceuticals. *Sci Rep* **9**, 8867 (2019).
270. Bianchi, M. G. *et al.* Lipopolysaccharide Adsorbed to the Bio-Corona of TiO<sub>2</sub> Nanoparticles Powerfully Activates Selected Pro-inflammatory Transduction Pathways. *Front Immunol* **8**, 866 (2017).
271. Coll, R. C. *et al.* MCC950 directly targets the NLRP3 ATP-hydrolysis motif for inflammasome inhibition. *Nat Chem Biol* **15**, 556–559 (2019).
272. Trogden, K. P. *et al.* An image-based small-molecule screen identifies vimentin as a pharmacologically relevant target of simvastatin in cancer cells. *FASEB J* **32**, 2841–2854 (2018).
273. Päll, T. *et al.* Soluble CD44 interacts with intermediate filament protein vimentin on endothelial cell surface. *PLOS ONE* **6**, e29305 (2011).
274. Surolia, R. *et al.* Vimentin intermediate filament assembly regulates fibroblast invasion in fibrogenic lung injury. *JCI Insight* **4**, (2019).
275. Ramos, I., Stamatakis, K., Oeste, C. L. & Pérez-Sala, D. Vimentin as a Multifaceted Player and Potential Therapeutic Target in Viral Infections. *Int J Mol Sci* **21**, 4675 (2020).
276. Mónico, A., Duarte, S., Pajares, M. A. & Pérez-Sala, D. Vimentin disruption by lipoxidation and electrophiles: Role of the cysteine residue and filament dynamics. *Redox Biol* **23**, 101098 (2019).

277. Del Grosso, C. A. *et al.* Surface hydration for antifouling and bio-adhesion. *Chem Sci* **11**, 10367–10377 (2020).
278. Banerjee, S. S., Aher, N., Patil, R. & Khandare, J. Poly(ethylene glycol)-Prodrug Conjugates: Concept, Design, and Applications. *J Drug Deliv* **2012**, 1–17 (2012).
279. Zurad, E. G. & Johanson, J. F. Over-the-counter laxative polyethylene glycol 3350: an evidence-based appraisal. *Curr Med Res Opin* **27**, 1439–1452 (2011).
280. Thi, T. T. H. *et al.* The Importance of Poly(ethylene glycol) Alternatives for Overcoming PEG Immunogenicity in Drug Delivery and Bioconjugation. *Polymers* **12**, 298 (2020).
281. Webster, R. *et al.* PEGylated proteins: evaluation of their safety in the absence of definitive metabolism studies. *Drug Metab Dispos* **35**, 9–16 (2007).
282. Neun, B. W., Barenholz, Y., Szebeni, J. & Dobrovolskaia, M. A. Understanding the Role of Anti-PEG Antibodies in the Complement Activation by Doxil *in vitro*. *Molecules* **23**, 1700 (2018).
283. Ganson, N. J. *et al.* Pre-existing anti-polyethylene glycol antibody linked to first-exposure allergic reactions to pegnivacogin, a PEGylated RNA aptamer. *J Allergy Clin Immunol* **137**, 1610–1613.e7 (2016).
284. Erdeljic Turk, V. Anaphylaxis associated with the mRNA COVID-19 vaccines: Approach to allergy investigation. *Clin Immunol* **227**, 108748 (2021).
285. Dams, E. T. *et al.* Accelerated blood clearance and altered biodistribution of repeated injections of sterically stabilized liposomes. *J Pharmacol Exp Ther* **292**, 1071–1079 (2000).
286. Li, C. *et al.* Prolongation of time interval between doses could eliminate accelerated blood clearance phenomenon induced by pegylated liposomal topotecan. *Int J Pharmaceut* **443**, 17–25 (2013).
287. Luo, N. *et al.* PEGylated graphene oxide elicits strong immunological responses despite surface passivation. *Nat Commun* **8**, 14537 (2017).
288. Suzuki, T. *et al.* Influence of dose and animal species on accelerated blood clearance of PEGylated liposomal doxorubicin. *Int J Pharmaceut* **476**, 205–212 (2014).

289. Suzuki, T. *et al.* Accelerated blood clearance of PEGylated liposomes containing doxorubicin upon repeated administration to dogs. *Int J Pharmaceut* **436**, 636–643 (2012).
290. Hashimoto, Y., Shimizu, T., Abu Lila, A. S., Ishida, T. & Kiwada, H. Relationship between the concentration of anti-polyethylene glycol (PEG) immunoglobulin M (IgM) and the intensity of the accelerated blood clearance (ABC) phenomenon against PEGylated liposomes in mice. *Biological Pharm Bulletin* **38**, 417–424 (2015).
291. Ishihara, T. *et al.* Accelerated Blood Clearance Phenomenon Upon Repeated Injection of PEG-modified PLA-nanoparticles. *Pharmaceut Res* **26**, 2270–2279 (2009).
292. Mima, Y., Hashimoto, Y., Shimizu, T., Kiwada, H. & Ishida, T. Anti-PEG IgM Is a Major Contributor to the Accelerated Blood Clearance of Polyethylene Glycol-Conjugated Protein. *Mol Pharmaceutics* **12**, 2429–2435 (2015).
293. Kozma, G. T. *et al.* Pseudo-anaphylaxis to Polyethylene Glycol (PEG)-Coated Liposomes: Roles of Anti-PEG IgM and Complement Activation in a Porcine Model of Human Infusion Reactions. *ACS Nano* **13**, 9315–9324 (2019).
294. Szebeni, J. *et al.* Role of complement activation in hypersensitivity reactions to doxil and hynic PEG liposomes: experimental and clinical studies. *J Liposome Res* **12**, 165–172 (2002).
295. Lila, A. S. A., Kiwada, H. & Ishida, T. The accelerated blood clearance (ABC) phenomenon: Clinical challenge and approaches to manage. *J Control Release* **172**, 38–47 (2013).
296. Romberg, B. *et al.* Poly(amino acid)s: promising enzymatically degradable stealth coatings for liposomes. *Int J Pharmaceut* **331**, 186–189 (2007).
297. Pytela, J., Saudek, V., Drobnik, J. & Rypáček, F. Poly (N5-hydroxyalkylglutamines). IV. Enzymatic degradation of N5-(2-hydroxyethyl)-L-glutamine homopolymers and copolymers. *J Control Release* **10**, 17–25 (1989).
298. O'Brien, M. E. R. *et al.* Randomized phase III trial comparing single-agent paclitaxel Poliglumex (CT-2103, PPX) with single-agent gemcitabine or vinorelbine for the treatment of PS 2 patients with chemotherapy-naïve advanced non-small cell lung cancer. *J Thorac Oncol* **3**, 728–734 (2008).
299. Li, C. & Wallace, S. Polymer-drug conjugates: recent development in clinical oncology. *Adv Drug Deliv Rev* **60**, 886–898 (2008).

300. Negwer, I. *et al.* Monitoring drug nanocarriers in human blood by near-infrared fluorescence correlation spectroscopy. *Nat Commun* **9**, 5306 (2018).
301. Cheng, J. & Deming, T. J. Synthesis of polypeptides by ring-opening polymerization of  $\alpha$ -amino acid N-carboxyanhydrides. *Top Curr Chem* **310**, 1–26 (2012).
302. Hartrampf, N. *et al.* Synthesis of proteins by automated flow chemistry. *Science* **368**, 980–987 (2020).
303. Lawrenson, S. B. Greener solvents for solid-phase organic synthesis. *Pure Appl Chem* **90**, 157–165 (2018).
304. Pickel, D. L., Politakos, N., Avgeropoulos, A. & Messman, J. M. A Mechanistic Study of  $\alpha$ -(Amino acid)-N-carboxyanhydride Polymerization: Comparing Initiation and Termination Events in High-Vacuum and Traditional Polymerization Techniques. **42**, 7781–7788 (2009).
305. Habraken, G. J. M., Wilsens, K. H. R. M., Koning, C. E. & Heise, A. Optimization of N -carboxyanhydride (NCA) polymerization by variation of reaction temperature and pressure. *Polym Chem* **2**, 1322–1330 (2011).
306. Leuchs, H. & Geiger, W. Über die Anhydride von  $\alpha$ -Amino-N-carbonsäuren und die von  $\alpha$ -Aminosäuren. *Ber Dtsch Chem Ges* **41**, 1721–1726 (1908).
307. Fuchs, F. Über N-Carbonsäure-anhydride. *Ber Dtsch Chem Ges* **55**, 2943–2943 (1922).
308. Farthing, A. C. 627. Synthetic polypeptides. Part I. Synthesis of oxazolid-2 : 5-diones and a new reaction of glycine. *J Chem Soc* **0**, 3213–3217 (1950).
309. Deming, T. J. Facile synthesis of block copolypeptides of defined architecture. *Nature* **390**, 386–389 (1997).
310. Semple, J. E., Sullivan, B. & Sill, K. N. Large-scale synthesis of  $\alpha$ -amino acid- N-carboxyanhydrides. *Synth Commun* **47**, 53–61 (2016).
311. Soria-Carrera, H. *et al.* On-POM Ring-Opening Polymerisation of N-Carboxyanhydrides. *Angew Chem Int* **60**, 3449–3453 (2021).
312. Xia, Y. *et al.* Accelerated polymerization of N -carboxyanhydrides catalyzed by crown ether. *Nat Commun* **12**, 1–8 (2021).

313. Statz, A. R., Barron, A. E. & Messersmith, P. B. Protein, cell and bacterial fouling resistance of polypeptoid-modified surfaces: effect of side-chain chemistry. *Soft Matter* **4**, 131–139 (2008).
314. Wang, J., Gong, C., Wang, Y. & Wu, G. Magnetic and pH sensitive drug delivery system through NCA chemistry for tumor targeting. *RSC Adv* **4**, 15856–15862 (2014).
315. Xu, G. *et al.* PEG-*b*-(PELG-*g*-PLL) nanoparticles as TNF- $\alpha$  nanocarriers: potential cerebral ischemia/reperfusion injury therapeutic applications. *Int J Nanomedicine* **12**, 2243–2254 (2017).
316. Rideau, E., Dimova, R., Schwille, P., Wurm, F. R. & Landfester, K. Liposomes and polymersomes: a comparative review towards cell mimicking. *Chem Soc Rev* **47**, 8572–8610 (2018).
317. Israelachvili, J. N., Mitchell, D. J. & Ninham, B. W. Theory of self-assembly of hydrocarbon amphiphiles into micelles and bilayers. *J Chem Soc, Faraday Trans 2* **72**, 1525–1568 (1976).
318. Yan, Y. *et al.* Molecular Packing Parameter in Bolaamphiphile Solutions: Adjustment of Aggregate Morphology by Modifying the Solution Conditions. *J Phys Chem B* **111**, 2225–2230 (2007).
319. Khalil, R. A. & Al-hakam, Z. A. Theoretical estimation of the critical packing parameter of amphiphilic self-assembled aggregates. *Nano Today* **318**, 85–89 (2014).
320. Watanabe, N., Suga, K. & Umakoshi, H. Functional Hydration Behavior: Interrelation between Hydration and Molecular Properties at Lipid Membrane Interfaces. *J Chem* **2019**, 1–15 (2019).
321. Nagarajan, R. Molecular Packing Parameter and Surfactant Self-Assembly: The Neglected Role of the Surfactant Tail. *Langmuir* **18**, 31–38 (2001).
322. Lairion, F. & Disalvo, E. A. Effect of dipole potential variations on the surface charge potential of lipid membranes. *J Phys Chem B* **113**, 1607–1614 (2009).
323. Voggel, M. *et al.* Sweet surfactants: packing parameter-invariant amphiphiles as emulsifiers and capping agents for morphology control of inorganic particles. *Soft Matter* **14**, 7214–7227 (2018).

324. Shamay, Y. *et al.* Quantitative self-assembly prediction yields targeted nanomedicines. *Nat Mater* **17**, 361–368 (2018).
325. Fan, J. *et al.* Multi-responsive polypeptide hydrogels derived from N -carboxyanhydride terpolymerizations for delivery of nonsteroidal anti-inflammatory drugs. *Org Biomol Chem* **15**, 5145–5154 (2017).
326. Fetsch, C., Grossmann, A., Holz, L., Nawroth, J. F. & Luxenhofer, R. Polypeptoids from N-Substituted Glycine N-Carboxyanhydrides: Hydrophilic, Hydrophobic, and Amphiphilic Polymers with Poisson Distribution. *Macromolecules* **44**, 6746–6758 (2011).
327. Wibowo, S. H., Sulistio, A., Wong, E. H. H., Blencowe, A. & Qiao, G. G. Functional and Well-Defined  $\beta$ -Sheet-Assembled Porous Spherical Shells by Surface-Guided Peptide Formation. *Adv Funct Mater* **25**, 3147–3156 (2015).
328. Hanay, S. B., Brougham, D. F., Dias, A. A. & Heise, A. Investigation of the triazolinedione (TAD) reaction with tryptophan as a direct route to copolypeptide conjugation and cross-linking. *Polym Chem* **8**, 6594–6597 (2017).
329. Mohamed, M. G., Tu, J.-H., Huang, S.-H., Chiang, Y.-W. & Kuo, S.-W. Hydrogen bonding interactions affect the hierarchical self-assembly and secondary structures of comb-like polypeptide supramolecular complexes displaying photoresponsive behavior. *RSC Adv* **6**, 51456–51469 (2016).
330. Huesmann, D. *et al.* Exploring new activating groups for reactive cysteine NCAs. *Tetrahedron Lett* **57**, 1138–1142 (2016).
331. Cotarca, L., Geller, T. & Répási, J. Bis(trichloromethyl)carbonate (BTC, Triphosgene): A Safer Alternative to Phosgene? *Org Process Res Dev* **21**, 1439–1446 (2017).
332. Pauluhn, J. Acute nose-only inhalation exposure of rats to di- and triphosgene relative to phosgene. *Inhal Toxicol* **23**, 65–73 (2011).
333. Doriti, A., Brosnan, S. M., Weidner, S. M. & Schlaad, H. Synthesis of polysarcosine from air and moisture stable N-phenoxy carbonyl-N-methylglycine assisted by tertiary amine base. *Polym Chem* **7**, 3067–3070 (2016).
334. Endo, T. & Sudo, A. Well-defined, environment-friendly synthesis of polypeptides based on phosgene-free transformation of amino acids into urethane derivatives and their applications. *Polym Int* **69**, 219–227 (2020).

335. Koga, K., Sudo, A. & Endo, T. Revolutionary phosgene-free synthesis of  $\alpha$ -amino acid N-carboxyanhydrides using diphenyl carbonate based on activation of  $\alpha$ -amino acids by converting into imidazolium salts. *J Polym Sci Part A: Polym Chem* **48**, 4351–4355 (2010).
336. Rivero, I. A., Heredia, S. & Ochoa, A. Esterification of amino acids and mono acids using triphosgene. **31**, 2169–2175 (2001).
337. Chan, N. J.-A. *et al.* Spider-silk inspired polymeric networks by harnessing the mechanical potential of  $\beta$ -sheets through network guided assembly. **11**, 1630 (2020).
338. Skoulas, D., Stavroulaki, D., Santorinaios, K. & Iatrou, H. Synthesis of Hybrid-Polypeptides m-PEO-*b*-poly(His-co-Gly) and m-PEO-*b*-poly(His-co-Ala) and Study of Their Structure and Aggregation. Influence of Hydrophobic Copolypeptides on the Properties of Poly(L-histidine). *Polymers* **9**, (2017).
339. Tickler, A. K. & Wade, J. D. Overview of Solid Phase Synthesis of ‘Difficult Peptide’ Sequences. *Curr Protoc Protein Sci* **50**, 18.8.1–18.8.6 (2007).
340. Mueller, L. K., Baumruck, A. C., Zhdanova, H. & Tietze, A. A. Challenges and Perspectives in Chemical Synthesis of Highly Hydrophobic Peptides. *Front Bioeng Biotechnol* **8**, 162 (2020).
341. Lorusso, M., Pepe, A., Ibris, N. & Bochicchio, B. Molecular and supramolecular studies on polyglycine and poly-L-proline. *Soft Matter* **7**, 6327–6336 (2011).
342. Bykov, S. & Asher, S. Raman studies of solution polyglycine conformations. *J Phys Chem B* **114**, 6636–6641 (2010).
343. Ohnishi, S., Kamikubo, H., Onitsuka, M., Kataoka, M. & Shortle, D. Conformational preference of polyglycine in solution to elongated structure. *J Am Chem Soc* **128**, 16338–16344 (2006).
344. Karandur, D., Wong, K.-Y. & Pettitt, B. M. Solubility and aggregation of Gly(5) in water. *J Phys Chem B* **118**, 9565–9572 (2014).
345. Keten, S., Xu, Z., Ihle, B. & Buehler, M. J. Nanoconfinement controls stiffness, strength and mechanical toughness of beta-sheet crystals in silk. *Nat Mater* **9**, 359–367 (2010).
346. Tokareva, O., Jacobsen, M., Buehler, M., Wong, J. & Kaplan, D. L. Structure-function-property-design interplay in biopolymers: spider silk. *Acta Biomater* **10**, 1612–1626 (2014).

347. Liu, J. & Ling, J. DFT Study on Amine-Mediated Ring-Opening Mechanism of  $\alpha$ -Amino Acid N-Carboxyanhydride and N-Substituted Glycine N-Carboxyanhydride: Secondary Amine versus Primary Amine. *J Phys Chem B* **119**, 7070–7074 (2015).
348. Lau, K. H. A. *et al.* Surface-grafted polysarcosine as a peptoid antifouling polymer brush. *Langmuir* **28**, 16099–16107 (2012).
349. Bleher, S. *et al.* Poly(Sarcosine) Surface Modification Imparts Stealth-Like Properties to Liposomes. *Small* **15**, e1904716 (2019).
350. Heller, P. *et al.* Directed interactions of block copolypept(o)ides with mannose-binding receptors: PeptoMicelles targeted to cells of the innate immune system. *Macromol Biosci* **15**, 63–73 (2015).
351. Weber, B. *et al.* Polysarcosine-Based Lipids: From Lipopolypeptoid Micelles to Stealth-Like Lipids in Langmuir Blodgett Monolayers. *Polymers* **8**, (2016).
352. Isidro-Llobet, A., Álvarez, M. & Albericio, F. Amino acid-protecting groups. *Chem Rev* **109**, 2455–2504 (2009).
353. Espeel, P. & Prez, Du, F. E. One-pot multi-step reactions based on thiolactone chemistry: A powerful synthetic tool in polymer science. *Eur Polym J* **62**, 247–272 (2015).
354. Garel, J. & Tawfik, D. S. Mechanism of Hydrolysis and Aminolysis of Homocysteine Thiolactone. *Chem Eur J* **12**, 4144–4152 (2006).
355. Krannig, K.-S., Doriti, A. & Schlaad, H. Facilitated Synthesis of Heterofunctional Glycopolypeptides. *Macromolecules* **47**, 2536–2539 (2014).
356. Schäfer, O., Huesmann, D., Muhl, C. & Barz, M. Rethinking Cysteine Protective Groups: S-Alkylsulfonyl-L-Cysteines for Chemoselective Disulfide Formation. *Chemistry* **22**, 18085–18091 (2016).
357. Al-Amin, M. D. *et al.* Dexamethasone Loaded Liposomes by Thin-Film Hydration and Microfluidic Procedures: Formulation Challenges. *Int J Mol Sci* **21**, (2020).
358. Torres-Flores, G., Gonzalez-Horta, A., Vega-Cantu, Y. I., Rodriguez, C. & Rodriguez-Garcia, A. Preparation and Characterization of Liposomal Everolimus by Thin-Film Hydration Technique. *Adv in Polym Technol* **2020**, 1–9 (2020).

359. Tao, J., Chow, S. F. & Zheng, Y. Application of flash nanoprecipitation to fabricate poorly water-soluble drug nanoparticles. *Acta Pharm Sin B* **9**, 4–18 (2019).
360. Kumar, V. & Prud'homme, R. K. Nanoparticle stability: Processing pathways for solvent removal. *Chem Eng Sci* **64**, 1358–1361 (2009).
361. Chow, S. F. *et al.* Development of highly stabilized curcumin nanoparticles by flash nanoprecipitation and lyophilization. *Eur J Pharm Biopharm* **94**, 436–449 (2015).
362. Markwalter, C. E., Pagels, R. F., Wilson, B. K., Ristroph, K. D. & Prud'homme, R. K. Flash NanoPrecipitation for the Encapsulation of Hydrophobic and Hydrophilic Compounds in Polymeric Nanoparticles. *J Vis Exp* **143**, e58757 (2019).
363. Danaei, M. *et al.* Impact of Particle Size and Polydispersity Index on the Clinical Applications of Lipidic Nanocarrier Systems. *Pharm* **10**, (2018).
364. Sletten, E. M. & Bertozzi, C. R. Bioorthogonal chemistry: fishing for selectivity in a sea of functionality. *Angew Chem Int* **48**, 6974–6998 (2009).
365. Boutureira, O. & Bernardes, G. J. L. Advances in chemical protein modification. *Chem Rev* **115**, 2174–2195 (2015).
366. Proietti, G., Rainone, G., Hintzen, J. C. J. & Mecinović, J. Exploring the Histone Acylome through Incorporation of  $\gamma$ -Thialysine on Histone Tails. *Bioconjugate Chem* **31**, 844–851 (2020).
367. Tinajero-Díaz, E., Martínez de Ilarduya, A. & Muñoz-Guerra, S. Copolymacrolactones Grafted with L-Glutamic Acid: Synthesis, Structure, and Nanocarrier Properties. *Polymers* **12**, (2020).
368. Yu, H., Gu, X., Shen, X., Li, Y. & Duan, Y. Synthesis and characterization of biodegradable block copolymer pluronic-b-poly(L-lysine). *J Appl Polym Sci* **112**, 3371–3379 (2009).
369. Dmitrovic, V. *et al.* Random Poly(Amino Acid)s Synthesized by Ring Opening Polymerization as Additives in the Biomimetic Mineralization of CaCO<sub>3</sub>. *Polymers* **4**, 1195–1210 (2012).
370. Bortolotti, A. *et al.* On the purported 'backbone fluorescence' in protein three-dimensional fluorescence spectra. *RSC Adv* **6**, 112870–112876 (2016).

371. Bellmaine, S., Schnellbaecher, A. & Zimmer, A. Reactivity and degradation products of tryptophan in solution and proteins. *Free Radic Biol Med* **160**, 696–718 (2020).
372. Uchida, C., Iizuka, Y., Ohta, E., Wakamatsu, K. & Oya, M. Synthesis and Properties of High-Molecular-Weight Polypeptides Containing Tryptophan II. Copolypeptides of Tryptophan with Various Amino Acids. *Bull Chem Soc Jpn* **69**, 791–796 (1996).
373. Xiang, Y., Si, J., Zhang, Q., Liu, Y. & Guo, H. Homogeneous graft copolymerization and characterization of novel artificial glycoprotein: Chitosan-poly(L-tryptophan) copolymers with secondary structural side chains. *J Polym Sci Part A: Polym Chem* **47**, 925–934 (2008).
374. Profit, A. A., Felsen, V., Chinwong, J., Mojica, E.-R. E. & Desamero, R. Z. B. Evidence of  $\pi$ -stacking interactions in the self-assembly of hIAPP(22-29). *Proteins* **81**, 690–703 (2013).
375. Song, B. *et al.* The Introduction of  $\pi$ - $\pi$  Stacking Moieties for Fabricating Stable Micellar Structure: Formation and Dynamics of Disklike Micelles. *Angew Chem Int* **44**, 4731–4735 (2005).
376. Liang, Y. *et al.* The effect of  $\pi$ -Conjugation on the self-assembly of micelles and controlled cargo release. *Artif Cells Nanomed Biotechnol* **48**, 525–532 (2020).
377. Lu, Y.-S., Lin, Y.-C. & Kuo, S.-W. Separated Coil and Chain Aggregation Behaviors on the Miscibility and Helical Peptide Secondary Structure of Poly(tyrosine) with Poly(4-vinylpyridine). *Macromolecules* **45**, 6547–6556 (2012).
378. Saha, A. *et al.* Combined atom-transfer radical polymerization and ring-opening polymerization to design polymer–polypeptide copolymer conjugates toward self-aggregated hybrid micro/nanospheres for dye encapsulation. *J Polym Sci Part A: Polym Chem* **53**, 2313–2319 (2015).
379. Liu, R., Shi, Z., Sun, J. & Li, Z. Enzyme responsive supramolecular hydrogels assembled from nonionic peptide amphiphiles. *Sci China Chem* **61**, 1314–1319 (2018).
380. Bischoff, R. & Schlüter, H. Amino acids: chemistry, functionality and selected non-enzymatic post-translational modifications. *J Proteomics* **75**, 2275–2296 (2012).
381. Kirkham, S. *et al.* Self-Assembly of Telechelic Tyrosine End-Capped PEO and Poly(alanine) Polymers in Aqueous Solution. *Biomacromolecules* **17**, 1186–1197 (2016).

382. Inada, A. & Kanazawa, H. Crystal structure of O-benzyl-L-tyrosine N-carb-oxy anhydride. *Acta Crystallogr E Crystallogr Commun* **73**, 553–555 (2017).
383. Hermanson, G. T. *Bioconjugate Techniques*. (Academic Press, 2010).
384. Discher, B. M. *et al.* Polymersomes: tough vesicles made from diblock copolymers. *Science* **284**, 1143–1146 (1999).
385. Lodish, H. *et al.* in *Molecular Cell Biology* (W. H. Freeman, 2000).
386. Chaudhuri, T. K. & Paul, S. Protein-misfolding diseases and chaperone-based therapeutic approaches. *FEBS J* **273**, 1331–1349 (2006).
387. Fields, G. B. Introduction to peptide synthesis. *Curr Protoc Protein Sci* **Chapter 18**, Unit 18.1 (2002).
388. Kreidt, E., Leis, W. & Seitz, M. Direct solid-phase synthesis of molecular heterooligonuclear lanthanoid-complexes. *Nat Commun* **11**, 1–7 (2020).
389. Shamout, F., Fischer, L., Snyder, N. L. & Hartmann, L. Recovery, Purification, and Reusability of Building Blocks for Solid Phase Synthesis. *Macromolecular Rapid Communications* **41**, e1900473 (2020).
390. Merrifield, R. Solid phase peptide synthesis. I. The synthesis of a tetrapeptide. *Macromolecules* **85**, 2149–2154 (1963).
391. Kallmyer, N. E., Rider, N. E. & Reuel, N. F. Design and validation of a frugal, automated, solid-phase peptide synthesizer. *PLOS ONE* **15**, e0237473 (2020).
392. Isidro-Llobet, A. *et al.* Sustainability Challenges in Peptide Synthesis and Purification: From R&D to Production. *J Org Chem* **84**, 4615–4628 (2019).
393. Paradís-Bas, M., Tulla-Puche, J. & Albericio, F. The road to the synthesis of ‘difficult peptides’. *Chem Soc Rev* **45**, 631–654 (2016).
394. Hibi, Y., Ouchi, M. & Sawamoto, M. A strategy for sequence control in vinyl polymers via iterative controlled radical cyclization. *Nat Commun* **7**, 1–9 (2016).
395. Zhou, L.-Y. *et al.* Novel zwitterionic vectors: Multi-functional delivery systems for therapeutic genes and drugs. *Comput Struct Biotechnol J* **18**, 1980–1999 (2020).

396. Ziemba, C. *et al.* Antifouling Properties of a Self-Assembling Glutamic Acid-Lysine Zwitterionic Polymer Surface Coating. *Langmuir* **35**, 1699–1713 (2019).
397. Nishimori, K. & Ouchi, M. AB-alternating copolymers via chain-growth polymerization: synthesis, characterization, self-assembly, and functions. *Chem. Commun.* **56**, 3473–3483 (2020).
398. Huang, J. & Turner, R. Recent advances in alternating copolymers: The synthesis, modification, and applications of precision polymers. *Polymer* **116**, 572–586 (2017).
399. Li, L., Raghupathi, K., Song, C., Prasad, P. & Thayumanavan, S. Self-assembly of random copolymers. *Chem. Commun.* **50**, 13417–13432 (2014).
400. Patyukova, E., Xi, E. & Wilson, M. R. Phase Behavior of Correlated Random Copolymers. *Macromolecules* **54**, 2763–2773 (2021).
401. Lynd, N. A., Ferrier, R. C., Jr & Beckingham, B. S. Recommendation for accurate experimental determination of reactivity ratios in chain copolymerization. **52**, 2277–2285 (2019).
402. Hagiopol, C. *Copolymerization*. (Springer Science+Business Media New York, 1999). doi:10.1007/978-1-4615-4183-7
403. Fogler, H. S. *Elements of Chemical Reaction Engineering*. (Prentice Hall, 1998).
404. Schulz, G. V. in *Polymerization Kinetics and Technology* (ed. Platzner, N. A. J.) **128**, 1–20 (1973).
405. Mayo, F. R. & Lewis, F. M. Copolymerization. I. A Basis for Comparing the Behavior of Monomers in Copolymerization; The Copolymerization of Styrene and Methyl Methacrylate. **66**, 1594–1601 (1944).
406. Fineman, M. & Ross, S. D. Linear method for determining monomer reactivity ratios in copolymerization. *J Polym Sci* **5**, 259–262 (1950).
407. Kelen, T. & Tüdös, F. Analysis of the Linear Methods for Determining Copolymerization Reactivity Ratios. I. A New Improved Linear Graphic Method. *J Macromol Sci A* **9**, 1–27 (1975).
408. Ishiwari, K., Hayashi, T. & Nakajima, A. Monomer Reactivity Ratios in Copolymerization of  $\gamma$ -Benzyl L -Glutamate and L -Valine N -Carboxyanhydrides. *Polym J* **10**, 87–91 (1978).

409. Wall, F. T. The Structure of Copolymers. II1. *J Am Chem Soc* **66**, 2050–2057 (1944).
410. Reis, M. H., Davidson, C. L. G. & Leibfarth, F. A. Continuous-flow chemistry for the determination of comonomer reactivity ratios. *Polym Chem* **9**, 1728–1734 (2018).
411. Burt, RA. Stealth Polyamino-acid Biomaterials: Chemical Synthesis, Polymer Design & Nanomedicine Applications. (Northwestern University, 2019).
412. Zelzer, M. & Heise, A. Determination of copolymerisation characteristics in the N-carboxy anhydride polymerisation of two amino acids. *Polym Chem* **4**, 3896–3904 (2013).
413. Bargagna-Mohan, P. *et al.* The tumor inhibitor and antiangiogenic agent withaferin A targets the intermediate filament protein vimentin. *Chem Biol* **14**, 623–634 (2007).
414. Krishnan, S. M. *et al.* Pharmacological inhibition of the NLRP3 inflammasome reduces blood pressure, renal damage, and dysfunction in salt-sensitive hypertension. *Cardiovasc Res* **115**, 776–787 (2019).
415. Kalafatovic, D. & Giralt, E. Cell-Penetrating Peptides: Design Strategies beyond Primary Structure and Amphipathicity. *Molecules* **22**, (2017).
416. Ellert-Miklaszewska, A., Poleszak, K. & Kaminska, B. Short peptides interfering with signaling pathways as new therapeutic tools for cancer treatment. *Future Med Chem* **9**, 199–221 (2017).
417. Sorgdrager, F. J. H., Naudé, P. J. W., Kema, I. P., Nollen, E. A. & Deyn, P. P. D. Tryptophan Metabolism in Inflammaging: From Biomarker to Therapeutic Target. *Front Immunol* **10**, 2565 (2019).
418. Liu, X. *et al.* 1-L-MT, an IDO inhibitor, prevented colitis-associated cancer by inducing CDC20 inhibition-mediated mitotic death of colon cancer cells. *Int J Cancer* **143**, 1516–1529 (2018).
419. Agaugué, S., Perrin-Cocon, L., Coutant, F., André, P. & Lotteau, V. 1-Methyl-tryptophan can interfere with TLR signaling in dendritic cells independently of IDO activity. *J Immunol* **177**, 2061–2071 (2006).
420. Lovelace, M. D. *et al.* Current Evidence for a Role of the Kynurenine Pathway of Tryptophan Metabolism in Multiple Sclerosis. *Front Immunol* **7**, 246 (2016).

421. Stone, T. W. & Darlington, L. G. The kynurenine pathway as a therapeutic target in cognitive and neurodegenerative disorders. *Br J Pharmacol* **169**, 1211–1227 (2013).
422. Perron, V. *et al.* A Method for the Selective Protection of Aromatic Amines in the Presence of Aliphatic Amines. *Synthesis* **2009**, 283–289 (2008).
423. Wu, H.-Y. *et al.* Assessing the Similarity between Random Copolymer Drug Glatiramer Acetate by Using LC-MS Data Coupling with Hypothesis Testing. *Anal Chem* **91**, 14281–14289 (2019).
424. Komlosh, A. *et al.* Physicochemical and Biological Examination of Two Glatiramer Acetate Products. *Biomedicines* **7**, (2019).

## Curriculum Vitae

### Molly Frey

---

#### EDUCATION

2023, <i>planned</i>	M.D.	Feinberg School of Medicine	
2021, <i>planned</i>	Ph.D.	Northwestern University	Biological Sciences
2014	B.S.	Drake University	Biology
2014	B.S.	Drake University	Biochemistry, Cell & Molecular Biology
2014	B.A.	Drake University	Chemistry

---

#### RESEARCH AND PROFESSIONAL EXPERIENCE

2016 – present	PhD Candidate Researcher	Scott Lab, Northwestern University
2018 – present	PhD Candidate Researcher	Meade Lab, Northwestern University
2010 – 2014	Undergraduate Researcher	Mirafzal Lab, Drake University
2011 – 2014	Undergraduate Researcher	Dao Lab, Drake University

---

#### AWARDS, FELLOWSHIPS & GRANTS

2020	MSTP Travel Grant for BMES 2020
2014 – present	Medical Scientist Training Program Northwestern University Administered T32 Training Grant
2017 – 2019	Chemistry of Life Processes Training Grant Northwestern University Administered T32 Training Grant

---

#### HONORS, DISTINCTIONS

2013 – 2014	Outstanding Senior Award, Chemistry Department, Drake University
2013 – 2013	E.A. Sheslow Prize for Distinguished Leadership, Drake University
2011 – 2012	Ward H. Wilson and Marguerite M. Wilson Endowment Award, Drake University
2010 – 2011	ACS Polyed Organic Chemistry Award, Drake University

---

#### PROFESSIONAL SOCIETY MEMBERSHIPS

2014 – 2016	Phi Rho Sigma Medical Society
-------------	-------------------------------

---

**TEACHING**

June 2019 Biochemistry, Grader, Northwestern University  
Jan – March 2017 Cellular Processes Lab, Teaching Assistant, Northwestern University

---

**VOLUNTEERING AND OUTREACH**

2016 – present MSTP Admissions Committee Member, Feinberg School of Medicine  
2020 – 2021 Graduate Student Program Committee, CLP Symposium  
2017 – 2020 Shadowing/Tour Volunteer, Evanston High School Women in STEM  
Dec 2019 Group Leader, Expanding Your Horizons Winter 2019

---

**PUBLICATIONS**

**Frey M**, Vincent M, Bobbala S, Burt R, Scott EA. Mapping the supramolecular assembly space of poly(sarcosine)-*b*-poly(propylene sulfide) using a combinatorial copolymer library. *Chem Comm* **56**, 6644-6647 (2020). doi:10.1039/D0CC00925C.

Burke JA, Zhang X, Bobbala SXR, **Frey MA**, Bohorquez Furentes CB, Freire Haddad H, Allen SD, Richardson RAK, Ameer GA\*, Scott EA\*. Subcutaneous nanotherapy repurposes the immunosuppressive mechanism of rapamycin to enhance allogeneic islet graft viability. *Nat Nano* Accepted. Pending Publication. (2021).

Karabin NB\*, Vincent MP\*, Allen SD, Bobbala S, **Frey MA**, Yi S, Yang Y, Scott EA. The combination of morphology and surface chemistry defines the biological identity of nanocarriers in human blood. *Adv Ther*, 2100062 (2021).

Stack T, Liu YG, **Frey M**, Bobbala S, Vincent M, Scott EA. Enhancing subcutaneous injection and target tissue accumulation of nanoparticles via co-administration with macropinocytosis inhibitory nanoparticles (MiNP). *Nanoscale Horiz* **6**, 393-400 (2021).

Vincent M, Bobbala S, Karabin NB, **Frey M**, Liu Y, Navidzadeh JO, Stack T, Scott EA. Surface chemistry-mediated modulation of adsorbed albumin folding state specifies nanocarrier clearance by distinct macrophage subsets. *Nat Commun* **12**, 648 (2021).

Yi S, Karabin NB, Zhu J, Bobbala SK, Lyu H, Li S, Liu Y-G, **Frey MA**, Vincent MP, and Scott EA. An injectable hydrogel platform for sustained delivery of anti-inflammatory nanocarriers and induction of regulatory T cells in atherosclerosis. *Front Bioeng Biotechnol* **8**, 542 (2020). doi: 10.3389/fbioe.2020.00542.

Bobbala SK, Allen SD, Yi S, Vincent MP, **Frey MA**, Karabin NB, Scott EA. employing bicontinuous-to-micellar transitions in nanostructure morphology for on-demand photo-oxidation responsive cytosolic delivery and off-on cytotoxicity. *Nanoscale*. **12**, 5332-5340 (2020).

Modak M, **Frey MA**, Yi S, Liu Y, Scott EA. Employment of targeted nanoparticles for imaging of cellular processes in cardiovascular disease. *Curr Opin Biotechnol* **66**, 59-68 (2020).

**Frey MA**, Bobbala SK, Karabin NB, Scott EA. Influences of nanocarrier morphology on therapeutic immunomodulation. *Nanomedicine (Lond)* **13**, 1795-1811 (2018)

---

## MANUSCRIPTS IN PREPARATION

**Frey MA**, Vincent M, Scott EA. Improved synthesis and purification of functionalized poly(ethylene glycol) for the preparation of thiolate-initiated copolymer blocks for nanomaterials. 2021.

Burt RA\*, **Frey MA\***, Torkelson JM, Scott EA. Kinetic Analysis Reveals General Sequence Control Capability of NCA Copolymerization with Implications for Zwitterionic Poly(amino acid) Biomaterials. (2021).

Yi S\*, Kim SY\*, Vincent M, **Frey M**, Du F, Scott EA. Cationic Dendritic Peptide Conjugated Synthetic Nanovector to Improve Large Plasmid DNA Delivery in Various Immune Cells for Efficient Genetic Engineering Technology. (2021).

---

## CONFERENCE PRESENTATIONS AND ABSTRACTS

Oral and poster presentations: Burke JA, Zhang X, Bobbala SKR, **Frey MA**, Bohorquez Fuentes C, Freire Haddad H, Allen SD, Richardson RAK, Ameer GA, Scott EA. "Subcutaneous nanotherapy repurposes the immunosuppressive mechanism of rapamycin to enhance allogeneic islet graft viability." Autumn Immunology Conference, Chicago, IL, 2021.

Oral presentation: Burke JA, Zhang X, Bobbala SKR, **Frey MA**, Bohorquez Fuentes C, Freire Haddad H, Allen SD, Richardson RAK, Ameer GA, Scott EA. "Subcutaneous nanotherapy repurposes the immunosuppressive mechanism of rapamycin to enhance allogeneic islet graft viability." 18<sup>th</sup> World Congress of the International Pancreas and Islet Transplant Association, virtual, 2021.

Poster presentation: Burke JA, Zhang X, Bobbala SKR, **Frey MA**, Bohorquez Fuentes C, Freire Haddad H, Allen SD, Richardson RAK, Ameer GA, Scott EA. "Subcutaneous nanotherapy repurposes the immunosuppressive mechanism of rapamycin to enhance allogeneic islet graft viability." Biomedical Engineering Society Annual Meeting, Orlando, FL, 2021.

Oral presentation: Burke JA, Zhang X, Bobbala SKR, **Frey MA**, Bohorquez Fuentes C, Freire Haddad H, Allen SD, Richardson RAK, Ameer GA, Scott EA. "Subcutaneous nanotherapy repurposes the immunosuppressive mechanism of rapamycin to enhance allogeneic islet graft viability." NUGoKidney Kidney Disease Therapeutic Innovation Symposium, Chicago, IL, 2021.

Oral presentation: **Frey M**, Vincent M, Bobbala S, Burt R, Scott EA. "Optimizing Polymersome Self-Assembly from a Novel Poly(Sarcosine)-*b*-Poly(Propylene Sulfide) Copolymer." Biomedical Engineering Society Virtual Annual Meeting, virtual, 2020.

Oral presentation: **Frey M**, Vincent M, Bobbala S, Burt R, Scott EA. "Optimizing Polymersome Self-Assembly from a Novel Poly(Sarcosine)-*b*-Poly(Propylene Sulfide) Copolymer." IBiS Annual Retreat, virtual, 2020

Oral presentation: Burke JA, Zhang X, Bobbala SK, **Frey MA**, Ameer GA, Scott EA. "Costimulation blockade via cell-selective delivery of rapamycin-loaded nanobiomaterials." 11<sup>th</sup> World Biomaterials Congress 2020, Glasgow, Scotland, virtual, 2020.

Poster presentation: **Frey MA**, Scott EA. "The modular design of highly tunable polymer materials for targeted immunotheranostics." 2019 MSTP Annual Retreat. Chicago, IL, 2019.

Oral presentation: Burke JA, Zhang X, Bobbala SK, **Frey MA**, Ameer GA, Scott EA. "Immune call targeted delivery of immunosuppression of allogenic islet transplantation." 17<sup>th</sup> World Congress of the International Pancreas and Islet Transplant Association, Lyon, France. 2019.

Oral presentation: **Frey MA**, Scott EA. "NCA-based hydrophilic blocks for multi-functional theranostics." CLP Research Forum (Spring), Evanston, IL, 2019.

Poster presentation: **Frey MA**, Allen SD, Du F, Yi S, Liu Y, Bobbala SK, Karabin NB, Stack T, Modak M, Li S, Burke JA, Vincent MP, Scott EA. "Development of polymeric nanocarriers for basic science and translational immunomodulation." IBiS Admissions Days, Evanston, IL, 2019.

Oral presentation: **Frey MA**, Scott EA. "The modular design of highly tunable polymer materials for targeted immunotheranostics." CLP Research Forum (Winter), Evanston, IL, 2018.

Oral presentation: Burke JA, Zhu Y, Zhang X, Bobbala SKR, **Frey MA**, GA, Scott EA. "Targeted Rapamycin Nanoparticle Delivery For Enhanced Islet Transplantation Outcomes." Biomedical Engineering Society Annual Meeting, Atlanta, GA, 2018.

Poster presentation: **Frey MA**, Scott EA. "The modular design of highly tunable polymer materials for targeted immunotheranostics." Rising Stars of SQI Poster Session, Chicago, IL, 2018.

Poster presentation: **Frey MA**, Scott EA. "The modular design of highly tunable polymer materials for targeted immunotheranostics." CLP Kick-Off Poster Session, Chicago, IL, 2018.

Poster presentation: **Frey MA**, Allen SD, Du F, Yi S, Liu Y, Bobbala SK, Karabin NB, Stack T, Modak M, Li S, Burke JA, Vincent MP, Scott EA. "Development of polymeric nanocarriers for basic science and translational immunomodulation." 2018 IBiS Annual Retreat, Delavan, WI, 2018.

Poster presentation: **Frey MA**, Scott EA. "The modular design of highly tunable polymer materials for targeted immunotheranostics." 2018 MSTP Annual Retreat. Lake Geneva, WI, 2018

Oral presentation: **Frey MA**, Scott EA. "The modular design of highly tunable polymer materials for targeted immunotheranostics." CLP Research Forum (Spring), Evanston, IL, 2018.

Oral presentation: **Frey MA**, Scott EA. "Synthesis and characterization of a novel diblock copolymer for targeted MRI theranostics." CLP Research Forum (Winter), Evanston, IL, 2018.

Poster presentation: **Frey MA**, Allen SD, Du F, Yi S, Liu Y, Bobbala SK, Karabin NB, Stack T, Modak M, Li S, Burke JA, Vincent MP, Scott EA. "Development of polymeric nanocarriers for basic science and translational immunomodulation." IBiS Admissions Days, Evanston, IL, 2018

Poster presentation: **Frey MA**, Scott EA. "SPION-loaded oxidation responsive nanostructures as a targeted immunotheranostic tool." 2017 IBiS Annual Retreat, Zion, IL, 2017.

Poster presentation: **Frey MA**, Scott EA. "SPION-loaded oxidation responsive nanostructures as a targeted immunotheranostic tool." 2017 MSTP Annual Retreat. Delavan, WI, 2017.

Oral presentation: **Frey MA**, Shuda LE. "Synthesis of ultra-fast probe substrates to investigate the mechanism of P-450 monooxygenase enzyme." Sixth Annual American Chemical Society Illinois-Iowa Undergraduate Research Conference, Davenport, IA, 2013.